NORTHWESTERN UNIVERSITY

Electronic Implications of Thermal Processes in Nanomaterials

A DISSERTATION

SUBMITTED TO THE GRADUATE SCHOOL

IN PARTIAL FULFILLMENT OF THE REQUIREMENTS

for the degree

DOCTOR OF PHILOSOPHY

Field of Chemistry

By

Matthew S. Kirschner

EVANSTON, ILLINOIS

June 2019

ABSTRACT

Electronic Implications of Thermal Processes in Nanomaterials

Matthew S. Kirschner

Extensive study of nanomaterial chemical and optical properties has enabled their integration into a variety of applications. However, less thoroughly investigated are the heat generation and dissipation processes of nanomaterials following optical excitation. These phenomena are of immense importance as thermal energy can distort a material's structure, which has profound electronic implications. Here, two distinct thermal processes are examined. First, the physical integrity of nanocrystals under high fluence photoexcitation is examined. It is found that some semiconductor nanoparticles transiently disorder, or melt, following photoexcitation at sufficiently high fluences while other materials undergo reversible solid-solid phase transitions. The electronic implications of these structural distortions are also examined and the induced changes may be responsible for decreased device performances at high fluences. Second, coherent structural changes in plasmonic nanoparticles resulting from impulsive lattice heating are investigated. Rapidly generated, low order vibrations can cause periodic oscillations in particle geometry which in turn shift the plasmon resonance. This process is characterized using ultrafast spectroscopy across a wide range of sizes and excitation fluences. In an attempt to further understand and potentially utilize these thermally-induced electronic changes, these nanoparticles

are surface-functionalized with a molecular dye that electronically couples to the plasmon resonance. Through the development of new analysis techniques, it is revealed that the hybridization between the dye and the nanoparticles can be modulated by vibrations in the nanoparticle. These works emphasize the importance of understanding thermal processes in nanomaterials as there significant implications from heat induced structural changes.

ACKNOWLEDGEMENTS

This thesis would not exist if it were not for the efforts of many people. I'd first like to thank **Richard Schaller** and **Lin Chen**, my advisors. Rich, your wealth of knowledge and willingness to discuss research strategies has shaped the way I approach problems. Lin, your constant encouragement and support has proven invaluable over the past five year. I would also like to thank my undergraduate advisor **Herschel Rabitz** and the researcher I worked with, **Francois Laforge**. The lessons I learned helped me hit the ground running in graduate school and helped me be as productive as I was. I'd also like to thank the other members of my committee **Emily Weiss** and **Toru Shiozaki** for providing feedback and making sure my research was on the right track.

I would also like to thank many of the people I have worked with. My two research groups, the **Chen Group** and the **Schaller Group**, greatly contributed to my success. I would especially like to thank **Daniel Hannah** for being a great mentor and collaborator, even after leaving Northwestern. I would also like to thank **Sam Brown-Xu**, **Denis Leshchev**, **Austin Spencer**, **Matt Kelly**, **Tom Fauvell**, **Dolev Rimmerman**, **Nathan Flanders**, **Ariel Leonard**, and **Waleed Helweh** for making it worthwhile to come in every day. I would like to thank **Xiao-Min Lin** and **Ben Diroll** for being great synthetic collaborators; I never had to worry about having access to the best materials, I only had to ask. I'd also like to thank **George Schatz**, **Clotilde Letheic**, **Craig Chapman**, **Wendu Ding**, and **Yeonjun Jeong** for all of the theoretical work—the insight provided made the science make sense. I'm also extremely grateful for Clotilde helping me write my first

paper. Understanding how to write a paper is hard, but it was made much easier through having someone to work with.

I would like to thank the people who kept me sane as well. I'd like to thank all of my soccer team, **Give 'Em El**. It was weird having a year in graduate school where so much time of my free time was spent managing a soccer team. I would not have predicted it, but am extremely glad it happened. Recently, it's been really great seeing **ACiDS** take off, which of course, would not have been possible without **Jordan Nelson** or **Denis Leshchev**. I would also like to thank my former roommate, **Paul Ohno**—we're a ways away from slacklining at 2 am, but it's been a great run. Finally, I'd like to thank my family, especially my immediate family. They've listened to me complain a lot over the past five year, and I'm sure in the future, they'll continue to listen to me complain a lot more.

TABLE OF CONTENTS

LIST OF FIGURES

Figure 6.3. (a) Experimental (in blue, arbitrary unit) absorption spectrum measured on Sample C. The absorption spectrum calculated on a gold bipyramid with the same dimensions as Sample C is also plotted (in red). The theoretical spectrum displays both the transverse (around 512 nm) and longitudinal (at 829 nm, dash line) plasmon resonances. The experimental transverse plasmon resonance overlaps with the plasmon band from the impurities in the sample. Inset: FDTD simulation of the 2D projected near-field enhancement around the same gold bipyramid as in a, calculated at 829 nm. (b) Measured (blue) and calculated (red) oscillation period of the vibrational mode as a function of the longitudinal plasmon resonance for the five samples of gold bipyramids. Inset: simulated displacement of a bipyramid during acoustic mode oscillation (not at scale).. 116

Figure 6.4. (a) LSPR shift from different particle expansions as estimated from FDTD and FEA simulations. While the particle elongations in these theory calculations are much larger than is observed experimentally, they can be extrapolated to predict dynamics on experimental scales that are not computationally feasible. Since FDTD is highly sensitive to small changes in bipyramid geometry and high-resolution meshing there is some uncertainty in these calculations, on the order of a few wavenumbers. (b) LSPR shifts observed from coherent acoustic phonons normalized for particle size. Unit cells were assumed to be FCC structure (4 atoms per unit cell) and particle absorption cross sections, listed in Table D.1, were taken from FDTD calculations. Error bars are the 95% confidence interval from the fitting algorithm. (c) Particle elongation versus photons absorbed per unit cell from the experimental data in b combined with a calibration curve generated from theory results in a. Error bars are the same as those in b. (d) Slopes of linear fits of the data in c along with expected slopes based on the linear thermal expansion coefficient and

LIST OF TABLES

CHAPTER 1:THE UNIQUE PROPERTIES OF NANOMATERIALS

Parts of this chapter is based on the following review:

Diroll, B. T.; Kirschner, M. S.; Guo, P.;Schaller, R. D. Annu. Rev. Phys. Chem. (In Review)

1.1. Nanomaterials and Their Appeal

Materials with one or more dimension on the length scale of 1 to 100's of nanometers are categorized as nanomaterials. Nanomaterials have a long history of human usage dating back to the 5th century B.C when they were first used, unknowingly, to give color to decorative ceramics and glasses.[1] In recent decades, advances in nanomaterial fabrication and synthesis, as well as characterization, have led to the integration of nanomaterials into numerous modern applications, in everything ranging from sunscreens[2] to televisions.[3,4] On a fundamental level, it is valuable to fabricate and manipulate materials on this length scale. Miniaturization of existing technologies is desirable in a wide range of contexts, perhaps most notably in the realm of electronics where reductions in transistor size into the nanoscale have enabled the current revolution in computing power.[5,6] Further, in some applications smaller materials are inherently more effective, such as in drug delivery, where smaller particles have higher cellular uptakes.[7]

However, as a material's size is reduced, the effective physics that material experiences might change. Physical forces have different distance dependencies and so the relative importance of these various forces can be drastically altered on the nanoscale. Some of the most notable examples of this phenomenon occur as the result of the increased surface area to volume ratio

inherent to smaller sizes. Because a higher percentage of atoms are at the surface, the relative importance of surface energy compared to internal energy increases which can result in nanomaterials having crystal structures distinct from their bulk counterparts.[8,9] Further, manipulating surface states becomes one of the primary engineering concerns when trying to make use of the electronic properties of a nanomaterial.[10] Through the remainder of this chapter, I will lay out two specific examples of phenomena that are distinct to nanomaterials and discuss how they enable new applications. I then move on to discuss how the thermal properties of a material can be different on the nanoscale and finally conclude with an overview of this thesis.

1.2. Semiconductor Nanocrystals

In a bulk semiconductor, there is a characteristic length scale that electron-hole pairs or excitons delocalize out into known as the Bohr Radius. This is a material specific constant that depends on the Coulombic interactions between electrons and holes in the material. When a semiconducting material has one or more of its dimensions on order of or smaller than its Bohr Radius, excitons in that material experience quantum confinement increasing their energy. When a material has all of its dimensions on this length scale, it is referred to as a semiconductor nanocrystal (NC) or quantum dot. The band gap of a NC, as determined by the lowest energy exciton, is described by the equation

$$E_g(R) = E_{g\,\text{bulk}} + \frac{\pi^2\hbar^2}{2m_r R^2} \qquad (1.1)$$

where E_g is the band gap, R is the NC radius, and $m_r = (m_e^{-1} + m_h^{-1})^{-1}$ with m_e and m_h being the effective mass of the electron and hole respectively.[11] Thereby, by synthetically tuning NC size, it is possible to control NC band gap resulting in NCs of the same composition having drastically different optical properties. This type of behavior is diagrammed out in Figure 1.1 which cartoons out how decreases in NC size result in increases in band gap. Another effect of the reduction in semiconductor size is that electronic states become more molecular-like and discrete in contrast to the continuous energy bands seen in bulk materials.[12] These excitonic states have finite degeneracies with the lowest energy, band-edge state typically having a degeneracy of two for spherical NCs.[12]

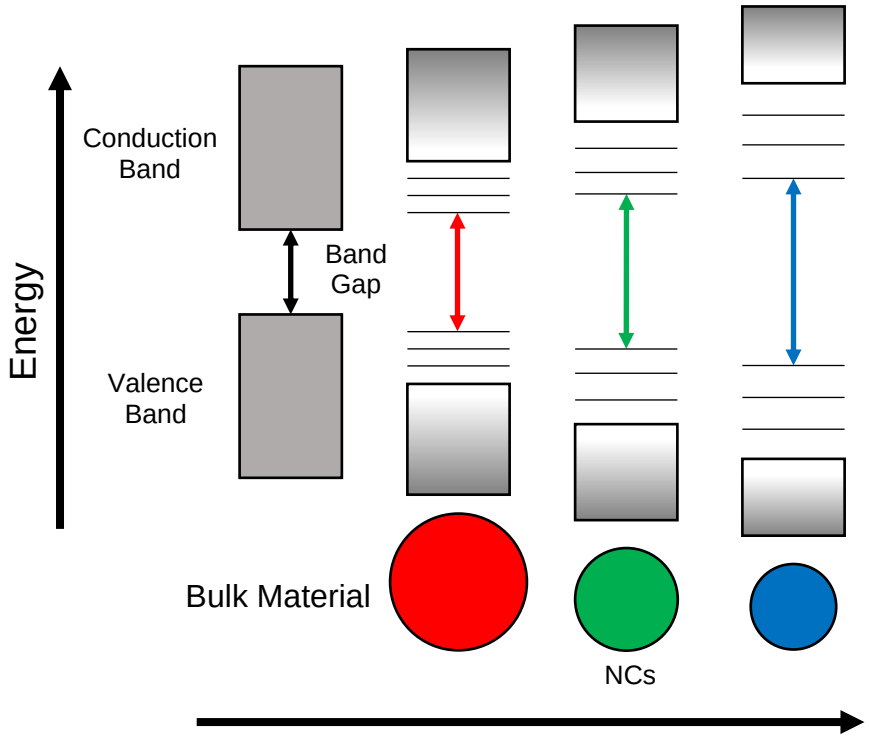

Figure 1.1. Schematic of changing band gap energy by tuning NC Size.

Having synthetically tunable electronic properties, as well as other favorable intrinsic characteristics, have led to the integration of NCs into a range of applications. The ability to change NC surfaces to target specific biomolecules[13] coupled with their favorable optoelectronic properties have enabled NCs to be used for bioimaging and cellular labeling.[14–16] There have also been efforts to integrate them as a sensitizing agent in photovoltaic devices due to their ability to efficiently absorb a wide range of wavelengths of light, with devices efficiencies over 10%.[17–19] The high degree of control exertable on NC photoluminescence makes them appealing for display devices as well. The light is emitted almost exclusively from the band edge state, which can be tuned by over 1 eV for many compositions,[11] with linewidths often narrower than 100 meV.[20] Figure 1.2 shows the photoemission of potential NC phosphors plotted on the CIE color triangle which, notably, enable a much more dynamic color range than standard HDTVs. This tunability, coupled with high emission efficiency[21–23] have led to commercially available QLED TVs,[3,4] as well as the development of solid state lights that use NCs as the active material. [24–28] These properties also make them appealing candidates for the gain media in lasers. In addition to being inexpensive and enabling access to an extremely broad range of lasing wavelengths, the experimentally developed NC lasers have exhibited other favorable properties such as low lasing thresholds.[29–35]

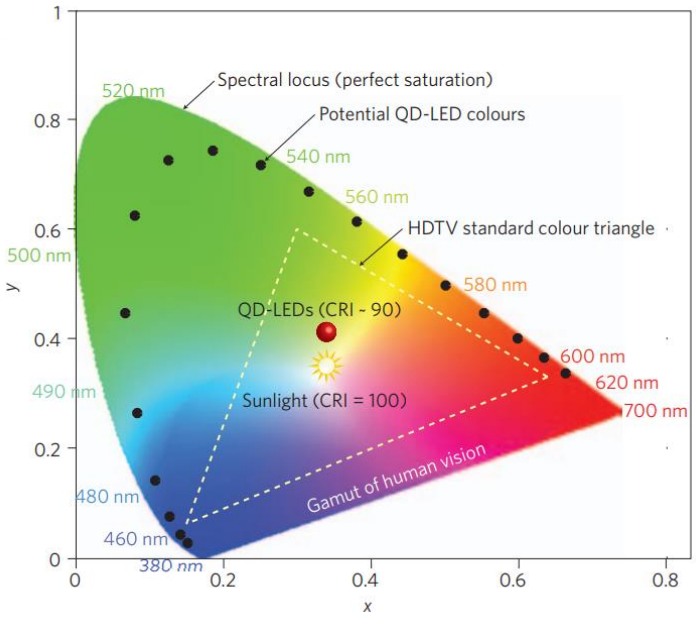

Figure 1.2. Color of emission of NC phosphors (potential QD-LED colours) compared to the standard HDTV colour triangle (white dashed line) on the CIE color triangle. Adapted with permission from Shirasaki *et al.*[36]

Such applications involve above bandgap photoexcitation which results in heating of the NC lattice. Once an exciton is generated, it rapidly (within a few picoseconds) relaxes to the lowest energy available excitonic state. Any excess energy is deposited in the lattice through the generation of phonons—quantized lattice vibrations—in a process known as intraband relaxation as diagrammed out in Figure 1.3a.[11,37–40] These phonons rapidly thermalize, transferring energy between the various available phonon modes.[41] When there are multiple excitons present in a NC, they experience Coulombic interactions which can alter the energies of these multiexcitonic states.[11,42] NCs with multiple excitons can also undergo a process known as Auger recombination by which one exciton relaxes to its ground state by transferring its energy to another exciton as diagrammed out in Figure 1.3b. This energized exciton then proceeds to undergo intraband

relaxation to the band edge. The rate for which this occurs for two excitons, the biexciton recombination rate, depends on NC size and composition but is generally on the timescale of 10's of picoseconds up to a nanosecond.[11] In addition, Auger recombination rates scale quadratically with the number of carriers[43,44] resulting in fast recombination in the case where many excitons are present. As a result of Auger recombination and intraband relaxation, high fluence excitation results in significant impulsive heating of NCs, the effects of which are explored in Chapters 3-5.

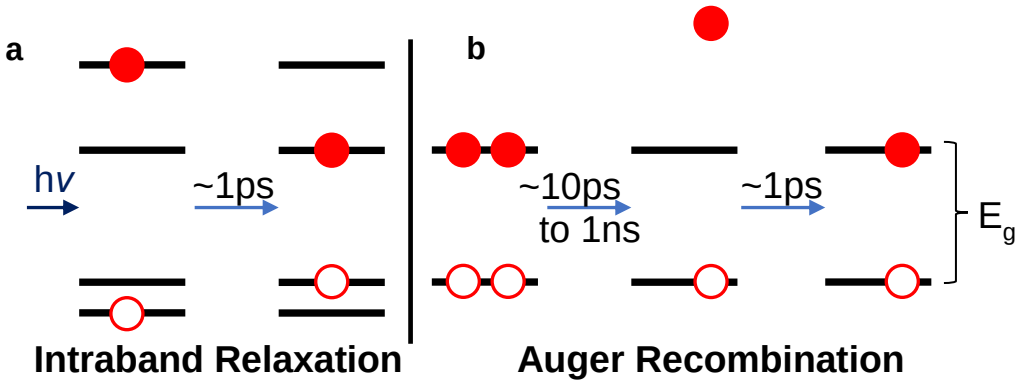

Figure 1.3. Diagrams of (a) intraband relaxation and (b) Auger recombination.

1.3. Plasmonic Materials

The behavior of electrons in a metal can generally be described by the Drude model.[45] Here the frequency-dependent dielectric constant (ϵ) is described by the following equation:

$$\epsilon(\omega) = 1 - \frac{\omega_p^2}{\omega^2 + i\Gamma\omega} \qquad (1.2)$$

where Γ is a damping term, ω is frequency and ω_p is referred to as the plasma frequency and defined as

$$\omega_p = \sqrt{\frac{ne^2}{m_e \epsilon_0}} \qquad (1.3)$$

where n is conduction electron density, e is the elementary charge, m_e is the electron mass, and ϵ_0 is the permittivity of free space.[45] This dielectric constant, however, typically differs from that of whatever medium surrounds the metal. When the change in dielectric environment at this interface is sufficiently different—and meets specific criteria,[46,47] the electrons exhibit behavior that is often described through surface plasmons which are quantized oscillations of electron density. Here, the surface plasmon propagates along the material's surface as shown in Figure 1.4a.[46] Exciting surface plasmons with light requires the photons to match the surface plasmon in both frequency and momentum which is generally quite challenging owing to differences in dispersion relations. As a result, exciting a surface plasmon on a smooth surface requires the usage of a grating or a prism.[48] However, roughening the surface, which essentially creates a superposition of interfaces, facilitates the frequency and momentum matching. As a result, surface roughening is commonly used in the excitation and utilization of surface plasmons.[46] When a material exists with features on the order of or smaller than the wavelength of light used to excite the surface plasmon resonance, it becomes a localized surface plasmon with a localized surface plasmon resonance (LSPRs).[46,47] This results in the strong, localized electric field enhancement near the nanoscale feature that rapidly falls off with distance as shown in Figure 1.4b. [46,47] There are analytical descriptions of this behavior for spherical[49] and rod-like particles,[50] although for

more complex geometries computational methods such as Finite Difference Time Domain calculations or the Discrete Dipole Approximation are needed.[51]

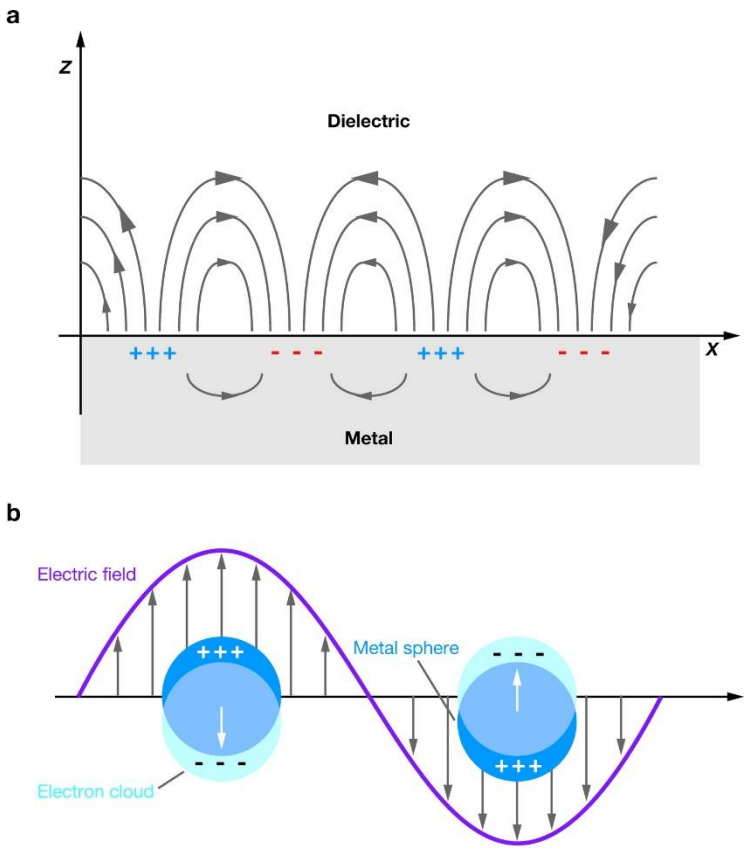

Figure 1.4. Behavior of plasmons. (a) A surface plasmon propagating along a metal surface. (b) a localized surface plasmon in a plasmonic nanoparticle. Adapted with permission from Willets and Van Duyne.[46]

Localized surface plasmons have proven useful in a wide number of contexts. First, the frequency of a LSPR is highly sensitive to the local dielectric environment it experiences. Small changes in the chemical species at the plasmonic material's surface can cause large optical changes

enabling extremely powerful chemical and biological sensors.[52–54] The localization of light can also enable other forms of surface sensitive, optical characterization. Perhaps most common is surface enhanced Raman spectroscopy (SERS) where the LSPR can dramatically increase Raman scattering to the point at which the vibrations of a single particle can be measured. [46,55–57] Additionally, plasmonic materials have been used in photovoltaic devices. Their ability to strongly scatter light can increase the effective path length that light travels in the photovoltaic cell leading to increased absorption in thinner devices.[58,59]

The light involved in these applications often heats the plasmonic material. Following photoexcitation of a plasmon resonance, there is very rapid dephasing of the oscillating electrons (typically on the order of a few fs), which leads to a non-thermal distribution of excited electrons.[47,60] These electrons scatter off of one another which results in a thermal distribution of electrons, typically on the timescale of hundreds of femtoseconds.[47,61,62] The thermalized electrons couple to the lattice through the generation of phonons. This process is typically described by the two-temperature model:

$$C_e(T_e)\frac{dT_e}{dt} = -G(T_e - T_L), \qquad (1.4)$$

and

$$C_L\frac{dT_L}{dt} = G(T_e - T_L) \qquad (1.5)$$

where $C_e(T_e)$/ $C_L(T_L)$ is the temperature-dependent electron/lattice heat capacity, T_e/T_L is the electron/lattice temperature, and G is the electron-phonon coupling constant.[47,61,63] Since the lattice

has a much larger specific heat than the electrons, most of the energy ends up in the lattice. Generally, the equilibration between the lattice and the electrons occurs on the timescale of a few picoseconds.[47,64,65] This process is diagrammed out in Figure 1.5 where the energy distribution is shown at the various timescales.

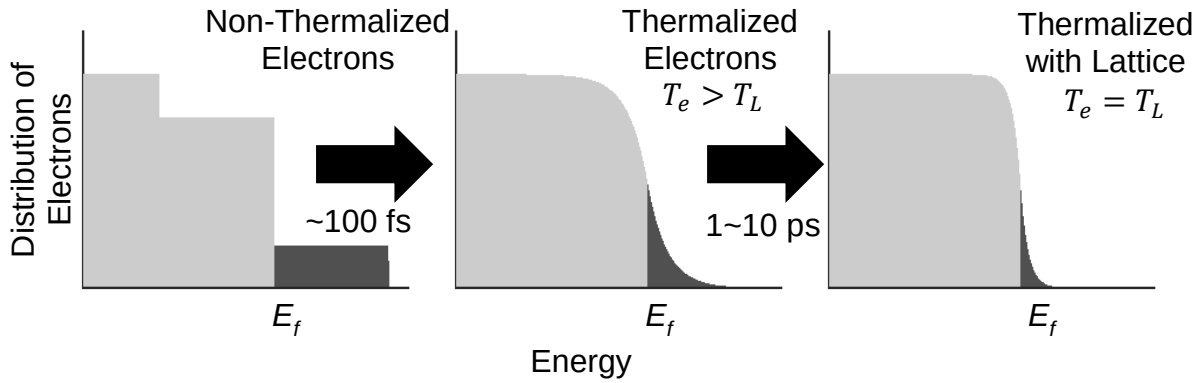

Figure 1.5. Schematic of thermal processes of a plasmonic nanoparticle following photoexcitation. A non-thermal distribution of electrons is generated which rapidly thermalize with other electron and eventually the lattice.

When energy is transferred to the lattice on a timescale that is faster than the period of phonons a specific mode, phonons of that mode are considered in-phase or coherent. These coherent phonons can constructively interfere and cause oscillations in the geometry of the overall system through combined distortions of the crystal lattice.[47,65,74–76,66–73] The resulting geometric changes can induce changes in the LSPR. As a result, this phenomenon is commonly characterized in the time domain with optical measurements, although some other characterization techniques have also been used.[68,69] Generally, the phonon frequencies depend on particle geometry. As a result, in heterogeneous ensembles, the individual particles oscillate at slightly different

frequencies resulting in rapid inhomogenous dephasing.[47,65] This can be overcome with the usage of monodisperse ensembles[70,76–78] or through single particle measurements.[71–73] It's worth noting that there can also be coherent phonons in NCs[66,67] although they are much more apparent in plasmonic nanoparticles owing to larger cross sections, faster electron-phonon coupling rates, and higher sensitivity of localized surface plasmon resonances to geometry.

1.4. General Nanomaterial Thermal Properties

The heating that occurs in NCs and plasmonic materials can be problematic as a result of generally poor thermal stability of nanomaterials. On a fundamental level, nanomaterials have reduced thermodynamic stability; the melting point depression of nanomaterials relative to their bulk counterparts is well characterized and is likely due to increased surface energy reducing thermodynamic stability.[79,80] Even below their melting point, nanocrystals are known to undergo undesirable physical changes including sintering and shape changes. For instance, Law *et al.* showed by Scherrer analysis of x-ray diffraction that PbSe NCs grew a few percent in size by 200 °C and seemingly increased by 3x and 5x the original size by 250 and 300 °C, respectively.[81] Relatedly, Goodfellow showed that an ordered, solid superlattice of PbSe nanoparticles became more closely spaced above 110 °C then observed deteriorating superlattice ordering between 110 and 150 °C followed by sintering and full loss of ordering by 168 °C.[82] At temperatures above 168 °C, the spheroids turn into rods of $PbSeO_3$. Further, particle shape can change so as to reduce surface energy as shown by transmission electron microscopy for CdSe nanoplatelets that sinter

by ~280 °C and form more spherical drops by 350 °C.[83] Each of these examples relate active particle surfaces and undesired chemistry that necessitate further improved routes to stabilization or exploitation.

The effects of this thermal instability can be worsened by slow thermal dissipation. In fact, the thermal conductivity of nanocrystal arrays are generally so low that they are challenging to measure. Nanoparticle arrays with a variety of nanoparticle compositions, sizes, and ligand coatings show thermal conductivities of 0.1-0.3 W/m·K, approximately a factor of 1000 lower thermal conductivity than silicon and below the limit predicted for amorphous materials.[84] The poor thermal conductivity of many nanostructured media is likely caused by relatively poor phonon transport and phonon-phonon coupling at nanostructure/matrix interfaces, often between disparate materials. The so-called thermal boundary resistance problem revolves around typical impedance mismatching of high density, high speed of sound inorganic particles and typically lower density, lower speed of sound surrounding media such as ligands, polymer, or solvent. At such interfaces, phonons tend to exhibit low transmission and reduce thermal transport rates.[85,86] Thermalization of a hot nanoparticle is understood to occur under one of two limiting regimes of either thermal diffusion, with lifetime $\tau_d = \frac{\mathrm{r^2 C_p^2}}{\mathrm{9 C_f \Lambda_f}}$, or under the limitation of interfacial thermal conductivity with lifetime $\tau_i = \frac{\mathrm{r C_p}}{\mathrm{3G}}$. Here C_f and C_p are the fluid (medium) and particle heat capacities, r is particle radius, Λ_f is the fluid thermal conductivity, and G is an interfacial thermal conductivity. The two limits relate different scaling of thermalization time with particle radius and pre-suppose that the particles experience thermal impedance mismatch. Although the relatively

low thermal conductivity of nanoparticle arrays may be useful in thermoelectric applications, where it may be decoupled from electrical conductivity, it presents a substantial challenge for optoelectronic devices like LEDs or lasers in which large amounts of heat are likely to build up in the nanocrystal layer.

1.5. Overview of Thesis

The remainder of this thesis explores the physical response and electronic implications of the thermal energy generated from photoexctitation. In Chapter Two, I review some of the methods that I have used to explore these phenomena. I then examine nanomaterials under two regimes of photoexcitation. First, in Chapters 3-5, I demonstrate that high fluence excitation causes NCs to transiently disorder. In Chapter 3, I establish that reversible, photoinduced phase transitions occur in NCs by demonstrating that a crystalline-to-amorphous transition occurs in CdSe, the quintessential NC. I then demonstrate that solid-solid phase transitions are also possible by characterizing an orthorhombic-to-cubic transition in $CsPbBr_3$ NCs in Chapter 4. Chapter 5 explores the electronic implications of these reversible phase transitions through the development of a novel, optical characterization technique to reveal disordering reduces NC bandgap. The latter half of the thesis examines the physical response of nanomaterials to milder excitation conditions; specifically, I characterize coherent acoustic phonons in plasmonic nanoparticles. In Chapter 6, I explore coherent acoustic phonons in gold bipyramids and nanojavelins to quantify induced changes in particle geometry finding the particles expand less

than 0.2%. In Chapter 7, I utilize those coherent phonons to manipulate electronic interactions between gold bipyramids and an attached excitonic dye. In Chapter 8, I develop a methodology, oscillation associated spectra, to better analyze and model these phonon-induced changes in plasmon-exciton coupling. Taken together, it becomes clear that photoexcitation changes the structure of nanomaterials and that the induced changes need to be considered when designing nanomaterial devices.

CHAPTER 2:GENERAL EXPERIMENTAL STRATEGIES

2.1. Pump-Probe Spectroscopy

Most of the data used in this thesis was gathered with pump-probe spectroscopy. This experimental strategy involves two pulses of light—a pump pulse and a probe pulse—and is widely used for its ability to obtain high time resolution measurements.[87] Initially, the "pump" pulse excites the sample and initiates the process of interest. Generally, the pump electronically excites the sample, although, other excitation strategies, such as a temperature jump,[88–90] are also possible. After a delay in time, a second, "probe" pulse interrogates the sample. By varying the time delay between the pump and probe pulses, one can measure the temporal evolution of the system. Many processes of interest occur on the ultrafast timescale (nanosecond or shorter), which is too fast to control with an electronic trigger or a mechanical shutter. Consequently, the timing of the two pulses is adjusted by utilizing the fact that light travels at a finite speed. By varying the distance that the pump and probe pulses need to travel, delay times can be tuned with sub-femtosecond ($<10^{-15}$ second) resolution. The timing of the resulting measurement is then only limited by how precise in time each of the pulses are defined. Therefore, the pulse widths, the temporal lengths of the pulses, determine the time resolution of pump-probe measurements. Changes observed in pump-probe measurements are usually quite small so the difference between "pump-on" (excited by pump pulse) and "pump-off" (no pump pulse) are commonly used. It's worth emphasizing that to get meaningful information, the probe pulse needs to interact with photoexcited species; in other words, the two pulses of light need to be spatially overlapped. To

simplify this overlap, as well as ensure homogenous excitation of the sample, often the pump pulse has a much larger spot size than the probe pulse.

2.2. Transient Absorption

Optical spectroscopy measures the interaction of light with a system. Practically, these measurements reveal a system's available electronic transitions. These measurements are encoding with the concentration of the chromophore through Beer Lambert's law:

$$A = \log\left(\frac{I}{I_0}\right) = \epsilon C l \qquad (2.1)$$

where A is absorbance, I is the intensity of the light transmitted through the sample, I_0 is the intensity of light before interacting with the sample, ϵ is an extinction coefficient, C is concentration, and l is the path length the light needs to travel. One can measure the electronic transitions from electronic excited states using transient absorption spectroscopy (TA), a pump-probe technique with an optical (uv-nir) pump and probe. The electronic transitions from a species' excited states are different from those of its ground state and the intensity of the new features are proportional to the population of the corresponding excited state. As a result, by monitoring how these features evolve in time, TA can reveal excited state dynamics.

The majority of the measurements taken in this thesis were performed with a set-up described in Figure 2.1. Initially, a Ti:S (titanium sapphire) amplifier was used to generate 2 kHz, 35 fs pulses of 800 nm light. The output was beamsplit to pump an optical parametric amplifier

that produced tunable pump—except when a 400 nm pump was used, where instead the OPA was bypassed and the 800 nm beam was frequency doubled with a β-Barium borate (BBO) crystal. A smaller portion of the 800 nm light was time-delayed and focused into sapphire to produce a white light probe beam. Pump pulses were mechanically chopped at 1 kHz to compare probe intensity though the sample with and without photoexcitation. The pump pulses were also passed through a neutral density (ND) filter wheel to control excitation power and filters to improve the color purity of the excitation pulse. To calculate the fluences used, pump spot sizes were measured via transmission through a pinhole. In Chapter 5, I describe a multiple excitation pump technique, but this will be explained in more detail in that chapter.

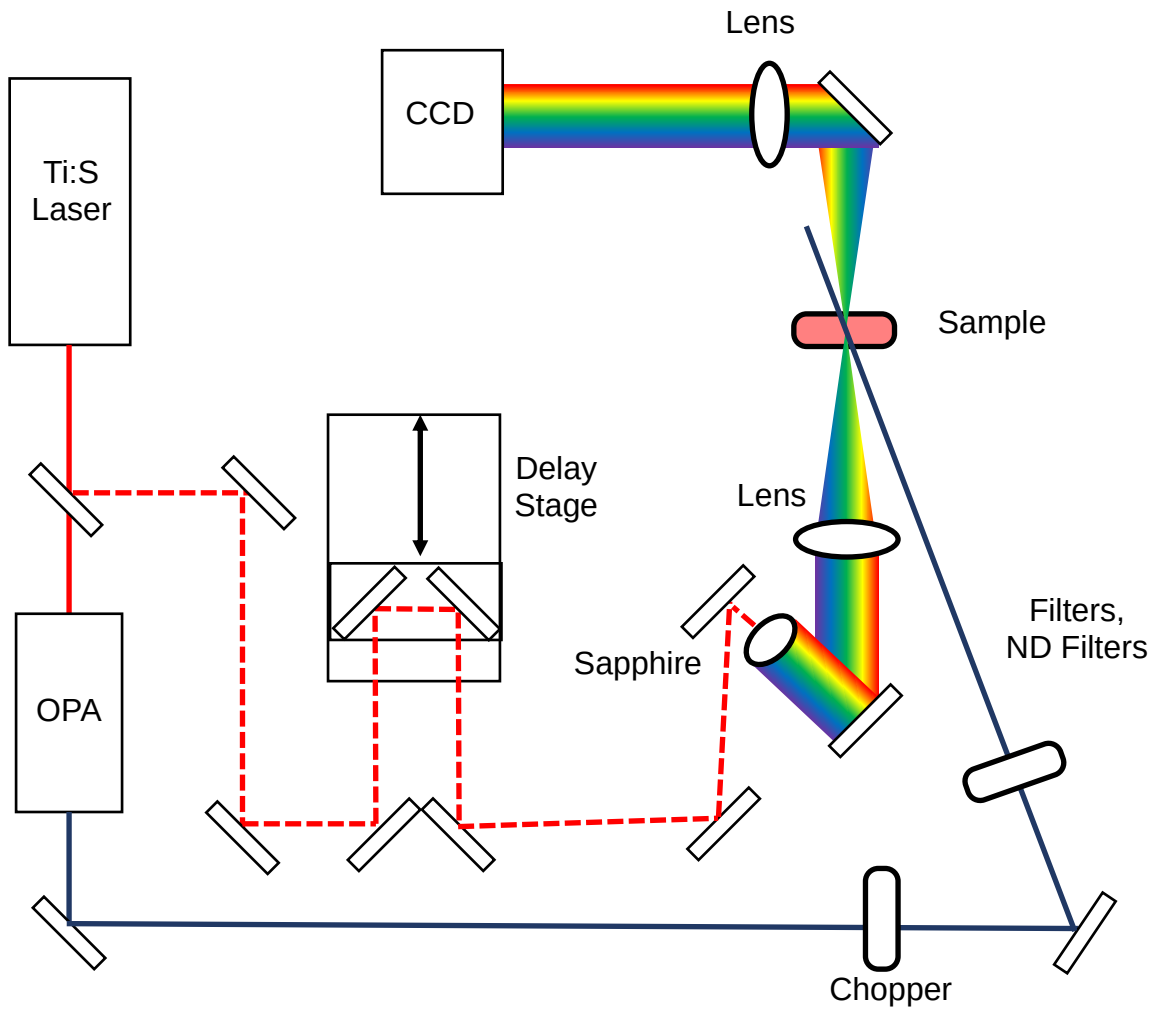

Figure 2.1. Diagram of the laser table used to perform transient absorption measurements. The sample is excited by a chopped pulse, spectrally tuned from an OPA and then probed with a broadband, white light source. By varying the distance that the pump and probe pulses travel, high temporal resolution is achieved.

2.3. Time-Resolved X-ray Diffraction

Crystals possess highly ordered structures where the distances between the periodic lattice planes are generally comparable to the wavelengths of x-rays. As a result, when x-rays scatter off crystals, there are constructive interference fringes, known as diffraction peaks, in

directions that correspond to the spacings between certain lattice planes. The lattice planes that generate diffraction peaks, as well as the relative amplitudes of those diffraction peaks, are dependent on the material's crystal structure. As a result, a crystal's x-ray diffraction (XRD) pattern can be used to determine its structure. Nanomaterials exhibit broader diffraction peaks compared to their bulk counterparts owing to their finite numbers of lattice planes. The width of a nanomaterial's diffraction peak is often described through the Scherrer equation:

$$\tau = \frac{K\lambda}{\beta \cos(\theta)} \qquad (2.2)$$

Where τ is the mean size of a crystalline domain (in the case of NCs, NC diameter), λ is the x-ray wavelength, K is a dimensionless shape factor with a value close to unity, β is the FWHM of the diffraction peak, and θ is the diffraction angle. This increased peak width with decreased crystal size is generally referred to as Scherrer broadening.[91,92]

Pump-probe XRD is commonly referred to as Time-Resolved X-ray Diffraction or TR-XRD. These measurements are generally quite challenging to perform as they require pulsed X-ray sources with picosecond time resolution and high brilliance. The TR-XRD measurements in this thesis were performed at Beamline 11-ID-D at the Advanced Photon Source (Argonne National Laboratory), and is one of the few facilities capable of conducting such measurements. A reservoir of NCs dispersed in solution was continuously flowed as a free jet into an air-free interaction region, which assured measurement of fresh, unperturbed material with each laser pulse. Pump pulses of 3.1 eV photon energy from a 100 fs Ti:S laser were attenuated and focused to achieve the desired fluence. After a controlled time delay, 11.7 keV X-ray pulses (79 ps fwhm)

were directed into the jet, and the resulting 2D diffraction pattern was collected on a time-gated Pilatus 2M, which was then radially integrated. This is diagrammed out below in Figure 2.2.

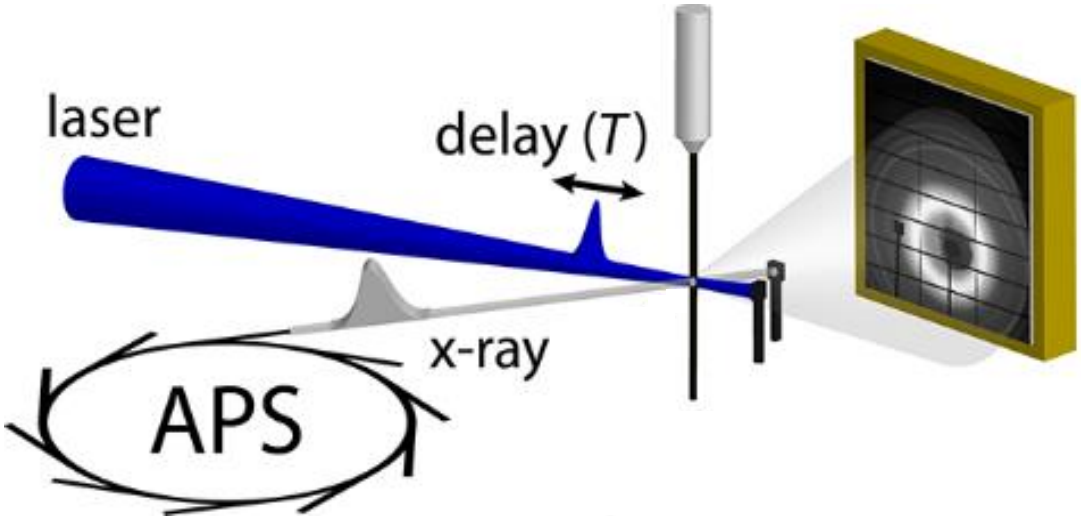

Figure 2.2. Schematic of TR-XRD measurements. A 400 nm laser optically excited a jet of NCs which was then probed by an x-ray pulse from the APS which was collected with a 2D detector.

There are a couple of strategies that can be employed to improve the probability of a successful TR-XRD experiment. First, materials with larger thermal expansion coefficients are more sensitive to increases in temperature and tend to produce TR-XRD patterns with higher signal-to-noise ratios. Second, larger NCs have less Scherrer broadening and sharper XRD peaks which also results in higher signal-to-noise TR-XRD patterns. However, the most important factor in a TR-XRD experiment is the quantity of sample obtainable. The experiments discussed in this thesis used highly concentrated solutions of NCs because preliminary studies with less concentrated samples were unsuccessful. It is possible that the more concentrated samples were

more successful because of they had stronger XRD diffraction peak intensities. Scattering intensity is proportional to concentration and the NC XRD peaks are much clearer over the solvent background at higher concentrations. It is also possible that the more concentrated samples produced better data because they had slower degradation rates. Since the sample volume was constant, the higher concentration samples had more NCs. If some number of photoexcited NCs were destroyed with each laser or X-ray pulse, this would represent a larger percentage of the total number of NCs in the less concentrated samples causing faster degradation. If this slower degradation rates was responsible for the success of the higher concentration samples, then lower concentrations might also be usable as long as there is also a sufficiently large sample volume. This modification would enable more homogeneous excitation of the ensemble, although it has yet to be explored experimentally. Regardless, the TR-XRD measurements I have performed indicate that the single greatest predictor for experimental success is the quantity of sample available, with at least 100 mg of NCs being required.

CHAPTER 3:TRANSIENT MELTING AND RECRYSTALLIZATION OF SEMICONDUCTOR NANOCRYSTALS UNDER MULTIPLE ELECTRON-HOLE PAIR EXCITATION

This chapter is based on the research described in the following publication:

Kirschner, M. S.; Hannah, D. C.; Diroll, B. T.; Zhang, X.; Wagner, M.J.; Hayes, D.; Chang, A. Y.; Rowland, C. E.; Lethiec, C. M.; Schatz, G. C.; Chen, L. X.; Schaller, R. D. Transient Melting and Recrystallization of Semiconductor Nanocrystals Under Multiple Electron-Hole Pair Excitation. Nano Lett. 2017, 17 (9) 53140-5320.

Ultrafast optical pump, X-ray diffraction probe experiments were performed on CdSe nanocrystal (NC) colloidal dispersions as functions of particle size, polytype, and pump fluence. Bragg peak shifts relate heating and peak amplitude reduction confers lattice disordering. For smaller NCs, melting initiates upon absorption of as few as ~15 electron-hole pair excitations per NC on average (0.89 excitations/nm^3 for a 1.5-nm radius) with roughly the same excitation density inducing melting for all examined NCs. Diffraction intensity recovery kinetics, attributable to recrystallization, occur over hundreds of picoseconds with slower recoveries for larger particles. Zincblende and wurtzite NCs revert to initial structures following intense photoexcitation suggesting melting occurs primarily at the surface, as supported by simulations. Electronic structure calculations relate significant band gap narrowing with decreased crystallinity. These findings reflect the need to consider the physical stability of nanomaterials and related electronic impacts in high intensity excitation applications such as lasing and solid-state lighting.

3.1. Introduction

Quantum-confined semiconductor nanocrystals (NCs) offer band-gap tunability, colloidal synthesis and processability, and discretized electronic densities of states in a departure from bulk semiconductors.[80,93,94] While many NC applications such as photoluminescent labels, light-emitting diodes (LEDs), and solar absorbers employ low-intensity generation of electron-hole pairs (often referred to as 'excitons' regardless of binding energy owing to spatial confinement within the NC), some applications such as optical amplifiers and high brightness LEDs excite multiple excitons.[29,30,95,96] Biexciton lifetimes in spherical NCs scale with particle volume for a wide range of compositions, while triexcitons and higher numbers of excitations per NC decay progressively faster according to the number of carriers present in the particle.[43,44,97] Thermal energy is transferred to the NC lattice upon both intraband cooling of each photogenerated exciton[37–40] and multiexcitonic Auger-recombination[98–100] that, given the reduced particle volume and lower equilibrium melting temperature relative to the bulk composition,[79,94] raises questions regarding the stability of the particle lattice.

Previous studies have generally considered the electronic and nuclear structure of NCs as static throughout the excitation and relaxation processes. However, consideration of earlier time-resolved studies suggests a need to re-examine whether energy landscapes for photoexcited NCs remain unchanged at high photon fluence. In particular, Malko et al. reported detailed optical gain studies of CdSe NCs.[101] Gain magnitude exhibited a maximum for certain sizes when ~10 to 20 excitations were photogenerated per NC on average, but strongly decreased at higher pump fluences purportedly owing to ever-increasing photoinduced absorption with larger carrier

populations. However, even for pump intensities yielding 100 excitations per NC on average, the photoinduced absorption amplitude, several picoseconds after excitation, still increases. Extrapolation of lower-order multiexciton lifetime scaling to high fluence gives an expected decay time for such high-multiexciton states that resides in the sub-picosecond regime, and thus these photocarriers likely recombine too fast to give rise to such photoinduced absorption. It is possible that loss of crystalline order from increased lattice temperature deleteriously affects observed optical properties. Transient loss of crystallinity also suggests that reports of a hot-phonon bottleneck[102] following intense excitation might require further scrutiny. Briefly, in the hot-phonon bottleneck mechanism, carrier cooling occurs at sub-ns rather than sub-ps time scales owing to equilibration with large numbers of phonons. Recently, time-resolved X-ray diffraction[103,104] and electron-diffraction[105] measurements on these photogenerated NCs have begun to permit observations of lattice structural changes.

Here transient lattice studies are reported for a series of CdSe NCs of varying sizes across a range of optical excitation photon fluences measured by time-resolved X-ray diffraction (TR-XRD). The results reveal that photoexcitation, even at reasonable pump fluence, can cause not only heating, but also transient disordering of NC lattices. The observed photo-induced lattice disorder in smaller NCs is achieved at lower average numbers of photoexcitations per particle and can recover to the ordered lattice more rapidly in comparison to larger NCs. Examinations of both wurtzite and zincblende CdSe NC polymorphs show that crystal structure is preserved even upon very intense excitation, which suggests an important role of surface melting as well as perhaps recrystallization with rates that exceed crystal reorganization. Ab-initio molecular dynamics and

density functional theory findings suggest, furthermore, that the optoelectronic properties of nanoparticles significantly change owing to disorder upon intense excitation.

3.2. Results and Discussion

3.2.1. Transient Melting of CdSe NCs

Figure 3.1a shows XRD data collected from a jet of 3.8-nm radius wurtzite CdSe NCs with solvent scattering subtracted. Differenced diffraction patterns (optical pump-on minus pump-off) at 80 ps after photoexcitation are shown in Figure 3.1b for a series of excitation fluences ranging from 0.15 mJ/cm^2 to 17.3 mJ/cm^2 that correspond to an indicated average number of photoexcited electron hole-pairs, <N>. The method used for accounting for sample degradation, dominated by loss of dispersibility, is detailed in Appendix A.1. For lower fluence (<N>=2.6), the differenced signals appear as derivatives, owing to increased diffraction at smaller Q and a decrease at larger Q. Such shifting of Bragg peaks relates to the deposition of thermal energy in the NCs, which causes modest lattice expansion. With increasing fluence, in addition to a Bragg peak shift, a significant decrease in diffraction intensity becomes apparent, which indicates a decrease in crystalline order due to melting that cannot be explained by the Debye Waller effect (see Appendix A.2).

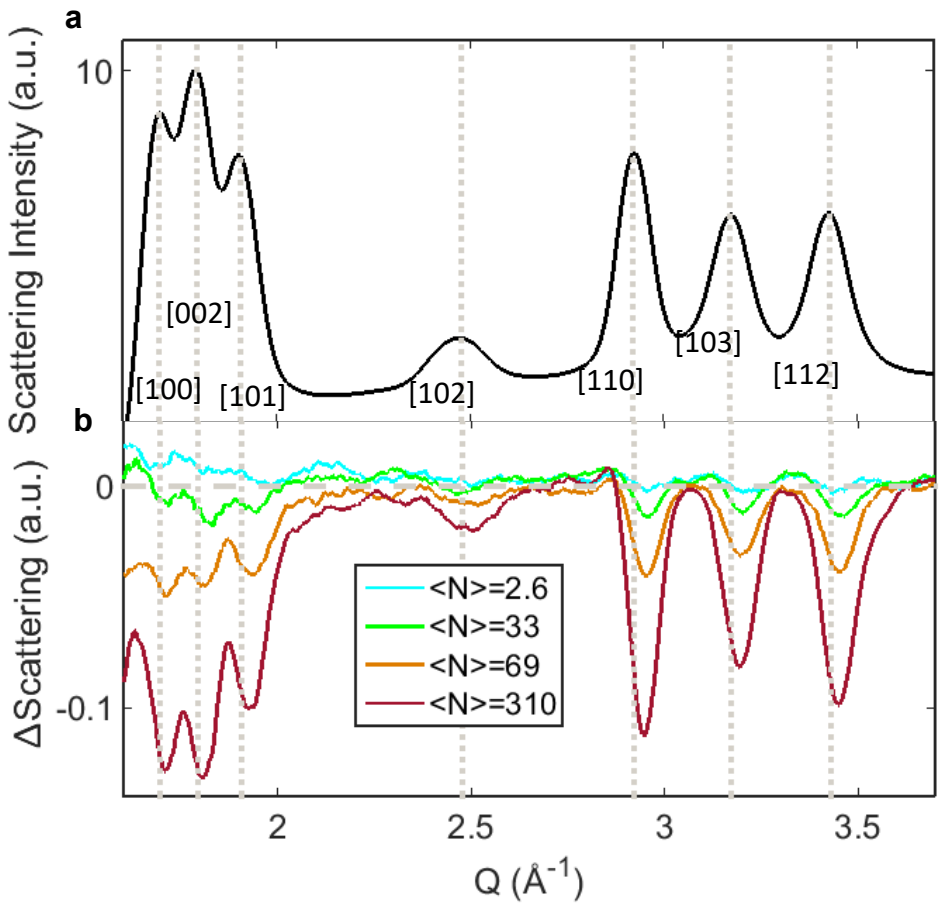

Figure 3.1. (a) Radially integrated X-ray diffraction from a liquid jet of wurtzite CdSe NCs in dodecane solution. (b) Differenced X-ray diffraction patterns (laser-on minus laser-off) for different average numbers of absorbed photons per particle, corresponding to photoexcitation fluences. The X-ray delay time was 80 ps after photoexcitation with 100 fs, 3.1 eV laser pulses.

Figure 3.2a shows time-evolution of the scattering intensity of 3.8-nm radius CdSe NCs upon 3.1-eV excitation at intensities of 0.67 mJ/cm^2 (<N>=12) and 24 mJ/cm^2 (<N>=430). Here, the presented scattering intensities show the average integrated XRD peak areas from three similarly behaved (as shown in the inset) lattice planes with the highest obtained signal to noise, namely the [110], [103], and [112] planes, which emphasize recrystallization since changes in peak

position do not impact integrated intensity. The data were fit to single exponential decays (solid lines), details of which are described in Appendix A.3. In these samples, melting occurs faster[103] than the instrument response function (79 ps), while recrystallization occurs with time constants of ~100 ps. These recovery times are about an order of magnitude slower than what as predicted for a simple heating and cooling of the particle from continuum theory (see Appendix A.4), and hence support the assertion that the decrease in peak intensity is attributable to melting rather than thermal expansion. As shown, higher excitation fluence results in only slight changes in the recovery time.

Figure 3.2b shows the time evolution of scattering intensity for 1.5, 2.0, and 3.8-nm radius CdSe NCs excited at 24 mJ/cm^2 clearly showing that recovery time increases significantly with particle size. Smaller NCs present a larger surface area to volume ratio, more rapid thermal outflow,[106] and lower melting points than larger particles,[79,94] and these effects combine to yield the observed trend. Figure 3.2c shows the fluence dependence of the integrated scattering intensity magnitude examined at 80 ps after excitation for three NC sizes. These data exhibit a particle-size dependent apparent threshold for melting. The dotted lines highlight threshold fluences that decreases the Bragg peak intensity in excess of noise levels. Larger nanoparticles having a larger per-particle specific heat and lower surface energy likely explains the NC-size-dependent trend. Upon accounting for particle volume, the disordering thresholds of the NCs of radius of 1.5 nm, 2.0 nm, and 3.8 nm are 0.89, 0.89, and 0.30 excitations/nm^3 respectively, which relates comparable excitation densities.

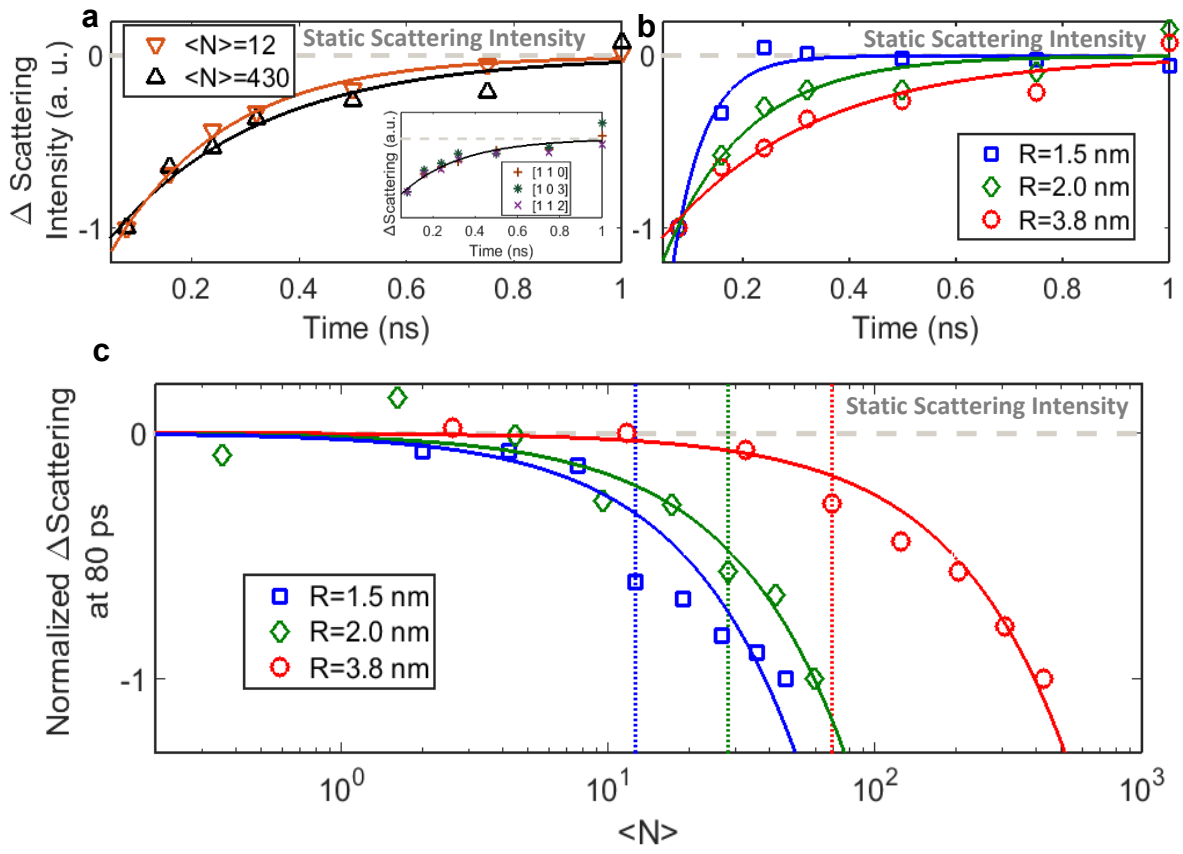

Figure 3.2. (a), Diffraction intensity recovery for 3.8-nm radius CdSe NCs after photoexcitation at 3.1 eV with intensities of 0.67 mJ/cm^2 (<N>=12, red) and 24 mJ/cm^2 (<N>=430, black) along with single exponential fits (solid lines) with respective lifetimes of 255 ± 117 ps and 369 ± 237 ps. Additional discussion about the fitting and normalization process, along with more power dependent kinetics data, is included in the Appendix A.3. Inset: Recovery of the [110], [103], and [112] lattice planes of the NCs excited at 24 mJ/cm^2 in the main figure along with the same single exponential fit. (b) Recovery of CdSe NCs with radii of 1.5 nm (blue squares), 2.0 nm (green diamonds), and 3.8 nm (red circles) after photoexcitation by a 24 mJ/cm^2 3.1 eV laser pulse along with single exponential fits (solid lines) with respective lifetimes 75 ± 91, 180 ± 160 and 369 ± 237 ps. (c) Normalized power dependence at 3.1 eV of the magnitude of the integrated scattering intensity loss after 80 ps for CdSe NCs with radii of 1.5 nm (blue squares), 2.0 nm (green diamonds), and 3.8 nm (red circles). The gray dashed line represent the un-pumped, static scattering intensity. Dotted lines correspond to melting thresholds as calculated using the methodology described in Appendix A.5.

3.2.2. Modeling Disordered NCs

To investigate the melting behavior of the CdSe NCs, molecular dynamics (MD) simulations of wurtzite NC heating utilizing the LAMMPS software package[107] were performed with interatomic forces described by the Rabani potential[108]:

$$V_{ij} = \left(\frac{q_i q_j}{r_{ij}}\right) + 4\epsilon_{ij}\left[\left(\frac{\sigma_{ij}}{r_{ij}}\right)^{12} - \left(\frac{\sigma_{ij}}{r_{ij}}\right)^{6}\right] \qquad (3.1)$$

where q_i is the charge on atom i, r_{ij} is the distance between atoms i and j, ϵ_{ij} is the depth of the potential energy well between atoms i and j, and σ_{ij} is the distance at which the interparticle potential is zero. To generate data, a spherical, stoichiometric 2.5-nm radius CdSe NC containing 3,282 atoms was thermalized at 300 K followed by heating in steps of 100 K using a velocity rescaling procedure.[109] Here, a temperature of 1600 K is needed to ensure simulation of a fully molten NC (the measured bulk melting temperature is 1531K).[110] Note that the absolute temperatures needed to melt the NC are assuredly higher than those required experimentally; this represents a challenge of statistical sampling rather than physics and is required to observe the melting event with 100% probability during a simulation-accessible timescale.[111] Figure 3.3a displays the temperature-dependent XRD patterns obtained using the Debye scattering equation. Similar to the TR-XRD experiments, the heated NCs exhibit a shift to lower Q values as a result of thermal expansion of the wurtzite lattice as well as substantial peak broadening related to loss of crystalline order.

The MD simulations presented here examine NC heating in the thermodynamic limit that assumes heat has distributed evenly throughout the particle. While it is difficult to ascertain the validity of this assumption with regard to heating via pulsed laser excitation, prior evidence of sub-picosecond exciton-phonon coupling[37,38,41,67] lends credence to the notion that thermalization between the electron and lattice baths occurs prior to structural rearrangements. To further examine the melting mechanism in this thermodynamic limit, an orientational ordering parameter q was used as has been previously used to quantify nucleation events in supercooled liquid Si.[112] Using the atomic positions at a given time point, the term $\bar{q}$ is computed as shown below:

$$\bar{q}_{lm}(i) = \frac{1}{N_b(i)} \sum_{j=1}^{N_b(i)} Y_{lm}\left(\theta(\boldsymbol{r}_{ij}), \phi(\boldsymbol{r}_{ij})\right) \qquad (3.2)$$

Here, $N_b(i)$ is the number of bonds for atom i, while θ and ϕ denote the azimuthal and polar angles of orientation, respectively, for bond $\boldsymbol{r}_{ij}$. Y_{lm} denotes the spherical harmonics. From $\bar{q}_{lm}$ $2l$+1 dimensional vector $\boldsymbol{q}_l = \left[\bar{q}_{l,-l}, \bar{q}_{l,-l+1} \ldots \bar{q}_{l,l-1}, \bar{q}_{l,l}\right]$ can be constructed for each atom i which enables the computation:

$$\boldsymbol{q}_l = \frac{1}{N_b(i)} \sum_{j=1}^{N_b(i)} \frac{q_l(i) \cdot q_l(j)}{|q_l(i)||q_l(j)|} \qquad (3.3)$$

By comparing various values of l for completely molten and completely crystalline particles, it was found that q_4 provided the greatest distinction between melted and crystalline particles. In particular, decreasing crystallinity yields a higher q_4 value. The cutoff was selected to be $q_4 = 0.6$, as more than 90% of the atoms exhibiting $q_4 > 0.6$ reside in a melted environment. At 10 equally spaced time points throughout the production run trajectories, q_4 was computed for each atom in

the NC at all equilibrium temperatures considered during the MD simulations presented here. Then, defining simple radial cutoffs, the average q_4 values were computed, which is defined as q_{order}, for a series of concentric slices represented by radial bins. The results of this analysis are presented in Figure 3.3b. The transition from q_{order} = 0.5 (crystalline) to q_{order} = 0.6 (melted) happens gradually over temperature. However, q_{order} increases more rapidly as a function of distance from the NC center at lower temperatures. As temperature is increased, the q_{order} values increase in a surface-inward fashion, indicating that some degree of surface pre-melting occurs even in the thermodynamic limit at temperatures below the bulk melting temperature. In non-equilibrium conditions, surface melting effects will likely be even more pronounced; heat that has not been evenly distributed throughout the NC is likely concentrated near the surface owing to interfacial thermal boundary resistance.

To assess the electronic structure of CdSe NCs at elevated temperatures, ab-initio MD simulations (AIMD) of a heated $Cd_{33}Se_{33}H^*_{46}$ were performed. The $Cd_{33}Se_{33}$ NC size is significant in that it represents the smallest NC size accessible experimentally (~1.2 nm) while still containing few enough atoms to permit AIMD simulations. The H* represents a pseudohydrogen having an effective nuclear charge sufficient to achieve passivation of lone pairs (i.e. dangling bonds) associated with surface atoms (Z = 1.5 for H* atoms passivating a surface Cd and Z = 0.5 for H* atoms passivating a surface Se. These Z values are determined by considering the number of electrons contributed by each species in a tetrahedral coordination environment; in particular, the resulting formula is $Z = (8 - m_i)/4$, where m is the formal number of valence electrons in the species i.). Again, pseudohydrogen was chosen in lieu of full-size organic ligands to permit AIMD.

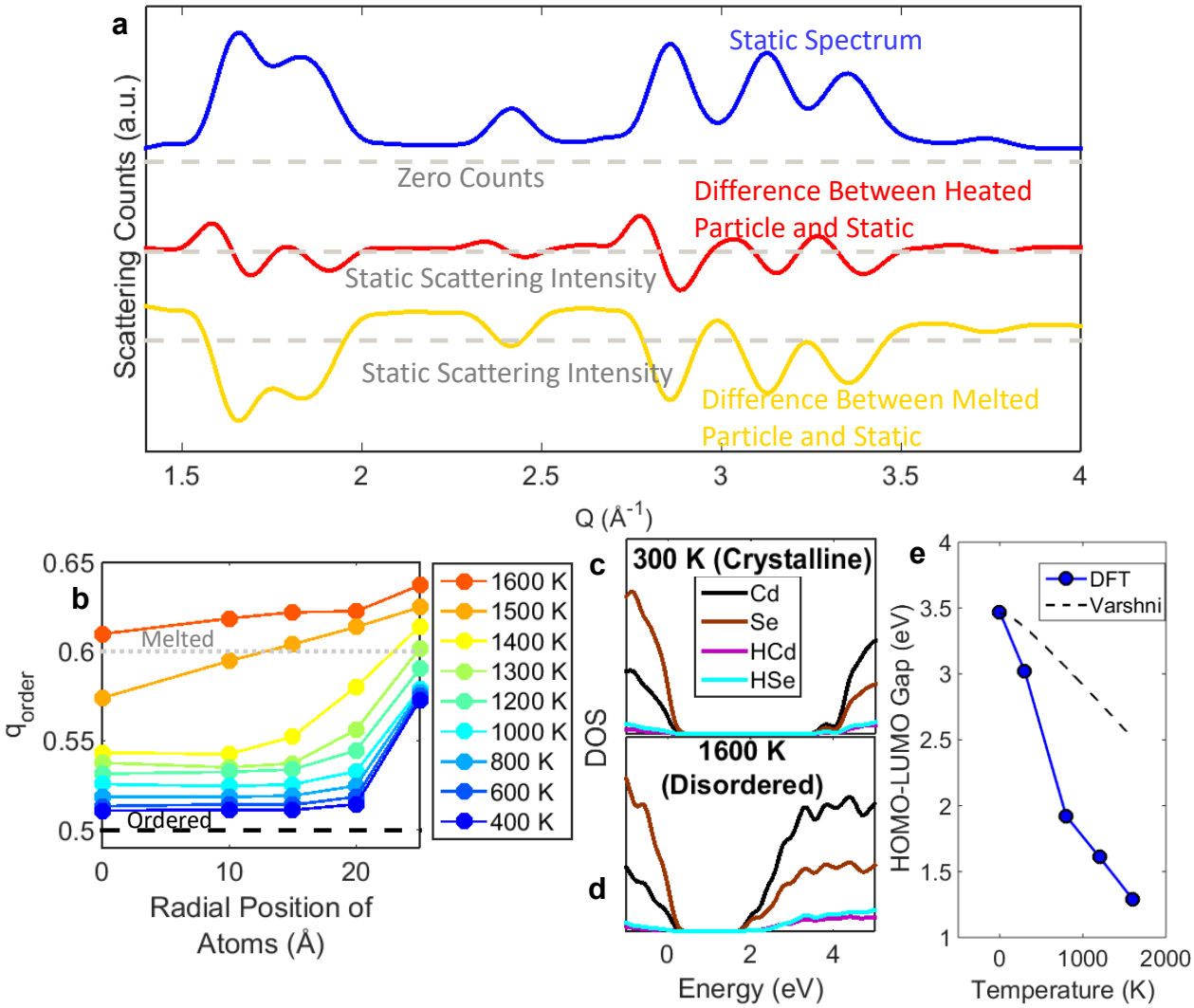

Figure 3.3. (a) Calculated X-ray diffraction patterns for static (400 K blue), heated (800K red), and melted (1600 K yellow) CdSe NCs. The particle simulated is smaller than that in Figure 3.1 resulting in broader peaks and overlapping of the [100], [002], and [101] peaks. (b) Ordering parameter vs. radial position for CdSe NCs at a range of temperatures. (c) and (d) Density of states for a CdSe NC that it is ordered (q_{order} <0.6) or disordered (q_{order} >0.6), respectively. (e) Bandgap energy of CdSe NC (blue) along with changes that would be expected by solely thermal effects as expected from the Varshni relation (black).

As shown in Fig. 3.3c and 3.3d, a substantial reduction in band gap occurs between 300 and 1600 K. Importantly, this reduction far exceeds thermal effects as described by the Varshni relation such as phonon renormalization that predicts only a 950 meV reduction across the whole temperature range (further explored in Appendix A.6). Here band gaps of 3.9 eV at 0 K and ~2 eV at 1600 K were calculated. 1600 K was chosen to ensure uniform melting of the particle on timescales accessible to AIMD. Note that while the absolute magnitude of the band gap may be overestimated due to well-known self-interaction errors in the PBE functional,[113] relative quantities and trends (including the change of band gap with temperature-induced structural changes) are generally correctly captured.

The density of states data presented in Figures 3.3c and 3.3d reveal, importantly, that the valence and conduction band edge states remain predominantly comprised of Se and Cd orbitals, respectively. This suggests such states remain "core"-like (e.g. semiconducting CdSe); the absence of significant participation of surface ligand states at the band edge is indicative that gap closure is not due to surface trap formation (which would be irreversible) but rather intrinsic changes to the CdSe electronic structure. Such changes should reverse upon recrystallization, although accurate simulation of the cooling process requires careful transition path sampling and is beyond the scope of the present study.

As the redshift of the NC gap far exceeds what would be expected from simple lattice heating, as demonstrated in Figure 3.3e, the origin of the gap closure can likely be understood in terms of orbital hybridization. As the wurtzite lattice becomes hot and eventually molten (lacking in long-range order), a combination of increased bond lengths (due to heating) and a randomization

of the bond angle distribution (due to melting) results in a higher concentration of weak and dangling bonds. As these bonds necessarily involve less hybridization, the magnitude of bonding/anti-bonding splitting decreases, resulting in an overall reduction in band gap. While further simulation would be necessary to unambiguously demonstrate this point, the same phenomenon is known to yield metallization in molten Si and molten Ge.[114,115]

3.2.3. Effects of Polytype on Disordering

Figure 3.4a shows static XRD from 3.1-nm radius, zincblende CdSe NCs. While CdSe NCs can exist in either crystal polymorph, wurtzite is thermodynamically slightly more stable.[116] Figure 3.4b shows differenced XRD patterns for these zincblende NCs excited at 17 mJ/cm^2 (<N>=160, 1.3 excitons/nm^3) at a series of time delays. The loss and recovery of crystallinity demonstrated suggest the excitation fluence induces transient melting. However, perhaps surprisingly, the NCs recrystallize back into the zincblende polytype with no evidence for a phase transition to the thermodynamically more stable wurtzite. This trend suggests that nucleation occurs faster than crystal reorganization for this composition. For pump fluences nearer to the disordering threshold, if only the surface or an outer shell disorders, this would leave a core to facilitate recrystallization, but we would also expect broadened diffraction peaks from a reduced crystalline core size. Still, such a template recrystallization explanation would be consistent with previous explorations of NCs preferentially melting at the surface.[117,118]

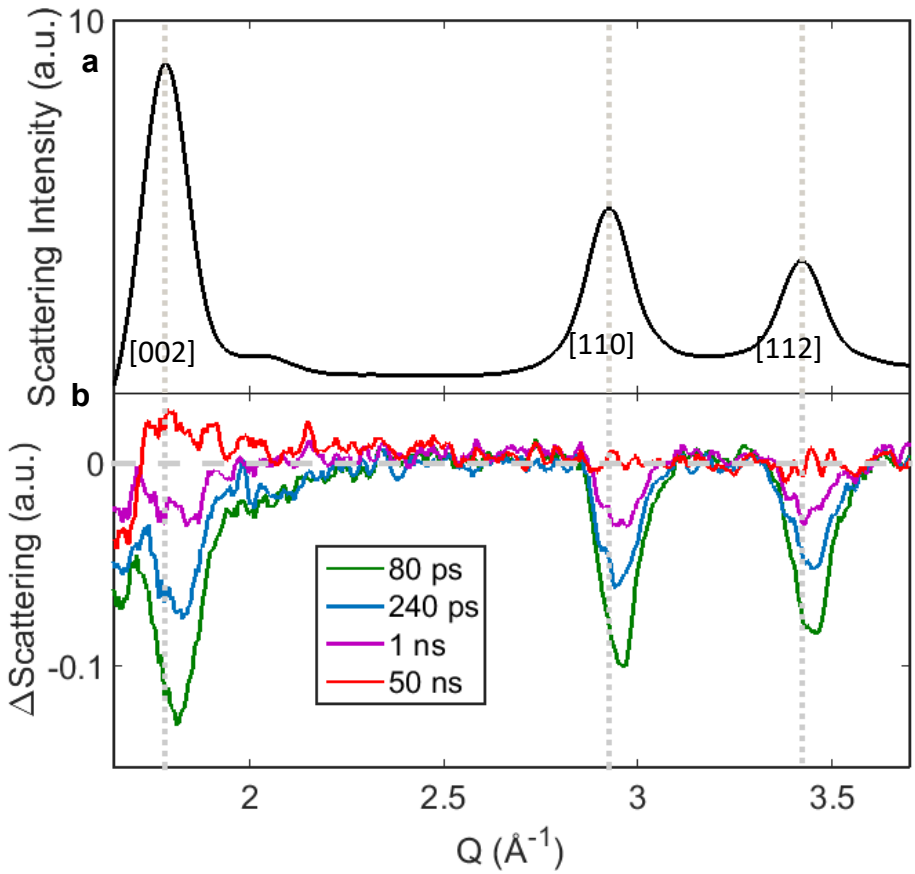

Figure 3.4. (a) Radially integrated X-ray diffraction from a liquid jet of zincblende CdSe NCs in dodecane solution. (b) Differenced diffraction patterns for optical pump-on minus pump-off with indicated pump-probe delay times, for excitation fluence of 17 mJ/cm^2 (<N> =160).

3.3. Conclusions

With understanding that lattice ordering can change substantially upon deposition of sufficient energy, it is worth revisiting the manner in which such disordering can impact optical gain. As previously reported,[101] excited carriers do contribute photoinduced absorption over broad

spectral ranges that contribute to optical loss and compete with gain. As the lattice heats owing to intraband cooling of carriers and Auger heating processes, the loss of lattice ordering can more substantially impact gain; the semiconductor energy gap itself red-shifts upon losing crystalline order. The red-shifted species both contribute strong absorption at gain wavelengths corresponding to crystalline material and also cease to exhibit stimulated emission. Modifications of NC structure and excitation characteristics can each influence thresholds of NC disordering. Structures that increase particle specific heat and stabilize the surface, such as core-shell and giant-NC approaches, would be expected to partially alleviate the noted thermal effects on crystallinity. Indeed, such structures exhibit improved gain properties[29,31,119,120] and even sustained lasing properties.[121] However, this relationship presents complexity as such shells also alter the rate of NC thermal outflow.[122] For a given number of photons absorbed, redder excitation wavelengths deposit less thermal energy, and longer pump pulsewidths deposit energy more slowly; ultimately the maximum lattice temperature achieved depends on the relative rates of NC heating and cooling. Consequently, one would expect improved gain with longer, redder excitation sources. In fact, the pump fluence required to observe gain has been reported to decrease with redder excitation,[40] and longer pump pulse duration. [121] Similar considerations also apply for NCs under electrical excitation.

In conclusion, following photoexcitation, CdSe NCs undergo a transient loss of crystallinity with a threshold corresponding to 0.89 excitons/nm^3, which recovers on the hundred picosecond timescale with slower recovery for larger particles. The magnitude of this loss of Bragg peak intensity linearly depends on the excitation fluence above the size-dependent melting

threshold. These changes in crystal structure drastically reduce the particle band gap, suggesting that this effect needs to be accounted for in nanoparticle systems with either large pulsed electron-hole pair populations, such as NC-based lasers, and can also be important in continuous high-intensity excitation such as solid-state lighting or concentrated photovoltaics. It was found that polytypism is preserved for this composition upon transient disordering that suggests investigation with still higher temporal resolution might show that recrystallization outpaces crystal reorganization to preserve the initial crystal structure. Surface melting with templated recrystallization can explain such retention, but this observation might represent a characteristic of nanomaterial behavior even from homogeneously melted structures. Furthermore, transient disordering in core-only NCs might help explain why core-shell structures often outperform the former in high-intensity applications beyond the rationale that such inorganic shell materials improve electronic surface passivation. As such, increased understanding of transient disordering can advance materials design and boost resultant device performance since, if for example melting in NC-based lasers could be reduced, larger and more sustained optical gain should be achievable. Conversely, applications that take advantage of the transient physical and electronic structure of the disordered state might also be achievable.

3.4. Methods

3.4.1. Material Synthesis

The synthesis of wurtzite CdSe nanocrystals followed a modified and scaled-up version of literature procedures.[123] First, a selenium precursor solution was made by dissolving 348 mg powdered selenium (99.99%, Aldrich) in 1.7 mL of trioctylphosphine (90%, Aldrich) in a nitrogen glovebox. In a 3-neck flask, 360 mg CdO (99.99%, Aldrich), 18.0 g trioctylphosphine oxide (99%, Aldrich), and either 1.40 g of tetradecylphosphonic acid (Strem, 99+% used for synthesis of larger CdSe nanocrystals) or 1.68 g octadecylphosphonic acid (Strem, 99+%, used for synthesis of smaller CdSe nanocrystals) were combined and held under vacuum at 120˚C for 1 hour, then heated to 300˚C under nitrogen and held until the reaction mixture became clear, indicating the formation of cadmium phosphonate complexes. Then, 10 mL trioctylphosphine was injected and the reaction mixture was heated to 340-370˚C. (Higher temperatures for smaller particles.) After reaching the set-point temperature, the selenium precursor solution was rapidly injected and the temperature was maintained from 0-15 minutes: for larger nanocrystals, lower temperatures and longer reaction times were used. To synthesize the smallest nanocrystals in this study, an additional 300 uL of diphenylphosphine (98%) was added to the selenium precursor solution prior to injection and the reaction was cooled immediately afterward. Nanocrystals were purified by methanol precipitation and two additional hexanes/isopropanol washes, redispersing the nanocrystals in dodecane.

The synthesis of zinc blende CdSe nanocrystals followed modified literature procedures.[124] Cadmium myristate powder was synthesized by dissolving 1.5 g sodium myristate (>99%,

Aldrich) in methanol and then mixing with 600 mg cadmium nitrate tetrahydrate (99.997%, Aldrich). The white precipitate was isolated, washed twice with methanol, once with acetone, then dried in a vacuum oven. An additional selenium injection solution were prepared by dissolving Se powder in octadecene (90%, Aldrich) at 0.1 M concentration at 200˚C under nitrogen, then evacuating the flask at 100˚C for 1 hour. An additional cadmium injection solution was prepared by dissolving 0.5 M cadmium oxide in oleic acid (90%, Aldrich) at 250˚C under nitrogen until the reaction flask turned clear and subsequently evacuating the flask for 1 hour at 120˚C and held at that temperature to remain a liquid. The synthesis of nanocrystals was achieved by mixing 39 mg Se powder, 30 mL octadecene, and 275 mg cadmium myristate in a 100 mL 3-neck flask, then evacuated at 80˚C for 1 hour, and heated to 240˚C. After 3 minutes at 240˚C, a dropwise injection of degassed 4 mL octadecene, 1 mL oleylamine (70%, Aldrich), and 1 mL oleic acid was added over 5 minutes. After 30 more minutes, the reaction was heated to 280˚C and a 20 mL of a 5:1 mixture of selenium: cadmium injection solutions (1:1 by mol) at 0.2 mL/minute. After the injection, the reaction flask was cooled to room temperature. Purification of the nanocrystals was performed using precipitation by isopropanol, followed by two additional hexanes/isopropanol washes, redispersing the nanocrystals in dodecane.

3.4.2. X-ray Diffraction Measurements

A dodecane suspension of CdSe NCs was circulated by a peristaltic pump from a large reservoir continuously purged with N_2 to protect the sample from O_2. The liquid suspension was flowed continuously through a stainless steel tube to give a free liquid jet to minimize radiation

damage. A laser pulse was used to excite CdSe NCs, followed by an X-ray probe pulse at a specified time delay to interrogate the transient states. The laser and X-ray beams overlapped spatially on the liquid jet at a 20° relative angle. The laser pump pulse was the second harmonic output of a Ti:S regeneratively amplified laser with 10 kHz repetition rate (Coherent Micra oscillator + Legend Elite HP Duo regenerative amplifier), giving 400 nm (3.1 eV) laser pulses with 100 fs fwhm. The laser fluence at the sample was then adjusted using neutral density filters. The X-ray probe beam was derived from electron bunches extracted from the storage ring, giving pulses with a 79 ps fwhm and 6.5 M Hz repetition rate. A Pilatus 2M detector was temporally gated to collect the scattering pattern from the laser-synchronized X-ray pulse from the pulse train, and the measurement was repeated for a certain integration time. The X-ray energy was set at 11.7 keV for all measurements. To account for variations in X-ray brilliance and the liquid jet thickness, the scattering patterns were normalized in the Q range of 4 to 4.1. Based on the absorption spectra of the NCs, we calculated their sizes and cross sections at 400 nm using previous work by Wu et al[125] and Klimov[126] respectively. The numbers of excitons per particle were estimated for each condition using the cross sections and the measured laser fluence. The initial optical densities of our samples at 400 nm were 4.0, 6.1, 9.9, and 3.6 for the 3.8-nm radius, 2.0-nm radius, 1.5-nm radius, and zincblende NCs respectively.

3.4.3. Molecular Dynamics Velocity Rescaling Procedure

At each temperature, thermalization was achieved *via* 12 ps of simulation in the canonical (constant particle number N, volume V, and temperature T) ensemble. This was found to be

sufficient to ensure temperature fluctuations of less than ± 20 K. Following thermalization at each temperature, a simulation of 8 ps in the microcanocial ensemble (constant N, V, and energy E) was used to generate production data. For all simulations, a time-step of 1 fs was utilized.

3.4.4. Generating XRD Patterns with the Debye Scattering Equation

To generate XRD patterns, the Debye scattering equation was solved using atomic positions taken from the MD production trajectories:

$$I(Q) = \sum_i \sum_j f_i f_j \frac{\sin Q|r_i - r_j|}{Q|r_i - r_j|} \qquad (3.4)$$

In this equation, $|r_i - r_j|$ is the distance between atoms *i* and *j*, and f_i is the atomic scattering factor of atom *i*, an element-specific quantity.

3.4.5. *Ab Initio* Molecular Dynamics

Initially, the atomic positions of the NC were relaxed until the forces on each atom were less than 0.02 eV/Å. Following relaxation, the NC was heated to the temperature of interest (i.e. 300, 500, 800, 1200, or 1600 K) and equilibrated for 2 ps (MD timestep = 2 fs) using a canonical sampling through velocity rescaling (CSVR) procedure[109] with a time constant of 10 fs. Following equilibration in the canonical ensemble, the structure was relaxed to the nearest local minimum and a final self-consistent field cycle was performed to calculate the electronic structure of the (locally) relaxed NC.

CHAPTER 4: PHOTOINDUCED, REVERSIBLE PHASE TRANSITIONS IN ALL-INORGANIC PEROVSKITE NANOCRYSTALS

This chapter is based on the research described in the following publication:

Kirschner, M. S.; Diroll, B. T.; Guo, P.; Harvey, S. M.; Helweh, W.; Flanders, N. C.; Brumberg, A.; Watkins, N. E.; Leonard, A. A.; Evans, A. M.; Wasielewski, M. R.; Dichtel, W. R.; Zhang, X.; Chen, L. X.; Schaller, R. D. Photoinduced, Reversible Phase Transitions in All-Inorganic Perovskite Nanocrystals. Nature Comm. 2019, 10 (1) 504.

Significant interest exists in lead trihalides that present the perovskite structure owing to their demonstrated potential in photovoltaic, lasing, and display applications. These materials are also notable for their unusual phase behavior often displaying easily accessible phase transitions. In this chapter, time-resolved X-ray diffraction (TR-XRD), performed on perovskite $CsPbBr_3$ NCs, maps the crystal lattice response to controlled excitation fluence. $CsPbBr_3$ undergoes a photoinduced orthorhombic-to-cubic phase transition which is discernable at fluences $\geq$ 0.34 mJ/cm^2 through the loss of orthorhombic features and shifting of high-symmetry peaks. This transition is reversible and recovers on the timescale of 510 ± 100 ps. A reversible crystalline-to-amorphous transition, observable through loss of Bragg diffraction intensity, occurs at higher fluences ($\geq$ 2.5 mJ/cm^2). These results demonstrate that light-driven phase transitions occur in perovskite materials, which will impact optoelectronic applications and enable the manipulation of electronic non-equilibrium phase characteristics of the broad perovskite material class.

4.1. Introduction

Much of the work on lead halide perovskites has focused on understanding the origin of their impressive optoelectronic properties including a tunable bandgap, high carrier mobility, long carrier lifetimes, and large absorption cross section.[23,127–133] Such advances have enabled thin-film, solution-processable photovoltaics with efficiencies comparable to state of the art Si technologies[127,134–139] as well as low-threshold lasers[140,141] and highly efficient light emitting diodes.[142–144] However, the effects of the heating induced from the injection conditions relevant to display and gain applications are not yet understood. Among the possible responses are crystal phase transitions[145–149] that could become accessible for even moderate excitation fluences. These materials exhibit poor thermal conductivity[150] which is compounded in NC systems which have low interfacial thermal conductance.[84] Improving the understanding of these phenomena may also provide insight into perovskite phase stability that will be important in applications.[145,151,152] Previous investigations of lead halides have demonstrated slow thermalization times in hybrid perovskites,[153–158] partially attributable to the mismatch between the phonon density of states for the organic and inorganic sub-lattices. Studies on the response of nanocrystals to high fluence excitations have revealed fast biexciton lifetimes,[129,159] although the effects of Auger heating on the integrity of the NC lattice remain unexplored. This concern is particularly relevant as elevated temperatures have been shown to reduce photoluminescence, although resiliency can be improved by tuning the halide composition.[160]

One methodology for examining the implications of photoinduced heating in perovskites is time-resolved X-ray diffraction (TR-XRD). Through exciting above the bandgap, fast electron-

phonon coupling and Auger heating impulsively deposit energy into the lattice, which could initiate a phase transition. Examining this effect in perovskite NCs will help evaluate their stability under the high carrier injection conditions that they will experience in display and lasing applications. Here, TR-XRD on $CsPbBr_3$ NCs is performed, which are prototypical all-inorganic lead trihalide perovskite NCs.[161–164] The studies reveal multiple regimes of material response ranging from a reversible orthorhombic-to-cubic phase transition, up to reversible- and then irreversible melting. In addition to characterizing these photoinduced phase transition, this work demonstrates that TR-XRD is a promising methodology for understanding phase transitions in perovskite materials.

4.2. Results and Discussion

4.2.1. The Crystal Structures of $CsPbBr_3$

Figure 4.1a shows crystal structures of $CsPbBr_3$ in the orthorhombic and higher-temperature (above 130˚C in the bulk and 117˚C in the NCs) cubic phases that are differentiated by $PbBr_6$ octahedral tilting in the orthorhombic phase as have previously been characterized.[145–149] The resulting reduction in symmetry has implications in the XRD patterns as demonstrated in Figure 4.1b. Primarily, the orthorhombic phase (blue) has a much higher density of diffraction peaks than the cubic phase (red), most of which are located near corresponding cubic features. For NCs, Scherrer broadening smears together these closely-spaced peaks such that a single broader peak appears relative to the expected width in the cubic phase. There are also several diffraction

peaks absent from the cubic phase. The clearest of these features occur around Q = 1.7 $Å^{-1}$, 1.8 $Å^{-1}$, and 2 $Å^{-1}$, which are all present in the XRD of $CsPbBr_3$ NCs (black) and confirm the orthorhombic structure.[165,166] To emphasize these features, they are labeled “a”, “b”, and “c” respectively in Figure 4.1b. Further, for simplicity the high-symmetry peaks—those that occur in both phases—are labeled with their corresponding cubic planes in Figure 4.1b and I will use these assignments to refer to diffraction peaks in the corresponding Q regions. $CsPbBr_3$ can also exist in a tetragonal phase (88˚C >T>130˚C for the bulk material and 59˚C>T>117˚C for the nanocrystals) which has a diffraction pattern very similar to the orthorhombic phase with the notable exception of its lack of the “b” peak.

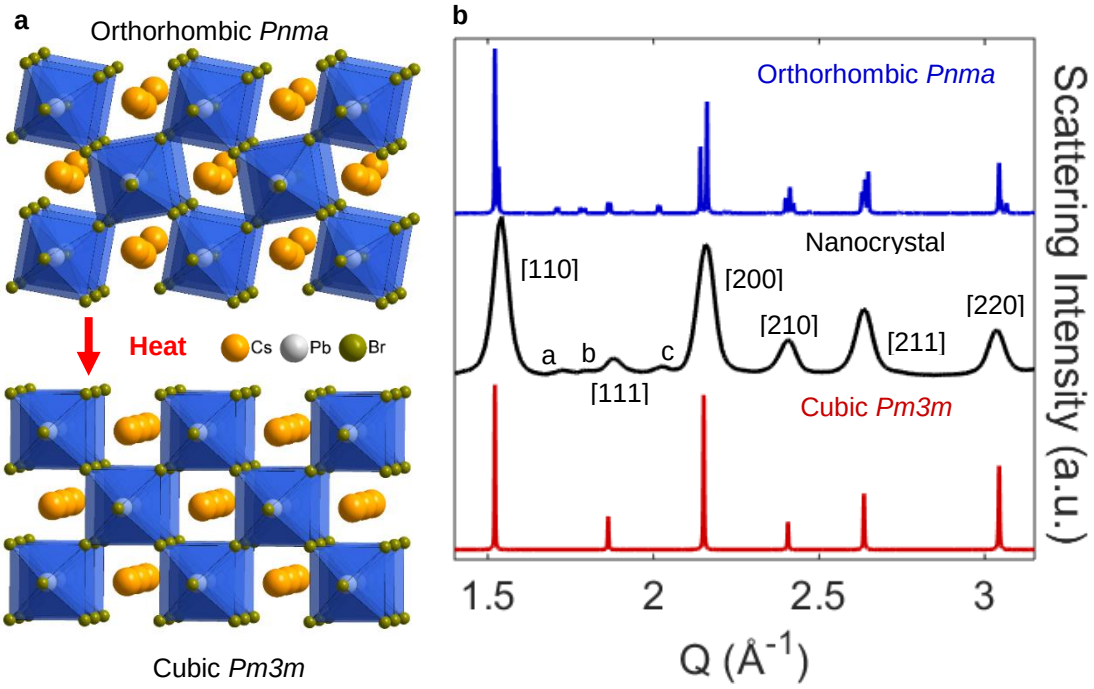

Figure 4.1. (a) Schematic of $CsPbBr_3$ in the orthorhombic (top) and cubic phases (bottom). (b) XRD patterns for the orthorhombic (blue) and cubic phases (red) as generated with VESTA along with the experimental NC XRD pattern (black). The bulk crystal structures are based on a CIF data from Stoumpos *et al.*[147] which were adapted.

4.2.2. Dynamics of Orthorhombic-to-Cubic Phase Transition

To understand how the NC lattice responds to controlled-fluence, impulsive heating, TR-XRD experiments were performed using Beamline 11-ID-D at the Advanced Photon Source (Argonne National Laboratory). The general methodology used was consistent with that in Chapter 3. Briefly, a reservoir of 11.2 ± 2.9 nm edge length, oleic acid and oleylamine-passivated $CsPbBr_3$ NCs, synthesized according to Protesescu *et al.*[23] but scaled by a factor of 8 to provide enough sample for experiments dispersed in dodecane was continuously flowed as a free jet into a dry

nitrogen-purged interaction region, which assured measurement of fresh, unperturbed material with each laser pulse. The ability to flow NCs in solution is a practical advantage partially motivating their usage over bulk perovskites for TR-XRD measurements. Pump pulses of 3.1 eV photon energy from a 1.6 ps Ti:S laser with a 10 kHz repetition rate were attenuated and focused to achieve the desired fluence. After a controlled time delay, 11.7 keV X-ray pulses (79 ps fwhm) were directed into the jet, and the resulting 2D diffraction pattern was collected on a time-gated Pilatus 2M detector, which was then radially integrated. The data was normalized for X-ray flux in the Q range of 3.5 to 3.6 $Å^{-1}$.

Figure 4.2a shows the TR-XRD pattern of $CsPbBr_3$ NCs under an excitation fluence of 4.8 mJ/cm^2. The static XRD pattern is also included in a top panel with vertical lines denoting the orthorhombic (solid, gray) and high-symmetry peak positions (dotted, black). The high-symmetry diffraction features systematically exhibit increased scattering at lower Q and decreased scattering at higher Q, the result of the peaks shifting to lower Q values and consistent with thermal expansion. However, the peaks associated with the lower-symmetry orthorhombic phase exhibit distinct behavior, as emphasized in Figure 4.2b, which zooms in on the Q range of 1.6 $Å^{-1}$ to 2.1 $Å^{-1}$. The TR-XRD signals of these peaks mirrors their static XRD patterns with local minima occurring at the static peak positions, a result of a loss of scattering intensity rather than a change in position. Selective reduction in orthorhombic peak intensity suggests that this excitation

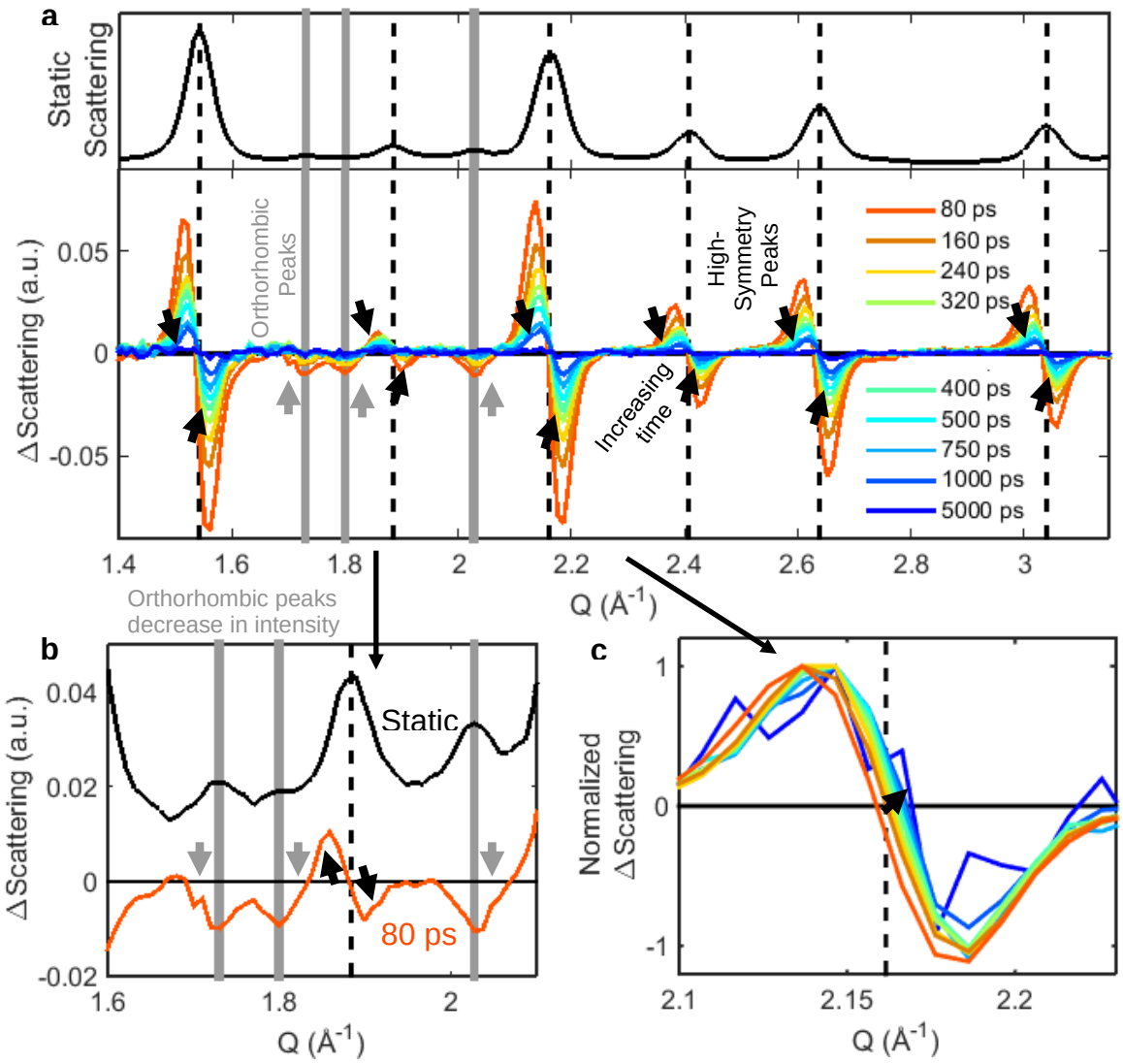

Figure 4.2. (a) TR-XRD pattern of CsPbBr3 NCs at various times following excitation at 4.8 mJ/cm^2 along with the static XRD pattern for reference on peak positions (black). The orthorhombic peaks are delineated with gray solid lines and the high-symmetry black dashed. A solid black line also denotes ΔScattering=0 and arrows emphasize how the TR-XRD pattern evolves in time. (b) Zoomed in TR-XRD for 80 ps in the Q range of 1.6 Å^{-1} to 2.1 Å^{-1}. Once again, the static pattern is displayed with the same features marked as in a. Arrows emphasize how the TR-XRD pattern deviates from the static XRD. (c) TR-XRD pattern for the [200] peak normalized such that the maximum ΔScattering=1. The arrow denotes how the pattern evolves in time.

condition induces a transition to the cubic structure. Related observations have also noted octahedral tilting of lead halides under intense excitation using ultrafast electron diffraction measurements on hybrid perovskite thin films[167]. This photoinduced phase transition is reversible as the orthorhombic peaks completely recover during the observation window and the high-symmetry peaks return to their static positions. This recovery is emphasized in Figure 4.2c, which shows the [200] peak normalized at each time as it shifts to the original, higher Q position. To convert these shifts in the diffraction peaks to changes in temperature, series of static, temperature dependent XRD patterns were collected on a thin film of NCs suspended in a polymer matrix (Figure 4.3a). This methodology is used as the experimental data does not follow a Debye-Waller-like dependence as explored in Appendix B.1. The four most prominent diffraction peaks ([110], [200], [211], [220] and denoted with black dashed lines) were fit to Gaussian functions at each temperature and the shifts in peak positions are plotted in Figure 4.3b. Using a linear fit to extract a thermal expansion coefficient yields a value of $28.4 \pm 3.5 \times 10^{-6}$ K^{-1} (solid black line) which is on the same order as the measured bulk value of 40×10^{-6} K^{-1} (dashed gray line)[147].The lower value measured for the NCs might be partially caused by annealing, which causes a slight decrease in lattice size after extended times at elevated temperatures (Appendix B.2). Additionally, while the three lattice parameters have been shown to exhibit different temperature dependencies in the bulk, the Scherrer broadening in the NC makes it difficult to distinguish these differences. However, treating the lattice parameters as if they were equivalent still yielded values consistent with bulk values suggesting that this assumption is reasonable. It is also worth noting that the analysis done by Cottingham and Brutchey on refining lattice parameters of temperature dependent XRD

measurements with an assumed cubic structure[149] would predict a thermal expansion coefficient around 30×10^{-6} K^{-1}, consistent with the measurements reported here.

Figure 4.3c shows recovery dynamics of the NC lattice derived from TR-XRD signals from the same four diffraction peaks ([110], [200], [211], [202]), which all exhibit consistent kinetics and fluence dependencies (Appendix B.3). To account for the fact that the transient signal has negative and positive components, the absolute value of the change in scattering is used. These kinetics are well fit to a biexponential function with time components of 86 ± 24 ps—possibly due to NC cooling as it is on the order of CdSe NC cooling[106]—and a component of 510 ± 100 ps—which can be attributed to the cubic-to-orthorhombic phase transition as it is on the same order as the amorphous-to-crystalline transition in CdSe NCs,[168] the most analogous process. There may also be faster features, which would require higher-time resolution instruments to resolve. There were not significant variations in dynamics observed with different excitation fluences as shown in Appendix B.4. Figure 4.3d shows NC temperature, calibrated from the thermal expansion coefficient derived from static XRD, as a function of time. While lattice temperature decreases following photoexcitation, the crystals spend an extended amount of time at a plateau around 175˚C. This discontinuity in the change in lattice temperature could be caused by reversion to the orthorhombic phase releasing energy and slowing the cooling process. Additionally, the NCs exhibit narrower peak widths when they are transiently in the cubic phase as displayed in Figure 4.3e, likely a result of the increased crystal symmetry as the cubic phase exhibits narrower peaks as shown in Appendix B.5. Some initial cooling causes further peak narrowing for the first

nanosecond following photoexcitation until the return to the orthorhombic structure causes broadening to the original peak width.

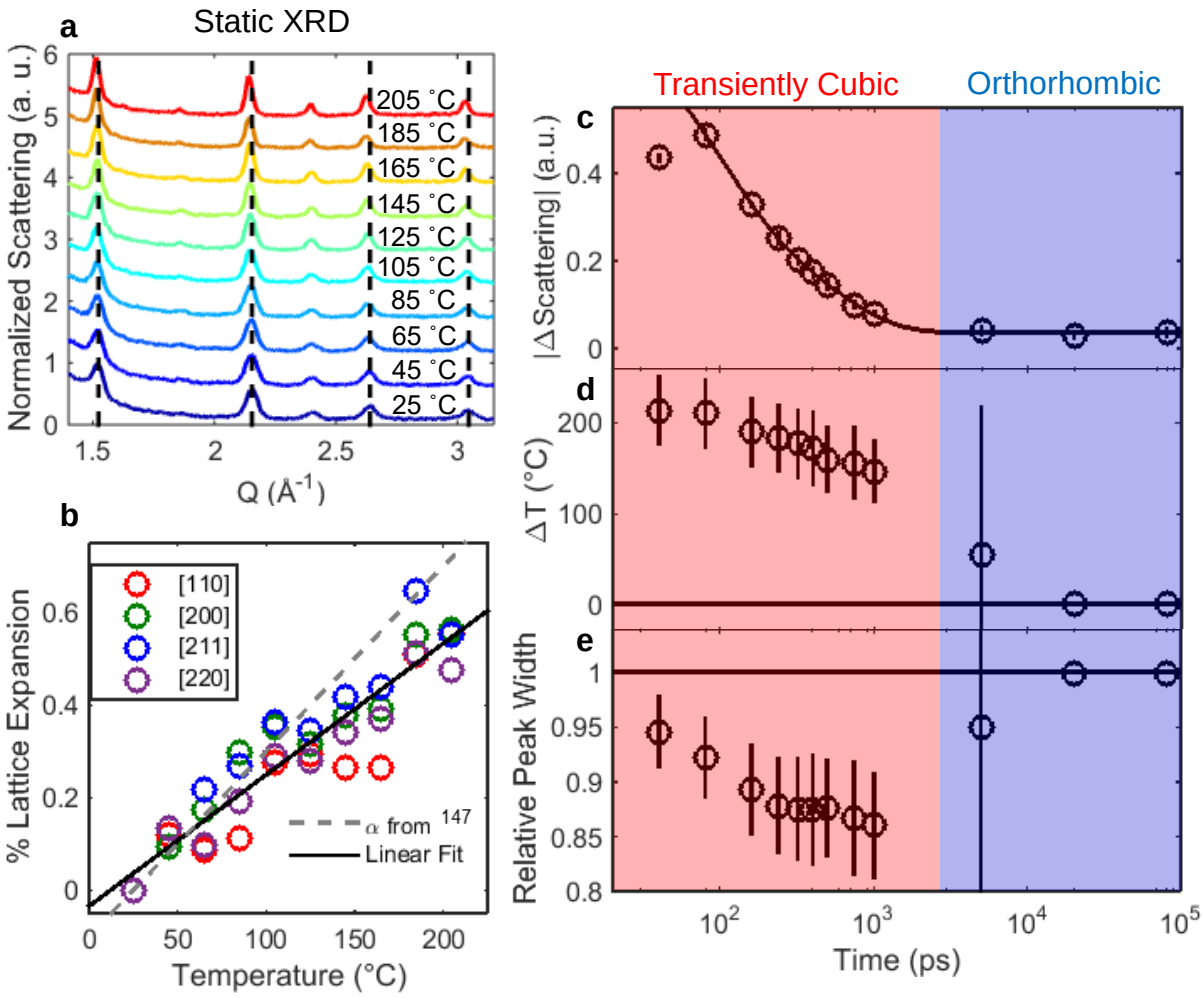

Figure 4.3. (a) Temperature dependent XRD with black dashed lines to emphasize the room temperature peak position. (b) Expansion of lattice planes from static experiments versus temperature along with a linear fit which suggests a thermal expansion coefficient of 28.4 ± 3.5 × 10^{-6} K^{-1} along with the bulk thermal expansion coefficient from Stoumpos et al.[147] (c) Integrated absolute change in scattering signal for NCs versus time under a fluence of 4.8 mJ/cm^2 along with a biexponential fit. Error bars indicate standard deviation in the measurement. (d) Change in NC temperature versus time as calculated from the temperature dependent XRD measurements. Error bars indicate 95% confidence intervals from the fitting algorithm. (e) Change in relative diffraction peak width as calculated from fitting the TR-XRD pattern. Error bars indication 95% confidence intervals from the fitting algorithm.

4.2.3. Fluence Dependence of Disordering

The mechanism for the deposition of energy into the lattice involves several processes which have already been the subject of thorough investigation. Initially, there is rapid intraband relaxation which has been reported to occur on sub picosecond timescales.[129,159,169] At higher excitation fluxes, there has been evidence of a hot-phonon bottleneck of a few picoseconds in nanocrystals[159] that is absent in the bulk measurements.[155] This initial relaxation is understood to be the result of the generation of longitudinal-optical phonons, through Fröhlich electron-phonon coupling, which rapidly down convert to acoustic phonons,[41,153,154] with the specific vibrational density of states of $CsPbBr_3$ having been the subject of previous characterization.[154,170] Additionally many of the multiexcitons undergo Auger recombination—where one exciton relaxes to the ground state by transferring its energy to another exciton which then proceeds to decay to the band-edge. Generally, biexciton lifetimes depend on NC composition and size—they have been reported to be on the order of ~100 ps for NCs of this size and composition[129,159]—while multiexcitonic rates scale quadratically with number of carriers[43,44] resulting in rapid recombination under high fluence excitation conditions. Taken together, these methods result in rapid deposition of energy in the lattice. The subsequent phase transition is fundamentally non-equilibrium as it is impulsively induced. The transition pathway is distinct from a thermal transition as it does not proceed through an observable intermediate, tetragonal phase (Appendix B.6) as has been reported in the thermally induced phase transitions of NCs.[149] Similarly, the temperature of the NCs before the cubic-to-orthorhombic transition does not match with the

thermal transitions which occurs at 117˚C.[149] This non-equilibrium behavior is consistent with the behavior in analogous systems.[103,168,171,172]

Figure 4.4 shows the TR-XRD signals 40 ps after photoexcitation at a range of fluences. As the fluence increases, the high-symmetry diffraction peaks move to lower Q values resulting in larger TR-XRD signal. However, at the highest fluences, the peaks also decrease in intensity, with the change in scattering signal becoming asymmetric with the negative feature becoming larger in magnitude than the positive feature. This change suggests the initiation of a second phase transition: crystalline-to-amorphous (melting). Additionally, at these higher fluences there was a loss of signal on a laboratory time scale associated with a loss of sample as displayed in the inset. This effect is likely the result of NCs crashing out of solution following the loss of ligands as NCs could be seen deposited on the tubing of the jet. The degradation is negligible at fluences below 7.7 mJ/cm^2 but at 18 mJ/cm^2 the degradation was so rapid, extensive, and problematic that I have excluded the corresponding TR-XRD pattern from the main panel. Fluences around 7-12 mJ/cm^2 should therefore be an upper limit to excitation density for applications of these materials in NC form.

To determine the onset of melting, the change in total peak intensity was examined as a function of fluence, (Figure 4.5a). The observed behavior is threshold-like, with no notable changes below the fluence threshold of 2.5 mJ/cm^2, which is indicative of the start of the crystalline-to-amorphous transition.[168] Figure 4.5b shows the absolute value of the TR-XRD signal as a function of fluence. This value increases linearly at low fluences but becomes sublinear after the melting threshold. This trend may reflect shifts in peak position contributing more |ΔScattering|

than decreases in peak intensity as a result of having both positive and negative components. Percent peak loss and |ΔScattering| exhibit very similar dynamics (Appendix B.7), which is further evidence of the non-equilibrium nature of these phase transitions: instead of transitioning from amorphous to cubic before returning to the orthorhombic phase, the NCs transition directly back to the orthorhombic phase. Figure 4.5c shows corresponding increases in temperature as calibrated from the temperature dependent XRD measurements.

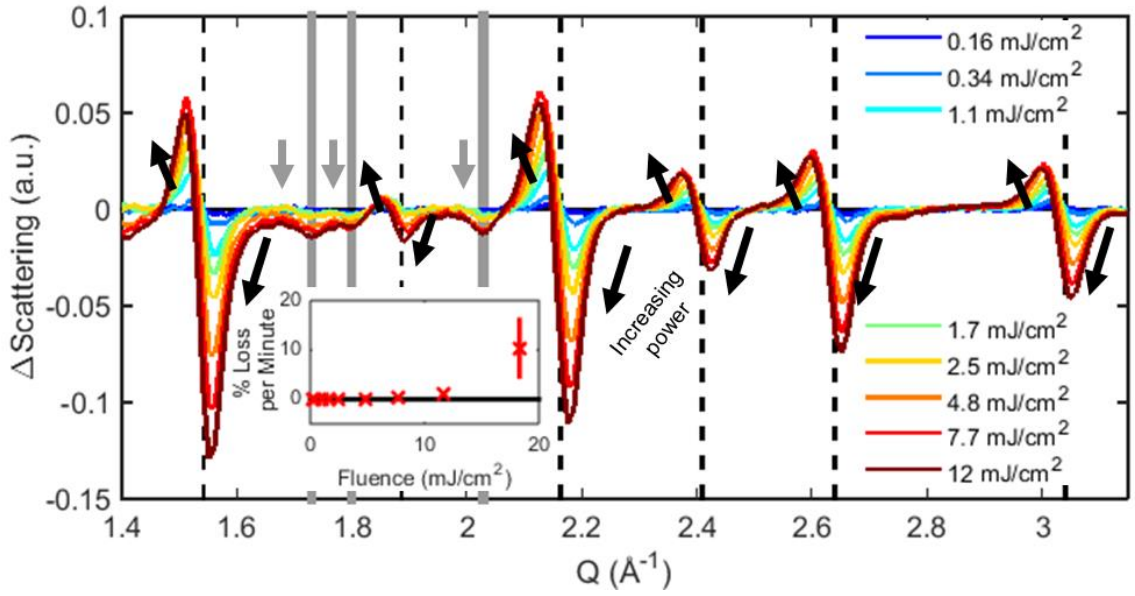

Figure 4.4. TR-XRD patterns of CsPbBr3 NCs 40 ps after photoexcitation at a range of excitation fluences. The orthorhombic peaks are delineated with gray solid lines and the high-symmetry black dashed. A solid black line also denotes ΔScattering=0 and arrows emphasize how the TR-XRD pattern evolves with power. Inset: Irreversible percent loss of peak intensity versus excitation power. The error bar indicates standard deviation in the measurement.

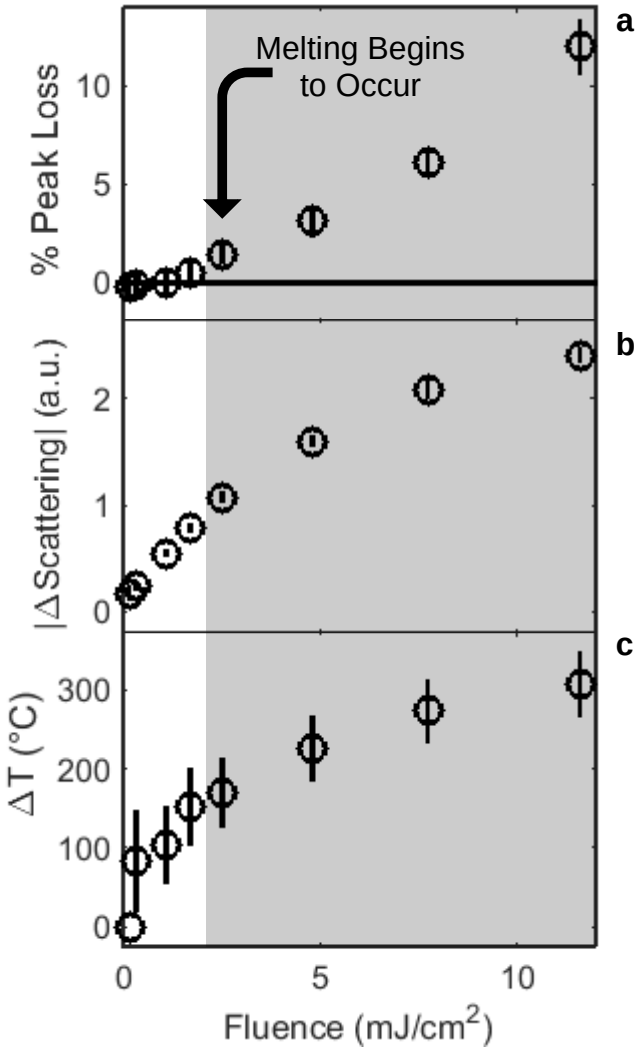

Figure 4.5. (a) Reversible percent loss of peak intensity 40 ps following photoexcitation versus excitation fluence. Error bars indicate standard deviation in the measurement. The gray box indicates fluences past the melting threshold. (b) Integrated absolute change in scattering signal versus excitation fluence. Error bars indicate standard deviation in the measurement. (c) Change in NC temperature versus excitation fluence. Error bars indicate 95% confidence intervals from the fitting algorithm.

4.3. Conclusion

In summary, following moderate to high fluence photoexcitation, $CsPbBr_3$ NCs experience significant impulsive heating. This heating causes the NCs to undergo an orthorhombic-to-cubic phase transition observable through TR-XRD. Lattice recovery dynamics show extended time at elevated temperatures and narrower diffraction peak widths providing further evidence of the phase transition which recovers on the timescale of 510 ± 100 ps. At fluences $\geq$ 2.5mJ/cm^2 reversible melting begins to occur with significant irreversible damage occurring at fluences $\geq$ 18 mJ/cm^2. The success of characterizing $CsPbBr_3$ with TR-XRD suggests it is a promising avenue for studying thermal effects in other lead halide perovskites. These processes, particularly phase transitions, need to be considered for perovskite materials under intense excitation as optoelectronic characteristics have been shown to be strongly influenced by elevated temperatures.[160]

4.4. Methods

4.4.1. Material Synthesis

$CsPbBr_3$ NCs were synthesized according to Protesescu *et al.*[23] scaled up by a factor of eight. NC size was determined via TEM using a JEOL-1400 microscope.

4.4.2. Temperature Dependent X-ray Diffraction Measurements

Temperature dependent XRD measurements were performed on a Rigaku Smartlab instrumentwith a temperature controller under a nitrogen environment.

4.4.3. Calculating Changes in Peak Position.

The changes in peak position were calculated by a global fitting method. First, the static [110], [200], [211], and [202] peaks were fit to Gaussians. Then, at each time point the TR-XRD pattern for each peak $\underline{i}$ was fit to the following equation:

$$\Delta S_i(Q) = A_i(-e^{-\left(\frac{Q-b_{0i}}{c_{0i}}\right)^2} + \frac{\gamma}{\beta}e^{-\left(\frac{Q-(1+\alpha)b_{0i}}{\beta c_{0i}}\right)^2}) \qquad (4.1)$$

where ΔS is the change in scattering intensity, A is a normalization term, b_0 and c_0 are the static peak positions, α is the lattice expansion, β is the relative peak width, and γ is a relative peak intensity. This fit represents simply replacing the initial diffraction peak with a shifted peak. While A was allowed to vary for each diffraction peak, the other three terms were globally fit to increase the stability of the fitting algorithm.

4.4.4. Accounting for Degradation.

To account for degradation, static XRD patterns taken during different scans at the same delay after laser excitation were compared with the following equations

$$d_{i,j}(Q) = \frac{1}{n}\sum_{i=1}^{n} S_{i,j+1}(Q) - S_{i,j}(Q) \qquad (4.2)$$

$$\overline{d_j}(Q) = \frac{1}{n}\sum_{i=1}^{n} d_{i,j}(Q) \qquad (4.3)$$

$$\Delta S_{i,j}(Q) = S_{i,j}(Q) - S_{\tilde{m},j}(Q) - (i - \tilde{m}) * \overline{d_j}(Q) \qquad (4.4)$$

Here, $S_{i,j}$ is scattering intensity for the *i*th time point in the *j*th scan, there are a total of *n* time points in a scan, d_j is the average irreversible loss that occurs over scan *j*, and $\tilde{m}$ is the nearest pre-time zero point. For the final scan, the value of *d* taken from the penultimate scan was used.

4.4.5. Generated X-ray Diffraction Pattern.

The XRD patterns in Figure 4.1 were generated using VESTA based on a CIF file from Stoumpos *et al.*[147]

CHAPTER 5:OPTICAL SIGNATURES OF TRANSIENTLY DISORDERED SEMICONDUCTOR NANOCRYSTALS

This chapter is based on the research described in the following publication:

Kirschner, M. S.; Diroll, B. T.; Brumberg, A.; Leonard, A. A.; Hannah, D. C.; Chen, L. X.; Schaller, R. D. Optical Signatures of Transiently Disordered Semiconductor Nanocrystals. ACS Nano 2018, 12 (10) 10008-10015.

The optoelectronic properties of semiconductor nanocrystals (NCs) have led to efforts to integrate them as the active material in light-emitting diodes, solid-state-lighting, and lasers. Understanding related high carrier injection conditions is therefore critical as resultant thermal effects can impact optical properties. The physical integrity of NCs is indeed questionable as recent transient X-ray diffraction studies have suggested that nanoscopic particles reversibly lose crystalline order, or melt, under high fluence photoexcitation. Informed by such studies, here, CdSe NCs are examined under elevated fluences to determine the impact of lattice disordering on optical properties. To this end, intensity-dependent transient absorption are implemented using both one- and two-pump methods where the latter effectively subtracts out the NC optical signatures associated with lower fluence photoexcitation, especially band-edge features. At elevated fluences, a long-lived induced absorption are observed at a lower energy than the crystalline-NC bandgap across a wide range of sizes that follows power dependent trends and kinetics consistent with the prior transient X-ray measurements. NC photoluminescence studies provide further evidence that melting influences optical properties. These methods of

characterizing bandgap narrowing caused by lattice disordering could facilitate routes to improved optical amplification and band-edge emission at high excitation density.

5.1. Introduction

Interest persists regarding the behavior of quantum-confined semiconductor nanocrystals (NCs) under high fluence excitation.[11,24–35,40,95,99–102,168,173–176] In addition to addressing fundamental questions about NC physics,[11, 99–102,168,173–177] characterizing NCs in this regime has practical implications in display and lighting technologies that operate under sustained, high carrier injection conditions.[25–28,31–33,95] NCs can exhibit narrow linewidth, band-edge photoluminescence and high emission quantum yields. Consequently, NC-based devices in some cases exhibit excellent color purity as well as high quality white light when combined, which benefit NC LEDs[24–28] and commercial displays. Related are lasers that utilize NCs as gain media that, in addition to offering a tunable emission wavelength, exhibit low lasing thresholds.[29–35]

Heat dissipation in such applications becomes important as elevated temperatures reduce device performance and long-term NC stability.[178–180] While thermal management represents a central consideration in existing analogous commercial devices that utilize bulk materials,[178] these concerns become increasingly pressing in NCs due to reduced thermodynamic stability[79] and low thermal conductivity.[84] Indeed, as demonstrated in Chapters 3 and 4, NCs undergo reversible transient disordering, or melting, at sufficiently elevated excitation fluences.[168] The energy required to induce this transition is highly dependent on NC volume (<N>~0.5 excitons per nm^3

for CdSe) with recrystallization occurring within 1 ns for the particle sizes studied. Perhaps most notably, density functional theory modeling of disordered NCs suggest that they may present dramatically perturbed electronic structures that would transiently alter their optical characteristics.

Fluence-dependent optical properties of CdSe NCs have previously been studied in depth with transient absorption.[11,40,101,181] Studies that explore pump fluence found long-lived photoinduced absorptions emerging for elevated intensities, however, the extent to which these optical observations are caused by thermal processes has yet to be investigated. Such features cannot result from multiexcitonic effects since Auger recombination rates are understood to scale quadratically with the number of carriers[43,177] such that, within tens of picoseconds, highly excited NCs are reduced to containing only one or two excitons. Frequently, the origin of long-lived photoinduced absorption at high fluences has been attributed to NCs undergoing Auger ionization and surface charging.[40,101,181] Here, ejected carriers become trapped on the NC surface resulting in an unequal distribution of charges in the NC core which can influence the optical properties of subsequent excitons. These previously observed photoinduced absorptions tend to share several notable characteristics: a spectral position lower in energy than the bandgap, an increased amplitude with higher photon energy and fluence, and a reduced amplitude with surface passivation and sample stirring/flowing. Characterizing this interplay would enable better understanding and routes to optimization of thermal management in relevant devices.

Here, the transient optical properties of NCs under high fluence photoexcitation are reported. I begin by examining NCs with conventional pump-probe transient absorption (TA),

which, at high pump fluences, results in convoluted dynamics. Consequently, the majority of this chapter focuses on two-pump pulse TA (2pTA), wherein only the second pump pulse is alternatingly blocked. 2pTA effectively simplifies the response of the NCs by saturating the lowest energy band-edge states that otherwise dominate the TA spectra, increasing the sensitivity to high fluence photoexcitation effects. In this regime, a lower energy photoinduced absorption appears on the ultrafast timescale with an onset that is proportional to the NC volume, occurring at an exciton density around <N>=0.15-0.32 excitons per nm^3. Further, high fluence photoluminescence measurements show a reduction in the bandgap on the ultrafast timescale. The consistency of these results with previous observations from TR-XRD suggest that there are electronic implications due to NC disordering under high fluence photoexcitation. These characterization techniques provide an avenue for understanding and improving the function of NCs in high carrier injection applications.

5.2. Results and Discussion

5.2.1. Differences between Low Fluence and High Fluence Dynamics

Figure 5.1 exemplifies the differences in photoresponse of NCs under low and high photoexcitation fluences. Figures 5.1a and 5.1b show TA spectral maps of 2.0 nm radius CdSe NCs under low (<N>=0.27) and high (<N>=100) fluences, respectively, with the low fluence data normalized for having fewer photoexcited NCs. At low fluences where most NCs contain only a single exciton, the TA spectrum exhibits a bleach feature (decreased absorption upon optical

pumping) around 2.15 eV owing to state filling of the 1S exciton state.[11,40] With increasing pump-probe delay time, the amplitude of this feature decays, but there are not significant spectral changes. This contrasts with NC behavior under high fluence photoexcitation where in the first few ps there are significant bleach features and increases in absorption (photoinduced absorptions) that quickly decay away as a result of intraband relaxation (known to occur on sub-picosecond

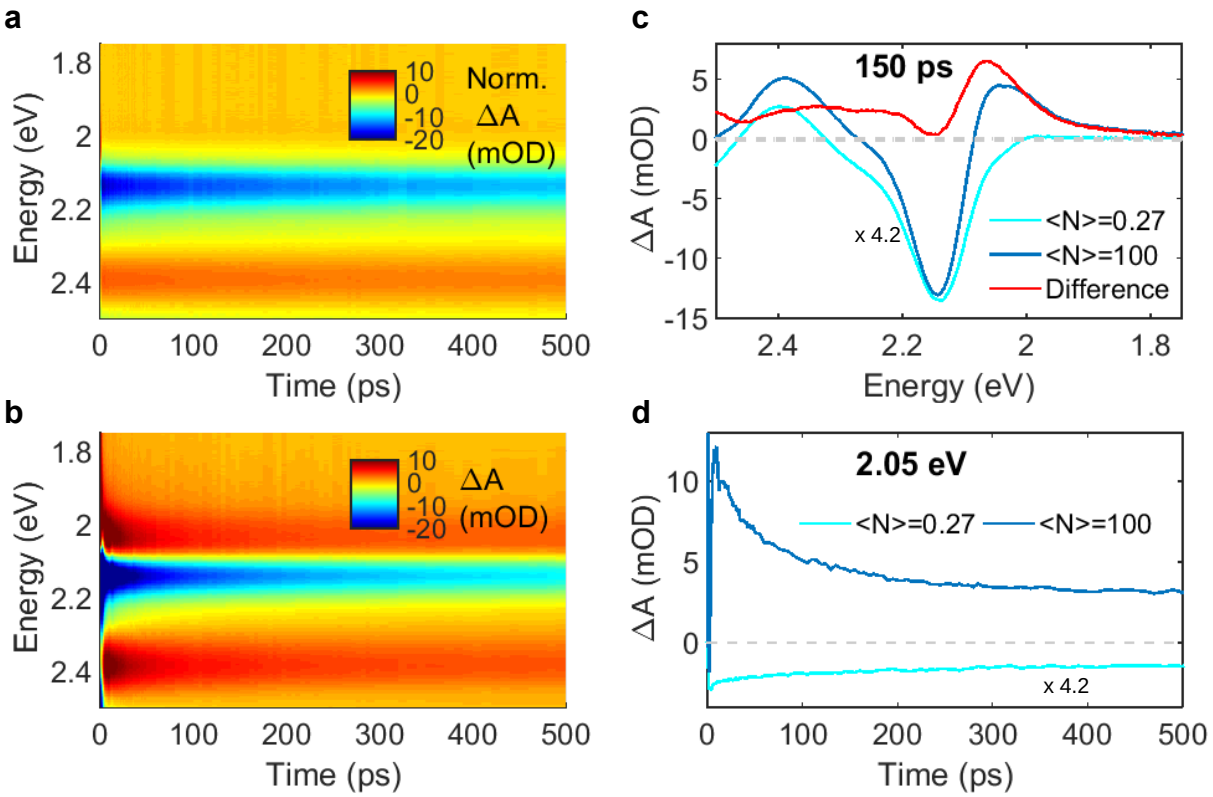

Figure 5.1. TA spectral maps of 2 nm NCs under (a) low and (b) high fluence photoexcitation with average numbers of excitons of 0.27 and 100 respectively. In the low fluence data, the absorption is normalized for the fact that fewer NCs are photoexcited by dividing by 1-P(N=0) as calculated with Poisson statistics. (c) Transient absorption spectra at 150 ps under low (light blue) and high (dark blue) fluence photoexcitation, along with the difference (red). (d) Dynamics under both fluences monitored at 2.05 eV.

timescales for hot excitons) and Auger recombination,[11,40,126] as well as solvent recovery (Appendix C.5). Particles of this size and composition are expected to exhibit a biexciton lifetime around 33 ps,[100,126] which is observed through the bleach feature around 2.15 eV undergoing a significant recovery within the first 100 ps, and suggests that the particles should only contain a single exciton after this time period. However, a spectrally broad photoinduced absorption persists for much longer. This feature is emphasized in Figure 5.1c which shows the high fluence (dark blue) and the scaled low fluence (light blue) TA spectra, each at 150 ps along with the calculated difference between the two spectra (red). Notably, the difference relates a photoinduced absorption around 2.05 eV, which is lower in energy than the bandgap. Dynamics, monitored at 2.05 eV are displayed in Figure 5.1d.

5.2.2. Strategies for Transient Absorption with Two Pump Pulses

Previous characterization of this photoinduced absorption has been limited owing to the fact that it has significant spectral overlap with the optical response of single- and biexcitons. To overcome this complexity, I implemented a two-pump TA technique (2pTA) as related in Figure 5.2a. While TA reveals differences between a ground state and an excited state, here I aim to measure the effects of photoexcitation not solely attributable to single- and biexcitons. Therefore, instead of comparing pump-on (photoexcited) vs pump-off (ground state) absorption spectra, I compare the spectra under high pump power vs lower pump power photoexcitation. A lower power "pump 1" photoexcites the sample to generate a population of single and biexcitons, and then 2

picoseconds later (allowing sufficient time for intraband relaxation), a chopped, controlled fluence "pump 2" photoexcites the same region of sample. By continuously comparing the sample photoexcited by just pump 1 to photoexcitation by both pumps 1 and 2, the resulting difference yields spectra and dynamics with greatly reduced effects from single- and biexcitons. The fluence of pump 1 only has the requirement that it needs to be below the threshold to induce melting as then it might subtract away these effects. However, as the intensity of pump 1 increases, it more effectively subtracts away band-edge bleaching effects owing to the Poisson distribution. To this end, the majority of this work utilized pump 1 fluences that generated an average number of excitons around 1.3 to ensure that most of the NCs had at least one exciton while minimizing NCs that are sufficiently excited to induce melting. The topic of pump 1 fluence is explored further in Appendix C.1.

2pTA measurements minimize signals from processes that occur on laboratory timescales (minutes and hours) while remaining sensitive to ultrafast processes. Specifically, as is often conveyed in the literature,[40,101,181] NCs might build up charge after numerous photoexcitations. The dynamics of excitons in charged NCs are understood to be different than those in neutral NCs.[97] 2pTA should minimize these types of effects as single-exciton dynamics are subtracted away regardless if they are perturbed by surface charging. Using this technique, the low fluence dynamics are subtracted away as a constant percentage rather than as a constant number of photoexcited NCs, as would occur with an algorithm that subtracts away low fluence data.

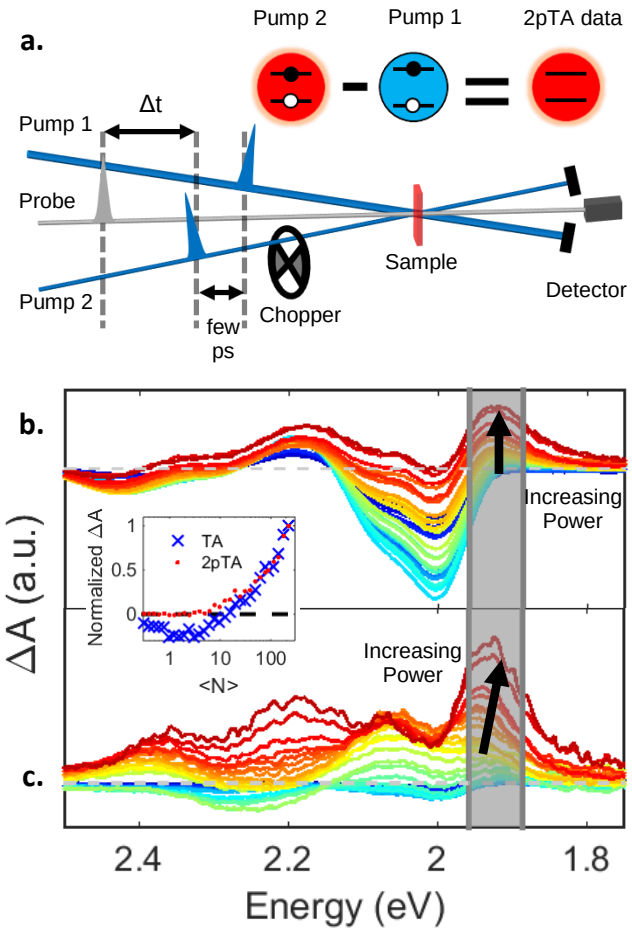

Figure 5.2. (a) Schematic of 2pTA where pump 1 and the probe are incident on the sample at 500 Hz and pump 2, at a few ps time delay after pump 1, is alternatingly blocked or chopped. (b) and (c) Power dependence of (b) one-pump TA and (c) 2pTA (with pump 1 set to generate an average of 1.3 excitons), in each case showing transient spectra of 2.9 nm NCs 150 ps after photoexcitation. In (c), <N> refers to the excitons generated by pump 2. Inset: The integrated peak area of the gray region.

Figures 5.2b and 5.2c display comparisons between TA and 2pTA where the former relates the power dependence of the TA spectra of 2.9 nm radius NCs while the latter shows the power dependence of the 2pTA spectra (pump 1 fixed to generate on average of 1.3 excitons). Presented spectra were acquired at 150 ps to enable sufficient time for Auger processes to occur. While the

TA spectra are dominated by state filling effects, the 2pTA spectra reveal a photoinduced absorption feature at higher fluences that progressively grows in amplitude and decreases in energy. There is a slightly negative feature around 2.0 eV caused by the single and biexcitons not perfectly subtracting out. The inset shows the normalized integrated peak intensity for the highlighted spectral region as a function of power. In TA experiments, this region is dominated by the bleach feature at low fluences, which is successfully removed in the 2pTA spectra. At higher fluences, the photoinduced absorption dominates both the TA and 2pTA spectra, with the two techniques eventually converging. The onset of this induced absorption feature indicates that some physical phenomenon, specific to high power photoexcitation, is occurring, with an onset that is clearer in the 2pTA experiments.

5.2.3. Fluence Dependence of Transient Disordering

Figure 5.3a shows the power dependence of the photoinduced absorption peak observed with 2pTA for NCs of a range of sizes at 150 ps after photoexcitation. The peak areas were calculated by integrating 25 nm spectral windows starting from a wavelength 12 nm longer than the NC absorption maximum. Notably, all the NCs exhibit threshold-like behavior. The fluence of the absorption onset was determined by fitting the data to a piecewise linear function (as detailed in Appendix C.2), which reveals a strong dependence on NC size. For the smallest particles examined, this threshold occurs around <N>=1.4, which does not include the excitons generated by pump 1 (on average 0.85 for these 1.3 nm radius NCs). Additionally, the distribution of

photoexcited NCs is Poissonic which results in the population of highly excited NCs in the ensemble to be relatively large and to absorb relatively more photons when the mean is smaller. Consequently, in these small NCs, the highly excited population might cause photoinduced absorptions to begin to appear at lower fluences while much of the ensemble is still exhibiting single-exciton dynamics. Conversely, the largest particles require around 80 excitons for this high fluence feature to appear, which runs against suggestions that Auger-ionization-induced charging might yield the observed photoinduced absorptions. Interestingly, if normalized by particle volume, as is shown in Figure 5.3b, the power dependence of induced absorption becomes nearly size independent occurring around 0.15-0.32 excitons per nm^3 for all sizes. A thermal process might be expected to exhibit a dependence on volume as larger particles have larger specific heats. Notably, the pump-fluence threshold associated with the observed low-energy photoinduced absorption for each sample is consistent with the previous TR-XRD observations, as is presented in the inset of Figure 5.3b. In the TR-XRD experiments, the disordering threshold occurs between 0.30-0.89 excitons per nm^3, where the lower signal to noise in TR-XRD experiments may accounts for the slight difference from 2pTA results.[168] Appendix C.3 includes additional information about the 2pTA experimental procedures.

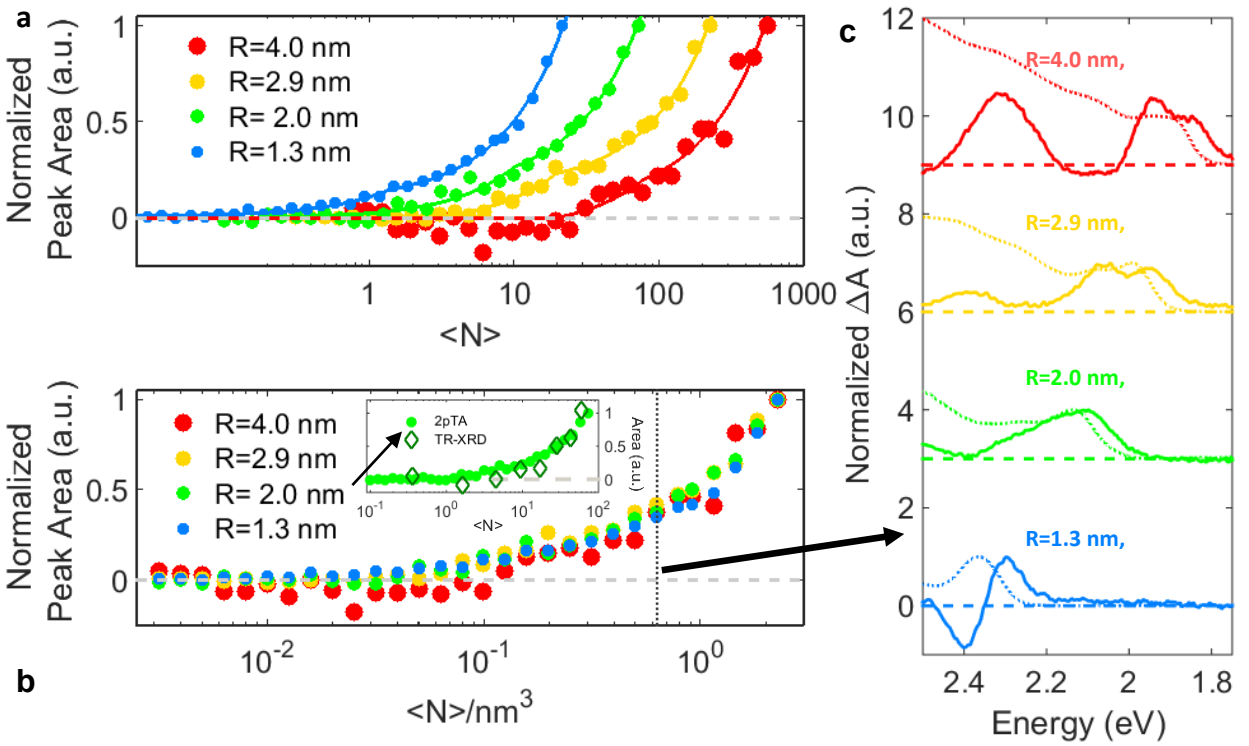

Figure 5.3. Power dependence of the photoinduced absorption observed in 2pTA spectra 150 ps after photoexcitation for NCs of a range of sizes as a function of the average number of excitons generated by pump 2 (a) and excitons normalized by volume (b). Dashed gray lines indicate ΔA=0 and the dotted black line indicates the power utilized in Figure 5.3c which is past the melting threshold. Solid lines in (a) are from fits of a piecewise linear function and the solid black line in (b) is a fit to the average of NCs of all sizes. Inset: 2pTA power dependence compared to the dependence observed in TR-XRD experiments for 2.0 nm radius NCs. (c) 2pTA spectra (solid) compared to static absorption spectra (dotted) with ΔA=0 indicated (dashed). These spectra reveal the additional electronic transitions enabled by NC melting.

Figure 5.3c shows 2pTA spectra of NCs 150 ps after overall photoexcitation at 0.63 excitons per nm^3. Consistent with Figure 5.2b, the photoinduced absorptions are broader and occur at lower energies compared to the static spectra (included as dotted lines). The defined position of these photoinduced absorptions implies that they represent a transition into a distinct state rather than a continuum, where the latter is often argued occurs with photocharging. [40,181] It is also worth

noting that while heating NCs should result in a slight decrease in bandgap owing to crystal expansion, it would not result in the observed net increase in absorption.[182]. Conversely, the observed decrease in energy is consistent with theoretical predictions of NCs undergoing melting. [168] Therefore, based on the threshold-like behavior—for fluences that are consistent with TR-XRD measurements[168]—and the spectral properties of the high fluence photoinduced absorption, this low energy photoinduced absorption can be attributed to NC melting. Although the increased oscillator strength and peak broadening that lattice disordering induces is detrimental to some applications such as lasing,[101] it may prove beneficial in other contexts.

It is worth considering how the thermal energy responsible for inducing this transition from crystalline to disordered is transferred to the lattice. Following photoexcitation, LO phonons are rapidly generated through Frolich electron-phonon coupling as the exciton relaxes to the band-edge[183] depositing energy into the lattice equal to the difference between the photon energy and the lowest-accessible energy level. Consequently, higher energy photons should deposit more energy, which may be responsible for previous observation of larger photoinduced absorptions for excitation with higher frequency photons rather than its prior attribution to differences between the relaxation pathways of various excitonic states.[40] Additionally, most of the multiexcitons undergo Auger recombination, where one exciton relaxes to the ground state by transferring its energy to either an additional electron or hole. This hot carrier then undergoes intraband relaxation depositing thermal energy equivalent to the energy of the exciton with which it Auger recombined. This process is often referred to as Auger heating.[99] The energy deposited from Auger heating is thus the bandgap times the number of excitons minus 1—since the final exciton cannot undergo

Auger recombination—provided the NC is charge neutral and with the simplifying assumption that only band-edge excitons undergo Auger recombination. The relative contributions of these two heating pathways then depends on the NC bandgap and the pump photon energy. Just as an example, for the case of a 3-eV pump and 2-eV bandgap with 10 excitons generated, direct intraband relaxation then yields 10 eV of deposited energy (assuming eventual cooling of all excitons to the band-edge prior to Auger processes), and Auger heating produces 18 eV of energy. Dismissing this assumption would shift more energy deposition to Auger heating.

5.2.4. Disordering Dynamics

Figure 5.4a shows the 2pTA spectra of 2.0 nm radius CdSe NCs under high fluence photoexcitation (pump 1 generating an average of 1.3 excitons, pump 2 at <N>=11) at several time points. During the first few picoseconds after pump 2, there are broad, low energy, photoinduced absorptions commensurate with intraband relaxation and solvent response, as was observed in TA, along with bleach features from the low or unexcited NC population following pump 1. These features decay away rapidly and are followed by the subsequent development of the photoinduced absorption attributable to melting. The spectral properties of this photoinduced absorption changes over the first few hundreds of picoseconds and then decay away on the timescale of a few nanoseconds. The data later than 10 ps was globally fit to three exponential decays and an offset to account for slow, nanosecond timescale processes. The decay lifetimes were kept constant across the spectrum while the various pre-exponential factors and offset terms were varied

independently at each wavelength. Figure 5.4b shows the relative values of those pre-exponential factors. The spectral characteristics of these time components are not necessarily representative of distinct species, but do provide insight regarding how the 2pTA spectrum evolves in time. Notably, the 135 ps time component is consistent with observations from TR-XRD. Additionally, it is spectrally similar to what is predicted for a molten NC with a lower energy absorption peak, suggesting it is the result of the spectrum changing from NC recrystallization. This measurement is, however, sensitive to effects on NC bandgap, which does not necessarily follow a linear relationship with NC crystallinity—not to mention that recrystallization does not necessarily follow exponential kinetics. Consequently, recovery timescales observed here are not a direct analog of TR-XRD measurements.

Figure 5.4c shows the fast and slow (inset) 2pTA dynamics of all the NCs from Figure 5.3 in the spectral region attributed to the photoinduced absorption peak. Again, intraband transitions and fast solvent response are responsible for an early induced absorption that in roughly a picosecond transitions into a bleach feature—likely the result of state filling in the portion of NCs lacking 2 or more excitons[11,40]—and then rapidly transitions back into a photoinduced absorption. The rise of the later photoinduced absorption scales with NC size, occurring faster for smaller NCs. The few-picosecond development of the photoinduced absorption could represent the timescale of NC melting where the rate of Auger heating combined with reduced melting temperature could dictate the size-dependent rate of disordering. The magnitude of this photoinduced absorption rise time does depend on the fluence of pump 1 (Appendix C.1) with less initial bleach observed for higher pump 1 intensity. Therefore, this rise time represents a lower limit on the melting timescale

as faster processes might be obscured by the dynamics of NCs unexcited by pump 1. The inset displays the kinetics of the NCs at longer times along with global fits, as performed in Figure 5.4b. All NC samples exhibit time components consistent with reordering (on the order of 150 ps).

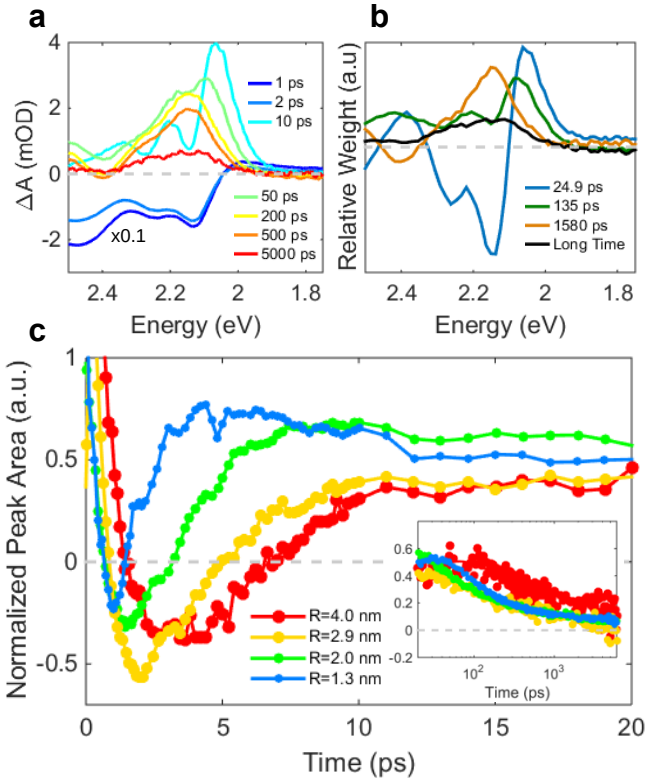

Figure 5.4. (a) 2pTA spectra of 2.0 nm NCs at <N>=11 (pump 1 generating an average of 1.3 excitons) at several time points. The spectra at 1 and 2 ps are scaled down by a factor of 10. (b) Pre-exponential factors of a global fit of the 2pTA spectra from (a). (c) Kinetics for the first 20 ps of the spectral region where the induced absorption occurs for NCs of a range of sizes. Peak areas are normalized such that the maximum of the second induced absorption minus the minimum of the bleach feature is 1. Inset: Dynamics for 20 ps to 6 ns for those NCs along with fits. Details of the fits are included in Appendix C.3.

5.2.5. Photoluminescence Measurements

To further investigate the effects of high fluence photoexcitation on NCs, a series of photoluminescence (PL) measurements was performed. Previous work characterized CdSe PL under this excitation regime with a focus on distinguishing biexciton and higher-multiexciton radiative transitions.[99,174–176] However, here I am examining if emission consistent with radiative recombination from melted NCs is observable. Figure 5.5 shows normalized PL spectra of 2.0 nm NCs for the first 20 ps after photoexcitation under a range of fluences obtained using a streak camera. At higher fluences a peak attributable to radiative decays from higher-energy exciton states is observed. However, as the power increases even more, the PL spectrum begins to lose distinct features. This breakdown is consistent with melting which would cause a decrease in the band structure and a broader, less structured transition. It is also notable that as the fluence increases, the lower-energy edge of the PL shifts to lower energies. In previous work, such shifting has been attributed to a combination of neutral and charged biexcitons derived from Coulomb binding energies.[99,174–176] Given the continual decreases in energy, thermal processes may contribute to the lower energy emission. The inset displays the total spectrally integrated PL intensity under the same fluences, here collected with a CCD. The total intensity increases with excitation power until <N>=10 for this sample where the intensity saturates and then slightly decreases. The PL spectra and dynamics are included in Appendix C.4 and do not significantly change with fluence, suggesting that NC disordering does not alter the decay pathway of single excitons.[97]

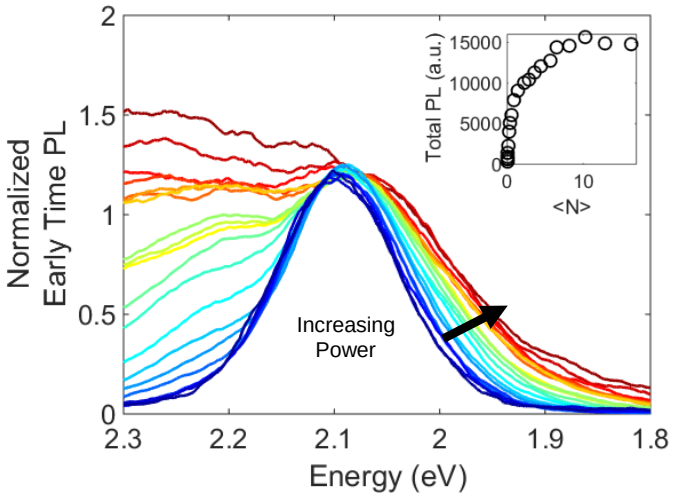

Figure 5.5. Normalized photoluminescence spectra of the first 20 ps following photoexcitation in 2.0 nm NCs. Inset: Total photoluminescence as integrated with a CCD.

5.3. Conclusion

In summary, high fluence photoexcitation of CdSe NCs causes optical changes consistent with the reversible melting noted in recent TR-XRD studies. At sufficiently high fluences (<N> ~ 0.25 excitons/nm^3), an induced absorption lower in energy than the NC bandgap begins to appear with a recovery component on the timescale of 150 ps. The reduction in bandgap, suggests that reversible melting would likely have a deleterious effect on most devices that rely on high carrier injection conditions. The ability to characterize this phenomenon without a synchrotron will enable an improved understanding of the behavior of highly excited NCs. This insight could enable the design of NCs with improved resilience to melting and thus higher performing devices. The findings suggest also that shell growth on particle cores may improve performance owing to

increased specific heat and reduced surface energy, rather than improved surface passivation as commonly believed.

5.4. Methods

5.4.1. Material Synthesis

The synthesis of wurtzite CdSe nanocrystals followed a modified and scaled-up version of literature procedures.[123] First, a selenium precursor solution was made by dissolving 348 mg powdered selenium (99.99%, Aldrich) in 1.7 mL of trioctylphosphine (90%, Aldrich) in a nitrogen glovebox. In a 3-neck flask, 360 mg CdO (99.99%, Aldrich), 18.0 g trioctylphosphine oxide (99%, Aldrich), and either 1.40 g of tetradecylphosphonic acid (Strem, 99+% used for synthesis of larger CdSe nanocrystals) or 1.68 g octadecylphosphonic acid (Strem, 99+%, used for synthesis of smaller CdSe nanocrystals) were combined and held under vacuum at 120˚C for 1 hour, then heated to 300˚C under nitrogen and held until the reaction mixture became clear, indicating the formation of cadmium phosphonate complexes. Then, 10 mL trioctylphosphine was injected and the reaction mixture was heated to 340-370˚C. (Higher temperatures for smaller particles.) After reaching the set-point temperature, the selenium precursor solution was rapidly injected and the temperature was maintained from 0-15 minutes: for larger nanocrystals, lower temperatures and longer reaction times were used. To synthesize the smallest nanocrystals in this study, an additional 300 µL of diphenylphosphine (98%) was added to the selenium precursor solution prior to injection and the reaction was cooled immediately afterward. Nanocrystals were purified by

methanol precipitation and two additional hexanes/isopropanol washes, re-dispersing the nanocrystals in hexanes.

5.4.2. Optical Measurements

All samples were suspended in hexanes for optical measurements and rapidly stirred and translated. Transient absorption measurements were performed using a 500 Hz, 35 fs Ti:S amplifier. The 800 nm output was beamsplit with one portion frequency doubled to generate the pump pulses, and a smaller portion time-delayed and focused into sapphire to produce a white light probe beam. Pump pulses were mechanically chopped at 250 Hz to compare probe intensity though the sample with and without photoexcitation. Pump spot sizes were measured via transmission through a pinhole. The 2pTA experiments utilized the same laser. The delay between the pump and the probe was 2 ps. The pump 1 powers generated an average number of excitons of 0.85, 1.3, 1.3, and 3.1 for NCs of R=1.3, 2.0, 2.9, and 4.0 nm respectively. In the photoluminescence measurements, the laser rep rate was raised to 2 kHz. For the time resolved PL (early time in the main text), the photons were directed into a 150 mm spectrograph and single-photon- sensitive streak camera. Detector regions were binned vertically or horizontally to produce time-resolved spectra or spectrally resolved dynamics. The total PL was collected with a CCD.

Based on absorption spectra, NC sizes and cross sections were calculated at 400 nm using previous work by Yu et al[125] and Klimov,[126] respectively. The numbers of excitons per particle were estimated for each condition using the cross sections and the measured laser fluence.

CHAPTER 6: SIZE-DEPENDENT COHERENT-PHONON PLASMON MODULATION AND DEFORMATION QUANTIZATION IN GOLD BIPYRAMIDS AND NANOJAVELINS

This chapter is based on the research described in the following publication:

Kirschner, M. S.; Lethiec, C. M.; Lin, X. M.; Schatz, G. C.; Chen, L. X.; Schaller, R. D. Size-Dependent Coherent-Phonon Plasmon Modulation and Deformation Characterization in Gold Bipyramids and Nanojavelins. ACS Nano 2018, 12 (10) 10008-10015.

Localized surface plasmon resonances (LSPRs) arising from metallic nanoparticles offer an array of prospective applications that range from chemical sensing to biotherapies. Bipyramidal particles exhibit particularly narrow ensemble LSPR resonances that reflect small dispersity of size and shape but until recently were only synthetically accessible over a limited range of sizes with corresponding aspect ratios. Narrow size dispersion offers the opportunity to examine ensemble dynamical phenomena such as coherent phonons that induce periodic oscillations of the LSPR energy. Here, transient optical behavior of a large range of gold bipyramid sizes are characterized, as well as higher aspect ratio nanojavelin ensembles with specific attention to the lowest-order acoustic phonon mode of these nanoparticles. Coherent phonon-driven oscillations of the LSPR position are reported for particles with resonances spanning 670 to 1330 nm. Nanojavelins were shown to behave similarly to bipyramids but offer the prospect of separate control over LSPR energy and coherent phonon oscillation period. A new methodology for quantitatively measuring mechanical expansion caused by photo-generated coherent phonons is developed. Using this method, an elongation of approximately 2% per photon absorbed per unit

cell is found and that particle expansion along the lowest frequency acoustic phonon mode is linearly proportional to excitation fluence for the fluence range studied. These characterizations provide insight regarding means to manipulate phonon period and transient mechanical deformation.

6.1. Introduction

Synthetic control over the size, shape, and composition of metallic nanoparticles affords tunability of localized surface plasmon resonances (LSPRs) from the ultraviolet through the mid-infrared.[47,184–188] Controlling the LSPR energy facilitates nanoparticle-based applications that range from use as SERS substrates[46,55–57] and chemical/biological sensors[46,55–57] to medical therapeutic applications[57,189,190] and photocatalysis.[191,192] Whereas the large extinction cross-sections presented by LSPRs draw interest for applications, ensemble polydispersity represents another key feature as reflected in the LSPR linewidth. Gold bipyramids exhibit narrow ensemble linewidths, largely dominated by homogeneous dephasing[70,75,76,193] (especially narrow in comparison to spheres and rods), which reflects the monodispersity of the sample. The comparative homogeneity of the ensemble permits time-dependent, ensemble characterization of coherent acoustic phonon oscillations[70,75,76] that interestingly yield prominent, periodic shifts of the LSPR energy owing to expansion and contraction of the particles. While other nanostructures can exhibit the same phenomenon, particle size dispersion leads to variation in phonon frequencies causing fast inhomogeneous damping that typically dominates ensemble dynamics.[47,65,187,188]

Previously, Pelton *et al*. examined bipyramids with an LSPR near 700 nm, characterized and also modeled the LSPR oscillations via a parameter-free model.[70] They could separate damping processes related to energy dissipation into solvent (fluidic damping) vs particle-intrinsic damping and found that intrinsic damping was consistent across a range of suspension media. In subsequent work, they generalized this model to include particles with an arbitrarily slender shape and, by characterizing a series of similarly sized particles, argued that damping is a property of material and geometry.[76] Fernandes *et al*. demonstrated use of bipyramid acoustic phonons to perform mass sensing.[75] Upon growing a thin layer of silver on a gold bipyramid sample they were able to observe a shift in vibrational frequency and correlated the shift to the mass of silver added. Their work also led to observation of higher-order vibrational modes of bipyramids and the characterization of how such higher-order modes changed with the geometric alteration induced by the addition of silver.

Despite these preceding works, some properties of these coherent phonons remain ambiguous. One such aspect is the fluence- and particle-size-dependent displacement amplitude of the phonon-induced particle deformation in bipyramids, although some studies have measured such for other nanoparticle systems. Hartland measured the expansions of gold nanospheres from coherent acoustic phonons based on shifts in LSPR position obtained from optical transient absorption spectroscopy.[187] He found radial increases around 0.4% for excitation fluxes around 2.5×10^{15} photons/cm^2 of 390 nm pump photons.[187] Other studies utilized x-ray characterizations. Plech observed lattice expansions of <1.2% for laser pump intensities up to near 8×10^{16} photons/cm^2 from a 400 nm source using transient x-ray scattering.[68] Using truncated gold

octahedral nanocrystals pumped at a fluence of 4×10^{15} photons/cm^2 from a 800 nm source, expansions of around 0.5% were reported by Clark *et al.*[69] However, these efforts rely on isotropic systems or complex spectroscopic techniques. A more robust methodology is required to understand acoustic phonon vibration in the ever increasing variety of particle geometries. This need is especially relevant for bipyramids as the most recent synthetic progress is able to produce a wider range of bipyramids with high yield[194,195] as well as nanojavelins—extremely elongated bipyramids with surface plasmon resonances that extend into the near-infrared range.[195]

Here, time-resolved spectroscopic measurements and theoretical modeling of a large range of gold bipyramids and nanojavelins are reported with LSPR extinction maxima that range from 650 to 1350 nm. First, the dependence of coherent phonon dynamics with particle size and aspect ratio are characterized, and it is demonstrated that LSPR position and phonon frequency can independently be varied. Then, a methodology to calculate particle expansion caused by coherent acoustic phonons is developed using transient absorption spectroscopy in conjunction with theoretical modeling. Using this approach, it is shown that particle expansion is linearly dependent on excitation power with larger particles exhibiting slightly higher relative expansions. Taken together, these results provide a better understanding of how to manipulate phonon dynamics as well as their mechanical impact on nanoparticles.

6.2. Results and Discussion

6.2.1. Independent Manipulation of Plasmon Resonance and Phonon Frequency.

Figure 6.1a shows transmission electron micrographs (TEMs) and extinction spectra (absorption and scattering contribute) for a series of gold bipyramids and nanojavelins (herein referred to as samples A-G) suspended in water with a broad range of LSPR positions, spanning from 650 to 1350 nm. Samples A-E were synthesized following the procedure published by Liu and Guyot-Sionnest,[193] whereas samples F-G were prepared using the procedure outlined by Chateau *et al*. which results in rougher, sawtooth-like edges.[195] The redder LSPR extinction maxima arise from longitudinal plasmon resonances while features near 550 nm originate from both transverse LSPR modes of the bipyramids/nanojavelins and undesired synthetic side products such as small nanospheres and nanorods.[196] Figure 6.1b shows that these longitudinal LSPRs depend linearly on aspect ratio, defined as particle length/width, which is consistent with previous measurements.[195]

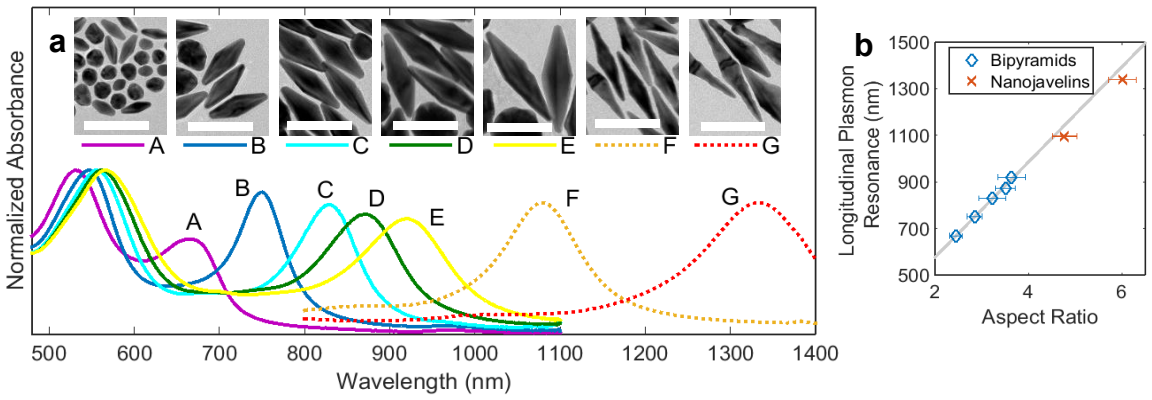

Figure 6.1. (a)(top) Transmission electron microscopy of samples A thru G, (bottom) extinction spectra for the indicated samples where solid lines indicate bipyramids (A-E) and dashed lines indicate nanojavelins (F and G). The white scale bars are all 100 nm in length. (b) Position of the longitudinal LSPR vs aspect ratio for samples A-G from panel (a) where red "x" shapes indicate nanojavelins. The solid line is a linear fit of the five bipyramid samples. Error bars represent standard deviation in ensemble aspect ratio as derived from TEM.

For each of these samples, broadband transient absorption was performed using a pump wavelength tuned to the LSPR extinction maximum. Despite the differences in the synthesis and surface details, both types of particles present coherent acoustic phonons reflected in their transient absorption spectrum. Figure 6.2a shows the raw transient absorption spectrum for nanojavelin sample G. There is substantial oscillatory red and blue shifting of the LSPR center wavelength owing to the photo-induced generation of coherent acoustic phonons. Upon elongation, the LSPR broadens and red-shifts to produce an induced absorption feature, as well as a concurrent bleach of the static LSPR position in addition to some evidence of broadening. For all seven samples, and as shown in the inset of Figure 6.2b, the LSPR oscillatory features was fit to obtained the coherent

phonon frequency as well as oscillation quality factors with a procedure detailed in Appendix D.1. It was found that phonon periods depend linearly on particle length for bipyramids and nanojavelins, consistent with the lowest-confined acoustic mode.[75] At present, bipyramid syntheses do not permit facile independent tuning of both aspect ratio and length. As a result, adjusting the LSPR yields a concomitant change in the phonon period, which is set by the nanoparticle length. However, it is possible to create nanojavelins with nearly the same length as bipyramids but significantly different aspect ratios such as samples D and F. These two ensembles exhibit similar phonon periods of 93 ps and 85 ps but quite different LSPR resonances of 872 nm and 1096 nm. These measurements then demonstrate that, through utilizing nanojavelins, one can further control particle LSPR energy and phonon period.

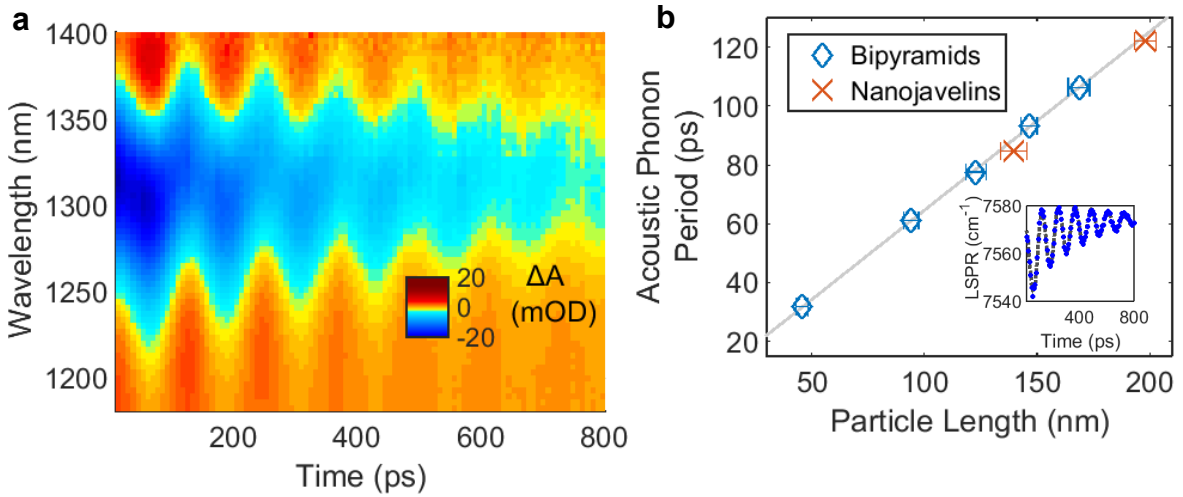

Figure 6.2. (a) Representative experimental broadband transient absorption dynamics, here for sample G. (b) Particle length vs measured phonon period. This solid line is a linear fit for the five bipyramid samples. Error bars indicate standard deviations in ensemble size. Variation in the phonon period is less than 0.3% so no vertical error bars are included. Inset: LSPR peak center modulation caused by acoustic phonons for the data in panel (a). Experimental data points are shown in blue and the dark grey line arise from fitting to Equation 1. Note that the shift in LSPR in the inset relates both coherent phonons and lattice heating. Lattice heating in the samples is discussed in Appendix D.2.

6.2.2. Mechanical Deformation from Acoustic Phonons.

Understanding lattice distortion extent in metal nanoparticles is generally quite challenging. However, here I develop a technique to quantify the effects of lattice distortions on plasmonic properties. To determine this particle deformation caused by the coherent acoustic phonons several theoretical tools were used in conjunction with experimental data. First, finite-difference time-domain (FDTD) simulations were performed using particle dimensions based on TEM images to calculate the extinction spectra of the samples. Figure 6.3a shows the calculated and experimental optical spectra for sample C. The redder, longitudinal plasmon resonances exhibit good agreement. The calculated higher energy peak, around 512 nm, corresponds to the transverse plasmon mode and is masked in the experimental spectra by the large peak around 555 nm corresponding to the LSPRs of spherical nanoparticles in the sample. These FDTD calculations also provide spatial mapping of the electric field distribution at the particle surface, shown as an inset in Figure 6.3a of sample C. As expected, the highest field intensity appears close to the tips of the bipyramid, corresponding to the longitudinal plasmon resonance.

Finite-element analysis (FEA) was used to calculate the frequency of the acoustic vibrations associated with the samples. In Figure 6.3b the measured and calculated periods of the acoustic mode are shown as a function of the longitudinal plasmon resonance. The calculated periods closely match those of the measured oscillations with a slight systematic increase. Figure 6.4a shows how FDTD and FEA were combined to calculate particle deformation after photo-excitation. Using FEA the direction of the geometric change induced by the acoustic phonon was determined. The LSPR peak shift with expansions of different magnitudes along that phonon mode

were then calculated via FDTD. These calculations on bipyramids were performed with a long axis extended in a range of 0.1% to 1% of its original value and contracted along the short axis. Figure 6.4a shows a rather linear dependence of the LSPR shift as the particle undergoes elongation. These calculations were then used to generate a calibration plot to allow the conversion of peak shift to mode-specific particle elongation.

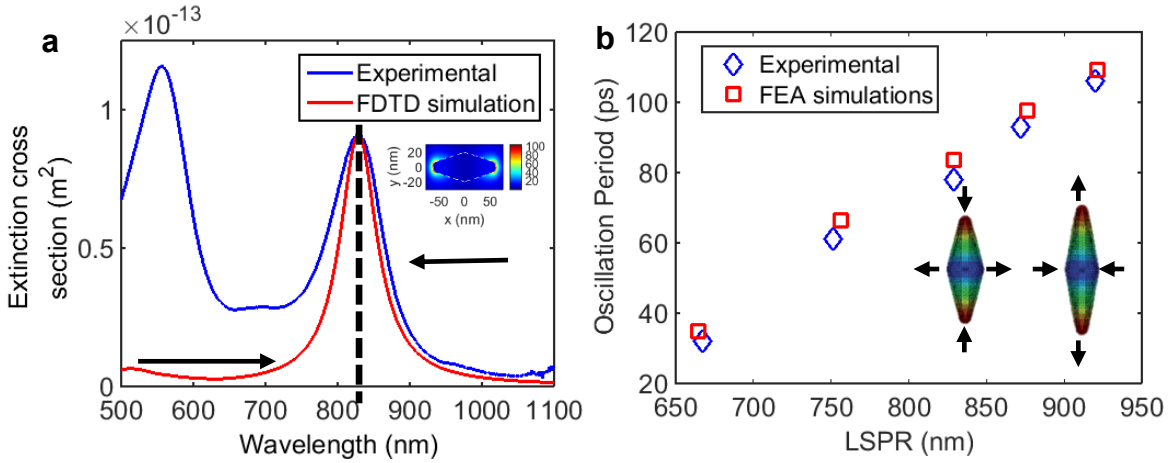

Figure 6.3. (a) Experimental (in blue, arbitrary unit) absorption spectrum measured on Sample C. The absorption spectrum calculated on a gold bipyramid with the same dimensions as Sample C is also plotted (in red). The theoretical spectrum displays both the transverse (around 512 nm) and longitudinal (at 829 nm, dash line) plasmon resonances. The experimental transverse plasmon resonance overlaps with the plasmon band from the impurities in the sample. Inset: FDTD simulation of the 2D projected near-field enhancement around the same gold bipyramid as in a, calculated at 829 nm. (b) Measured (blue) and calculated (red) oscillation period of the vibrational mode as a function of the longitudinal plasmon resonance for the five samples of gold bipyramids. Inset: simulated displacement of a bipyramid during acoustic mode oscillation (not at scale).

To relate these calculations to experimental data, the time dependent position of the LSPR after photoexcitation was fit to a function of the following form

$$\omega_\varepsilon(t) = \sum_j \beta_j \, e^{-t/\tau_{1j}} \, e^{-\left(\frac{t}{\tau_{2j}}\right)^2} \sin\left(\frac{2\pi t}{T_j} + \varphi_j\right) + \omega_0 + \alpha e^{-t/\tau_{cool}} \qquad (6.1)$$

This equation includes for a given phonon mode j, the maximum coherent phonon displacement β, homogeneous lifetime τ_1, inhomogeneous lifetime due to nanoparticle polydispersity τ_2, the period of the acoustic vibrations T, and phase shift φ, along with the static LSPR position ω_0, a lattice heating term α, and a lattice cooling lifetime τ_{cool}. Here, a single frequency, the lowest-energy phonon mode, dominates the oscillatory behavior of the LSPR signal and therefore obviates the summation as only one phonon mode is modeled in the fit. Homogeneous quality factors did not exhibit monotonic dependence on particle size, but these values (which range from roughly 10-30) likely depend on details of the particles such as surface roughness and facet imperfections evident in TEM as examined and discussed in Appendix D.3 along with information regarding fitting procedures.

Figure 6.4b shows the coherent phonon-induced shift in the LSPR peak position (β) measured as a function of pump intensity for the bipyramid samples. Note that the extrapolation to zero photons absorbed gives a residual, apparent particle expansion in both theoretical (6.4a) and experimental data (6.4b). It is unclear why this trend is observed. For the theoretical data it is possibly caused by uncertainty from the high-resolution meshing and prohibitively high precision calculations impedes still smaller-expansion modeling. The low power regime also yields experimentally reduced signal-to-noise. Still, the trend may relay physical meaning. For instance, scattering of hot electrons and higher-energy phonons may cause pre-existing acoustic phonons to enter into phase as phonon injection locking has been reported in other systems,[197] though such a notion requires future research.

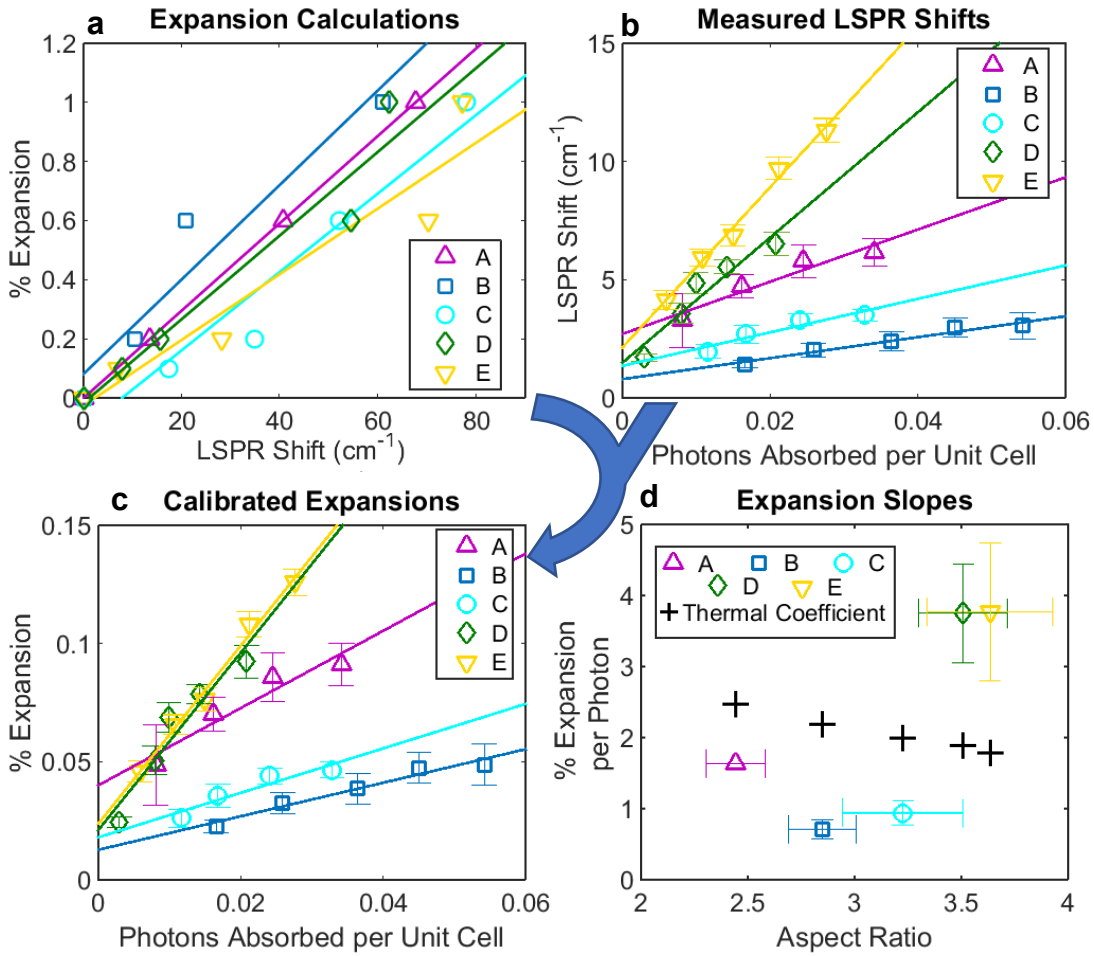

Figure 6.4. (a) LSPR shift from different particle expansions as estimated from FDTD and FEA simulations. While the particle elongations in these theory calculations are much larger than is observed experimentally, they can be extrapolated to predict dynamics on experimental scales that are not computationally feasible. Since FDTD is highly sensitive to small changes in bipyramid geometry and high-resolution meshing there is some uncertainty in these calculations, on the order of a few wavenumbers. (b) LSPR shifts observed from coherent acoustic phonons normalized for particle size. Unit cells were assumed to be FCC structure (4 atoms per unit cell) and particle absorption cross sections, listed in Table D.1, were taken from FDTD calculations. Error bars are the 95% confidence interval from the fitting algorithm. (c) Particle elongation versus photons absorbed per unit cell from the experimental data in b combined with a calibration curve generated from theory results in a. Error bars are the same as those in b. (d) Slopes of linear fits of the data in c along with expected slopes based on the linear thermal expansion coefficient and specific heat of gold. Horizontal error bars are standard deviations in size from TEM images and the vertical error bars represent the uncertainty from the calibration curves (Figure 6.4a) calculated from the ratio of the residual sum of squares to the total sum of squares.

Combining the slope information from theory (Figure 6.4a) and experiment (Figure 6.4b), the power dependence of particle elongation in Figure 6.4c can be evaluated. This analysis shows that elongation exhibits a fairly linear dependence on excitation intensity, which is consistent with observations for nanospheres using transient x-ray scattering.[198] As can be seen in Figure 6.4b, LSPR shifts do not exceed 15 cm^{-1} across this range of powers and samples, which translates to transient particle elongations of less than 0.2%, comparable to what has been reported for nanospheres.[68,69,187] However, here strictly coherent, mode-specific expansion is considered whereas prior efforts also included incoherent lattice heating, making it difficult to perform direct comparisons between different reports. I do not expect it is possible to obtain significantly larger changes in particle elongation than those shown in Figure 6.4 as additional deposited energy from still higher pump intensity likely goes toward rapid melting rather than coherent expansion of the particle.[68,199] In Appendix D.4, overall changes in particle size from coherent phonons are estimated.

Figure 6.4d shows the slope of percent elongation over photon absorption for the data shown in Figure 6.4c along with expected slopes from the thermal expansion coefficient of gold.[68] These measured values, when normalized for particle size, exhibit only a slight size dependence with more expansion occurring for larger particles, which could be explained by the longer particles having lower energy phonons. If the bipyramidal phonon modes were populated with a Boltzmann like distribution of energy, higher percentages of the energy would be converted into lower energy phonon modes for these bigger bipyramids. Alternatively, larger bipyramids have higher scattering cross-sections. Provided that some of that scattering is inelastic, it will contribute

to generation of phonons. However, this effect is expected to be small since scattered photons impart significantly less energy than absorbed photons and the scattering cross section is on the same order of magnitude as the absorption cross sections. Although these differences exist, the expansion per photon absorbed is on the same order of magnitude across the examined size range, which indicates that size dependent effects on elongation are weak. These measurements are also on the same order as estimated from the thermal expansion coefficients of gold which are dependent on the excitation wavelength with more expansion expected for higher energy photons. This similarity is surprising as the experimental data reflects coherent phonons which constructively interfere, whereas thermal expansion is an incoherent process which also involves destructive interference. Likely, only a small percentage of the absorbed energy goes into these coherent acoustic phonon modes and other heat dissipation pathways are also quite important. These dissipation pathways could be further explored using the analysis developed by Crut and his coworkers which could provide added insight into the size dependence of the expansion per photon absorbed.[73,75,200]

6.3. Conclusion

In conclusion, it was demonstrated that coherent acoustic phonons in nanojavelins exhibit similar size dependent trends as bipyramids providing a method to separately control LSPR position and phonon frequency. Additionally, by using theoretical tools and transient absorption spectroscopy, it is possible to quantify particle expansion from photogenerated coherent acoustic

phonons which has a linear power dependence that slightly increases with particle size. This information provides a guide for designing particles with tunable LSPR as well as understanding the resulting mechanical response to photoexcitation. Future work could include using these design principle to create gold bipyramids with low frequency phonons excited by convenient wavelengths for mass sensing applications or utilizing the ability to measure mechanical displacement to further develop models of phonon-solvent interactions.

6.4. Methods

6.4.1. Material Synthesis

Gold bipyramids and nanojavelins used in this study were both synthesized using a seed-mediated growth approach, but followed two separate synthesis routes published earlier.[193,195] Briefly, to synthesize gold bipyramids, gold seeds were created by reacting $HAuCl_4$ with $NaBH_4$ solution in the presence of sodium citrate. The seeds were aged for two hours before use. For growth of the bipyramid, $HAuCl_4$ solution with trace amount of $AgNO_3$ added were mixed with cetyltrime-thylammonium bromide (CTAB) solution, acidified by a small amount of HCl, and reduced by L-ascobic acid. Right after the reduction, small amounts of seeds were added, and the reaction was allowed to proceed in a 30°C bath for two hours. The aspect ratio of the bipyramid was controlled by the different amount of $AgNO_3$ added. To synthesize gold nanojavelins (sample F and G), seeds were created by reduction of $HAuCl_4$ in the presence of 25% cetyltrimethylammonium chloride (CTAC) solution with $NaBH_4$/NaOH solution. The seeds were

aged in a 85°C oil bath for 1h, and further aged in ambient conditions for one day prior to the growth reaction. The growth solution consisted of $HACl_4$, a mixture of CTAB and CTAC, small amount of silver nitrate, and initiated by adding a mild reducing agent 8-hydroxyquinoline. Immediately after the reduction, different amounts of seeds are added to control the aspect ratio of nanojavelins.

6.4.2. Optical Measurements

All samples were suspended in water for optical measurements and rapidly stirred. Transient absorption measurements were performed using a 2 kHz, 35 fs Ti:S amplifier. The 800 nm output was beamsplit to pump an optical parametric amplifier that produced tunable pump pulses at the LSPR of the sample, and a smaller portion was time-delayed and focused into sapphire to produce a white light probe beam. Pump pulses were mechanically chopped a 1 kHz to compare probe intensity though the sample with and without photoexcitation. Pump spot sizes were measured via transmission through a pinhole.

6.4.3. Electrodynamics and Continuum Mechanics Calculations

Finite-difference time-domain (FDTD, Lumerical Solutions) simulations were performed to calculate the absorption and scattering spectra of the samples. The dielectric permittivity tabulated by Johnson and Christy for gold was used[201] and the background refractive index was

set to 1.33 for water. As the measurements have been performed on an assembly of bipyramids in solution, the calculated absorption spectra correspond to the sum of the spectral response under plane-wave irradiation with polarization parallel and perpendicular to the bipyramid long axis.

FEA software (Abaqus, version 6.13-2) was used to calculate the frequency of the acoustic vibrations associated to each sample. These simulations have been performed on a continuous pentagonal bipyramid,[193] with material mechanical properties defined according to bulk gold (Young's modulus=79 GPa, Poisson's ratio=0.4 and density=19300 $kg.m^{-3}$). The modeling dimensions and shape (including length, width and radius of curvature) were based on the TEM measurement of several individual nanoparticle features.

CHAPTER 7: PHONON-DRIVEN OSCILLATORY PLASMONIC EXCITONIC NANOMATERIALS

This chapter is based on the research described in the following publication:

Kirschner, M. S.; Ding, W.; Li, Y.; Chapman, C. T.; Lei, A.; Lin, X.-M.; Chen, L. X.; Schatz, G. C.; Schaller, R. D. Nano Lett. ***2018****, 18 (1) 42-448.*

I demonstrate that coherent acoustic phonons derived from plasmonic nanoparticles can modulate electronic interactions with proximal excitonic molecular species. A series of gold bipyramids with systematically varied aspect ratios and corresponding localized surface plasmon resonance energies, functionalized with a J-aggregated thiacarbocyanine dye molecule, produce two hybridized states that exhibit clear anti-crossing behavior with a Rabi splitting energy of 120 meV. In metal nanoparticles, photoexcitation generates coherent acoustic phonons that cause oscillations in the plasmon resonance energy. In the coupled system, these photo-generated oscillations alter the metal nanoparticle's energetic contribution to the hybridized system and, as a result, change the coupling between the plasmon and exciton. I demonstrate that such modulations in the hybridization is consistent across a wide range of bipyramid ensembles. Finite-Difference Time Domain calculations are also used to develop a simple model describing this behavior. Such oscillatory plasmonic-excitonic nanomaterials (OPENs) offer a route to manipulate and dynamically-tune the interactions of plasmonic/excitonic systems and unlock a range of potential applications.

7.1. Introduction

Nuclear motions have long been examined in photochemistry, most often in the context of vibrationally mediated photodissociation.[202–204] Recent efforts have utilized vibrational motions to control the photoresponses of more complex systems. For example, in a variety of donor-bridge-acceptor molecules, charge transfer rates between the donor and acceptor could be manipulated by exciting bridge vibrations.[205–207] Additionally, selective excitation of vibrational modes in a pentacene/C60 photoresistor resulted in photocurrent enhancement.[208] An analogous set of systems that has yet to be considered are optically active nanomaterials such as plasmonic nanoparticles. These materials have pragmatic advantages such as tunable optical resonances and compositions, large photoabsorption cross sections, high photostabilities, and inexpensive, scalable syntheses. Further, they often have simpler electronic/geometric relationships, such as the linear relationship between aspect ratio and plasmon resonance in gold nanorods/bipyramids. Nanomaterials also offer the potential to control the distance and relative orientation between interacting systems. These benefits make nanoparticles an enticing system for advancing vibrationally mediated photochemistry and manipulating complex electronic phenomena in molecular systems.

Numerous studies of the vibrational modes of nanomaterials have been reported.[47,70,214–216,71,75,77,209–213] Much of these works have been concerned with time-dependent characterization of geometric changes induced by coherent acoustic phonons generated following photoexcitation. Small changes in particle geometry result in discernible changes in optical properties such as localized surface plasmon resonance (LSPR) energy, which permits the characterization of the

phonon modes that alter such resonances. However, the size dispersion in an ensemble of nanoparticles generally leads to a variety of phonon frequencies that can result in a significant inhomogeneous dephasing.[47,209,210] This dephasing can be circumvented through the use of single particle measurements[71,77,214,215] or relatively monodisperse ensembles.[70,75,77,216] Taken as a whole, these studies have provided insights into the nature of phonon-induced geometrical distortion of nanoparticles as well as phonon-solvent coupling.

Here, I show that acoustic phonons resulting from photoexcitation can transiently alter the electronic coupling between an LSPR and a molecular electronic transition. Similar systems that take advantage of the coupling of plasmonic nanomaterials have gained significant interest and shown potential in an array of applications.[217–225] In this way, molecular sensitivity to the vibrational mode of an inorganic solid undergoing acoustic deformation is demonstrated. Related behavior has been observed in the modulation of spatially-extended plasmonic superlattices.[224,225] A system of highly monodisperse gold bipyramids (AuBPs)[70,75,216] is used with thiacarbocyanine dye, 2,2'-dimethyl-8-phenyl-5,6,5',6'-dibenzothiacarbocyanine chloride (TCC) molecules on the AuBP surface, to achieve time-dependent ensemble characterization of the phonon-induced energetic modulation. Previous reports have shown that TCC can successfully attach to gold nanostructures and couple to the particle electronically resulting in a plexcitonic system with plasmon-exciton hybridized states.[219–222] The static properties of several different AuBPs, with corresponding LSPR energies, functionalized with TCC (herein called TCC-AuBPs), are characterized and then the ultrafast dynamics of these systems are analyzed to determine the effects coherent acoustic phonons on the electronic transitions. Finally, a qualitative explanation for the

direction and magnitude of the observed changes in coupling is offered. The resulting paradigm, which is described as an Oscillatory Plasmonic-Excitonic Nanomaterial (OPEN), could be used as a model system in the development of photochemistry facilitated by vibrational modes as well as provide fundamental insight into plexcitonic systems or enable new applications owing to the inherent fine-tuning of the plasmonic resonance.

7.2. Results and Discussion

7.2.1. Plasmon-Exciton Coupling

Figure 7.1a shows the extinction spectra of TCC in 1:1 water:ethanol (blue dotted [TCC]=70 μM), in 5:1 water:ethanol (green dashed [TCC]= 20 μM), and in the presence of AuBPs with a LSPR of 1385 nm and 5:1 water:ethanol (solid red [TCC]=20 μM). The inset shows the structure of TCC. At this concentration of TCC in a 1:1 water:ethanol solution, absorption features appear around 550 and 600 nm, characteristic of TCC monomer and ethanol induced aggregation respectively.[219] As the concentration of water in the solvent increases, the intensities of the previous absorption features decrease and a peak around 695 nm begins to form—indicative of J-aggregate formation. [219–222] In the presence of AuBPs with a NIR LSPR, a similar spectral feature appears at 700 nm, which can be attributed to the formation of J-aggregates on the surface of AuBPs likely due to a combination of van der Waals forces and electrostatic attraction.[219,221] These AuBPs have LSPRs in the NIR so there is likely no electronic interactions between TCC and

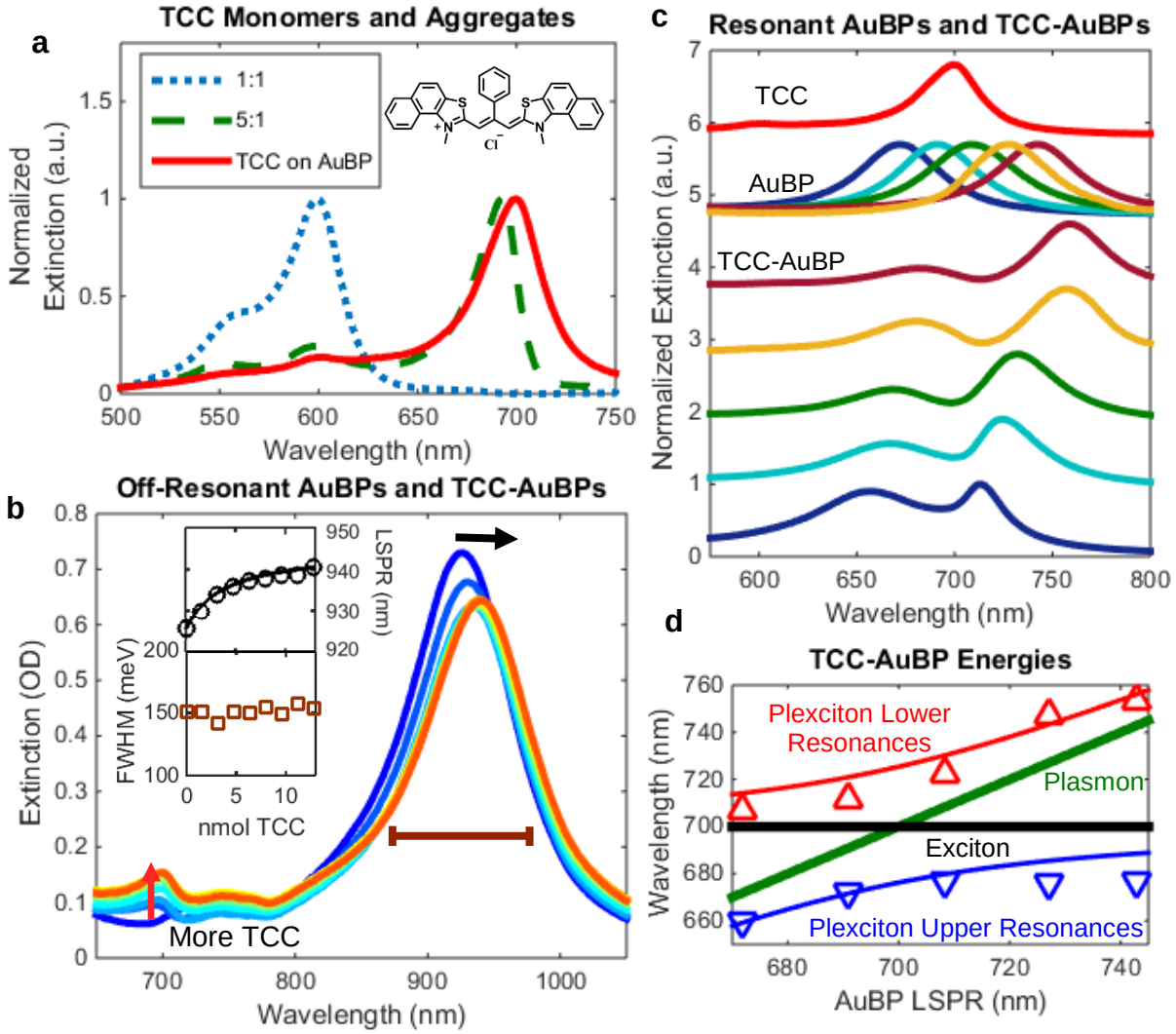

Figure 7.1. (a) Static spectra of TCC in 1:1 water:ethanol (blue dotted), 5:1 water:ethanol (green dashed), and in the presence of a 1385 nm LSPR AuBP in a 5:1 water:ethanol solution with the unfunctionalized AuBP extinction spectra subtracted out (red solid). Inset: The molecular structure of TCC. (b) Static spectra of TCC-AuBPs with a AuBP LSPR of 925 nm with varying amounts of TCC added. As dye is added, the LSPR redshifts with a constant full-width half-maximum as detailed in the insets and emphasized with a black arrow and a brown line. (c) Extinction spectra of TCCs on NIR AuBP as in (a) (red), AuBPs with LSPRs that range from 640 nm-750 nm, and TCC-AuBPs formed with the aforementioned AuBPs. Notably the TCC-AUBPs each have an upper and lower resonance. (d) The wavelength of the upper (blue triangles) and lower (red triangles) resonances of the TCC-AuBPs in (c) versus the LSPR of the AuBPs used in their synthesis along with a coupled oscillator model fit (red and blue lines). The positions of the AuBP LSPRs (green line) and the TCC resonance based on the fit (black line) are included.

AuBPs. Instead, this change in the TCC resonance is likely the result of AuBPs offering high surface areas, stable nucleation sites for the J-aggregates to form in addition to a slight dielectric screening effect. Similar changes have been previously observed for other gold nanoparticle/J-aggregate systems.[223] Figure 7.1b shows the LSPR extinction spectrum of a different AuBP ensemble with a LSPR near 925 nm as a function of increasing amounts of TCC. Upon addition of more dye, the J-aggregate peak appears at 700 nm, and additionally, the AuBP LSPR gradually redshifts by 14 nm. This change in LSPR is displayed in the inset with a Langmuir adsorption fit. The inset also demonstrates a fairly constant peak linewidth. These TCC-dependent optical properties of AuBPs likely originate from changes in the local dielectric environment arising from the added TCC, and are consistent with J-aggregate formation as explored by Finite Difference Time Domain (FDTD) Analysis. The changes observed in TCC (Figure 7.1a) and AuBP (Figure 7.1b) spectra demonstrate that TCC-AuBPs have successfully been formed.

Figure 7.1c shows the extinction spectra of the TCC J-aggregate formed on several different aspect ratio AuBP ensembles with LSPRs ranging from 670-750 nm before functionalization. The TCC-AuBP ensembles exhibit broader peaks with asymmetric Fano-type line shapes consistent with plasmon-exciton coupling. Further, the hybridized system undergoes an avoided crossing with an upper and lower resonance. This anti-crossing behavior is explicitly demonstrated in Figure 7.1d, which displays the spectral positions of each of the two TCC-AuBP peaks along with the LSPRs of the corresponding AuBPs and the absorption peak of TCC. Also included are fits based on a coupled harmonic oscillator model: [221,222,226]

$$E(\hbar\omega_p) = \frac{\hbar\omega_p + \hbar\omega_0}{2} \pm \frac{1}{2}\sqrt{(\hbar\Omega_r)^2 + (\hbar\omega_p - \hbar\omega_0)^2} \qquad (7.1)$$

where $\hbar\omega_p$ and $\hbar\omega_0$ are the energies of the AuBP LSPR and the TCC resonance respectively. The term $\hbar\Omega_r$ is referred to as the Rabi splitting or the coupling energy of the system, which was found to be 120 meV in this system. This coupling constant is on the same order of the coupling observed in J-aggregate nanogroove[222] (60-120 meV) and nanoshell[219,220] (120 meV) systems but lower than has been observed in nanodisk dimers[221] (230-450 meV). The redshift caused by TCC changing the local dielectric environment of the AuBPs complicates the implementation of this model and information about how this issue was corrected for is included in the Section 7.4.1.

7.2.2. Using Phonons to Modulate Plasmon-Exciton Hybridization

Figure 7.2 shows ensemble transient absorption maps and inset static extinction spectra of (a) a AuBP ensemble and (b) the same AuBPs functionalized with dye to form TCC-AuBPs. These spectra, and all subsequent transient absorption spectra discussed in this chapter, were taken at modest excitation powers (around 50 μJ/cm^2) to avoid sample damage. Excitation wavelengths were tuned to the sample-specific extinction maxima. For each AuBP-TCC sample, measurements were performed photoexciting at each extinction peak. As discussed later in the chapter, the excitation wavelength had little effect on the observed dynamics.

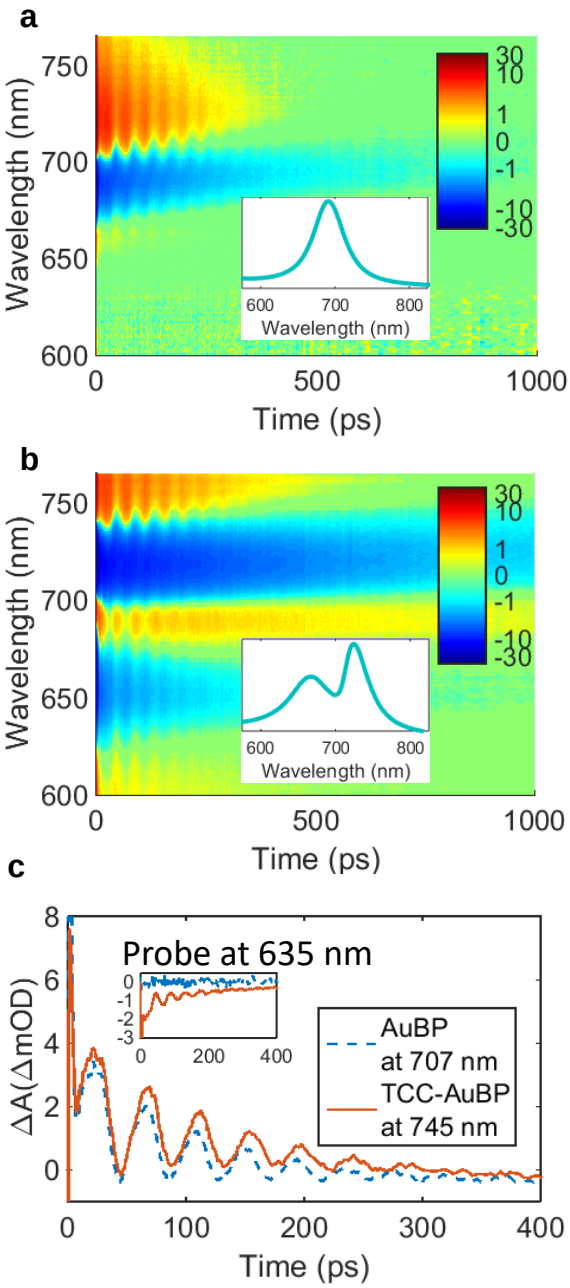

Figure 7.2. Transient absorption spectrum for AuBP (a) and the corresponding TCC-AuBP (b) photoexcited at 690 nm and 725 nm respectively with static spectra as insets. (c) Kinetic traces for the AuBP in (a) (blue dashed with period of 42.52±0.16ps) and the TCC-AuBP in (b) (red solid with period of 43.61± 0.14ps). Uncertainties are the 95% confidence intervals of the fitting algorithm. Inset: Kinetics of both at 635 nm where only TCC-AuBP exhibits significant oscillations with a period of 43.32±0.41 ps

The transient response of bare (ligand terminated) AuBPs have been previously presented and analyzed.[70,75,216] Briefly, in addition to the LSPR broadening and redshifting after photoexcitation, the impulsively-generated lowest order acoustic phonons cause the independent nanoparticles to periodically elongate and contract, which causes the LSPR to redshift and blueshift in an oscillatory fashion. As shown in Figure 7.2b, a similar phenomenon occurs in TCC-AuBPs. However, for TCC-AuBPs, there are two sets of photo-induced absorptions and bleaches that oscillate, corresponding to the two static peaks in the inset. These oscillations are further illustrated in Figure 7.2c where transient dynamics at indicated wavelengths are displayed for both bare AuBPs (dotted blue) and functionalized TCC-AuBPs (solid red). The displayed dynamics were chosen due to their position between the induced absorption and bleach peaks, where the oscillations are most pronounced. The oscillation period of bare AuBP spectral oscillations at 707 nm is 42.52±0.16ps (95% confidence interval from the fitting algorithm) while that of the functionalized AuBPs at 745 nm is 43.61±0.14ps. This slight shift in period likely arises due to the small additional mass of dye adsorbed to the particles, which emphasizes the potential of AuBPs in mass sensing applications.[75]

Oscillations in TCC-AuBPs arise either from changes in both the peaks or from a single peak undergoing significant changes that are spectrally broad with apparent, small oscillations at the location of the other peak. In the context of this TCC-AuBP system, the magnitude of the oscillations at the lower energy peak are larger than those at the higher energy peak, which suggests it is conceivable that in this TCC-AuBP only the lower energy peak is affected by the coherent phonons. To explore this concept, the inset of Figure 7.2c shows the dynamics of the AuBPs and

the TCC-AuBPs at 635 nm. The lower energy TCC-AuBP resonance is both redder (722 nm vs 691 nm) and narrower (FWHM of 34 nm vs 51 nm) than the bare AuBP LSPR, so one might expect that it would have a smaller effect on the dynamics observed at 635 nm. However, it is observed that only the TCC-AuBPs exhibit oscillations at this wavelength, indicating that the LSPR of the bare AuBP is too far away spectrally to have any effect at 635 nm, and that oscillations at the same wavelength in the TCC-AuBP case can only come from the higher energy peak. Therefore, the coherent acoustic phonons affect both peaks. Further, oscillations at 635 nm have a period of 43.32±0.41 ps consistent with those of the lower energy peak. Therefore, the functionalized system, in addition to having a reduced phonon frequency, undergoes changes in its plexcitonic coupling effecting the transition energies and relative intensities of the hybridized states. In other words, TCC-AuBPs constitute an oscillatory plasmonic-excitonic nanomaterial (OPEN).

Figure 7.3 shows transient absorption spectra of TCC-AuBP photoexcited with (a) 670 and (b) 730 nm pump pulses with bandwidths of 53 meV (19 nm and 23 nm respectively), corresponding to the two peaks observed in static extinction spectra. Static spectra are included as insets. Changing the excitation wavelength has little impact on dynamics; both photoexcitation energies result in an OPEN. To emphasize this similarity, normalized kinetics at 665 nm and 765 nm are included as Figure 7.3c as well as normalized spectra at different time points are included as Figures 7.3d-h with 670 nm (blue line) and 730 nm (red line) excitation. The presence of coherent phonons, observable through the oscillations in the spectra, necessitates dissipation of energy in the nanoparticle lattice. Further, the phase of the photo-generated phonons are

independent of excitation wavelength, suggesting that the electron-phonon coupling does not significantly change under different excitation conditions despite differences in the number and energy of the photons absorbed. Regardless of how or how much energy enters the system, it converts into nanoparticle vibrational modes in the same way.

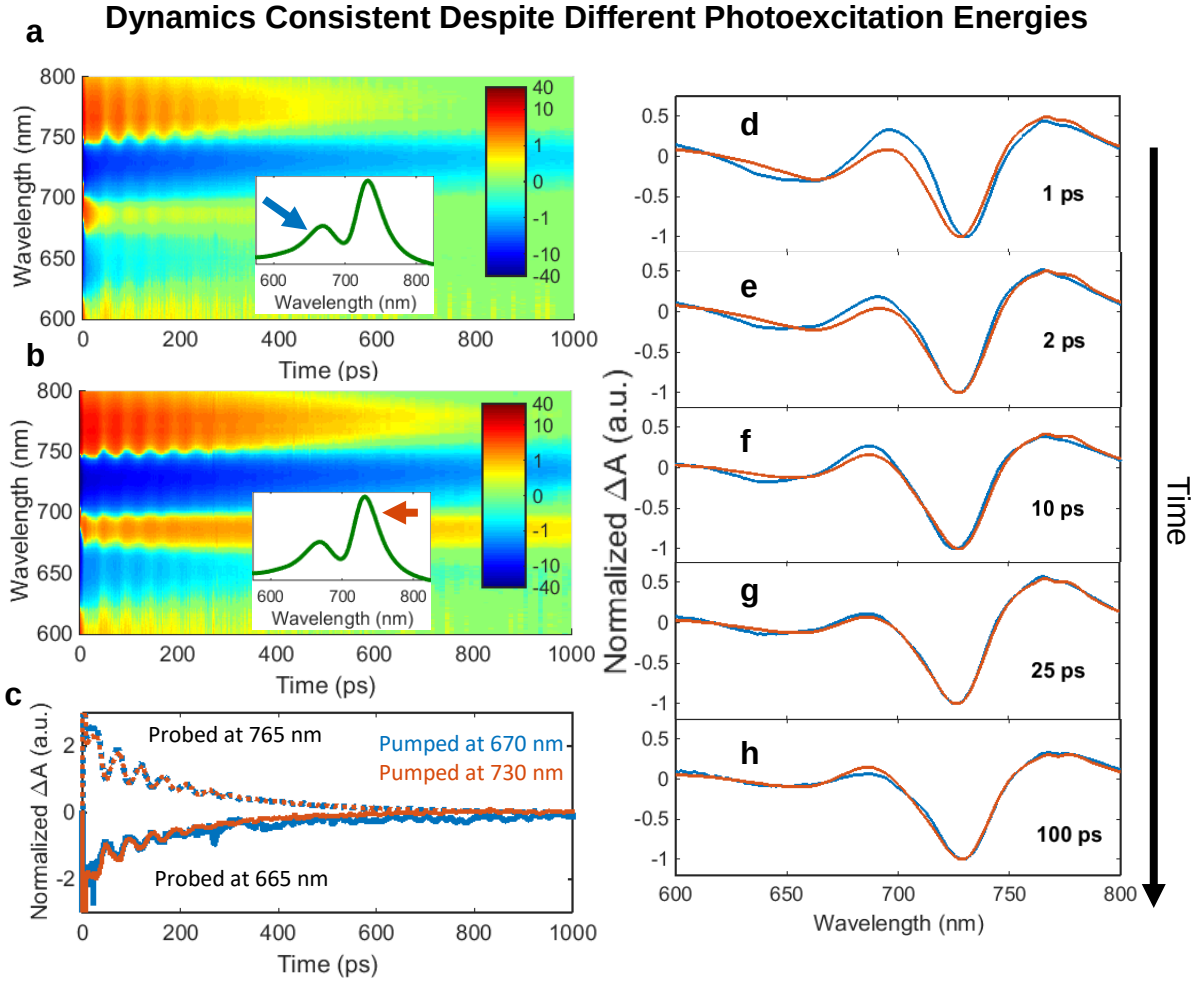

Figure 7.3. Transient absorption spectra for TCC-AuBP when it was pumped on its (a) higher energy (670 nm) and (b) lower energy (730 nm) peaks with static spectra as insets. (c) Normalized kinetics of TCC-AuBP pumped at 670 nm (blue) and 730 nm (red) and probed at 665 nm (solid lines) and 765 nm (dotted lines). (d-h) Transient absorption spectra for TCC-AuBP after being pumped on its blue (blue line) and red (red line) peaks after various times. Notably, the behavior of the two systems are rather similar regardless of the excitation wavelength.

It is also worth emphasizing that the coherence of the phonons implies that they must be generated on a timescale faster than that of the phonon period. Based on this result, it is assumed that on the timescale of coherent acoustic phonons, the system is primarily thermally, rather than electronically, excited. In other words, the lattice is excited while the electrons are not. This premise is consistent with the electronic lifetimes of TCC aggregates[220,222] and AuBPs,[47,70,75,216] which are on the order of ps, and the fast decay of TCC-AuBP photoluminescence (Appendix E.2). While these observations do not preclude the existence of long-lived electronic excitations, there seems to be little evidence that the excitation source significantly populates such a state and thus it would not have a practical impact on the analysis.

To understand the effects of these acoustic phonons in this OPEN, it is worth revisiting the simple coupled harmonic oscillator model described earlier. Within this model, the acoustic phonons change the LSPR energy (ω_p) and the resulting changes in the energies are

$$\frac{dE}{d\omega_p} = \frac{\hbar}{2}\left(1 \pm \frac{\hbar\omega_p - \hbar\omega_0}{\sqrt{\left(\hbar\omega_p - \hbar\omega_0\right)^2 + (\hbar\Omega_r)^2}}\right) \qquad (7.2)$$

Since the Rabi splitting ($\hbar\Omega_r$) is real (and positive), increasing the plasmon energy will always increase the energies of both transitions while decreasing the LSPR energy will always decrease the energies. From an experimental standpoint, this suggests that, at least with respect to spectral position, the two peaks should oscillate in phase: both peaks either redshift or blueshift. Further, if $\omega_p \approx \omega_0$, both peaks will oscillate significantly, while spectral separation causes asymmetric changes in energy.

While this simple framework provides some insight on peak positions, it does not provide insight regarding how the hybridization changes with phonon phase. To address these concerns, FDTD simulations were utilized on contracted and elongated particles—consistent with previous simulations of phonon-induced shifts in plasmon resonances.[77] Details about the FDTD calculations are included in the methods and Appendix E.1. Briefly, AuBP particles coated by a few nm TCC layer were expanded and contracted along their lowest order, acoustic phonon mode and the extinction spectra of the resulting particles were calculated. AuBPs with plasmon resonances of 651 nm and 706 nm were specifically examined and resulted in upper/lower resonances of 661 nm/725 nm and 671 nm/766 nm with the addition of TCC layers with absorption maxima of 675 nm. Notably, the addition of the dye layer likely causes a redshift in the LSPR resulting in lower energy resonances and increasing the energetic overlap with the dye for the bluer bipyramids. Figure 7.4 demonstrates how the resonances change in (a) energy and (b) extinction cross section along the phonon mode. For both particles, the two peaks change energy in phase together consistent with the simpler coupled harmonic model. In the 651 nm case, the resonance of bare AuBP is only 24 nm from that of the dye resulting in sensitivity to changes in the AuBP LSPR. Conversely, in the 706 nm case, the separation is 31 nm resulting in the upper resonance having a much weaker dependence on the AuBP LSPR than in the 651 nm case.

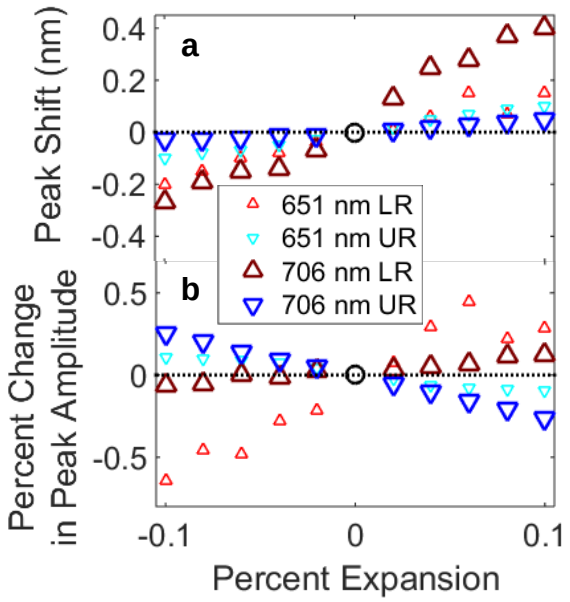

Figure 7.4. Differences in peak location (a) and amplitude (b) of the extinction spectra for a series of stretched TCC-AuBPs (40 nm in length with 651 nm LSPR and 120 nm in length with 706 nm LSPR) derived from FDTD calculations. Maximum deviation in length in the long axis of the AuBP is ±0.1%. The upper resonances are labeled UR and the lower resonances LR.

In Figure 7.4b, particle expansion (a redshift), increases the amplitude of lower resonances, but decreases that of the upper resonances. This trend occurs regardless of the relative energies of the AuBP LSPRs and the TCC resonance. As the AuBP redshifts, the lower resonance would be expected to have a slightly more AuBP-like character and the upper resonance a slightly more TCC-like character. Since much of the extinction cross section comes from the plasmonic nanoparticle, it follows that the peak intensity roughly correlates with the bipyramid character. This suggests that the phonon mode is modulating the hybridization in these states, even if it does

not change $\hbar\Omega_r$. This model assumes that systems are strongly coupled, if they were weakly coupled, behavior reflected in the model developed by Heylman *et al*.[227] would be expected.

These theoretical predictions are well matched experimentally, as demonstrated by Figure 7.5. Figures 7.5a and 7.5b show the transient absorption spectra of two TCC-AuBP composite ensembles using AuBPs with an unfunctionalized LSPR of (a) 672 nm or (b) 743 nm, on either side of the J-aggregated TCC absorption at 700 nm. Both of these systems exhibit two oscillatory features, demonstrating that OPEN behavior occurs across a wide range of AuBP LSPRs. To determine the nature of these changes, it is considered how the spectra change at different phases in the oscillation in Figures 7.5c and 7.5d. The phases displayed—0, π, 2π, and 3π—are the maxima or minima of the dynamics traces and correspond to the particles in their most elongated or contracted geometries. To emphasize peak positions, the spectra normalized to the maximum value at each peak appear as insets. The transient peak positions oscillate in phase with one another suggesting that the changes in the energy level of the contributing AuBPs dominate the energetics. Further, in Figure 7.5c, where the bare AuBPs have a resonance close to TCC, both peaks clearly oscillate in position based on the minima of the bleach features. Yet, in Figure 7.5d, with more spectral separation between the AuBP LSPR and the TCC electronic transition, only the redder peak undergoes significant oscillations in spectral position. It has been shown that the magnitude of the spectral oscillations depends on excitation power,[77] so one might expect that these differences could have arisen from differences in excitation fluence. However, given that oscillations of the red peak in 7.5d are larger than those in 7.5c, power dependence cannot explain this discrepancy.

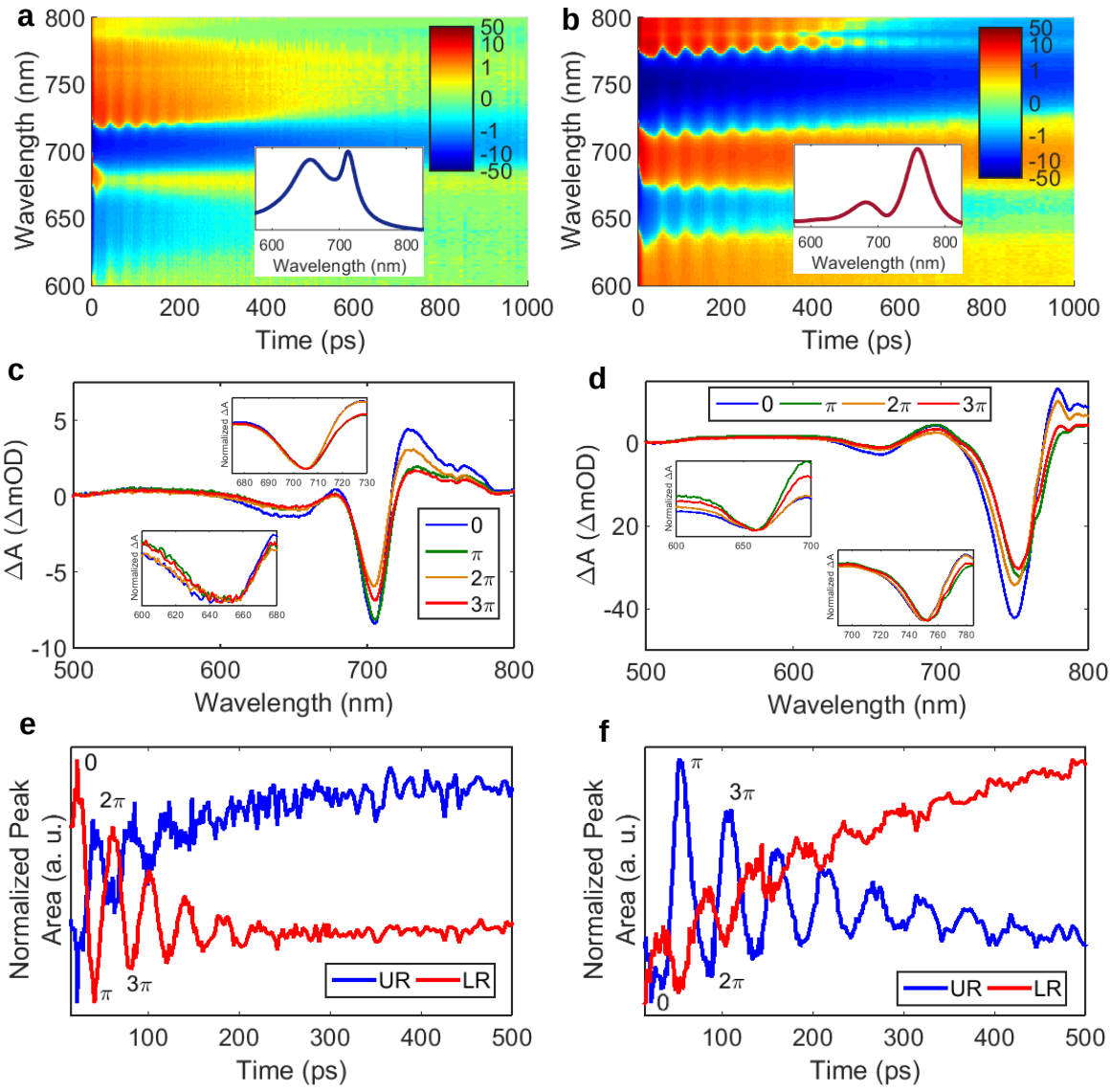

Figure 7.5. Transient absorption spectra for TCC-AuBP when the corresponding AuBP have an LSPR of 672 nm (a) and 743 nm (b) with static spectra as insets. (c) and (d). Transient spectra in (a) and (b) (c and d respectively) at different phases in the acoustic phonon. The insets are the peaks normalized to emphasize peak positions. (e) and (f). Normalized peak areas (maximum and minimum values set to -1 and 1) of the upper (labeled UR) and lower (labeled LR) of TCC-AuBPs from the transient absorption spectra of (a) and (b). In (e) upper resonance is integrated from 550 nm to 677 nm and the lower resonance 677 nm to 801 nm. In (f) the upper resonance is integrated from 600 nm to 698 nm and the lower 699 nm to 852 nm. Phase labels correspond to (c) and (d).

Figures 7.5e and 7.5f show how the transient peak areas change with time. At points in the phonon phase when the AuBP is expanded (0, 2π), the extinction of the upper resonance decreases and the lower resonance increases whereas the opposite occurs when the particle is contracted. Unfortunately, there is some convolution between the red tail of the upper resonance and the blue tail of the lower resonance that contributes to this trend. Therefore, while the data agrees with predicted trends, the extent to which it does is overstated; this observation should only be considered as being consistent with theory predictions rather than something independently suggested by the data. The phonon-dephasing times varied across these two ensembles as well as across the entire range of AuBPs and TCC-AuBP examined throughout this work. Most of these differences are likely due to differences in inhomogeneity and the resulting inhomogeneous dephasing rates. However, previous characterizations of gold nanoparticle acoustic phonons have demonstrated some range of quality factors (frequency normalized dephasing times), even after corrections for inhomogeneity and solvent effects,[47,70,75,77,215,216] suggesting additional factor maybe be in play. The exact origin of these variations, as well as variations in the particle cooling rates, certainly merits additional investigation.

7.3. Conclusions

In conclusion, AuBPs were successfully functionalized with TCC to form OPENs with hybridized states that are modulated by the coherent acoustic phonons of AuBPs. These changes are rationalized in the context of the static coupling between these two species. The existence of this new class of nanomaterials is promising in a number of contexts. The fine-tuning of the hybridization of OPENs could improve existing applications of plexcitonic materials. Further, such

systems could serve as a developmental testbed for the utilization of vibrational modes in controlling electronic interactions.

7.4. Methods

7.4.1. Material Synthesis

To create the AuBPs, syntheses consistent with previously reported methods were performed.[195] Briefly, gold seeds were created by reacting $HAuCl_4$ with $NaBH_4$ solution in the presence of cetyltrimethylammonium chloride (CTAC) and nitric acid. The seeds were aged in a 85°C oil bath for 1h, and further aged in ambient conditions for one day prior to the growth reaction. The growth solution consisted of $HACl_4$, CTAB, small amount of silver nitrate, and initiated by adding a mild reducing agent 8-hydroxyquinoline. The aspect ratio was varied by adjusting the concentration of 8-hydroxyquinoline.

To create the TCC-AuBP, TCC in 1:1 ethanol:water solution was combined with AuBPs in water and allowed sufficient time for the TCC to aggregate (usually around a day). Practically, this requires very little TCC. **It is also important to wait for the final formation of the TCC-AuBP.** To determine the amount of dye to add to a bipyramid solution, the optical density at the LSPR in a 1 mm cuvette was used as a stand-in for AuBP concentrations. While AuBPs of different geometries will have different extinction cross sections, these bipyramids were close in size and therefore this is a reasonable approximation. For the TCC-AuBPs used for static characterization, TCC concentration varied from 1-100 μM TCC/AuBP OD. Across this concentration range, the

peak shape was relatively constant, save for an initial region where the peaks split. However, the addition of TCC caused a redshift, consistent with what was observed in the non-resonant case. Therefore, to take this into account, I linearly extrapolated peak position—obtained by fitting the peaks to the combination of a Lorentzian function and a Fano resonance—to a TCC concentration of 0. The exception to this was the TCC-AuBP ensemble made from 727 nm LSPR AuBPs which was fit to the sum of two Lorentzians. These trends make observing the peak positions—and consequently the exact value for the Rabi splitting—imprecise. However, all of the TCC-AuBPs exhibited peaks with higher and lower energies than TCC and the component AuBPs, which is what the assertion of anticrossing behavior is based on. For each sample transient absorption was performed on, 150 µL of bipyramid solution with an OD around 1 had 20 µL of 80 µM TCC solution added to them. It is worth noting that going above the concentrations of TCC used here can result in significant changes in peak shape. Based on the cross sections in Chapter 6, there are likely 10,000 to 100,000 dye molecules per AuBP at the concentrations used for ultrafast spectroscopic investigation. Given the AuBPs have surface areas around 1,500-2,500 nm^2, [216] there are roughly 1-20 $Å^2$ of gold surface per dye molecule. If the dye molecules laid flat on the particle surface and the lower end of these estimates for space per molecule were more accurate, it is conceivable that there is complete coverage of the particles. However, given the consistent lineshapes seen across a wide concentration range, as well as the fact that there is strong evidence of the dye aggregating (100 nm redshift in absorption), it seems more likely that the coverage is sub-monolayer. Perhaps complete coverage is responsible for the more dramatic changes seen at higher concentrations, but the characterization of the specific attachment chemistry and its

electronic implications in anisotropic plexcitonic systems is an interesting subject which has yet to really be explored experimentally.

7.4.2. Electrodynamics Calculations

The calculations were performed within Lumerical FDTD Solutions. The optical response of the TCC is modeled using a Lorentz dielectric function with a central wavelength of 680 nm and a linewidth parameter of 20 nm while the dielectric properties of the AuBPs are modeled as pure Au from Johnson and Christy.[201] The Lorentz dielectric function has the following expression:[228]

$$\epsilon_r(\omega) = 1 - \frac{600^2}{\omega^2 - \omega_0^2 + 2i\delta\omega} \qquad (7.3)$$

where ω_0 is the central wavelength, and δ is the linewidth. A value of 2 is added to the real part of this function to qualitatively match the property of J-aggregates.[229]

Given, the relative size of the dye layer, it is difficult to experimentally probe its size and location. Therefore, FDTD calculations were performed on several differently partially coated TCC-AuBPs and found that a core-shell model, wherein a concentric shell of TCC encases the AuBP, most closely matched the experimental spectra. The 40 nm size core is covered by a 1 nm thick shell while the 120 nm core is paired with a 3 nm shell.

CHAPTER 8:OSCILLATION ASSOCIATED SPECTRA ELUCIDATE PHONON-INDUCED CHANGES IN PLASMON-EXCITON COUPLING

This chapter is based on the research described in the following publication:

Kirschner, M. S.; Jeong, Y.; Spencer, A. P.; Watkins, N. E.; Lin, X.-M.; Schatz, G. C.; Chen, L. X.; Schaller, R. D. (In Prep)

Coherent vibrations detected in optical experiments can offer insights regarding materials properties and electronic interactions, but also yield complex time-dependent optical signatures. Here, I adapt techniques from studies on vibrational wave packets in molecules to analyze optical signatures of coherent acoustic phonons in nanoparticles. This strategy enables improved understanding of the implications of energetic changes induced by coherent phonons. This approach is then applied to systems that target coherent acoustic phonons as a route to modulate plasmon-exciton coupling with the results compared to theoretical calculations. Taken together, the described approach provides an intuitive, simple means of analyzing new systems and facilitates attempts to utilize, rather than simply observe, nanomaterial phonon modes

8.1. Introduction

Often, following the impulsive electronic excitation of a material, a portion of that energy is channeled to generating phonons in the lattice. When phonons of a specific frequency are launched significantly faster than their period, coherent (in phase) oscillations in particle geometry can occur which often modulate optical properties.[47,65,71-78,187,215,216,230–233] Additionally, these

phonon modes can be affected by small mass changes and used to perform mass sensing with up to yoctogram resolution.[75,230] Because of the frequency range of acoustic phonons in finite-size nanoparticles, which is typically 0.01 to 1 THz, its characterization presents challenges for conventional Raman spectroscopy. However, they can be characterized in the time domain enabling unique insight into material properties.[72,74]Recently, it has been observed that coherent phonons can modulate electronic coupling between systems.[224,225,231] Particularly of note are hybrid materials that exhibit plasmon-exciton coupling[219,220,223] which can be modified by phonons in systems that are termed oscillatory plasmonic-excitonic nanomaterials (OPENs).[231] As the field advances, it should be possible to use the induced changes in electronic properties in other contexts such as manipulating electron or energy transfer to or from a nanomaterial.

Coherent acoustic phonons are typically characterized in the time domain by analyzing optical transient absorption (TA) spectra to determine the frequencies of the populated phonon modes. While this approach reveals the frequency of the mechanical changes, it does little to clarify the electronic implications of the lattice distortions caused by coherent acoustic phonons. Occasionally, more sophisticated transient spectral analysis is used wherein at every time point, the TA spectrum is fit to the difference of the ground state spectrum and a spectrally-shifted excited-state spectrum resulted from the lattice movements which can be used to quantify particle expansion along a phonon mode.[77,187,216] However, this requires optical spectra with simple line shapes. Systems that take advantage of the induced electronic changes, such as OPENs, exhibit substantially more complex spectra with multiple peaks and highly asymmetric spectral features which confound this type of analysis.[231]

Here, I present a strategy for analyzing these more complex systems derived from previous methods used in analyzing vibrational wave packets in molecular systems.[234–241] This technique, which is referred to as oscillation associated spectrum (OAS) analysis, determines the phase and magnitude of the oscillatory dynamics at each individual wavelength to reveal information about the underlying phenomenon. Initially, the technique is described when analyzing gold bipyramid transient spectra—a prototypical ensemble that exhibits well-defined coherent acoustic phonons.[70,75,216,231] In addition to agreeing with conventional understanding of this system, OAS provides new insights from deconvoluting ensemble inhomogeneity. Next, it is demonstrated that this technique can extract effects of phonons in OPENs which agree well with theoretical calculations. Finally, the contexts where OAS is particularly advantageous are discussed. Moving forward, OAS can help facilitate design of systems that take advantage of phonon-induced electronic changes, e.g. phase-controlled applications.

8.2. Results and Discussion

8.2.1. Defining Oscillation Associated Spectra

Figure 8.1a shows a two dimensional TA map (TA signal versus wavelength and pump-probe delay) of a typical ensemble of gold bipyramids excited on their localized surface plasmon resonance (LSPR). Following the generation of phonons through electron-phonon coupling,[47,65] the spectra are dominated by two phenomena. First, heating of the lattice causes the plasmon resonance to broaden and redshift. Second, coherent acoustic phonons produce oscillations in

LSPR energy. This bipyramidal phonon mode is known to involve elongation of the long axis and shortening of the short axis and vice versa. As the particles expand and contract, the LSPR red shifts and blue shifts, respectively, resulting in the observed periodic behavior. To characterize the effects dominated by coherent acoustic phonons, the non-oscillatory components of the data are subtracted. To this end, I made use of the matrix pencil method to model which subtracts exponential decays and damped oscillations simultaneously as a sum of complex exponentials at each wavelength, using information theoretic criteria to determine the optimal number of exponential functions.[242] By modeling both oscillatory and non-oscillatory components simultaneously, these signals can be more cleanly separated. The resulting 2D TA map isolating the oscillatory component is displayed in Figure 8.1b. Notably, the magnitude of the oscillations are distinct from the amplitude of the overall transient signal. Further, there is a nodal line near the static extinction maximum (denoted by a dashed gray line) representing a change of phase in the oscillations. This phase reversing behavior is also observed for acoustic phonons in other nanomaterials including nanospheres and nanorods. [187,232]

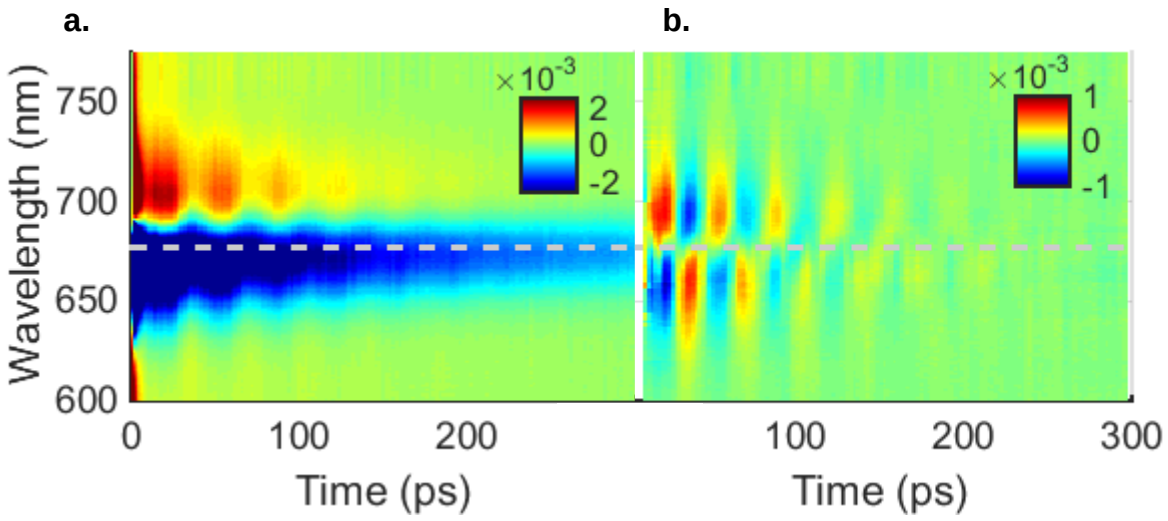

Figure 8.1. (a) A 2D TA map of photoexcited bipyramid ensemble with its LSPR of 677 nm indicated with a dashed gray line. (b) A TA map following subtraction of non-oscillatory dynamics from panel A with the static LSPR maximum indicated by a dashed gray line.

To gain a more quantitative understanding, Fourier transformations were performed at every wavelength as is commonly done in analyzing vibrational wave packets in molecular systems.[234–240] Averaged together, the maximum Fourier transform magnitude here occurred at a frequency of 28.7 GHz (period of 34.8 ps, FWHM of 9.0 GHz). Figure 8.2a demonstrates how the phases of the oscillations vary with wavelength at this frequency. To better illustrate trends, these phases are reported relative to a frequency-dependent reference phase to yield

$$\theta'(\lambda, f) = \theta(\lambda, f) - \theta_0(f) \quad (8.1)$$

where λ is wavelength, f is oscillation frequency, and θ', θ, and θ_0 are reported, observed, and reference phases respectively. Here, the convention that $\theta' = 0$ corresponds to the particle being expanded along its long axis at time zero is used, consistent with initial particle expansion

following photoexcitation. Theoretical calculations show expansion results in the LSPR redshifting which increases extinction at photon energies lower than the LSPR. Thus, θ_0 is defined

$$\theta_0(f) = \frac{\int_{\lambda_{\max}}^{\lambda_{\text{end}}} \theta(\lambda,f)\mathrm{d}\lambda}{\lambda_{\text{end}} - \lambda_{\max}} \qquad (8.2)$$

In this case, λ_{max} = 690 nm and λ_{end} = 714 nm. The cos(θ') is displayed as it outputs a value of 1 if a feature is perfectly in phase with initial particle expansion and -1 if it is out of phase. This change in oscillation phase is sharp and well-defined as a result of the behavior originating from a single phenomenon: coherent phonons simultaneously cause some regions to increase in extinction and other regions to decrease. This simplicity in phase behavior enables phonon-induced changes in extinction to be spectrally described by multiplying the relative phase with the Fourier transform magnitude. The resulting product is referred to as the afore-mentioned oscillation associated spectra (OAS) because these describe the spectral changes induced by the vibrations in analogy to decay associated spectra that describe how electronic excited states change the optical properties of a molecular system.[243–245] This method for calculating the OAS is equivalent to taking the real-part of the Fourier-transformed signal where the phase origin has been set to θ_0. Mathematically,

$$\mathrm{OAS}(\lambda, f) = \mathrm{Re}\left\{\mathcal{F}_t[\Delta A(\lambda, t)] \times e^{-i\theta_0(f)}\right\} \qquad (8.3)$$

where $\mathcal{F}_t[\Delta A(\lambda, t)]$ is the Fourier transform with respect to t of $\Delta A(\lambda, t)$ to yield $\Delta A(\lambda, f)$ and Re is the real-part function. The inclusion of phase information in analyzing oscillatory dynamics, as in the OAS approach, is not frequently applied in molecular systems as their phase behavior is more complex; OAS best describes phase shifts that are exactly π. Rather, OAS uses the same

underlying logic as damped oscillation associated spectra, although the simpler phase behavior of acoustic phonons in a nanomaterial makes the implementation and interpretation much simpler.[241]

The OAS of this sample at a frequency of 28.7 GHz (34.8 ps period) is shown in Figure 8.2b. As acoustic phonons cause a plasmonic particle to expand and contract, often it is assumed that the plasmon resonance red shifts and blue shifts while retaining the same general structure. With a constant peak structure, the extinction at any given wavelength will be determined by its proximity to the extinction maximum. Therefore, as coherent acoustic phonons cause the LSPR to shift, the extinction at any given wavelength will change based on its new proximity to the extinction maximum. The magnitude of this change will be proportional to how extinction changes with relative proximity to the LSPR, which are equivalent to changes in energy. In terms of observables, the amplitude of extinction changes resulting from oscillations in LSPR energy should be proportional to the derivative of the static extinction spectrum with respect to energy. This trend is evident in Figure 8.2b, where the OAS matches up well with the derivative of the static extinction with respect to energy. In the inset, it is demonstrated how the extinction spectrum would change if it was solely affected by coherent acoustic phonons by adding (red) or subtracting (blue) the OAS from the static extinction spectrum. Unsurprisingly, the resulting spectra simply suggest the LSPR is red shifting and blue shifting. Peak broadening or red shifting from incoherent heating both contradict the assumptions in the discussion and could create differences between the OAS and the derivative of the extinction spectrum, although these effects are generally quite small[216] justifying the neglect of them. In Appendix F.1, it is demonstrated that the similarity between OAS and differentiated extinction spectrum is consistent across the bipyramids I have

examined. It is worth mentioning that Hartland had previously considered the Fourier transform magnitude of phonons in gold nanospheres as a function of wavelength and found a maximum magnitude at a wavelength red of the LSPR.[187] That observation was likely the result of the same trend described above as it was caused by an analogous phenomenon.

In addition to confirming these conventional assumptions about acoustic phonons, OAS provides a method of deconstructing inhomogeneity in the ensemble. Phonon frequencies are dependent on particle geometry so differently sized particles oscillate at slightly different frequencies. These differences cause inhomogeneous dephasing which dominate dynamics in most nanoparticle ensembles[47,65] and consequently highly monodisperse nanoparticles—including gold bipyramids—are the focus of many coherent acoustic phonon studies.[70,75,77,78,216,231] However, in the analysis of such systems, inhomogeneity is considered only in the context of dephasing rates without considering that different particles present different extinction spectra and oscillation frequencies. There have also been some single particle measurements on coherent acoustic phonons which are able to circumvent issues of inhomogeneity,[72,215,233] but phonon-driven application will require ensembles of nanomaterials. OAS resolves issues of inhomogeneity by considering oscillation frequency at every wavelength independently. Figure 8.2c which shows a 2D map of the OAS. There are the same positive and negative features as shown in Figure 8.2b—which is essentially a line cut of this 2D map—but these two features have distinct spectral-phonon frequency behavior. Notably, the longer wavelength features tend to exhibit larger average periods. Oscillation period is known to increase with particle length and LSPR wavelength increases with aspect ratio. The trend can then be explained by longer bipyramids having higher aspect ratios.

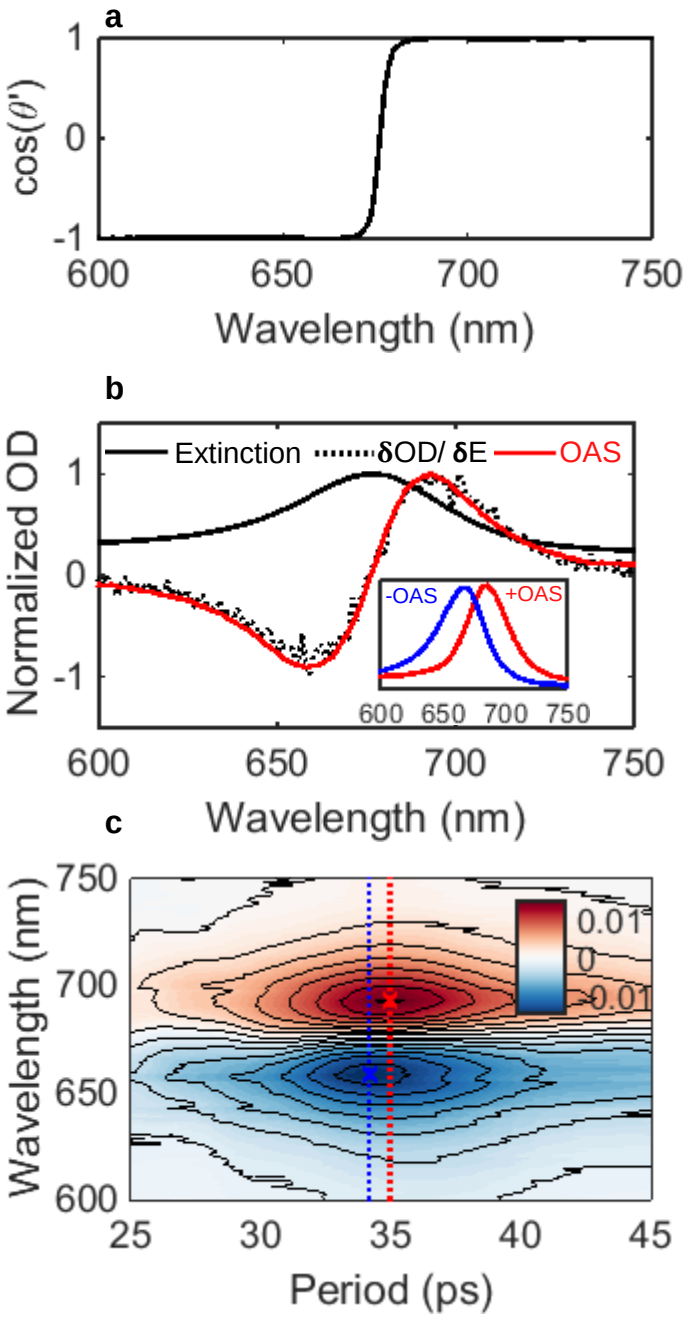

Figure 8.2. (a) Relative phase cos(θ_0') of bipyramid oscillations at a period of 34.8 ps. (b) Normalized extinction spectrum of the bipyramid ensemble (solid black), the derivative of that spectrum with respect to photon energy (dashed black), and the OAS (solid red). Inset: the extinction spectrum plus (red) and minus (blue) the OAS. (c) 2D map of OAS spectrum versus oscillation period with contour lines.

8.2.2. OAS on OPENS

This methodology can also be applied to systems that exhibit more complex transient optical signals such as OPENs. Figure 8.3a shows a 2D TA map of the bipyramids from Figures 8.1 and 8.2 decorated with a thiacarbocyanine dye, 2,2′-dimethyl-8-phenyl-5,6,5′,6′-dibenzothiacarbocyanine chloride (TCC). Following functionalization, the bipyramids electronically couple with TCC, resulting in two hybridized resonances with a Rabi splitting of 120 meV.[231] The TA spectra of the resulting ensemble system exhibits oscillatory behavior across its entire extinction spectrum from the coherent acoustic phonons of the bipyramids. These oscillations are quite challenging to interpret; in addition to having non-oscillatory dynamics to contend with, the extinction has a complex line shape making it difficult to extract the phonon induced spectral changes. As a result, previous analysis[231] was simplistic although, some insight into the underlying phenomena was gained. First, based on qualitative observations, it was argued that peak positions shift in phase with each other. Specifically, both hybridized resonances increase in energy and then, together, decrease in energy. This trend is consistent with predictions from a simple coupled oscillator model[226] as is commonly used to describe plasmon-exciton coupling.[221,222] Second, based on FDTD calculations, it was argued that the peak intensities changed out of phase with one another; while one increased the other would decrease. This was interpreted through the lens of most of the oscillator strength of the resonances coming from the bipyramids rather than the TCC molecules. As acoustic phonons cause the LSPR to redshift, the redder peak has relatively more bipyramid character and thus a higher extinction cross section.

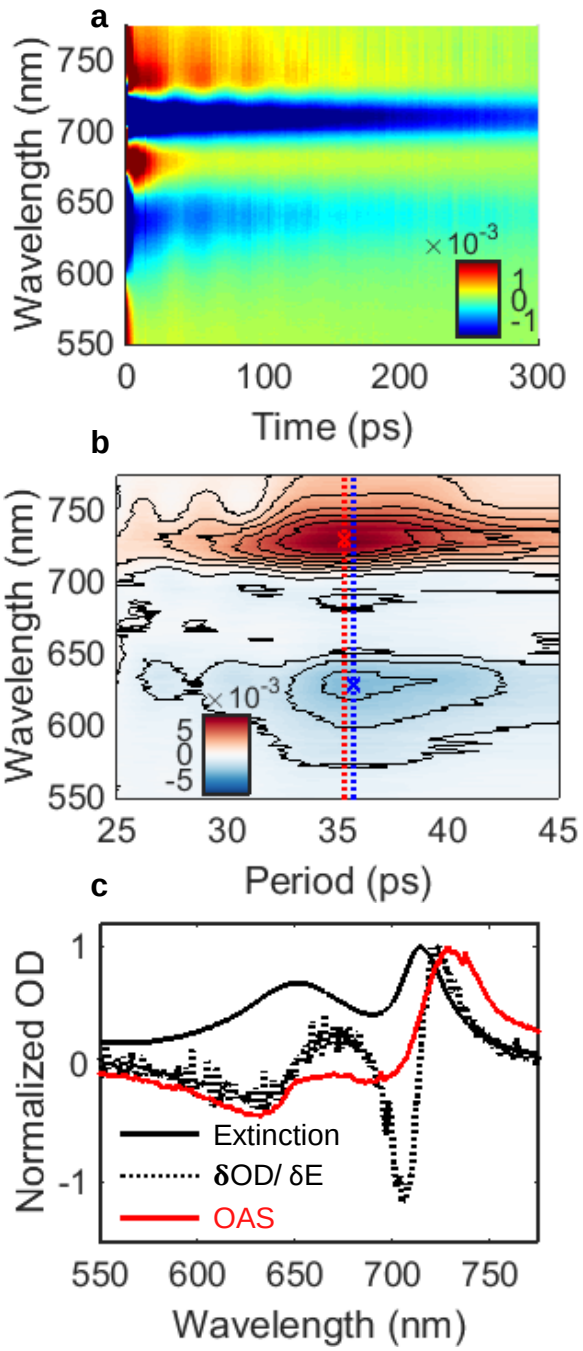

Figure 8.3. (a) A 2D TA map of a gold bipyramid functionalized OPEN ensemble. (b) A 2D OAS map of the OPEN ensemble. (c) Normalized extinction spectrum of the OPEN ensemble (solid black), the derivative of that spectrum with respect to photon energy (dashed black), and the OAS (solid red).

Fortunately, OAS is agnostic to line shape and can overcome this complexity. It is briefly worth noting that OPENs exhibit the same simple phase behavior as bipyramids (Appendix F.2) as they have the same underlying phenomenon of coherent acoustic phonons, validating the usage of OAS. The 2D map of the OAS is displayed in Figure 8.3b. There is an overall shift in frequency with the maximum Fourier transform magnitude at a frequency of 28.2 GHz (period of 35.4 ps, FWHM of 8.2 GHz). This change to lower frequency is likely due to the mass added by the dye, further conveying the prospective utility of gold bipyramids in mass sensing applications.[75] Relatedly, the period of the oscillations in the hybridized systems seems to be longer at bluer wavelengths. This may be due to the fact that the higher-energy peak is more TCC-like in character, as it should be more intense for particles that have more TCC attached to the bipyramid, which would increase the oscillation period.

The OAS at the maximum Fourier transform magnitude is shown in Figure 8.3c along with the static extinction spectrum and the derivative of the static extinction spectrum. In contrast to bare gold bipyramids, the OAS of an OPEN sample resembles—but does not match—the derivative of its extinction spectrum. This difference suggests the behavior is more complex than a simple shift in peak position. However, the shape of the OAS could be explained by changes in the relative amplitude of the two peaks. The spectral region between the two peaks would have competing factors from changes in peak amplitude and peak position changes which could result in the observed reduced oscillation strength and phase behavior. This trend is indeed observed in Figure 8.4a where the OAS is added or subtracted from the static extinction spectrum. Here, it becomes clear that particle expansion causes both resonances to red shift with the redder peak

increasing in intensity and the bluer peak decreasing in intensity. Conversely, particle contraction causes the peaks to blue shift with the bluer peak increasing in intensity while the redder peak decreases in intensity. It is worth comparing these results to theoretical (electrodynamics combined with continuum mechanics) calculations that were used to generate the original scientific model.[231] To accomplish this task, a series of FDTD calculations was performed. Bipyramids were coated with a TCC layer and then were expanded or contracted 1% along their lowest order acoustic phonon mode. The extinction spectra of these modified particles, along with that of the particle in its original geometry are shown in Figure 8.4b. These calculations and the experimental data analyzed with OAS are strikingly similar, demonstrating experimental evidence of the previously proposed model.

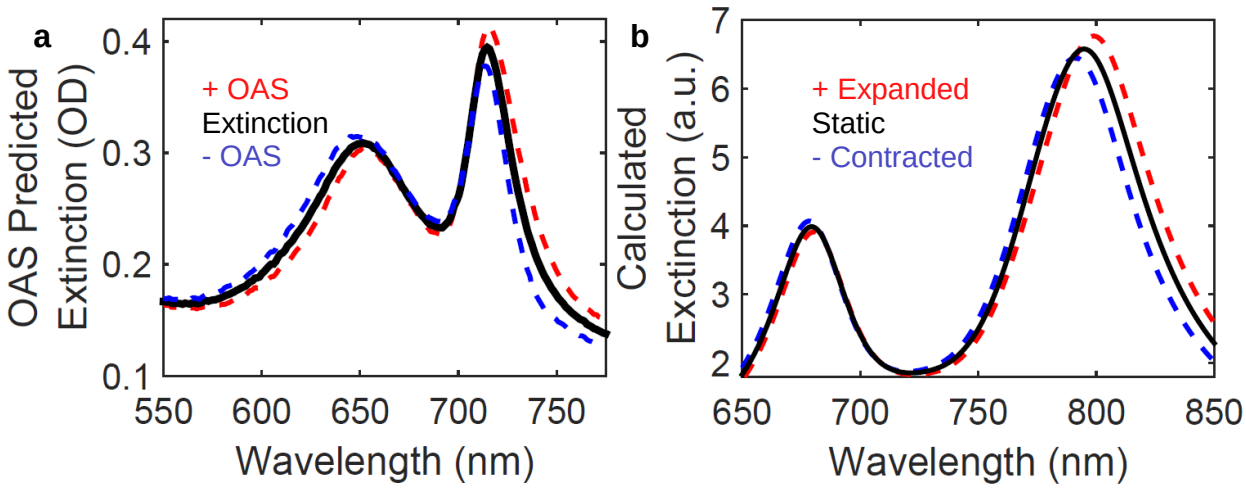

Figure 8.4. (a) The static extinction of the OPEN (black) with the addition (red) or subtraction (blue) of the OAS. (b) Extinction spectra of OPENs at maximally expanded or contracted conditions as predicted by FDTD calculations

8.3. Conclusion

In addition to improving the specific understanding of this system, it is worth considering the utility of OAS in several contexts. A major strength of OAS is its simplicity, which makes it scalable for especially complex or crowded spectra. For example, if there were multiple phonons of different frequencies affecting the dynamics at similar wavelengths, their separation in frequency space would make it trivial for OAS to separate their effects. Further, due to its lack of assumptions about line shape, it could also be used to evaluate changes in peak width or even the emergence of new resonances.

In conclusion, I have described OAS and applied it to analyze coherent acoustic phonons in nanomaterials. The assumption that phonons cause shifts in LSPR energy—with minimal changes in line shape—was validated while refining insight into sample inhomogeneity. OAS also experimentally validated previously-suggested models of phonon-induced changes in plasmon-exciton coupling in OPENs. This general strategy could be used to analyze oscillatory effects, such as from phonons or other periodic signals, on arbitrarily complex systems and aid in the design of new applications that use the coherent phonons of nanomaterials.

8.4. Methods

8.4.1. Material Synthesis

Gold bipyramids examined in this study were synthesized using a previously described seed-mediated growth approach.[193,216,231] Briefly, gold seeds were created by reacting $HAuCl_4$ with $NaBH_4$ solution in the presence of sodium citrate. The seeds were aged for two hours before use. For growth of the bipyramids, $HAuCl_4$ solution with trace amounts of $AgNO_3$ added were mixed with cetyltrime-thylammonium bromide (CTAB) solution, acidified by a small amount of HCl, and reduced by L-ascobic acid. Right after the reduction, small amounts of seeds were added, and the reaction was allowed to proceed in a 30°C bath for two hours. To form the OPENs, TCC in a water:ethanol solution was added to the bipyramid solution as consistent with previously described methods.[231]

8.4.2. Optical Measurements

All samples were suspended in water for optical measurements. Transient absorption measurements were performed using a 2 kHz, 35 fs Ti:S amplifier. The 800 nm output was beamsplit to pump an optical parametric amplifier that produced tunable pump pulses at the LSPR of the sample, and a smaller portion was time-delayed and focused into sapphire to produce a white light probe beam. For the data in this chapter, the bipyramids were excited at 670 nm and the OPENs at 650 nm. Pump pulses were kept at modest fluences, a few 100 uJ/cm^2, to minimize sample damage.

8.4.3. Analysis Code

While the main text includes the general method used to determine the OAS, explicit MATLAB code can be found at https://github.com/kirschner21/OscillationAssociatedSpectra.

8.4.4. Electrodynamics Calculations

We performed finite-difference time-domain (FDTD, Lumerical Solutions) simulations to calculate the absorption and scattering spectra of the samples consistent with previously described methods.[231] Briefly, the dielectric permittivity tabulated by Johnson and Christy for gold[27] was used and the background refractive index was set to 1.33 for water. The bipyramid size was 120 nm-long and 60 nm-wide. A 2.3260-nm thick TCC shell was added with an assumed Lorentzian permittivity with the resonant wavelength of 700 nm, linewidth of 35 nm, and the plasma frequency corresponding to 2.3485 eV. The plane-wave irradiation was polarized in the direction of the bipyramid long axis (Although the measurements have been performed on a randomly oriented bipyramids in solution, gold bipyramid extinction is the most prominent in the long axis direction, and therefore the theoretical analysis is comparable to experiment).

CHAPTER 9: REFERENCES

(1) Daniel, M.; Astruc, D. Gold Nanoparticles : Assembly , Supramolecular Chemistry , Quantum-Size-Related Properties , and Applications toward Biology , Catalysis , and Nanotechnology. *Chem. Rev.* **2004**, *104* (1), 293–346.

(2) Burnett, M. E.; Wang, S. Q. Current Sunscreen Controversies : A Critical Review. *Photodermatol. Photoimmunol. Photomed.* **2011**, *27* (6), 58–67.

(3) Bagher, A. M. Quantum Dot Display Technology and Comparison with OLED Display Technology. *Int. J. Adv. Res. Phys. Sci.* **2017**, *4* (1), 48–53.

(4) Jia, B. H. Who Will Win the Future of Display Technologies? *Natl. Sci. Rev.* **2018**, *5*, 427–431.

(5) Huff, H. *Into the Nano Era: Moore's Law beyond Planar Silicon CMOS*; Springer Science & Business Media, 2008; Vol. 106.

(6) Lu, W.; Lieber, C. M. Nanoelectronics from the Bottom Up. *Nat. Mater.* **2007**, *6*, 841–850.

(7) Singh, R.; Jr, J. W. L. Nanoparticle-Based Targeted Drug Delivery. *Exp. Mol. Pathol.* **2009**, *86* (3), 215–223.

(8) Liu, X.; Luo, J.; Zhu, J. Size Effect on the Crystal Structure of Silver Nanowires. *Nano Lett.* **2006**, *6* (3), 408–412.

(9) Cheng, H.; Yang, N.; Lu, Q.; Zhang, Z.; Zhang, H. Syntheses and Properties of Metal

Nanomaterials with Novel Crystal Phases. *Adv. Mater.* **2018**, *30*, 1707189.

(10) Li, L.; Reiss, P.; Protie, M. Core / Shell Semiconductor Nanocrystals. *Small* **2009**, *5* (2), 154–168.

(11) Klimov, V. I. Spectral and Dynamical Properties of Multiexcitons in Semiconductor Nanocrystals. *Annu. Rev.* **2007**, *58*, 635–673.

(12) Efros, A. L.; Efros, A. L. Interband Absorption of Light in a Semiconductor Sphere. *Sov. Phys. Semicond.* **1982**, *16* (7), 772–775.

(13) Knoblauch, C.; Griep, M.; Friedrich, C. Recent Advances in the Field of Bionanotechnology: An Insight into Optoelectric Bacteriorhodopsin, Quantum Dots, and Noble Metal Nanoclusters. *Sensors* **2014**, *14*, 19731–19766.

(14) Chan, W. C. W.; Nie, S. Quantum Dot Bioconjugates for Ultrasensitive Nonisotopic Detection. *Science* **1998**, *281*, 2016–2019.

(15) Medintz, I. L.; Uyeda, H. T.; Goldman, E. R.; Mattoussi, H. Quantum Dot Bioconjugates for Imaging , Labelling and Sensing. *Nat. Mater.* **2005**, *4*, 435–446.

(16) Wu, X.; Liu, H.; Liu, J.; Haley, K. N.; Treadway, J. A.; Larson, J. P.; Ge, N.; Peale, F.; Bruchez, M. P. Immunofluorescent Labeling of Cancer Marker Her2 and Other Cellular Targets with Semiconductor Quantum Dots. *Nat. Biotechnol.* **2003**, *21*, 41–46.

(17) Nozik, A. J. Quantum Dot Solar Cells. *Phys. E* **2002**, *14*, 115–120.

(18) Jun, H. K.; Careem, M. A.; Arof, A. K. Quantum Dot-Sensitized Solar Cells —

Perspective and Recent Developments : A Review of Cd Chalcogenide Quantum Dots as Sensitizers. *Renew. Sustain. Energy Rev.* **2013**, *22*, 148–167.

(19) Wang, R.; Shang, Y.; Kanjanaboos, P.; Zhou, W.; Nig, Z.; Sargent, E. H. Environmental Science Colloidal Quantum Dot Ligand Engineering for High Performance Solar Cells. *Energy Environ. Sci.* **2016**, *9*, 26–32.

(20) Cui, J.; Beyler, A. P.; Marshall, L. F.; Chen, O.; Harris, D. K.; Wanger, D. D.; Brokmann, X.; Bawendi, M. G. Direct Probe of Spectral Inhomogeneity Reveals Synthetic Tunability of Single-Nanocrystal Spectral Linewidths. *Nat. Chem.* **2013**, *5* (7), 602–606.

(21) Hines, M. A.; Guyot-sionnest, P. Synthesis and Characterization of Strongly Luminescing ZnS-Capped CdSe Nanocrystals. *J. Phys. Chem.* **1996**, *100*, 468–471.

(22) Xu, S.; Ziegler, J.; Nann, T. Rapid Synthesis of Highly Luminescent InP and InP / ZnS Nanocrystals. *J. Mater. Chem.* **2008**, *18*, 2653–2656.

(23) Protesescu, L.; Yakunin, S.; Bodnarchuk, M. I.; Krieg, F.; Caputo, R.; Hendon, C. H.; Yang, R. X.; Walsh, A.; Kovalenko, M. V. Nanocrystals of Cesium Lead Halide Perovskites (CsPbX3, X = Cl, Br, and I): Novel Optoelectronic Materials Showing Bright Emission with Wide Color Gamut. *Nano Lett.* **2015**, *15* (6), 3692–3696.

(24) Lim, J.; Park, Y.; Klimov, V. I. Optical Gain in Colloidal Quantum Dots Achieved with Direct-Current Electrical Pumping. *Nat. Mater.* **2018**, *17*, 42–50.

(25) Kwak, J.; Bae, W. K.; Lee, D.; Park, I.; Lim, J.; Park, M.; Cho, H.; Woo, H.; Yoon, D. Y.;

Char, K.; et al. Bright and Efficient Full-Color Colloidal Quantum Dot Light-Emitting Diodes Using an Inverted Device Structure. *Nano Lett.* **2012**, *12*, 2362–2366.

(26) Mashford, B. S.; Stevenson, M.; Popovic, Z.; Hamilton, C.; Zhou, Z.; Breen, C.; Steckel, J.; Bulovic, V.; Bawendi, M.; Coe-sullivan, S.; et al. High-Efficiency Quantum-Dot Light-Emitting Devices with Enhanced Charge Injection. *Nat. Photonics* **2013**, *7*, 407–412.

(27) Dai, X.; Zhang, Z.; Jin, Y.; Niu, Y.; Cao, H.; Liang, X.; Chen, L.; Wang, J.; Peng, X. Solution-Processed, High-Performance Light-Emitting Diodes Based on Quantum Dots. *Nature* **2014**, *515* (7525), 96–99.

(28) Yang, Y.; Zheng, Y.; Cao, W.; Titov, A.; Hyvonen, J.; Manders, J. R.; Xue, J.; Holloway, P. H.; Qian, L. High-Efficiency Light-Emitting Devices Based on Quantum Dots with Tailored Nanostructures. *Nat. Photonics* **2015**, *9* (4), 259–266.

(29) Klimov, V. I.; Mikhailovsky, A. A.; Xu, S.; Malko, A.; Hollingsworth, J. A.; Leatherdale, C. A.; Eisler, H.; Bawendi, M. G. Optical Gain and Stimulated Emission in Nanocrystal Quantum Dots. *Science* **2000**, *290*, 314–318.

(30) Klimov, V. I. Mechanisms for Photogeneration and Recombination of Multiexcitons in Semiconductor Nanocrystals: Implications for Lasing and Solar Energy Conversion. *J. Phys. Chem. B* **2006**, *110* (34), 16827–16845.

(31) García-Santamaría, F.; Chen, Y.; Vela, J.; Schaller, R. D.; Hollingsworth, J. A.; Klimov, V. I. Suppressed Auger Recombination in “Giant” Nanocrystals Boosts Optical Gain

Performance. *Nano Lett.* **2009**, *9* (10), 3482–3488.

(32) Iyer, V. H.; Mahadevu, R.; Pandey, A. Low Threshold Quantum Dot Lasers. *J. Phys. Chem. Lett.* **2016**, *7*, 1244–1248.

(33) Fan, F.; Voznyy, O.; Randy, P.; Bicanic, K. T.; Adachi, M. M.; Mcbride, J. R.; Reid, K. R.; Park, Y.; Li, X.; Jain, A.; et al. Continuous-Wave Lasing in Colloidal Quantum Dot Solids Enabled by Facet-Selective Epitaxy. *Nature* **2017**, *544*, 75–79.

(34) Kazes, B. M.; Lewis, D. Y.; Ebenstein, Y.; Mokari, T.; Banin, U. Lasing from Semiconductor Quantum Rods in a Cylindrical Microcavity. *Adv. Mater.* **2002**, *14* (4), 317–321.

(35) Cooney, R. R.; Sewall, S. L.; Sagar, D. M.; Kambhampati, P. Gain Control in Semiconductor Quantum Dots via State-Resolved Optical Pumping. *Phys. Rev. Lett.* **2009**, *102* (12), 127404.

(36) Shirasaki, Y.; Supran, G. J.; Bawendi, M. G.; Bulović, V. Emergence of Colloidal Quantum-Dot Light-Emitting Technologies. *Nat. Photonics* **2013**, *7*, 13–23.

(37) Klimov, V. I.; McBranch, D. W.; Leatherdale, C. A.; Bawendi, M. G. Electron and Hole Relaxation Pathways in Semiconductor Quantum Dots. *Phys. Rev. B* **1999**, *60* (19), 13740.

(38) Guyot-Sionnest, P.; Shim, M.; Matranga, C.; Hines, M. Intraband Relaxation in CdSe Quantum Dots. *Phys. Rev. B* **1999**, *60* (4), R2181.

(39) Wehrenberg, B. L.; Wang, C.; Guyot-Sionnest, P. Interband and Intraband Optical Studies

of PbSe Colloidal Quantum Dots. *J. Phys. Chem. B* **2002**, *106* (41), 10634–10640.

(40) Kambhampati, P. Unraveling the Structure and Dynamics of Excitons in Semiconductor Quantum Dots. *Acc. Chem. Res.* **2011**, *44* (1), 1–13.

(41) Hannah, D. C.; Brown, K. E.; Young, R. M.; Wasielewski, M. R.; Schatz, G. C.; Co, D. T.; Schaller, R. D. Direct Measurement of Lattice Dynamics and Optical Phonon Excitation in Semiconductor Nanocrystals Using Femtosecond Stimulated Raman Spectroscopy. *Phys. Rev. Lett.* **2013**, *111* (10), 1–5.

(42) Achermann, M.; Hollingsworth, J. A.; Klimov, V. I. Multiexcitons Confined within a Subexcitonic Volume : Spectroscopic and Dynamical Signatures of Neutral and Charged Biexcitons in Ultrasmall Semiconductor Nanocrystals. *Phys. Rev.* **2003**, *68*, 245302.

(43) Klimov, V. I.; McGuire, J. A.; Schaller, R. D.; Rupasov, V. I. Scaling of Multiexciton Lifetimes in Semiconductor Nanocrystals. *Phys. Rev. B - Condens. Matter Mater. Phys.* **2008**, *77* (19), 1–12.

(44) Robel, I.; Gresback, R.; Kortshagen, U.; Schaller, R. D.; Klimov, V. I. Universal Size-Dependent Trend in Auger Recombination in Direct-Gap and Indirect-Gap Semiconductor Nanocrystals. *Phys. Rev. Lett.* **2009**, *102* (17), 1–4.

(45) Kittel, C. *Introduction to Solid State Physics*; Wiley New York, 1976; Vol. 8.

(46) Willets, K. A.; Duyne, R. P. Van. Localized Surface Plasmon Resonance Spectroscopy and Sensing. *Annu. Rev. Mater. Res.* **2007**, *58*, 267–297.

(47) Hartland, G. V. Optical Studies of Dynamics in Noble Metal Nanostructures. *Chem. Rev.* **2011**, *111*, 3858–3887.

(48) Homola, J.; Koudela, I.; Yee, S. S. Surface Plasmon Resonance Sensors Based on Diffraction Gratings and Prism Couplers: Sensitivity Comparison. *Sensors Actuators B* **1999**, *54*, 16–24.

(49) Hulst, H. C.; van de Hulst, H. C. *Light Scattering by Small Particles*; Courier Corporation, 1981.

(50) Link, S.; Mohamed, M. B.; El-sayed, M. A. Simulation of the Optical Absorption Spectra of Gold Nanorods as a Function of Their Aspect Ratio and the Effect of the Medium Dielectric Constant. *J. Phys. Chem. A* **1999**, *103*, 3073–3077.

(51) Zhao, J.; Pinchuk, A. O.; Mcmahon, J. M.; Li, S.; Ausman, L. K.; Atkinson, A. L.; Schatz, G. C. Methods for Describing the Electromagnetic Properties of Silver and Gold Nanoparticles. *Acc. Chem. Res.* **2008**, *41* (12), 1710–1720.

(52) Haes, A. J.; Chang, L.; Klein, W. L.; Duyne, R. P. Van. Detection of a Biomarker for Alzheimer ' s Disease from Synthetic and Clinical Samples Using a Nanoscale Optical Biosensor. *J. Am. Chem. Soc* **2005**, *127* (11), 2264–2271.

(53) Mcfarland, A. D.; Duyne, R. P. Van. Single Silver Nanoparticles as Real-Time Optical Sensors with Zeptomole Sensitivity. *Nano Lett.* **2003**, *3* (8), 1057–1062.

(54) Yonzon, C. R.; Stuart, D. A.; Zhang, X.; Mcfarland, A. D.; Haynes, C. L.; Duyne, R. P.

Van. Towards Advanced Chemical and Biological Nanosensors — An Overview. *Talanta* **2005**, *67*, 438–448.

(55) Saha, K.; Agasti, S. S.; Kim, C.; Li, X.; Rotello, V. M. Gold Nanoparticles in Chemical and Biological Sensing. *Chem. Rev.* **2012**, *112*, 2739–2779.

(56) Vo-dinh, T.; Wang, H.; Scaffidi, J. Plasmonic Nanoprobes for SERS Biosensing and Bioimaging. *J. Biophotonics* **2010**, *102* (1), 89–102.

(57) Jain, P. K.; Huang, X.; El-sayed, I. H.; El-sayed, M. A. Noble Metals on the Nanoscale : Optical and Photothermal Properties and Some Applications in Imaging , Sensing , Biology , and Medicine. *Acc. Chem. Res.* **2008**, *41* (12), 1578–1586.

(58) Atwater, H. A.; Polman, A. Plasmonics for Improved Photovoltaic Devices. *Nat. Mater.* **2010**, *9*, 205–213.

(59) Green, M. A.; Pillai, S. Harnessing Plasmonics for Solar Cells. *Nat. Photonics* **2012**, *6*, 130–132.

(60) Sönnichsen, C.; Franzl, T.; Wilk, T.; Plessen, G. Von; Feldmann, J.; Wilson, O. M.; Mulvaney, P. Drastic Reduction of Plasmon Damping in Gold Nanorods. *Phys. Rev. Lett.* **2002**, *88* (7), 077402.

(61) Hohlfeld, J.; Wellershoff, S.-S.; Güdde, J.; Conrad, U.; Jähnke, V.; Matthias, E. Electron and Lattice Dynamics Following Optical Excitation of Metals. *Chem. Phys.* **2000**, *251*, 237–258.

(62) Voisin, C.; Christofilos, D.; Fatti, N. Del; Vallée, F.; Prevel, B.; Cottancin, E.; Lermé, J.; Pellarin, M.; Broyer, M. Size-Dependent Electron-Electron Interactions in Metal Nanoparticles. *Phys. Rev. Lett.* **2000**, *85* (10), 2200–2203.

(63) Sun, C.-K.; Vallée, F.; Acioli, L. H.; Fisica, D.; Pernambuco, D. Femtosecond-Tunable Measurement of Electron Thermalization in Gold. *Phys. Rev.* **1994**, *50* (20), 15337–15348.

(64) Hodak, J. H.; Henglein, A.; Hartland, G. V. Photophysics of Nanometer Sized Metal Particles: Electron−Phonon Coupling and Coherent Excitation of Breathing Vibrational Modes. *J. Phys. Chem. B* **2000**, *104* (43), 9954–9965.

(65) Major, T. A.; Lo, S. S.; Yu, K.; Hartland, G. V. Time-Resolved Studies of the Acoustic Vibrational Modes of Metal and Semiconductor Nano-Objects. *J. Phys. Chem. Lett.* **2014**, *5* (5), 866–874.

(66) Krauss, T. D.; Wise, F. W. Coherent Acoustic Phonons in a Semiconductor Quantum Dot. *Phys. Rev. Lett.* **1997**, *79* (25), 5102–5105.

(67) Sagar, D. M.; Cooney, R. R.; Sewall, S. L.; Dias, E. A.; Barsan, M. M.; Butler, I. S.; Kambhampati, P. Size Dependent, State-Resolved Studies of Exciton-Phonon Couplings in Strongly Confined Semiconductor Quantum Dots. *Phys. Rev. B - Condens. Matter Mater. Phys.* **2008**, *77* (23), 1–14.

(68) Plech, A.; Kotaidis, V.; Grésillon, S.; Dahmen, C.; Von Plessen, G. Laser-Induced

Heating and Melting of Gold Nanoparticles Studied by Time-Resolved x-Ray Scattering. *Phys. Rev. B - Condens. Matter Mater. Phys.* **2004**, *70* (19), 1–7.

(69) Clark, J. N.; Beitra, L.; Xiong, G.; Higginbotham, A.; Fritz, D. M.; Lemke, H. T.; Zhu, D.; Chollet, M.; Williams, G. J.; Messerschmidt, M.; et al. Ultrafast Three-Dimensional Imaging of Lattice Dynamics in Individual Gold Nanocrystals. *Science* **2013**, *341* (6141), 56–59.

(70) Pelton, M.; Sader, J. E.; Burgin, J.; Liu, M.; Guyot-Sionnest, P.; Gosztola, D. Damping of Acoustic Vibrations in Gold Nanoparticles. *Nat. Nanotechnol.* **2009**, *4* (8), 492–495.

(71) Van Dijk, M. A.; Lippitz, M.; Orrit, M. Detection of Acoustic Oscillations of Single Gold Nanospheres by Time-Resolved Interferometry. *Phys. Rev. Lett.* **2005**, *95* (26), 1–4.

(72) Zijlstra, P.; Tchebotareva, A. L.; Chon, J. W. M.; Gu, M.; Orrit, M. Acoustic Oscillations and Elastic Moduli of Single Gold Nanorods. *Nano Lett.* **2008**, *8* (10), 3493–3497.

(73) Major, T. A.; Crut, A.; Gao, B.; Lo, S. S.; Fatti, N. Del; Vallée, F.; Hartland, G. V. Damping of the Acoustic Vibrations of a Suspended Gold Nanowire in Air and Water Environments. *Phys. Chem. Chem. Phys.* **2013**, *15* (12), 4169–4176.

(74) Guo, P.; Schaller, R. D.; Ocola, L. E.; Ketterson, J. B.; Chang, R. P. H. Gigahertz Acoustic Vibrations of Elastically Anisotropic Indium-Tin-Oxide Nanorod Arrays. *Nano Lett.* **2016**, *16* (9), 5639–5646.

(75) Dacosta Fernandes, B.; Spuch-Calvar, M.; Baida, H.; Tréguer-Delapierre, M.; Oberlé, J.;

Langot, P.; Burgin, J. Acoustic Vibrations of Au Nano-Bipyramids and Their Modification under Ag Deposition: A Perspective for the Development of Nanobalances. *ACS Nano* **2013**, *7* (9), 7630–7639.

(76) Pelton, M.; Wang, Y.; Gosztola, D.; Sader, J. E. Mechanical Damping of Longitudinal Acoustic Oscillations of Metal Nanoparticles in Solution. *J. Phys. Chem. C* **2011**, *115* (48), 23732–23740.

(77) Soavi, G.; Tempra, I.; Pantano, M. F.; Cattoni, A.; Collin, S.; Biagioni, P.; Pugno, N. M.; Cerullo, G. Ultrasensitive Characterization of Mechanical Oscillations and Plasmon Energy Shift in Gold Nanorods. *ACS Nano* **2016**, *10* (2), 2251–2258.

(78) O'Brien, K.; Lanzillotti-Kimura, N. D.; Rho, J.; Suchowski, H.; Yin, X.; Zhang, X. Ultrafast Acousto-Plasmonic Control and Sensing in Complex Nanostructures. *Nat. Commun.* **2014**, *5*, 4042.

(79) Goldstein, A. N.; Echer, C. M.; Alivisatos, A. P. Melting in Semiconductor Nanocrystals. *Science* **1992**, *256* (5062), 1425–1427.

(80) Alivisatos, A. P. Semiconductor Clusters, Nanocrystals, and Quantum Dots. *Science* **1996**, *271* (5251), 933–937.

(81) Law, M.; Luther, J. M.; Song, Q.; Hughes, B. K.; Perkins, C. L.; Nozik, A. J. Structural, Optical, and Electrical Properties of PbSe Nanocrystal Solids Treated Thermally or with Simple Amines. *J. Am. Chem. Soc.* **2008**, *130* (18), 5974–5985.

(82) Goodfellow, B. W.; Patel, R. N.; Panthani, M. G.; Smilgies, D. M.; Korgel, B. A. Melting and Sintering of a Body-Centered Cubic Superlattice of PbSe Nanocrystals Followed by Small Angle X-Ray Scattering. *J. Phys. Chem. C* **2011**, *115* (14), 6397–6404.

(83) Rowland, C. E.; Fedin, I.; Diroll, B. T.; Liu, Y.; Talapin, D. V.; Schaller, R. D. Elevated Temperature Photophysical Properties and Morphological Stability of CdSe and CdSe/CdS Nanoplatelets. *J. Phys. Chem. Lett.* **2018**, *9* (2), 286–293.

(84) Ong, W.; Rupich, S. M.; Talapin, D. V; Mcgaughey, A. J. H.; Malen, J. A. Surface Chemistry Mediates Thermal Transport in Three-Dimensional Nanocrystal Arrays. *Nat. Mater.* **2013**, *12* (5), 410–415.

(85) Hopkins, P. E. Thermal Transport across Solid Interfaces with Nanoscale Imperfections: Effects of Roughness, Disorder, Dislocations, and Bonding on Thermal Boundary Conductance. *ISRN Mech. Eng.* **2013**, *2013* (1).

(86) Monachon, C.; Weber, L.; Dames, C. Thermal Boundary Conductance: A Materials Science Perspective. *Annu. Rev. Mater. Res.* **2016**, *46* (1), 433–463.

(87) Fleming, G. Chemical Applications of Ultrafast Spectroscopy. **1986**.

(88) Domen, K.; Bandara, A.; Kubota, J.; Onda, K.; Wada, A.; Kano, S. S.; Hirose, C. SFG Study of Unstable Surface Species by Picosecond Pump – Probe Method. *Surf. Sci.* **1999**, *427–428*, 349–357.

(89) Chung, H. S.; Khalil, M.; Smith, A. W.; Tokmakoff, A. Transient Two-Dimensional IR

Spectrometer for Probing Nanosecond Temperature-Jump Kinetics. *Rev. Sci. Instrum.* **2007**, *78*, 063101.

(90) Wernet, P.; Gavrila, G.; Godehusen, K.; Weniger, C.; Nibbering, E. T. J.; Elsaesser, T.; Eberhardt, W. Ultrafast Temperature Jump in Liquid Water Studied by a Novel Infrared Pump-x-Ray Probe Technique. *Appl. Phys. A* **2008**, *92*, 511–516.

(91) Wilson, A. J. C. Scherrer after Sixty Years: A Survey and Some New Results in the Determination of Crystallite Size. *J. Appl. Crystolography* **1978**, *11*, 102–113.

(92) Holzwarth, U.; Gibson, N. The Scherrer Equation versus the ' Debye – Scherrer Equation.' *Nat. Nanotechnol.* **2011**, *6*, 534.

(93) Brus, L. Electronic Wave-Functions in Semiconductor Clusters - Experiment and Theory. *J. Phys. Chem.* **1986**, *90* (12), 2555–2560.

(94) Alivisatos, A. P. Perspectives on the Physical Chemistry of Semiconductor Nanocrystals. *J. Phys. Chem.* **1996**, *100* (31), 13226–13239.

(95) Caruge, J. M.; Halpert, J. E.; Wood, V.; Bulović, V.; Bawendi, M. G. Colloidal Quantum-Dot Light-Emitting Diodes with Metal-Oxide Charge Transport Layers. *Nat. Photonics* **2008**, *2* (4), 247–250.

(96) Pal, B. N.; Ghosh, Y.; Brovelli, S.; Laocharoensuk, R.; Klimov, V. I.; Hollingsworth, J. A.; Htoon, H. 'Giant'CdSe/CdS Core/Shell Nanocrystal Quantum Dots as Efficient Electroluminescent Materials: Strong Influence of Shell Thickness on Light-Emitting

Diode Performance. *Nano Lett.* **2011**, *12* (1), 331–336.

(97) Jha, P. P.; Guyot-Sionnest, P. Trion Decay in Colloidal Quantum Dots. *ACS Nano* **2009**, *3* (4), 1011–1015.

(98) Downer, M. C.; Shank, C. V. Ultrafast Heating of Silicon on Sapphire by Femtosecond Optical Pulses. *Phys. Rev. Lett.* **1986**, *56* (7), 761.

(99) Achermann, M.; Bartko, A. P.; Hollingsworth, J. A.; Klimov, V. I. The Effect of Auger Heating on Intraband Carrier Relaxation in Semiconductor Quantum Rods. *Nat. Phys.* **2006**, *2* (8), 557–561.

(100) Klimov, V. I.; Mikhailovsky, A. A.; McBranch, D. W.; Leatherdale, C. A.; Bawendi, M. G. Quantization of Multiparticle Auger Rates in Semiconductor Quantum Dots. *Science* **2000**, *287* (5455), 1011–1013.

(101) Malko, A. V; Mikhailovsky, A. A.; Petruska, M. A.; Hollingsworth, J. A.; Klimov, V. I. Interplay between Optical Gain and Photoinduced Absorption in CdSe Nanocrystals. *J. Phys. Chem. B* **2004**, *108* (17), 5250–5255.

(102) Nozik, A. J. Spectroscopy and Hot Electron Relaxation Dynamics in Semiconductor Quantum Wells and Quantum Dots. *Annu. Rev. Phys. Chem.* **2001**, *52* (1), 193–231.

(103) Szilagyi, E.; Wittenberg, J. S.; Miller, T. A.; Lutker, K.; Quirin, F.; Lemke, H.; Zhu, D.; Chollet, M.; Robinson, J.; Wen, H.; et al. Visualization of Nanocrystal Breathing Modes at Extreme Strains. *Nat. Commun.* **2015**, *6*, 1–6.

(104) Wittenberg, J. S.; Miller, T. A.; Szilagyi, E.; Lutker, K.; Quirin, F.; Lu, W.; Lemke, H.; Zhu, D.; Chollet, M.; Robinson, J.; et al. Real-Time Visualization of Nanocrystal Solid-Solid Transformation Pathways. *Nano Lett.* **2014**, *14* (4), 1995–1999.

(105) Wang, X.; Rahmani, H.; Zhou, J.; Gorfien, M.; Plaskus, J. M.; Li, D.; Voss, R.; Nelson, C. A.; Lei, K. W.; Wolcott, A.; et al. Ultrafast Lattice Dynamics in Lead Selenide Quantum Dot Induced by Laser Excitation. *Appl. Phys. Lett.* **2016**, *109* (15), 153105.

(106) Hannah, D. C.; Dunn, N. J.; Ithurria, S.; Talapin, D. V.; Chen, L. X.; Pelton, M.; Schatz, G. C.; Schaller, R. D. Observation of Size-Dependent Thermalization in CdSe Nanocrystals Using Time-Resolved Photoluminescence Spectroscopy. *Phys. Rev. Lett.* **2011**, *107* (17), 13–16.

(107) Plimpton, S. Fast Parallel Algorithms for Short – Range Molecular Dynamics. *J. Comput. Phys.* **1995**, *117* (June 1994), 1–19.

(108) Rabani, E. An Interatomic Pair Potential for Cadmium Selenide. *J. Chem. Phys.* **2002**, *116* (1), 258–262.

(109) Bussi, G.; Donadio, D.; Parrinello, M. Canonical Sampling through Velocity Rescaling. *J. Chem. Phys.* **2007**, *126* (1), 14101.

(110) Cook, W. R. The CdS-MnS and CdSe-MnSe Phase Diagrams. *J. Am. Ceram. Soc.* **1968**, *51* (9), 518–520.

(111) Belonoshko, A. B.; Skorodumova, N. V; Rosengren, A.; Johansson, B. Melting and

Critical Superheating. *Phys. Rev. B* **2006**, *73* (1), 12201.

(112) Li, T.; Donadio, D.; Galli, G. Nucleation of Tetrahedral Solids: A Molecular Dynamics Study of Supercooled Liquid Silicon. *J. Chem. Phys.* **2009**, *131* (22), 224519.

(113) Perdew, J. P.; Zunger, A. Self-Interaction Correction to Density-Functional Approximations for Many-Electron Systems. *Phys. Rev. B* **1981**, *23* (10), 5048.

(114) Štich, I.; Car, R.; Parrinello, M. Structural, Bonding, Dynamical, and Electronic Properties of Liquid Silicon: An Ab Initio Molecular-Dynamics Study. *Phys. Rev. B* **1991**, *44* (9), 4262.

(115) Kresse, G.; Hafner, J. Ab Initio Molecular-Dynamics Simulation of the Liquid-Metal–amorphous-Semiconductor Transition in Germanium. *Phys. Rev. B* **1994**, *49* (20), 14251.

(116) Mohamed, M. B.; Tonti, D.; Al-Salman, A.; Chemseddine, A.; Chergui, M. Synthesis of High Quality Zinc Blende CdSe Nanocrystals. *J. Phys. Chem. B* **2005**, *109* (21), 10533–10537.

(117) Clark, J. N.; Beitra, L.; Xiong, G.; Fritz, D. M.; Lemke, H. T.; Zhu, D.; Chollet, M.; Williams, G. J.; Messerschmidt, M. M.; Abbey, B.; et al. Imaging Transient Melting of a Nanocrystal Using an X-Ray Laser. *Proc. Natl. Acad. Sci.* **2015**, *112* (24), 7444–7448.

(118) Wang, N.; Rokhlin, S. I.; Farson, D. F. Nonhomogeneous Surface Premelting of Au Nanoparticles. *Nanotechnology* **2008**, *19* (41).

(119) Guzelturk, B.; Kelestemur, Y.; Gungor, K.; Yeltik, A.; Akgul, M. Z.; Wang, Y.; Chen, R.;

Dang, C.; Sun, H.; Demir, H. V. Stable and Low-Threshold Optical Gain in CdSe/CdS Quantum Dots: An All-Colloidal Frequency Up-Converted Laser. *Adv. Mater.* **2015**, *27* (17), 2741–2746.

(120) Walsh, B. R.; Saari, J. I.; Krause, M. M.; Nick, R.; Coe-Sullivan, S.; Kambhampati, P. Controlling the Surface of Semiconductor Nanocrystals for Efficient Light Emission from Single Excitons to Multiexcitons. *J. Phys. Chem. C* **2015**, *119* (28), 16383–16389.

(121) Adachi, M. M.; Fan, F.; Sellan, D. P.; Hoogland, S.; Voznyy, O.; Houtepen, A. J.; Parrish, K. D.; Kanjanaboos, P.; Malen, J. A.; Sargent, E. H. Microsecond-Sustained Lasing from Colloidal Quantum Dot Solids. *Nat. Commun.* **2015**, *6*, 8694.

(122) Hannah, D. C.; Ithurria, S.; Krylova, G.; Talapin, D. V.; Schatz, G. C.; Schaller, R. D. Particle-Level Engineering of Thermal Conductivity in Matrix-Embedded Semiconductor Nanocrystals. *Nano Lett.* **2012**, *12* (11), 5797–5801.

(123) Carbone, L.; Nobile, C.; De Giorgi, M.; Sala, F. Della; Morello, G.; Pompa, P.; Hytch, M.; Snoeck, E.; Fiore, A.; Franchini, I. R.; et al. Synthesis and Micrometer-Scale Assembly of Colloidal CdSe/CdS Nanorods Prepared by a Seeded Growth Approach. *Nano Lett.* **2007**, *7* (10), 2942–2950.

(124) Yang, Y. A.; Wu, H.; Williams, K. R.; Cao, Y. C. Synthesis of CdSe and CdTe Nanocrystals without Precursor Injection. *Angew. Chemie* **2005**, *117* (41), 6870–6873.

(125) Yu, W. W.; Qu, L.; Guo, W.; Peng, X. Experimental Determination of the Extinction

Coefficient of CdTe, CdSe, and CdS Nanocrystals. *Chem. Mater.* **2003**, *15* (14), 2854–2860.

(126) Klimov, V. I. Optical Nonlinearities and Ultrafast Carrier Dynamics in Semiconductor Nanocrystals. *J. Phys. Chem. B* **2000**, *104*, 6112–6123.

(127) Stranks, S. D.; Eperon, G. E.; Grancini, G.; Menelaou, C.; Alcocer, M. J. P.; Leijtens, T.; Herz, L. M.; Petrozza, A.; Snaith, H. J. Electron-Hole Diffusion Lengths Exceeding 1 Micrometer in an Organometal Trihalide Perovskite Absorber. *Science* **2013**, *342* (6156), 341–344.

(128) Akkerman, Q. A.; D'Innocenzo, V.; Accornero, S.; Scarpellini, A.; Petrozza, A.; Prato, M.; Manna, L. Tuning the Optical Properties of Cesium Lead Halide Perovskite Nanocrystals by Anion Exchange Reactions. *J. Am. Chem. Soc.* **2015**, *137* (32), 10276–10281.

(129) Makarov, N. S.; Guo, S.; Isaienko, O.; Liu, W.; Robel, I.; Klimov, V. I. Spectral and Dynamical Properties of Single Excitons, Biexcitons, and Trions in Cesium-Lead-Halide Perovskite Quantum Dots. *Nano Lett.* **2016**, *16* (4), 2349–2362.

(130) Manser, J. S.; Christians, J. A.; Kamat, P. V. Intriguing Optoelectronic Properties of Metal Halide Perovskites. *Chem. Rev.* **2016**, *116* (21), 12956–13008.

(131) Dastidar, S.; Li, S.; Smolin, S. Y.; Baxter, J. B.; Fafarman, A. T. Slow Electron-Hole Recombination in Lead Iodide Perovskites Does Not Require a Molecular Dipole. *ACS*

Energy Lett. **2017**, *2* (10), 2239–2244.

(132) Wang, T.; Daiber, B.; Frost, J. M.; Mann, S. A.; Garnett, E. C.; Walsh, A.; Ehrler, B. Indirect to Direct Bandgap Transition in Methylammonium Lead Halide Perovskite. *Energy Environ. Sci.* **2017**, *10* (2), 509–515.

(133) Diroll, B. T.; Zhou, H.; Schaller, R. D. Low-Temperature Absorption, Photoluminescence, and Lifetime of $CsPbX_3$ (X = Cl, Br, I) Nanocrystals. *Adv. Funct. Mater.* **2018**, *3*, 1800945.

(134) Kim, H. S.; Lee, C. R.; Im, J. H.; Lee, K. B.; Moehl, T.; Marchioro, A.; Moon, S. J.; Humphry-Baker, R.; Yum, J. H.; Moser, J. E.; et al. Lead Iodide Perovskite Sensitized All-Solid-State Submicron Thin Film Mesoscopic Solar Cell with Efficiency Exceeding 9%. *Sci. Rep.* **2012**, *2*, 1–7.

(135) Burschka, J.; Pellet, N.; Moon, S. J.; Humphry-Baker, R.; Gao, P.; Nazeeruddin, M. K.; Grätzel, M. Sequential Deposition as a Route to High-Performance Perovskite-Sensitized Solar Cells. *Nature* **2013**, *499* (7458), 316–319.

(136) Liu, M.; Johnston, M. B.; Snaith, H. J. Efficient Planar Heterojunction Perovskite Solar Cells by Vapour Deposition. *Nature* **2013**, *501* (7467), 395–398.

(137) Yang, W. S.; Park, B.-W.; Jung, E. H.; Jeon, N. J. Iodide Management in Formamidinium-Lead-Halide – Based Perovskite Layers for Efficient Solar Cells. *Science* **2017**, *356*, 1376–1379.

(138) Kulbak, M.; Cahen, D.; Hodes, G. How Important Is the Organic Part of Lead Halide Perovskite Photovoltaic Cells? Efficient CsPbBr3 Cells. *J. Phys. Chem. Lett.* **2015**, *6* (13), 2452–2456.

(139) Wang, P.; Zhang, X.; Zhou, Y.; Jiang, Q.; Ye, Q.; Chu, Z.; Li, X.; Yang, X.; Yin, Z.; You, J. Solvent-Controlled Growth of Inorganic Perovskite Films in Dry Environment for Efficient and Stable Solar Cells. *Nat. Commun.* **2018**, *9* (1), 2225.

(140) Sutherland, B. R.; Sargent, E. H. Perovskite Photonic Sources. *Nat. Photonics* **2016**, *10* (5), 295–302.

(141) Yakunin, S.; Protesescu, L.; Krieg, F.; Bodnarchuk, M. I.; Nedelcu, G.; Humer, M.; De Luca, G.; Fiebig, M.; Heiss, W.; Kovalenko, M. V. Low-Threshold Amplified Spontaneous Emission and Lasing from Colloidal Nanocrystals of Caesium Lead Halide Perovskites. *Nat. Commun.* **2015**, *6*, 1–8.

(142) Song, J.; Li, J.; Li, X.; Xu, L.; Dong, Y.; Zeng, H. Quantum Dot Light-Emitting Diodes Based on Inorganic Perovskite Cesium Lead Halides (CsPbX3). *Adv. Mater.* **2015**, *27* (44), 7162–7167.

(143) Li, G.; Rivarola, F. W. R.; Davis, N. J. L. K.; Bai, S.; Jellicoe, T. C.; De La Peña, F.; Hou, S.; Ducati, C.; Gao, F.; Friend, R. H.; et al. Highly Efficient Perovskite Nanocrystal Light-Emitting Diodes Enabled by a Universal Crosslinking Method. *Adv. Mater.* **2016**, *28* (18), 3528–3534.

(144) Yassitepe, E.; Yang, Z.; Voznyy, O.; Kim, Y.; Walters, G.; Castañeda, J. A.; Kanjanaboos, P.; Yuan, M.; Gong, X.; Fan, F.; et al. Amine-Free Synthesis of Cesium Lead Halide Perovskite Quantum Dots for Efficient Light-Emitting Diodes. *Adv. Funct. Mater.* **2016**, *26* (47), 8757–8763.

(145) Moller, C. K. Crystal Structure and Photoconductivity of Caesium Plumbohalides. *Nature* **1958**, *182*, 1436.

(146) Rodová, M.; Brožek, J. Phase Transitions in Ternary Caesium Lead Bromide. *J. Therm. Anal. Calorim.* **2003**, *71* (62), 667–673.

(147) Stoumpos, C. C.; Malliakas, C. D.; Peters, J. A.; Liu, Z.; Sebastian, M.; Im, J.; Chasapis, T. C.; Wibowo, A. C.; Chung, D. Y.; Freeman, A. J.; et al. Crystal Growth of the Perovskite Semiconductor CsPbBr3: A New Material for High-Energy Radiation Detection. *Cryst. Growth Des.* **2013**, *13* (7), 2722–2727.

(148) Kubičár, L.; Vretenár, V.; Ƴves, R. Study of Phase Transitions by Transient Methods. *Solid State Phenom.* **2008**, *138*, 3–28.

(149) Cottingham, P.; Brutchey, R. L. Depressed Phase Transitions and Thermally Persistent Local Distortions in CsPbBr3Quantum Dots. *Chem. Mater.* **2018**.

(150) Lee, W.; Li, H.; Wong, A. B.; Zhang, D.; Lai, M.; Yu, Y.; Kong, Q.; Lin, E.; Urban, J. J.; Grossman, J. C.; et al. Ultralow Thermal Conductivity in All-Inorganic Halide Perovskites. *Proc. Natl. Acad. Sci.* **2017**, *114* (33), 201711744.

(151) Conings, B.; Drijkoningen, J.; Gauquelin, N.; Babayigit, A.; D'Haen, J.; D'Olieslaeger, L.; Ethirajan, A.; Verbeeck, J.; Manca, J.; Mosconi, E.; et al. Intrinsic Thermal Instability of Methylammonium Lead Trihalide Perovskite. *Adv. Energy Mater.* **2015**, *5* (15), 1–8.

(152) Misra, R. K.; Aharon, S.; Li, B.; Mogilyansky, D.; Visoly-Fisher, I.; Etgar, L.; Katz, E. A. Temperature- and Component-Dependent Degradation of Perovskite Photovoltaic Materials under Concentrated Sunlight. *J. Phys. Chem. Lett.* **2015**, *6* (3), 326–330.

(153) Yang, Y.; Ostrowski, D. P.; France, R. M.; Zhu, K.; Van De Lagemaat, J.; Luther, J. M.; Beard, M. C. Observation of a Hot-Phonon Bottleneck in Lead-Iodide Perovskites. *Nat. Photonics* **2016**, *10* (1), 53–59.

(154) Yang, J.; Wen, X.; Xia, H.; Sheng, R.; Ma, Q.; Kim, J.; Tapping, P.; Harada, T.; Kee, T. W.; Huang, F.; et al. Acoustic-Optical Phonon up-Conversion and Hot-Phonon Bottleneck in Lead-Halide Perovskites. *Nat. Commun.* **2017**, *8*, 1–9.

(155) Zhu, H.; Miyata, K.; Fu, Y.; Wang, J.; Joshi, P. P.; Niesner, D.; Williams, K. W.; Jin, S.; Zhu, X. Y. Screening in Crystalline Liquids Protects Energetic Carriers in Hybrid Perovskites. *Science* **2016**, *353* (6306), 1409–1413.

(156) Chang, A. Y.; Cho, Y. J.; Chen, K. C.; Chen, C. W.; Kinaci, A.; Diroll, B. T.; Wagner, M. J.; Chan, M. K. Y.; Lin, H. W.; Schaller, R. D. Slow Organic-to-Inorganic Sub-Lattice Thermalization in Methylammonium Lead Halide Perovskites Observed by Ultrafast Photoluminescence. *Adv. Energy Mater.* **2016**, *6* (15), 1–9.

(157) Guo, P.; Gong, J.; Sadasivam, S.; Xia, Y.; Song, T.-B.; Diroll, B. T.; Stoumpos, C. C.; Ketterson, J. B.; Kanatzidis, M. G.; Chan, M. K. Y.; et al. Slow Thermal Equilibration in Methylammonium Lead Iodide Revealed by Transient Mid-Infrared Spectroscopy. *Nat. Commun.* **2018**, *9* (1), 2792.

(158) Straus, D. B.; Hurtado Parra, S.; Iotov, N.; Gebhardt, J.; Rappe, A. M.; Subotnik, J. E.; Kikkawa, J. M.; Kagan, C. R. Direct Observation of Electron-Phonon Coupling and Slow Vibrational Relaxation in Organic-Inorganic Hybrid Perovskites. *J. Am. Chem. Soc.* **2016**, *138* (42), 13798–13801.

(159) De Jong, E. M. L. D.; Yamashita, G.; Gomez, L.; Ashida, M.; Fujiwara, Y.; Gregorkiewicz, T. Multiexciton Lifetime in All-Inorganic CsPbBr3perovskite Nanocrystals. *J. Phys. Chem. C* **2017**, *121* (3), 1941–1947.

(160) Diroll, B. T.; Nedelcu, G.; Kovalenko, M. V.; Schaller, R. D. High-Temperature Photoluminescence of CsPbX3 (X = Cl, Br, I) Nanocrystals. *Adv. Funct. Mater.* **2017**, *27* (21).

(161) Becker, M. A.; Vaxenburg, R.; Nedelcu, G.; Sercel, P. C.; Shabaev, A.; Mehl, M. J.; Michopoulos, J. G.; Lambrakos, S. G.; Bernstein, N.; Lyons, J. L.; et al. Bright Triplet Excitons in Caesium Lead Halide Perovskites. *Nature* **2018**, *553* (7687), 189–193.

(162) Fu, M.; Tamarat, P.; Huang, H.; Even, J.; Rogach, A. L.; Lounis, B. Neutral and Charged Exciton Fine Structure in Single Lead Halide Perovskite Nanocrystals Revealed by Magneto-Optical Spectroscopy. *Nano Lett.* **2017**, *17* (5), 2895–2901.

(163) Isarov, M.; Tan, L. Z.; Bodnarchuk, M. I.; Kovalenko, M. V.; Rappe, A. M.; Lifshitz, E. Rashba Effect in a Single Colloidal CsPbBr3perovskite Nanocrystal Detected by Magneto-Optical Measurements. *Nano Lett.* **2017**, *17* (8), 5020–5026.

(164) Rainoì, G.; Nedelcu, G.; Protesescu, L.; Bodnarchuk, M. I.; Kovalenko, M. V.; Mahrt, R. F.; Stöferle, T. Single Cesium Lead Halide Perovskite Nanocrystals at Low Temperature: Fast Single-Photon Emission, Reduced Blinking, and Exciton Fine Structure. *ACS Nano* **2016**, *10* (2), 2485–2490.

(165) Cottingham, P.; Brutchey, R. L. On the Crystal Structure of Colloidally Prepared $CsPbBr_3$ Quantum Dots. *Chem. Commun.* **2016**, *52* (30), 5246–5249.

(166) Kovalenko, M. V; Protesescu, L.; Bodnarchuk, M. I. Properties and Potential Optoelectronic Applications of Lead Halide Perovskite Nanocrystals. *Science* **2017**, *358*, 745–750.

(167) Wu, X.; Tan, L. Z.; Shen, X.; Hu, T.; Miyata, K.; Trinh, M. T.; Li, R.; Coffee, R.; Liu, S.; Egger, D. A.; et al. Light-Induced Picosecond Rotational Disordering of the Inorganic Sublattice in Hybrid Perovskites. *Sci. Adv.* **2017**, *3*, e1602388.

(168) Kirschner, M. S.; Hannah, D. C.; Diroll, B. T.; Zhang, X.; Wagner, M. J.; Hayes, D.; Chang, A. Y.; Rowland, C. E.; Lethiec, C. M.; Schatz, G. C.; et al. Transient Melting and Recrystallization of Semiconductor Nanocrystals under Multiple Electron-Hole Pair Excitation. *Nano Lett.* **2017**, *17* (9), 5315–5320.

(169) Chung, H.; Jung, S. Il; Kim, H. J.; Cha, W.; Sim, E.; Kim, D.; Koh, W. K.; Kim, J. Composition-Dependent Hot Carrier Relaxation Dynamics in Cesium Lead Halide (CsPbX3, X=Br and I) Perovskite Nanocrystals. *Angew. Chemie - Int. Ed.* **2017**, *56* (15), 4160–4164.

(170) Guo, P.; Xia, Y.; Gong, J.; Stoumpos, C. C.; McCall, K. M.; Alexander, G. C. B.; Ma, Z.; Zhou, H.; Gosztola, D. J.; Ketterson, J. B.; et al. Polar Fluctuations in Metal Halide Perovskites Uncovered by Acoustic Phonon Anomalies. *ACS Energy Lett.* **2017**, *2* (10), 2463–2469.

(171) Siders, C.; Cavalleri, A.; Sokolowski-Tinten, K. Direct Observation of Ultrafast Non-Thermal Melting by Ultrafast X-Ray Diffraction. *Science* **1999**, *286*, 1340–1343.

(172) Harb, M.; Ernstorfer, R.; Hebeisen, C. T.; Sciaini, G.; Peng, W.; Dartigalongue, T.; Eriksson, M. A.; Lagally, M. G.; Kruglik, S. G.; Miller, R. J. D. Electronically Driven Structure Changes of Si Captured by Femtosecond Electron Diffraction. *Phys. Rev. Lett.* **2008**, *100* (15), 1–4.

(173) Klimov, V. I.; McGuire, J. A.; Schaller, R. D.; Rupasov, V. I. Scaling of Multiexciton Lifetimes in Semiconductor Nanocrystals. *Phys. Rev. B* **2008**, *77* (19), 195324.

(174) Caruge, J. M.; Chan, Y.; Sundar, V.; Eisler, H. J.; Bawendi, M. G. Transient Photoluminescence and Simultaneous Amplified Spontaneous Emission from Multiexciton States in CdSe Quantum Dots. *Phys. Rev. B - Condens. Matter Mater. Phys.* **2004**, *70* (8), 1–7.

(175) Bonati, C.; Mohamed, M. B.; Tonti, D.; Zgrablic, G.; Haacke, S.; Mourik, F. Van; Chergui, M. Spectral and Dynamical Characterization of Multiexcitons in Colloidal CdSe Semiconductor Quantum Dots. *Phys. Rev. B* **2005**, *71*, 205317.

(176) Htoon, H.; Malko, A. V; Bussian, D.; Vela, J.; Chen, Y.; Hollingsworth, J. A.; Klimov, V. I. Highly Emissive Multiexcitons in Steady-State Photoluminescence of Individual " Giant " CdSe/CdS CoreShell Nanocrystals. *Nano Lett.* **2010**, *10*, 2401–2407.

(177) Robel, I.; Gresback, R.; Kortshagen, U.; Schaller, R. D.; Klimov, V. I. Universal Size-Dependent Trend in Auger Recombination in Direct-Gap and Indirect-Gap Semiconductor Nanocrystals. *Phys. Rev. Lett.* **2009**, *102* (17), 177404.

(178) Narendran, N.; Gu, Y. Life of LED-Based White Light Sources. *J. Disp. Technol.* **2005**, *1* (1), 167–171.

(179) Narayanaswamy, A.; Feiner, L. F.; Meijerink, A.; van der Zaag, P. J. The Effect of Temperature and Dot Size on the Spectral Properties of Colloidal InP/ZnS Core-Shell Quantum Dots. *ACS Nano* **2009**, *3* (9), 2539–2546.

(180) Rowland, C. E.; Schaller, R. D. Exciton Fate in Semiconductor Nanocrystals at Elevated Temperatures: Hole Trapping Outcompetes Exciton Deactivation. *J. Phys. Chem. C* **2013**, *117* (33), 17337–17343.

(181) Tyagi, P.; Kambhampati, P. False Multiple Exciton Recombination and Multiple Exciton Generation Signals in Semiconductor Quantum Dots Arise from Surface Charge Trapping.

J. Chem. Phys. **2011**, *094706*, 094706.

(182) Mooney, J.; Krause, M. M.; Kambhampati, P. Connecting the Dots: The Kinetics and Thermodynamics of Hot, Cold, and Surface-Trapped Excitons in Semiconductor Nanocrystals. *J. Phys. Chem. C* **2014**, *118*, 7730–7739.

(183) Hannah, D. C.; Brown, K. E.; Young, R. M.; Wasielewski, M. R.; Schatz, G. C.; Schaller, R. D. Direct Measurement of Lattice Dynamics and Optical Phonon Excitation in Semiconductor Nanocrystals Using Femtosecond Stimulated Raman Spectroscopy. *Phys. Rev. Lett.* **2013**, *111* (10), 107401.

(184) Murray, B. W. A.; Barnes, W. L. Plasmonic Materials. *Adv. Mater.* **2007**, *19*, 3771–3782.

(185) Stanley, R. Plasmonics in the Mid-Infrared. *Nat. Photonics* **2012**, *6*, 409–411.

(186) Knight, M. W.; King, N. S.; Liu, L.; Everitt, H. O.; Nordlander, P.; Halas, N. J. Aluminum for Plasmonics. *ACS Nano* **2014**, *8* (1), 834–840.

(187) Hartland, G. V. Coherent Vibrational Motion in Metal Particles : Determination of the Vibrational Amplitude and Excitation Mechanism. *J. Chem. Phys.* **2002**, *116* (18), 8048–8055.

(188) Link, S.; El-sayed, M. A. Spectral Properties and Relaxation Dynamics of Surface Plasmon Electronic Oscillations In. *J. Phys. Chem. B* **1999**, *103* (1), 8410–8426.

(189) Hu, M.; Chen, J.; Li, Z.; Au, L.; Hartland, G. V; Li, X.; Marquez, M.; Xia, Y. Gold Nanostructures : Engineering Their Plasmonic Properties for Biomedical Applications.

Chem. Soc. Rev. **2006**, *35*, 1084–1094.

(190) Bardhan, R.; Lal, S.; Joshi, A.; Halas, N. J. Theranostic Nanoshells: From Probe Design to Imaging and Treatment of Cancer. *Acc. Chem. Res.* **2011**, *44* (10), 936–946.

(191) Zhang, X.; Chen, Y. L.; Liu, R.; Tsai, D. P. Plasmonic Photocatalysis. *Reports Prog. Phys.* **2013**, *76*, 046401.

(192) Mukherjee, S.; Libisch, F.; Large, N.; Neumann, O.; Brown, L. V; Cheng, J.; Lassiter, J. B.; Carter, E. A.; Nordlander, P.; Halas, N. J. Hot Electrons Do the Impossible: Plasmon-Induced Dissociation of H2 on Au. *Nano Lett.* **2013**, *13*, 240–247.

(193) Liu, M.; Guyot-Sionnest, P. Mechanism of Silver(I)-Assisted Growth of Gold Nanorods and Bipyramids. *J. Phys. Chem. B* **2005**, *109* (47), 22192–22200.

(194) Lee, J. H.; Gibson, K. J.; Chen, G.; Weizmann, Y. Bipyramid-Templated Synthesis of Monodisperse Anisotropic Gold Nanocrystals. *Nat. Commun.* **2015**, *6*, 7571.

(195) Chateau, D.; Liotta, A.; Vadcard, F.; Navarro, J. R. G.; Chaput, F.; Lermé, J.; Lerouge, F.; Parola, S. From Gold Nanobipyramids to Nanojavelins for a Precise Tuning of the Plasmon Resonance to the Infrared Wavelengths: Experimental and Theoretical Aspects. *Nanoscale* **2015**, *7* (5), 1934–1943.

(196) Liu, M.; Guyot-Sionnest, P.; Lee, T. W.; Gray, S. K. Optical Properties of Rodlike and Bipyramidal Gold Nanoparticles from Three-Dimensional Computations. *Phys. Rev. B - Condens. Matter Mater. Phys.* **2007**, *76* (23), 1–10.

(197) Knunz, S.; Herrmann, M.; Batteiger, V.; Saathoff, G.; Hansch, T. W.; Vahala, K.; Udem, T. Injection Locking of a Trapped-Ion Phonon Laser. *Phys. Rev. Lett.* **2010**, *105*, 013004.

(198) Plech, a; Cerna, R.; Kotaidis, V.; Hudert, F.; Bartels, a; Dekorsy, T. A Surface Phase Transition of Supported Gold Nanoparticles. *Nano Lett.* **2007**, *7* (110), 1026–1031.

(199) Link, S.; Burda, C.; Mohamed, M. B.; Nikoobakht, B.; El-Sayed, M. A. Laser Photothermal Melting and Fragmentation of Gold Nanorods: Energy and Laser Pulse-Width Dependence. *J. Phys. Chem. A* **1999**, *103* (9), 1165–1170.

(200) Crut, A.; Juve, V.; Mongin, D.; Maioli, P.; Fatti, N. Del; Vallee, F. Vibrations of Spherical Core-Shell Nanoparticles. *Phys. Rev. B* **2011**, *83*, 205430.

(201) Johnson, P. B.; Christy, R. W. Optical Constants of Noble Metals. *Phys. Rev. B* **1972**, *6* (12), 4370–4379.

(202) Rosenwaks, S. *Vibrationally Mediated Photodissociation*; Royal Society of Chemistry, 2009.

(203) Likar, M. D.; Baggott, J. E.; Sinha, A.; Ticich, T. M.; Vander Wal, R. L.; Crim, F. F. Vibrationally Mediated Photodissociation. *J. Chem. Soc. Faraday Trans. 2 Mol. Chem. Phys.* **1988**, *84* (9), 1483–1497.

(204) Crim, F. F. Vibrationally Mediated Photodissociation: Exploring Excited-State Surfaces and Controlling Decomposition Pathways. *Annu. Rev. Phys. Chem.* **1993**, *44* (1), 397–428.

(205) Lin, Z.; Lawrence, C. M.; Xiao, D.; Kireev, V. V; Skourtis, S. S.; Sessler, J. L.; Beratan,

D. N.; Rubtsov, I. V. Modulating Unimolecular Charge Transfer by Exciting Bridge Vibrations. *J. Am. Chem. Soc.* **2009**, *131* (50), 18060–18062.

(206) Delor, M.; Scattergood, P. A.; Sazanovich, I. V; Parker, A. W.; Greetham, G. M.; Meijer, A. J. H. M.; Towrie, M.; Weinstein, J. A. Toward Control of Electron Transfer in Donor-Acceptor Molecules by Bond-Specific Infrared Excitation. *Science* **2014**, *346* (6216), 1492–1495.

(207) Delor, M.; Keane, T.; Scattergood, P. A.; Sazanovich, I. V; Greetham, G. M.; Towrie, M.; Meijer, A. J. H. M.; Weinstein, J. A. On the Mechanism of Vibrational Control of Light-Induced Charge Transfer in Donor–bridge–acceptor Assemblies. *Nat. Chem.* **2015**, *7* (9), 689.

(208) Bakulin, A. A.; Lovrincic, R.; Yu, X.; Selig, O.; Bakker, H. J.; Rezus, Y. L. A.; Cahen, D.; Nayak, P. K.; Fonari, A.; Coropceanu, V.; et al. Mode-Selective Vibrational Modulation of Charge Transport in Organic Electronic Devices. *Nat. Commun.* **2015**, *6*, 7880.

(209) Hartland, G. V; Hu, M.; Wilson, O. M.; Mulvaney, P.; Sader, J. E. Coherent Excitation of Vibrational Modes in Gold Nanorods. *J. Phys. Chem. B* **2002**, *106* (4), 743–747.

(210) Owrutsky, J. C.; Pomfret, M. B.; Brown, D. J. Coherent Acoustic Oscillations of Nanorods Composed of Various Metals. *J. Phys. Chem. B* **2009**, *113*, 10947–10955.

(211) Gouadec, G.; Colomban, P. Raman Spectroscopy of Nanostructures and Nanosized

Materials. *J. Raman Spectrosc.* **2007**, *38*, 598–603.

(212) Rolo, A. G.; Vasilevskiy, M. I. Raman Spectroscopy of Optical Phonons Confined in Semiconductor Quantum Dots and Nanocrystals. *J. Raman Spectrosc.* **2007**, *38* (April), 618–633.

(213) Yang, C. C.; Li, S. Size-Dependent Raman Red Shifts of Semiconductor Nanocrystals. *J. Phys. Chem. B* **2008**, *112*, 14193–14197.

(214) Hartland, G. V. Ultrafast Studies of Single Semiconductor and Metal Nanostructures through Transient Absorption Microscopy. *Chem. Sci.* **2010**, *1*, 303–309.

(215) Ruijgrok, P. V.; Zijlstra, P.; Tchebotareva, A. L.; Orrit, M. Damping of Acoustic Vibrations of Single Gold Nanoparticles Optically Trapped in Water. *Nano Lett.* **2012**, *12* (2), 1063–1069.

(216) Kirschner, M. S.; Lethiec, C. M.; Lin, X.; Schatz, G. C.; Chen, L. X.; Schaller, R. D. Size-Dependent Coherent-Phonon Plasmon Modulation and Deformation Characterization in Gold Bipyramids and Nanojavelins. *ACS Photonics* **2016**, *3*, 758–763.

(217) Luk'Yanchuk, B.; Zheludev, N. I.; Maier, S. A.; Halas, N. J.; Nordlander, P.; Giessen, H.; Chong, C. T. The Fano Resonance in Plasmonic Nanostructures and Metamaterials. *Nat. Mater.* **2010**, *9* (9), 707–715.

(218) Halas, N. J.; Lal, S.; Chang, W. S.; Link, S.; Nordlander, P. Plasmons in Strongly Coupled Metallic Nanostructures. *Chem. Rev.* **2011**, *111* (6), 3913–3961.

(219) Fofang, N. T.; Park, T.; Neumann, O.; Mirin, N. A.; Nordlander, P.; Halas, N. J. Plexcitonic Nanoparticles : Plasmon - Exciton Coupling in Nanoshell - J-Aggregate Complexes. *Nano Lett.* **2008**, *8* (10), 3481–3487.

(220) Fofang, N. T.; Grady, N. K.; Fan, Z.; Govorov, A. O.; Halas, N. J. Plexciton Dynamics : Exciton-Plasmon Coupling in a J-Aggregate-Au Nanoshell Complex Provides a Mechanism for Nonlinearity. *Nano Lett.* **2011**, *11*, 1556–1560.

(221) Schlather, A. E.; Large, N.; Urban, A. S.; Nordlander, P.; Halas, N. J. Near-Field Mediated Plexcitonic Coupling and Giant Rabi Splitting in Individual Metallic Dimers. *Nano Lett.* **2013**, *13*, 3281–3286.

(222) Vasa, P.; Wang, W.; Pomraenke, R.; Maiuri, M.; Manzoni, C.; Cerullo, G.; Lienau, C. Optical Stark Effects in J -Aggregate – Metal Hybrid Nanostructures Exhibiting a Strong Exciton – Surface-Plasmon-Polariton Interaction. *Phys. Rev. Lett.* **2015**, *114*, 036802.

(223) Wiederrecht, G. P.; Wurtz, G. A.; Hranisavljevic, J. Coherent Coupling of Molecular Excitons to Electronic Polarizations of Noble Metal Nanoparticles. *Nano Lett.* **2004**, *4* (11), 2121–2125.

(224) Mante, P.-A.; Chen, H.-Y.; Lin, M.-H.; Wen, Y.-C.; Gwo, S.; Sun, C.-K. Selectively Probing Vibrations in a Plasmonic Supracrystal. *Appl. Phys. Lett.* **2014**, *101*, 101903.

(225) Ruello, P.; Ayouch, A.; Vaudel, G.; Pezeril, T.; Delorme, N.; Sato, S.; Kimura, K.; Gusev, V. E. Ultrafast Acousto-Plasmonics in Gold Nanoparticle Superlattices. *Phys. Rev. B* -

Condens. Matter Mater. Phys. **2015**, *92* (17), 174304.

(226) Rudin, S.; Reinecke, T. L. Oscillator Model for Vacuum Rabi Splitting in Microcavities. *Phys. Rev. B - Condens. Matter Mater. Phys.* **1999**, *59* (15), 10227–10233.

(227) Heylman, K. D.; Thakkar, N.; Horak, E. H.; Quillin, S. C.; Cherqui, C.; Knapper, K. A.; Masiello, D. J.; Goldsmith, R. H. Optical Microresonators as Single-Particle Absorption Spectrometers. *Nat. Photonics* **2016**, *10* (12), 788–795.

(228) Oughstun, K. E.; Cartwright, N. A. On the Lorentz-Lorenz Formula and the Lorentz Model of Dielectric Dispersion. *Opt. Express* **2003**, *11* (13), 1541–1546.

(229) Cacciola, A.; Triolo, C.; Di Stefano, O.; Genco, A.; Mazzeo, M.; Saija, R.; Patanè, S.; Savasta, S. Subdiffraction Light Concentration by J-Aggregate Nanostructures. *ACS Photonics* **2015**, *2* (7), 971–979.

(230) Chaste, J.; Eichler, A.; Moser, J.; Ceballos, G.; Rurali, R.; Bachtold, A. A Nanomechanical Mass Sensor with Yoctogram Resolution. *Nat. Nanotechnol.* **2012**, *7* (5), 301–304.

(231) Kirschner, M. S.; Ding, W.; Li, Y.; Chapman, C. T.; Lei, A.; Lin, X.; Chen, L. X.; Schatz, G. C.; Schaller, R. D. Phonon-Driven Oscillatory Plasmonic Excitonic Nanomaterials. *Nano Lett.* **2018**, *18*, 442–448.

(232) Hu, M.; Wang, X.; Hartland, G. V; Mulvaney, P.; Juste, J. P.; Sader, J. E. Vibrational Response of Nanorods to Ultrafast Laser Induced Heating : Theoretical and Experimental

Analysis. *J. Am. Chem. Soc.* **2003**, *125* (48), 14925–14933.

(233) Yu, K.; Zijlstra, P.; Sader, J. E.; Xu, Q.; Orrit, M. Damping of Acoustic Vibrations of Immobilized Single Gold Nanorods in Different Environments. *Nano Lett.* **2013**, *13* (6), 2710–2716.

(234) Polli, D.; Antognazza, M. R.; Brida, D.; Lanzani, G.; Cerullo, G.; Silvestri, S. De. Broadband Pump-Probe Spectroscopy with Sub-10-Fs Resolution for Probing Ultrafast Internal Conversion and Coherent Phonons in Carotenoids. *Chem. Phys.* **2008**, *350*, 45–55.

(235) Liebel, M.; Kukura, P. Broad-Band Impulsive Vibrational Spectroscopy of Excited Electronic States in the Time Domain. *J. Phys. Chem. Lett.* **2013**, *4*, 1358–1364.

(236) Arpin, P. C.; Turner, D. B.; Mcclure, S. D.; Jumper, C. C.; Mirkovic, T.; Challa, J. R.; Lee, J.; Teng, C. Y.; Green, B. R.; Wilk, K. E.; et al. Spectroscopic Studies of Cryptophyte Light Harvesting Proteins : Vibrations and Coherent Oscillations. *J. Phys. Chem. B* **2015**, *119*, 10025–10034.

(237) Mcclure, S. D.; Turner, D. B.; Arpin, P. C.; Mirkovic, T.; Scholes, G. D. Coherent Oscillations in the PC577 Cryptophyte Antenna Occur in the Excited Electronic State. *J. Phys. Chem. B* **2014**, *118*, 1296–1308.

(238) Liebel, M.; Schnedermann, C.; Wende, T.; Kukura, P. Principles and Applications of Broadband Impulsive Vibrational Spectroscopy. *J. Phys. Chem. A* **2015**.

(239) Ruetzel, S.; Diekmann, M.; Nuernberger, P.; Walter, C.; Engels, B.; Brixner, T. Photoisomerization among Ring-Open Merocyanines . I . Reaction Dynamics and Wave-Packet Oscillations Induced by Tunable Femtosecond Pulses and Wave-Packet Oscillations Induced by Tunable Femtosecond Pulses. *J. Chem. Phys.* **2014**, *140* (22), 224310.

(240) Kim, P.; Kelley, M. S.; Chakraborty, A.; Wong, N. L.; Duyne, R. P. Van; Schatz, G. C.; Castellano, F. N.; Chen, L. X. Coherent Vibrational Wavepacket Dynamics in Platinum(II) Dimers and Their Implications. *J. Phys. Chem. C* **2018**, *122*, 14195–14204.

(241) van Stokkum, I. H. M.; Jumper, C. C.; Snellenburg, J. J.; Scholes, G. D.; Van Grondelle, R.; Maly, P. Estimation of Damped Oscillation Associated Spectra from Ultrafast Transient Absorption Spectra. *J. Chem. Phys.* **2016**, *145*, 174201.

(242) Lin, Y.; Hodgkinson, P.; Ernst, M.; Pines, A. A Novel Detection – Estimation Scheme for Noisy NMR Signals : Applications to Delayed Acquisition Data. *J. Magn. Reson.* **1997**, *41* (128), 30–41.

(243) Bonneau, R.; Wirz, J.; Zuberbühler, A. D. Methods for the Analysis of Transient Absorbance Data. *Pure Appl. Chem.* **1997**, *69*, 979.

(244) Dioumaev, A. K. Evaluation of Intrinsic Chemical Kinetics and Transient Product Spectra from Time-Resolved Spectroscopic Data. *Biophys. Chem.* **1997**, *67* (714), 1–25.

(245) Nagle, J. F. Solving Complex Photocycle Kinetics. *Biophys. J.* **1991**, *59* (2), 476–487.

(246) Lindenberg, A. M. Atomic-Scale Visualization of Inertial Dynamics. *Science* **2005**, *308* (5720), 392–395.

(247) Juvé, V.; Scardamaglia, M.; Maioli, P.; Crut, A.; Merabia, S.; Joly, L.; Fatti, N. Del. Cooling Dynamics and Thermal Interface Resistance of Glass-Embedded Metal Nanoparticles. *Phys. Rev. B* **2009**, *80*, 195406.

(248) Hernandez-Calderon, I. Optoelectronic Properties of Semiconductors and Superlattices. *Opt. Prop. Electron. Struct. Wide Band Gap II-VI Semicond. Ed. by MC Tamargo (Taylor Fr. New York, 2002)* **2002**, *12*.

(249) Salman, A. Al; Tortschanoff, A.; Mohamed, M. B.; Tonti, D.; Mourik, F. Van; Chergui, M.; Salman, A. Al; Tortschanoff, A.; Mohamed, M. B.; Tonti, D.; et al. Temperature Effects on the Spectral Properties of Colloidal CdSe Nanodots , Nanorods , and Tetrapods Temperature Effects on the Spectral Properties of Colloidal CdSe Nanodots , Nanorods , and Tetrapods. **2015**, *093104* (2007), 21–24.

(250) Yan, Y.; Liao, Z. M.; Bie, Y. Q.; Wu, H. C.; Zhou, Y. B.; Fu, X. W.; Yu, D. P. Luminescence Blue-Shift of CdSe Nanowires beyond the Quantum Confinement Regime. *Appl. Phys. Lett.* **2011**, *99*, 103103.

(251) Lunz, U.; Kuhn, J.; Goschenhofer, F.; Schüssler, U.; Einfeldt, S.; Becker, C. R.; Landwehr, G. Temperature Dependence of the Energy Gap of Zinc-Blende CdSe and Cd1 − x Zn x Se Epitaxial Layers. *J. Appl. Phys.* **1996**, *80*, 6861.

(252) Kaneta, A.; Adachi, S. Photoreflectance Study of Hexagonal CdSe. *J. Phys. Chem. Lett.* **1999**, *32*, 2337–2341.

(253) Shan, W.; Song, J. J.; Luo, H.; Furdyna, J. K. Determination of the Fundamental and Split-off Band Gaps in Zinc-Blende CdSe by Photomodulation Spectroscopy. *Phys. Rev. B* **1994**, *50* (11), 8012–8015.

APPENDIX A: SUPPORTING INFORMATION FOR TRANSIENT MELTING AND RECRYSTALLIZATION OF SEMICONDUCTOR NANOCRYSTALS UNDER MULTIPLE ELECTRON–HOLE PAIR EXCITATION

A.1. Accounting for Irreversible Sample Degradation

Under high intensity laser illumination, CdSe nanocrystals (NCs) undergo both reversible and irreversible loss of X-ray scattering intensity. Some of this irreversible process occurs over the course of real-time signal averaging at any given time point, resulting in the convolution of these irreversible and reversible effects. To account for this phenomenon, diffraction patterns taken during different scans at the same time delay were compared. The equations used are as follows,

$$d_{i,j}(Q) = \frac{1}{n}\sum_{i=1}^{n} S_{i,j+1}(Q) - S_{i,j}(Q) \qquad \text{(A.1)}$$

$$\bar{d}_j(Q) = \frac{1}{n}\sum_{i=1}^{n} d_{i,j}(Q) \qquad \text{(A.2)}$$

$$\Delta S_{i,j}(Q) = S_{i,j}(Q) - S_{1,j}(Q) - (i-1) * \bar{d}_j(Q) \qquad \text{(A.3)}$$

where $S_{i,j}$ is scattering intensity for the *i*th time point in the *j*th scan, there are a total of *n* time points in a scan, d_j is the average irreversible loss that occurs over scan *j*, and the first time point (*i*=1) is a measurement before laser excitation (i.e. negative pump-probe delay time). For the final scan, the value of *d* taken from the penultimate scan were used. An assumption of this type of analysis is that loss is locally linear with time. Evidence of the validity of this assumption is in the small variation observed in $d_{i,j}$ between different scans and time points (see Figure A.1). However, these are measurements of the average change that occurs over roughly twenty minutes. It seems

likely that while the average value is constant, there are significant changes that occur on the timescale of seconds or minutes, which corresponds to the rate at which individual measurements are taken. Therefore, accounting for this irreversible loss, while necessary, results in short term, random variations having the structure of the lost XRD signal. The main degradation mechanism of the samples seems to be loss of dispersibility of the particles in solvent, likely owing to ligand loss since electron microscopy of the optically degraded material still showed primarily crystalline, distinct particles of similar size and shape.

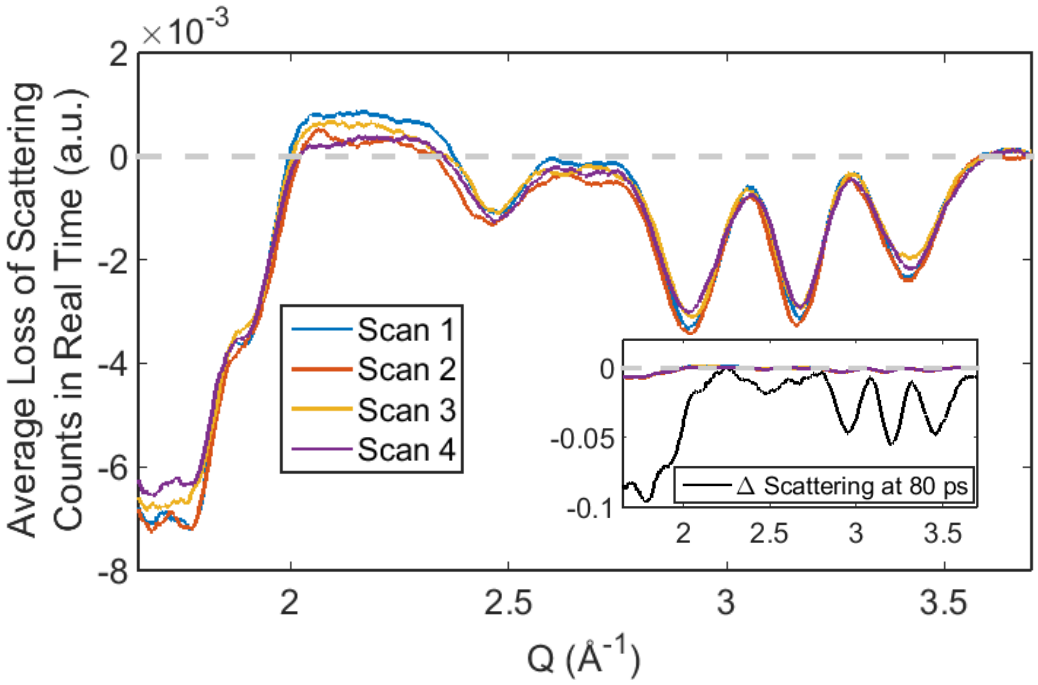

Figure A.1. Average sample degradation between scans ($\overline{d_j}(Q)$) for 2.0-nm radius NCs excited at 24 mJ/cm^2 with an inset of Δ Scattering 80 ps after photoexcitation to indicate the magnitude of the sample degradation.

A.2. Debye-Waller Effect

The percent scattering change observed experimentally is consistent across the Q-range examined (Figure A.2) suggesting that Debye-Waller effects do not significantly impact interpretation of decreased amplitude in Bragg peaks as resulting from melting.[246]

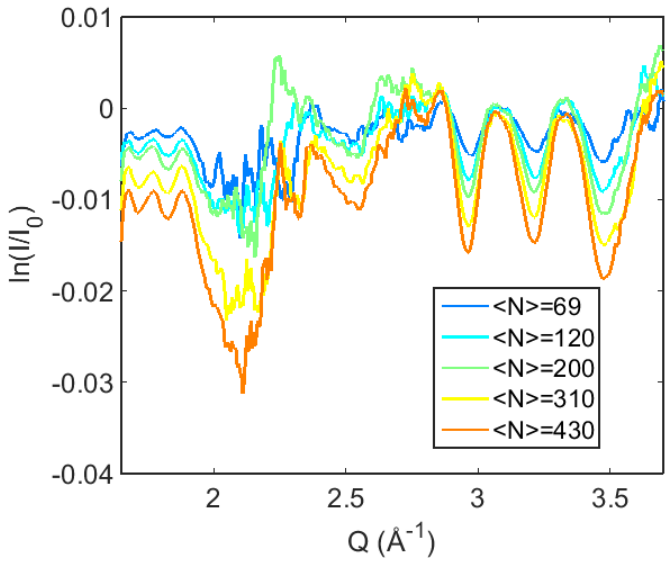

Figure A.2. Natural log of observed scattering intensity (I) over static scattering intensity (I_0) vs Q for 3.8-nm radius NCs for a range of fluences where melting is present.

A.3. Fitting Dynamics

To characterize the TR-XRD dynamics, data ranging from 80 ps to 1 ns was fit to a single exponential decay,

$$\int \Delta S(Q,t)dQ = \alpha e^{-t/\tau} + \beta \qquad \text{(A.4)}$$

where α is the magnitude of the loss of signal, τ is the recovery lifetime, and β is an offset. Since smaller crystals have broader peaks, the exact bounds of the integral varied from sample to sample. However, in all cases, only the [110], [103], and [112] peaks were considered, and they were integrated separately; areas between the three peaks were not integrated to reduce noise. To emphasize the differences in life times in Figure 3.3, the data is normalized such that the peak area at t=80 ps was unity and β was 0. The decision to set β to 0 is nontrivial. My principle concern was that it is easy to visually conflate an apparent non-zero, long lived signal with a longer lifetime. Further, the value of β could be misleading. The inherent noise in X-ray experiments, as well as problems introduced when accounting for irreversible damage makes it difficult to assess if apparent signals at longer times (>5 ns) are real, noise, or artifacts. Understanding processes that occur on this timescale could be a valuable future study, but the data in Chapter 3 is of insufficient quality to make any reasonable conclusions about it. Therefore, this normalization makes sense as it clarifies meaningful data at the cost of not displaying potentially spurious results.

We fit the data for each independent scan, and the values obtained from the fits are given in Table A.1. The mean τ is the reported value with the standard deviation as the reported range. The specific data displayed in Figure 3.2 are the mean data points with plots of the fits to the means.

Sample/Fluence Information			Average of Scans		Average Scan	
Particle Radius (nm)	Fluence (mJ/cm^2)	<N>	τ (ps)	Standard Deviation (ps)	τ (ps)	95% Confidence Interval (ps)
1.5	24	27	75.2	91.1	60.1	37.7
2.0	17	42	153	149	88.4	61.8
2.0	24	59	180	163	155	132
2.0	33	80	129	53	127	137
3.8	0.67	12	255	117	214	62
3.8	24	430	369	237	281	271

Table A.1. Constants derived are shown for the additional excitation fluences where average of scans are the average values and standard deviations for each of the scans fit independently, and average scan is the value and confidence interval of the fit when each data point fit is the average value at that certain time delay across the scans.

A.4. Continuum Theory

Using analysis consistent with what is described in Juve *et al.*,[247] NC cooling was modeled. While the calculated cooling process is not purely exponential, it was fit to a single exponential to compare it to what was observed experimentally. The time constants for 1.5 nm, 2.0 nm, and 3.8 nm radius NCs were found to be 15 ps, 22 ps, and 52 ps respectively.

A.5. Determination of Fluence-Dependent Melting Threshold

When measuring the power dependence, in addition to taking data points at negative delay times, scattering at long times was measured where the reversible melting was negligible (5 ns and 0.1 μs). However, there was often apparent signal, either positive or negative, owing to noise. Based on these data points a Gaussian distribution of noise was constructed, the validity of which was confirmed using a chi-squared test with a significance level of 10%. A one-tailed p-test was then performed on the data from 80 ps after photoexcitation, and the threshold was defined when the null hypothesis that the data could be explained by the noise distribution was rejected at the 10% significance level.

A.6. Varshni Equation

The well-known Varshni equation is written:

$$E_g = E_{g0} - \frac{AT^2}{B+T} \qquad \text{(A.5)}$$

Where E_g is the bandgap, T is temperature, E_{g0} is the bandgap at T=0, and A and B are material specific constants. In this analysis, E_{g0} was taken from the AIMD calculations and A and B from literature.[248–253] However, there is some controversy as to the precise values of these constants. This analysis considered a variety of reported values and found bandgap closures that ranged from 440 meV to 950 meV. Notably, Varshni parameters for CdSe nanoparticles[249,250] resulted in smaller changes in the bandgap , but given the surprising nature of these results, in the text the

most conservative estimate available is used with parameters from Hernández-Calderón.[248] The important result, however, is that in all cases, the calculated bandgap closure was more than a factor of 2 lower than the value calculated from AIMD, providing strong evidence of effects from NC melting.

APPENDIX B: SUPPORTING INFORMATION FOR PHOTOINDUCED, REVERSIBLE PHASE TRANSITIONS IN ALL-INORGANIC PEROVSKITE NANOCRYSTALS

B.1. Debye Waller Factors.

Measured changes in diffraction patterns do not match a Debye-Waller like dependence, that is

$$I(Q,t) \propto \exp\left(-\frac{1}{3}Q^2\langle u_{RMS}^2(t)\rangle\right) \qquad \text{(B.1)}$$

where I is the scattering intensity and $\langle u_{RMS}^2(t)\rangle$ is a time-dependent mean square displacement of the atoms[103,167,246]. If this were the case, there would be a linear relationship between -ln(I/I_0) and Q^2 (with I_0 being the static diffraction intensity) which is not observed as shown in Supplementary Figure B.1. This may be caused by the phase transition changing the relative intensities of the diffraction peaks.

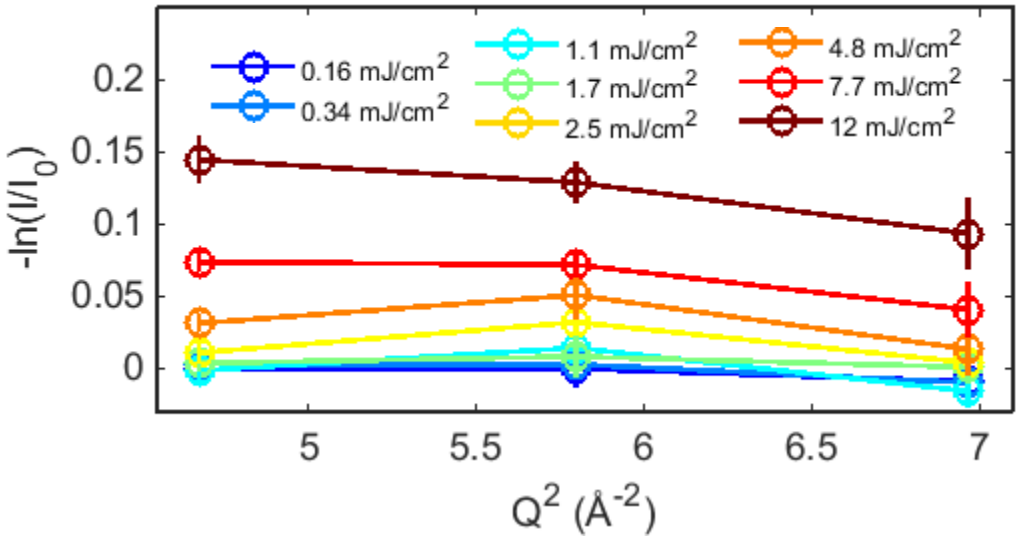

Figure B.1. The negative logarithm of scattering intensity 40 ps following photoexcitation over static scattering intensity *vs* Q^2 for a range of photoexcitation fluences. Error bars represent standard deviation in the measurements.

B.2. Hysteresis during Temperature-Dependent XRD Measurements.

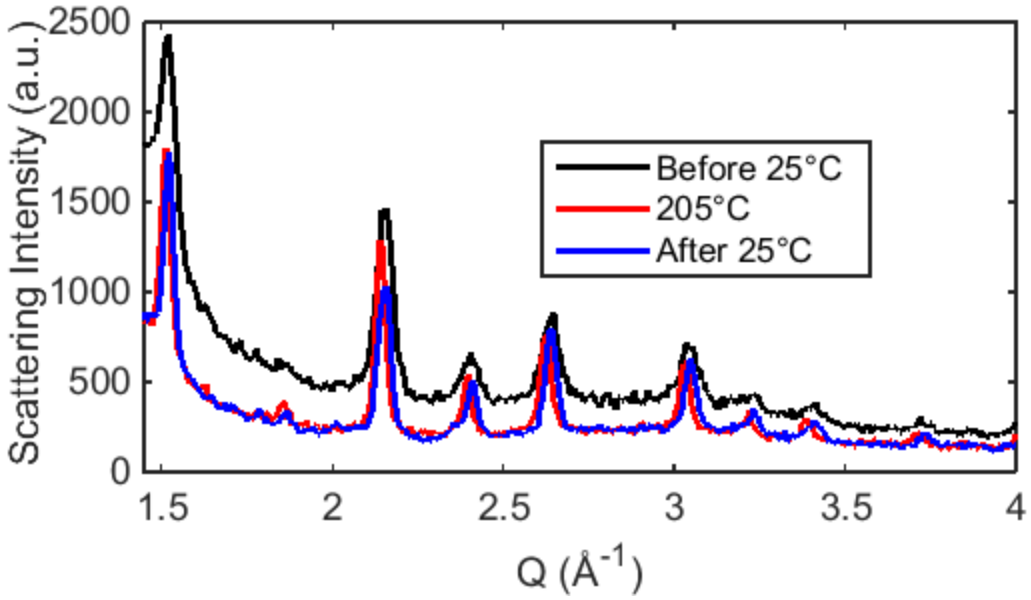

Figure B.2. XRD measurements of $CsPbBr_3$ NCs before (black) and after (blue) temperature-dependent XRD measurements, as well as the XRD pattern at the maximum temperature examined (red).

B.3. Consistency across Lattice Planes

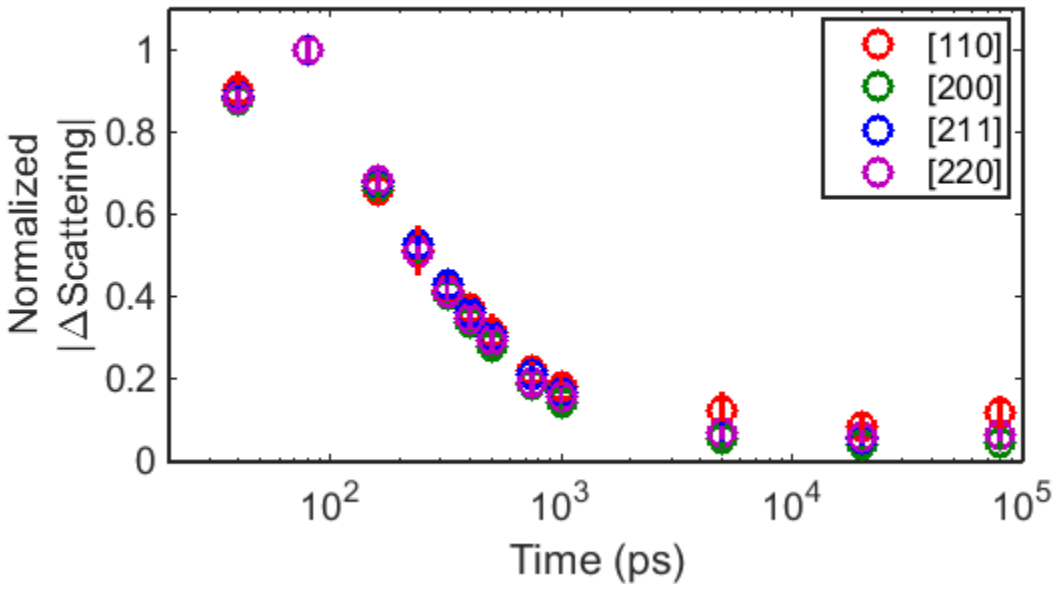

Figure B.3. Normalized |ΔScattering| for $CsPbBr_3$ NCs following photoexcitation at 4.8 mJ/cm^2 examined across the four examined diffraction peaks. Error bars represent standard deviations in the measurements.

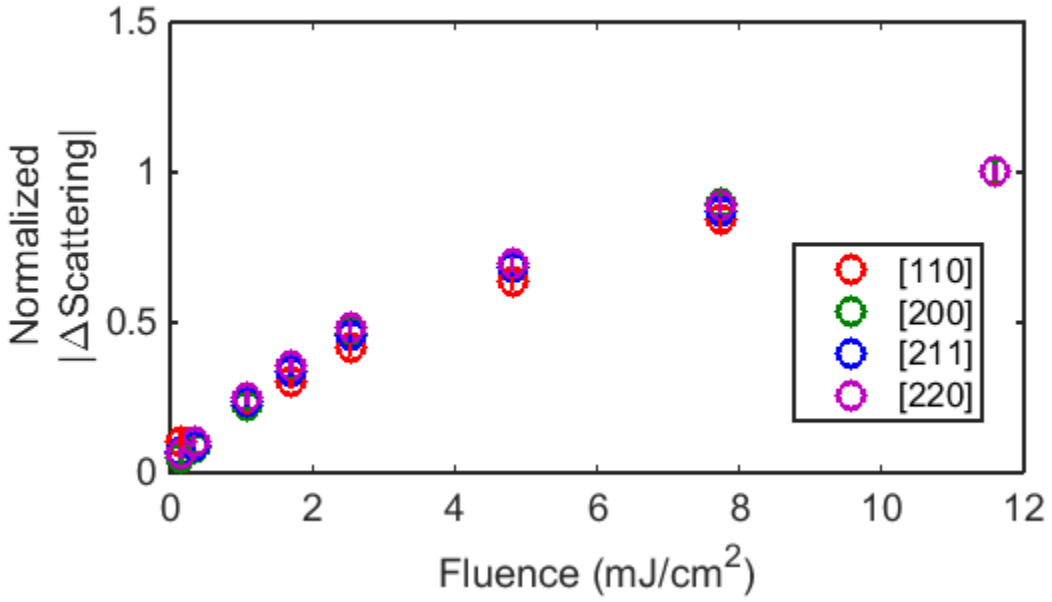

Figure B.4. Normalized |ΔScattering| for $CsPbBr_3$ NCs 40 ps following photoexcitation at a range of fluences examined across the four examined diffraction peaks. Error bars represent standard deviations in the measurements.

B.4. Consistency across Fluence

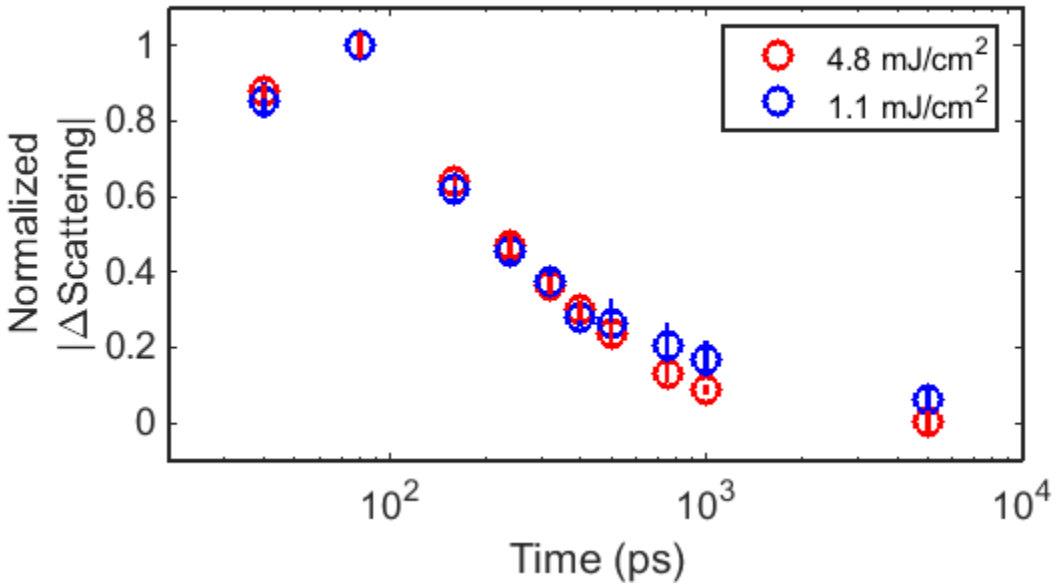

Figure B.5. Normalized |ΔScattering| for $CsPbBr_3$ NCs following photoexcitation at 1.1 mJ/cm^2 and 4.8 mJ/cm^2. Error bars represent standard deviations in the measurements.

B.5. Diffraction Peak Narrowing in the Cubic Phase.

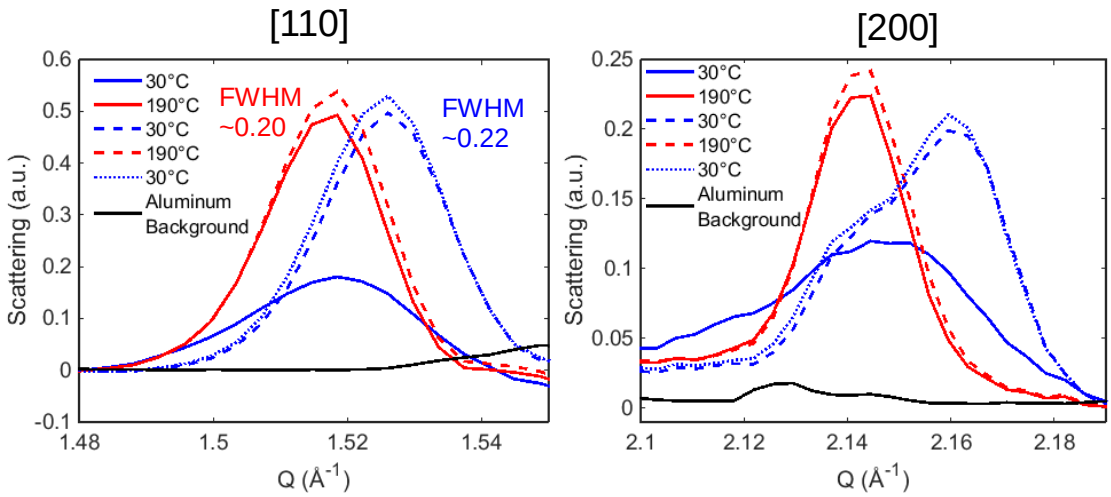

Figure B.6. Temperature-dependent XRD measurements of the [110] and [200] peaks of $CsPbBr_3$ NCs in a polymer matrix collected at Sector 5 at the Advanced Photon Source. The NCs started at 30°C and then were ramped up to 190°C (solid), back down to 30°C and then ramped up to 190°C (dashed), and then back down to 30°C. While there is an irreversible process occurring during the first increase in temperature, the [110] and [200] peaks are narrower at 190°C where the cubic phase is present. The pattern from the Al crucible is included (black) and was subtracted away from the displayed patterns.

B.6. Normalized TR-XRD Patterns Following Photoexcitation.

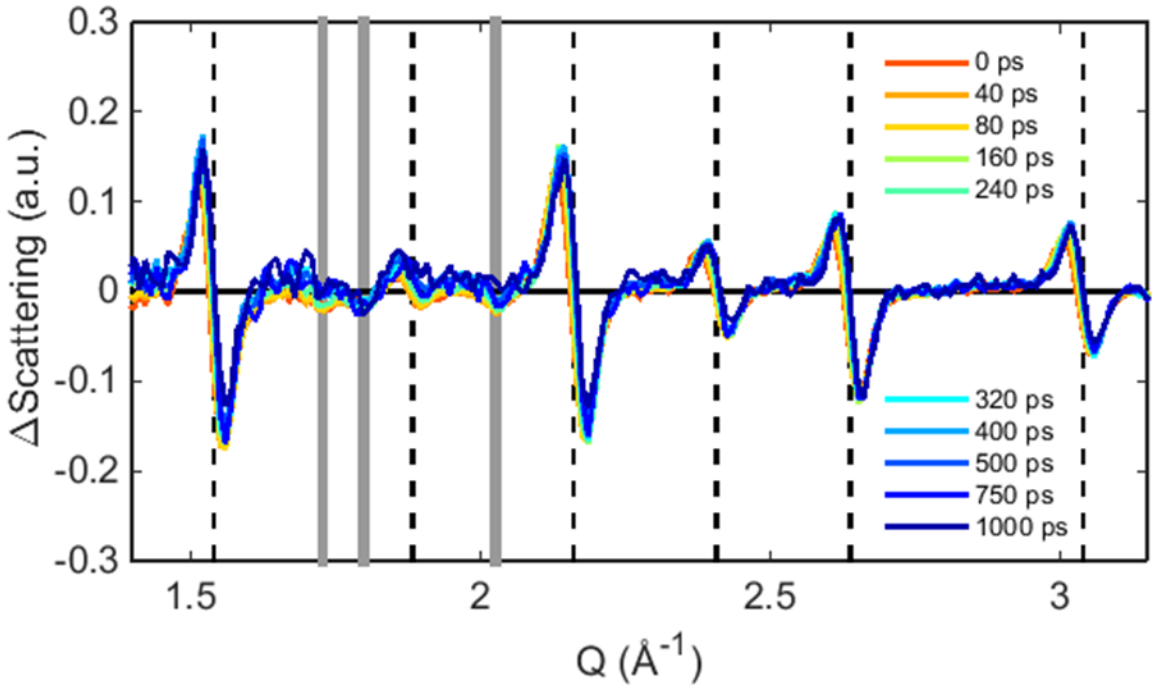

Figure B.7. Normalized TR-XRD pattern of $CsPbBr_3$ NCs at various times following excitation at 4.8 mJ/cm^2. The orthorhombic peaks are delineated with gray solid lines and the high-symmetry black dashed. A solid black line also denotes ΔScattering=0. The pattern is normalized by dividing by the |ΔScattering|. Notably, the orthorhombic peaks do not change significantly in time.

B.7. Consistency between |ΔScattering| and Percent Peak Loss.

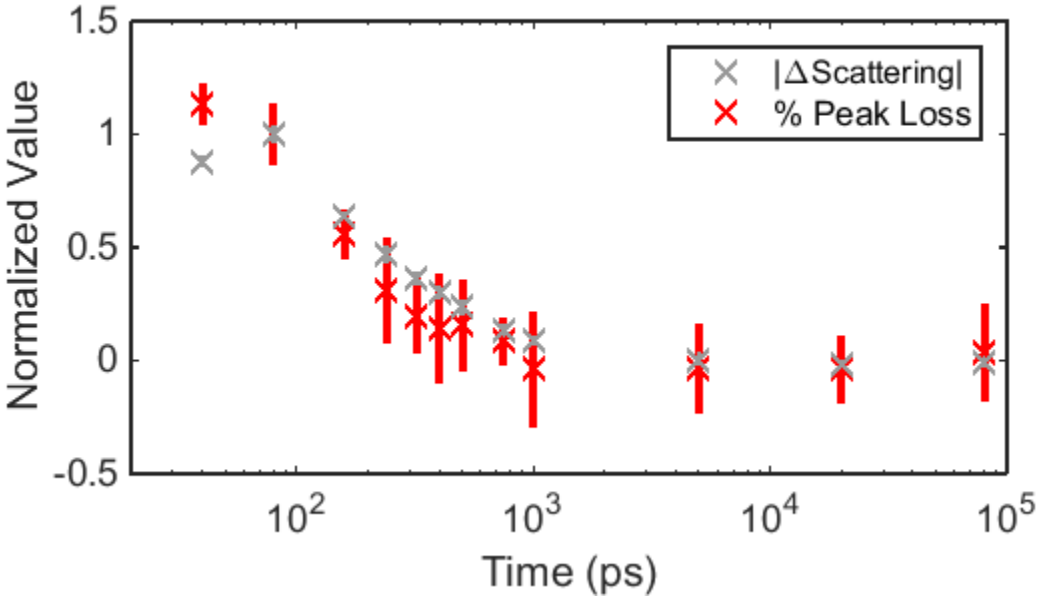

Figure B.8. Normalized |ΔScattering| and Percent Peak Loss for $CsPbBr_3$ NCs photoexcited at 4.8 mJ cm^{-2}. Error bars represent standard deviations in the measurements.

B.8. Relative Peak Width vs Fluence.

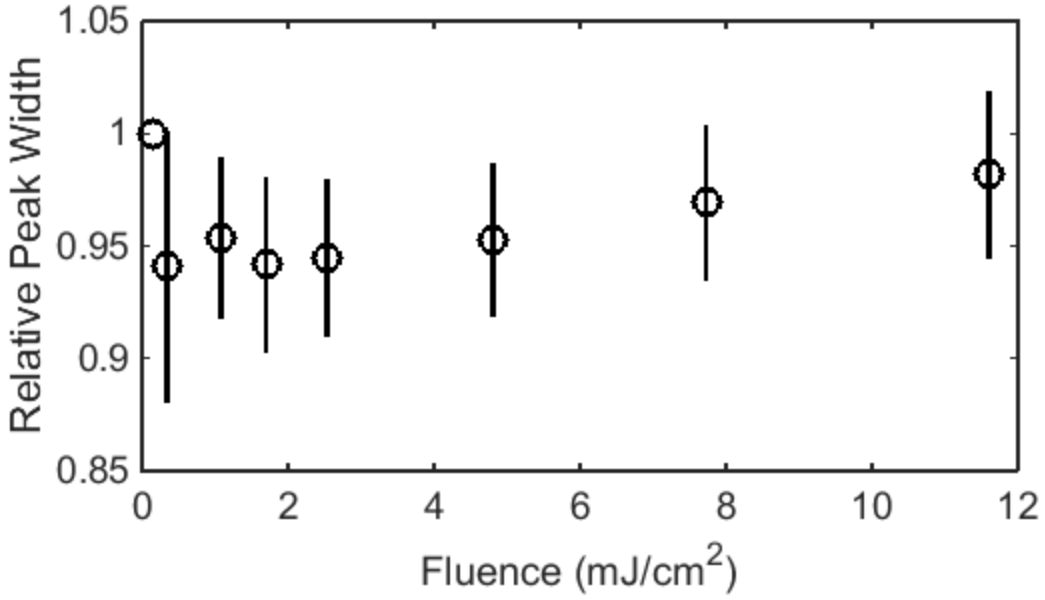

Figure B.9. Relative peak width for $CsPbBr_3$ NCs 40 ps following photoexcitation at a range of fluences. Error bars represent 95% confidence intervals in the fitting algorithm.

APPENDIX C: SUPPORTING INFORMATION FOR OPTICAL SIGNATURES OF TRANSIENTLY DISORDERED SEMICONDUCTOR NANOCRYSTALS

C.1. Effects of Pump 1 Fluence

As demonstrated in Figure C.1, the 2pTA spectrum doesn't change significantly with increasing pump 1 fluence. However, as demonstrated in Figure C.2, pump 1 fluence significantly impacts the magnitude of the early bleach features.

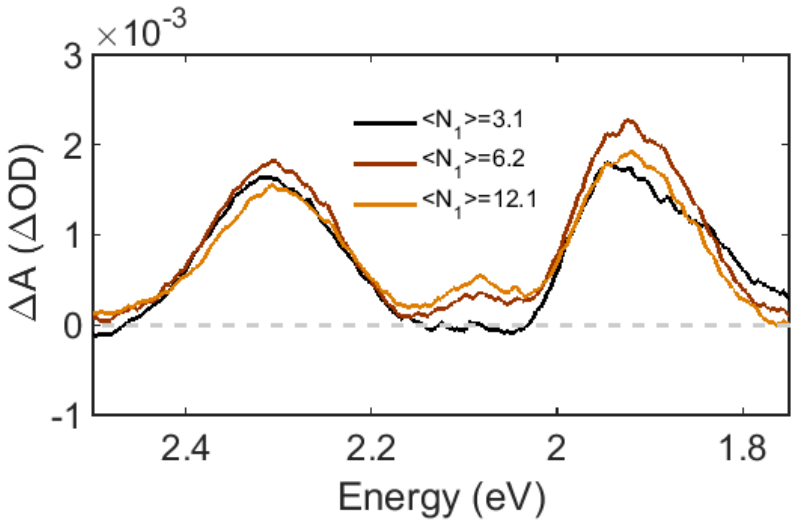

Figure C.1. 2pTA spectra of R=4.0 nm NCs 150 ps after photoexcitation at a fluence of <N>=97.

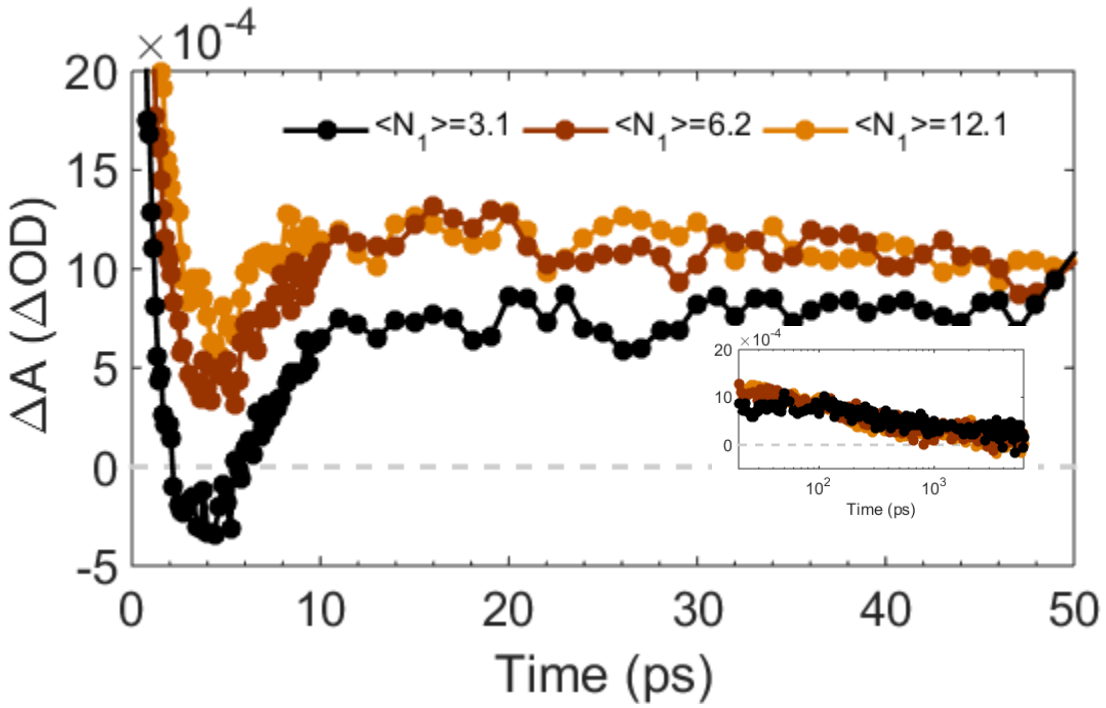

Figure C.2. Early time kinetics of R=4.0 nm NCs as a function of pump 1 fluence, with $\langle N_2 \rangle$=97, along with fits. Inset: Kinetics from 20 ps to 6 ns. Here, $\langle N_1 \rangle$ relates average number of excitons per NC created by pump 1.

C.2. Melting Threshold Calculation

The melting onset was determined by fitting the data to a piecewise linear function of the form:

$$f(x) = a_2 x + b_2 \; for \; x > \frac{(b_2 - b1)}{(a_1 - a_{2)}} \qquad \text{(C.1)}$$

$$f(x) = a_1 x + b_1 \;\; for \; \frac{(b_2 - b1)}{(a_1 - a_2)} \geq x \geq -\frac{b1}{a_1} \qquad \text{(C.2)}$$

$$f(x) = 0 \; for \; -\frac{b1}{a_1} > x \qquad \text{(C.3)}$$

with the threshold defined by $\frac{(b_2-b1)}{(a_1-a_{2)}}$. Using this method, the various thresholds are displayed in Table C.1.

Size	Threshold (Excitons)	Volume Normalized Threshold (Excitons/nm^3)
R=1.3 nm	1.4	0.149
R=2.0 nm	10	0.321
R=2.9 nm	20.	0.199
R=4.0 nm	79	0.322
Average		0.169

Table C.1. Melting Thresholds for NCs.

C.3. Additional Information About the Kinetic Fits

The spectra of the pre-exponential factors for the R=1.3 nm and R=2.9 nm samples are included in Figures C.3 and C.4 and the lifetimes of the various fits are included in Table C.2. Additionally, the same information for the R=4.0 as a function of pump 1 and pump 2 fluence are included as Figures C.5-C.9 and Table C.4.

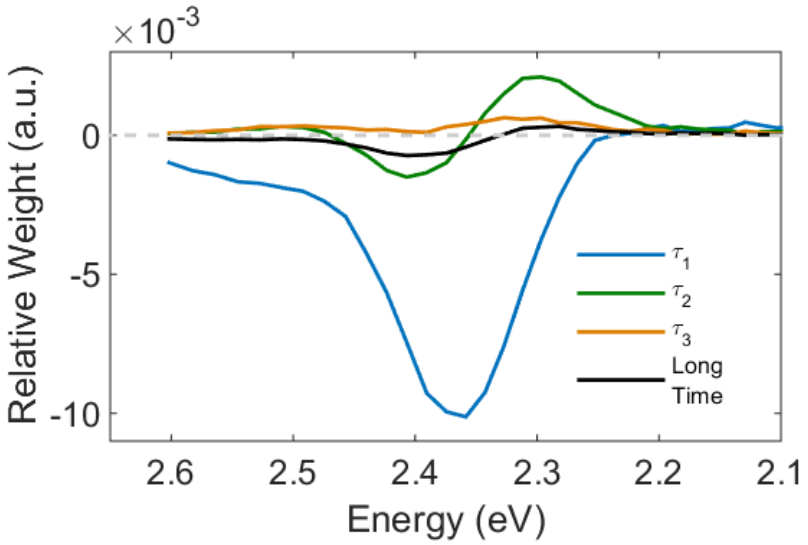

Figure C.3. Pre-exponential factors from the global fit of R=1.3 nm NCs.

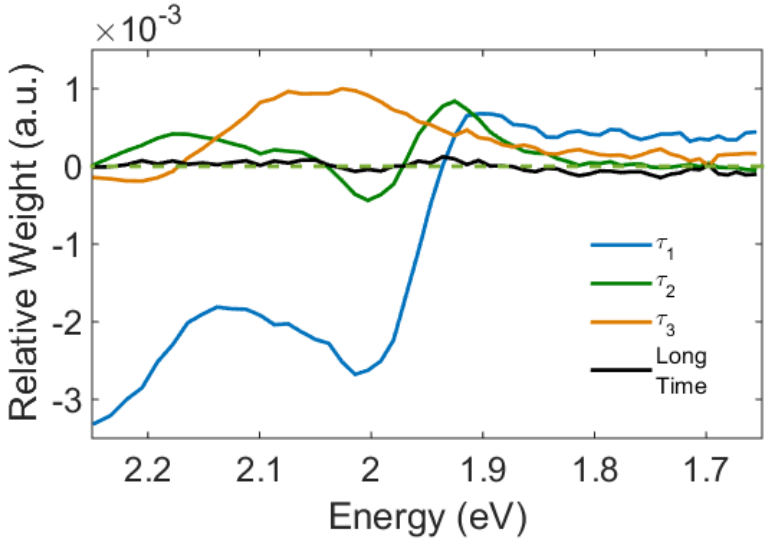

Figure C.4. Pre-exponential factors from the global fit of R=2.9 nm NCs.

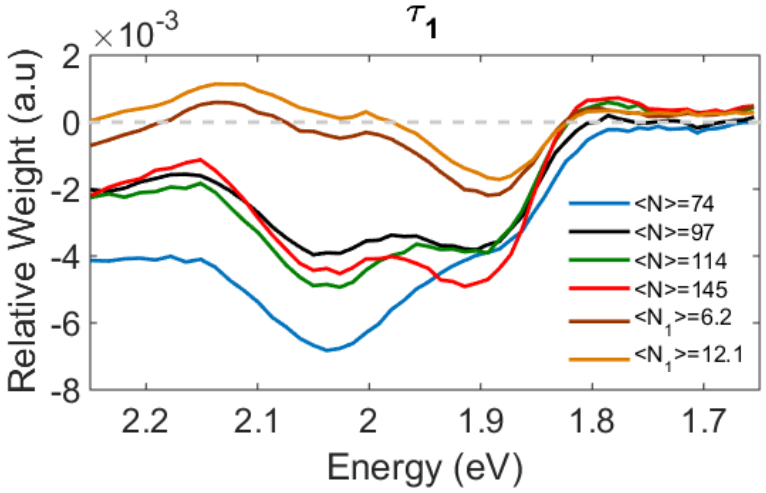

Figure C.5. Kinetics of R=4.0 nm NCs as a function of fluence. The main figure shows the first 20 ps and the inset shows data out to 6 ns along with fits (solid lines).

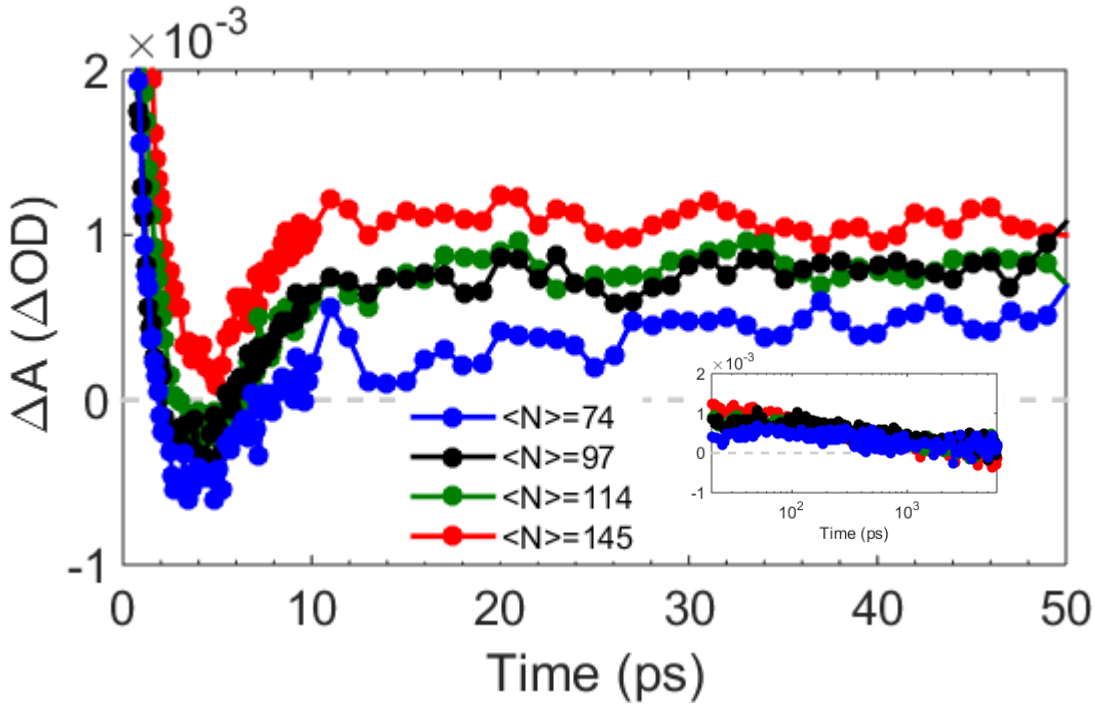

Figure C.6. Pre-exponential factors for the τ_1 components of the global fits of R=4.0 nm NCs.

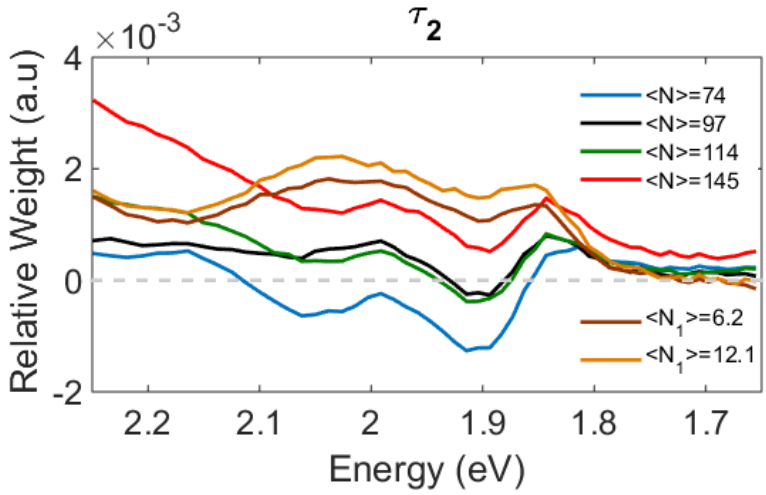

Figure C.7. Pre-exponential factors for the τ_2 components of the global fits of R=4.0 nm NCs.

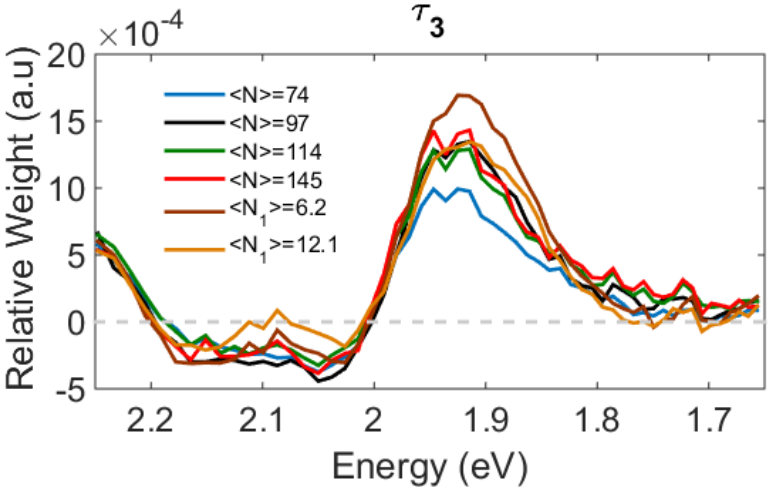

Figure C.8. Pre-exponential factors for the τ_3 components of the global fits of R=4.0 nm NCs.

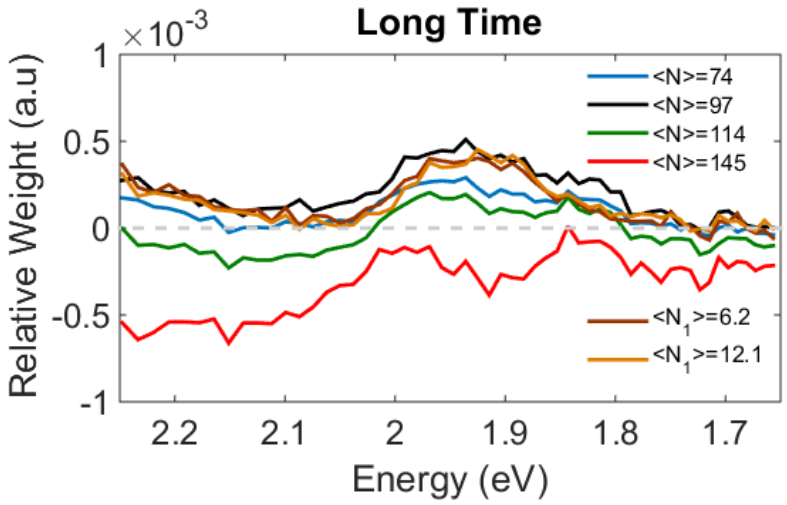

Figure C.9. Offsets representing the long time component of the global fits of R=4.0 nm NCs.

Size	$\langle N_1 \rangle$	$\langle N \rangle$	τ_1 (ps)	τ_2 (ps)	τ_3 (ps)
R=1.3	0.85	3.3	14.6 ± 0.5	73.1 ± 3.2	627±41
R=2.0	1.3	11	24.8 ± 1.8	135 ± 7	1580 ± 70
R=2.9	1.3	18	21.1 ± 1.0	136 ± 14	1720 ± 110
R=4.0	3.1	97	24.0 ± 0.9	130 ± 11	1520 ± 80

Table C.2. Kinetic fit decay constants for NC of various sizes. Uncertainties are 95% confidence intervals from the fitting algorithm.

Size	$\langle N_1 \rangle$	$\langle N \rangle$	τ_1 (ps)	τ_2 (ps)	τ_3 (ps)
R=4.0	3.1	74	16.3 ± 0.6	77.9 ± 7	1240 ± 80
R=4.0	3.1	114	20.8 ± 0.6	139 ± 7	1250 ± 60
R=4.0	3.1	145	21.6 ± 0.6	160 ± 3	2000 ± 110
R=4.0	6.2	97	27.5 ± 2.8	116 ± 5	1320 ± 60
R=4.0	12.1	97	35.0 ± 3.7	105 ± 4	1190 ± 60

Table C.3. Kinetic fit decay constants for R=4.0 nm NC for various pump fluences. Uncertainties are 95% confidence intervals from the fitting algorithm.

C.4. Power Dependence of Photoluminescence on Short and Long Timescales

The early time photoluminescence of the NCs increasingly redshifted with increasing fluence with minimal spectral changes in the total PL spectra. Further, the longtime PL kinetics don't change with increasing fluence.

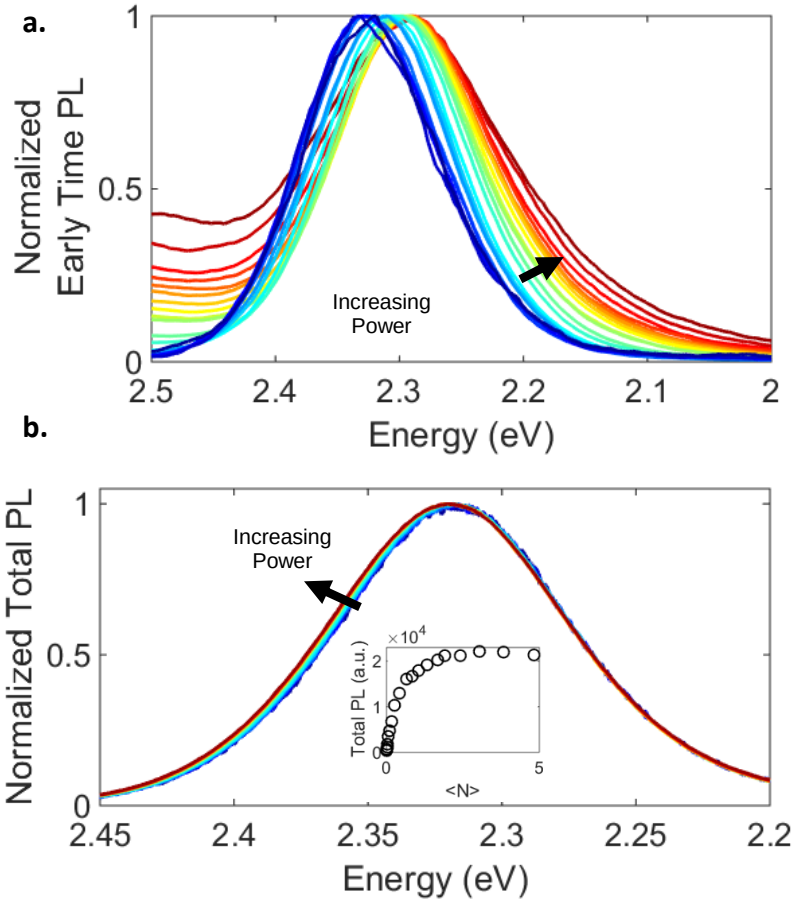

Figure C.10. (a) Normalized photoluminescence spectra of the first 20 ps following photoexcitation in 1.3 nm NCs. (b) Normalized total photoluminescence spectra as collected with a CCD. Inset: Total photoluminescence as integrated with a CCD. Fluences are the same as in (a) and (b).

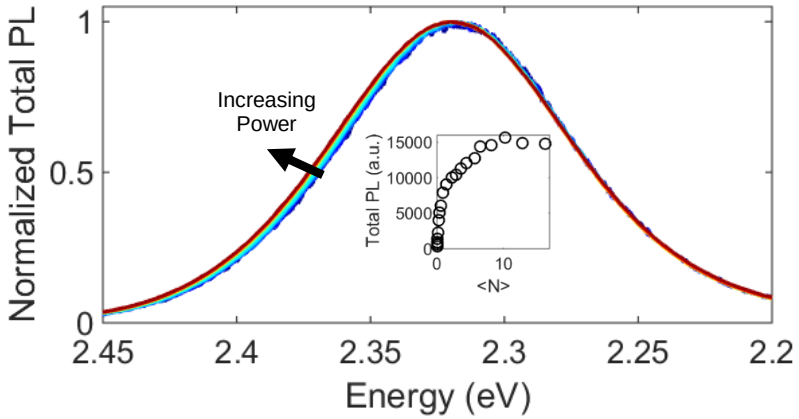

Figure C.11. Normalized total photoluminescence spectra of R=2.0 nm NCs as collected with a CCD. Inset: Total photoluminescence as integrated with a CCD. Fluences are the same as in Figure 5.5.

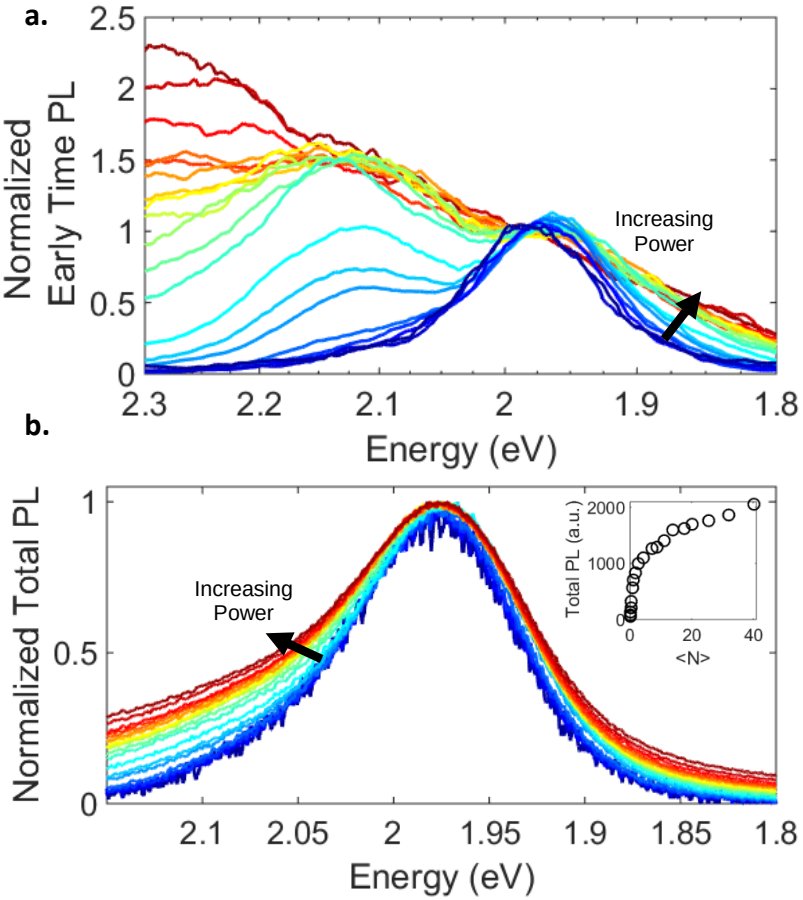

Figure C.12. (a) Normalized photoluminescence spectra of the first 20 ps following photoexcitation in 2.9 nm NCs. (b) Normalized total photoluminescence spectra as collected with a CCD. Inset: Total photoluminescence as integrated with a CCD. Fluences are the same as in (a) and (b).

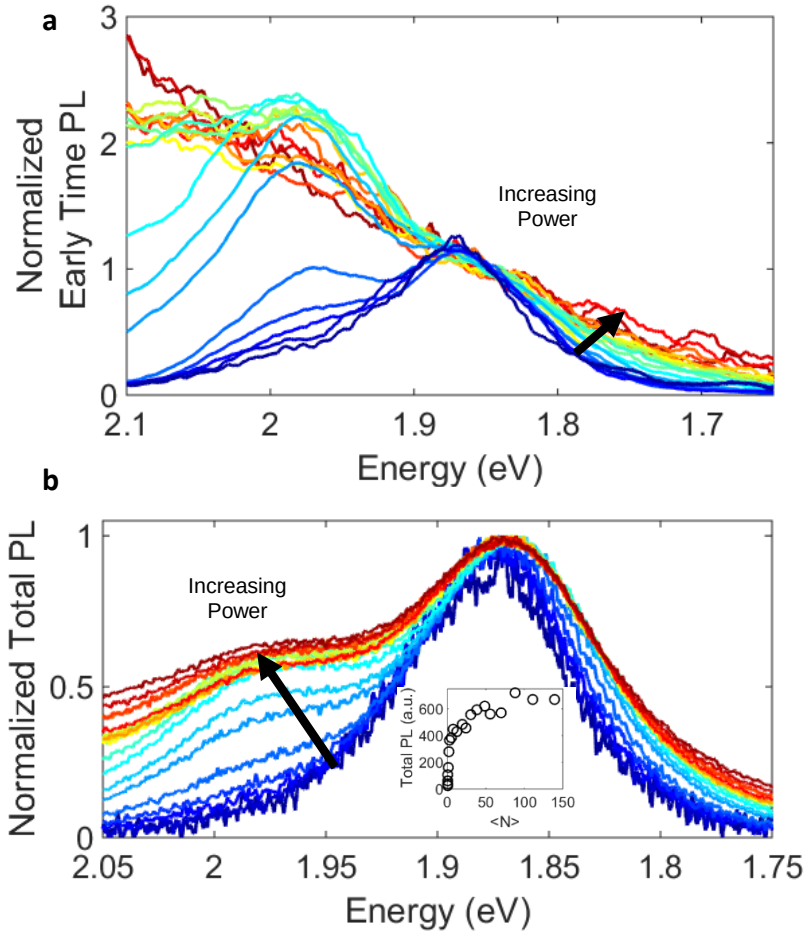

Figure C.13. (a) Normalized photoluminescence spectra of the first 20 ps following photoexcitation in 4.0 nm NCs. (b) Normalized total photoluminescence spectra as collected with a CCD. Inset: Total photoluminescence as integrated with a CCD. Fluences are the same as in (a) and (b).

Kinetics of the band edge PL are included. Notably, the decay timescales don't change with increasing fluences. At the highest fluences, there are decreases in PL intensity caused by sample degradation.

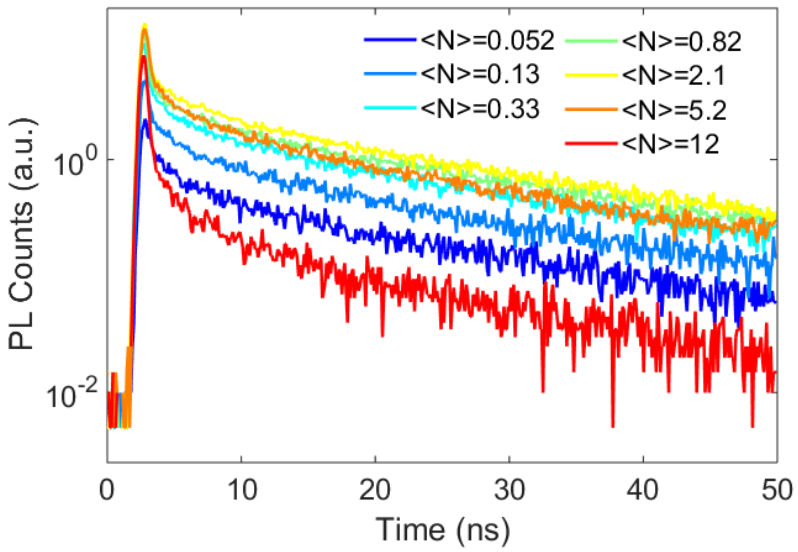

Figure C.14. Kinetics of the band edge PL of R=1.3 nm NCs as a function of fluence.

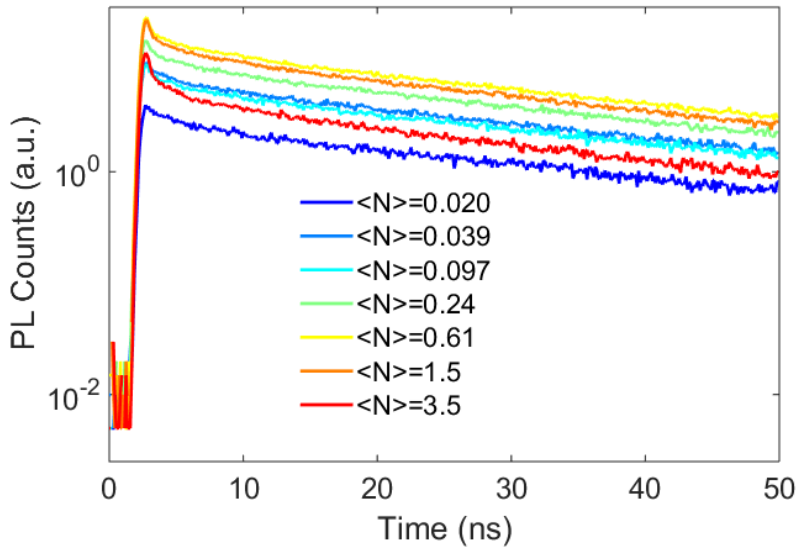

Figure C.15. Kinetics of the band edge PL of R=2.0 nm NCs as a function of fluence.

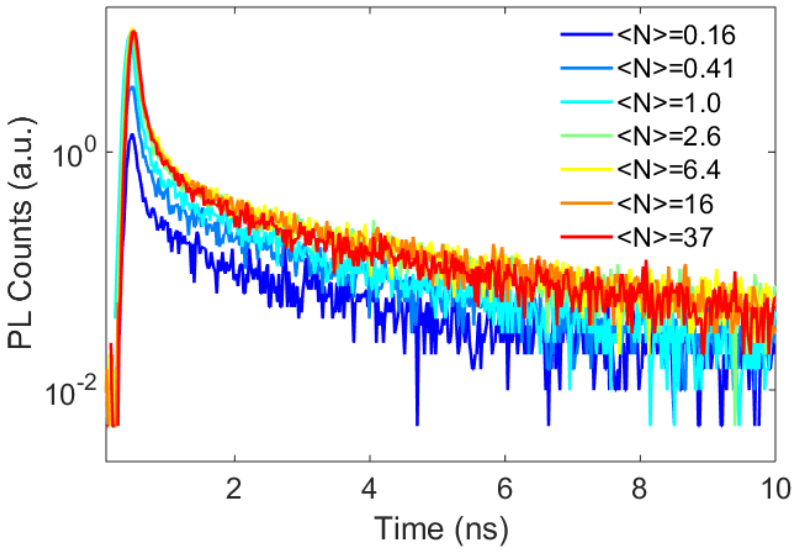

Figure C.16. Kinetics of the band edge PL of R=2.9 nm NCs as a function of fluence.

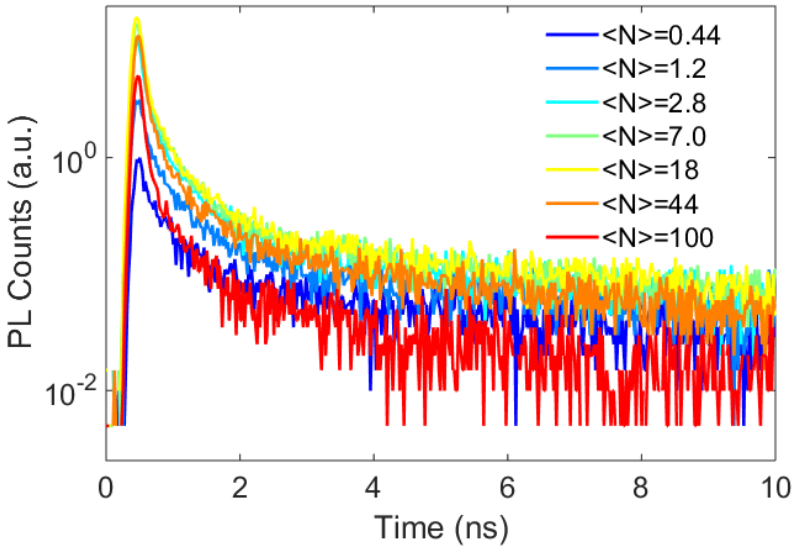

Figure C.17. Kinetics of the band edge PL of R=4.0 nm NCs as a function of fluence.

C.5. Solvent Response

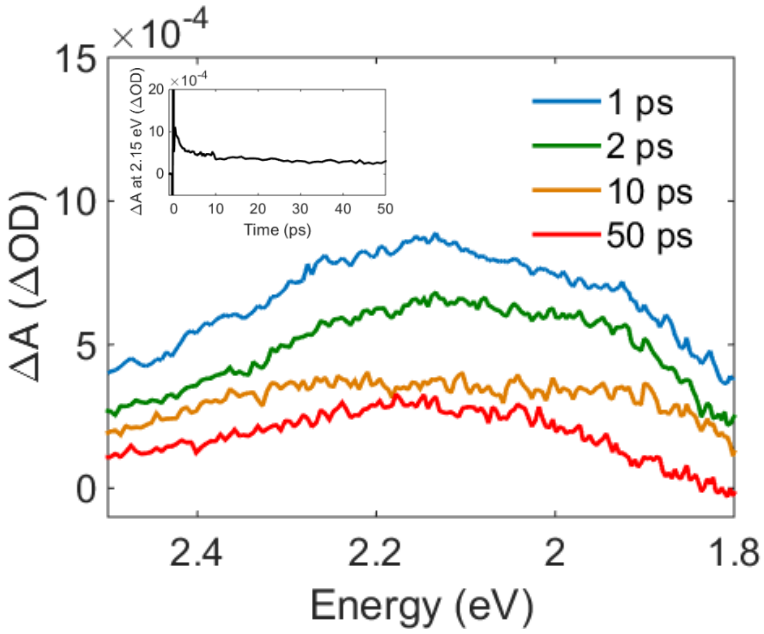

Figure C-18. TA spectra of hexanes under high fluence photoexcitation at several times. Inset: Kinetics at 2.15eV.

C.6. Varshni Relation

The Varshni relation is written:

$$E_g = E_{g0} - \frac{AT^2}{B+T} \qquad \text{(C.4)}$$

where E_g is the bandgap, T is temperature, E_{g0} is the bandgap at T=0, and A and B are material specific constants. With 0.15 photons absorbed/nm^3 (3.1 eV each) and the bulk values for density (5.81 g/cm^3) and specific heat (0.49 g/JK), there should be an increase of temperature of 26 K,

which from 300 K, would result in a reduction of the bandgap of 10.6 meV[248] which is on the order of the thermal energy of 28 meV.

APPENDIX D:SUPPORTING INFORMATION FOR SIZE-DEPENDENT COHERENT-PHONON PLASMON MODULATION AND DEFORMATION CHARACTERIZATION IN GOLD BIPYRAMIDS AND NANOJAVELINS

D.1. Transient Absorption Data Fitting

For gold bipyramids and nanojavelins, the longitudinal plasmon resonance is well modeled using Lorentzian functions. Since the photoexcited particles also present fairly low size- and aspect-ratio dispersity, the transient optical signal can be approximated as two Lorentzian functions[70,75,76,187]

$$\Delta A(\omega,t) = a(t)\left(\left(\frac{\Gamma_0}{(\omega-\omega_0)^2+(\frac{\Gamma_0}{2})^2}\right) - \left(\frac{\Gamma_\varepsilon(t)}{(\omega-\omega_\varepsilon(t))^2+(\frac{\Gamma_\varepsilon(t)}{2}))^2}\right)\right) \qquad \text{(D.1)}$$

where t is time, ω is frequency, Γ_0 and ω_0 are the static extinction width and center respectively taken from static spectra, and a(t), $\Gamma_\varepsilon(t)$, and $\omega_\varepsilon(t)$ are constants that are allowed to vary in time which represent a normalization factor, the resonance linewidth, and center frequency.

D.2. Phonon Dynamics Interpretation

As discussed in the main text, the time evolution of the LSPR center wavelength was modeled using the equation:

$$\omega_\varepsilon(t) = \sum_i \beta_i\, e^{-t/\tau_{1i}}\, e^{-\left(\frac{t}{\tau_{2i}}\right)^2} \sin\left(\frac{2\pi t}{T_i} + \varphi_i\right) + \omega_0 + \alpha e^{-t/\tau_{cool}} \qquad \text{(D.2)}$$

which includes for a given phonon mode i, the maximum coherent phonon displacement β, homogeneous lifetime τ_1, inhomogeneous lifetime due to nanoparticle polydispersity τ_2, the period of the acoustic vibrations T, and phase shift φ, along with the static LSPR position ω_0, a lattice heating term α, and a lattice cooling lifetime τ_{cool}. While fitting the data, T, φ, ω_0, and τ_2 were kept constant across excitation power. At first, these parameters were allowed to vary, but they exhibited no apparent power dependent trends and so they were kept constant to increase the stability of fitting the remaining parameters. The one exception was sample B, where ω_0, was allowed to vary in order to improve the quality of the fit. This variance was likely caused by sample inhomogeneity and was still quite small changing only by a few wavenumbers. The four other parameters were allowed to vary with excitation power. While β and phonon lifetimes are further discussed in Chapter 5, the data regarding α and τ_{cool} are included here in Figure D.1a and D.1b, respectively. Error bars here and in the main text represent 95% confidence intervals from the nonlinear least squares fitting algorithm.

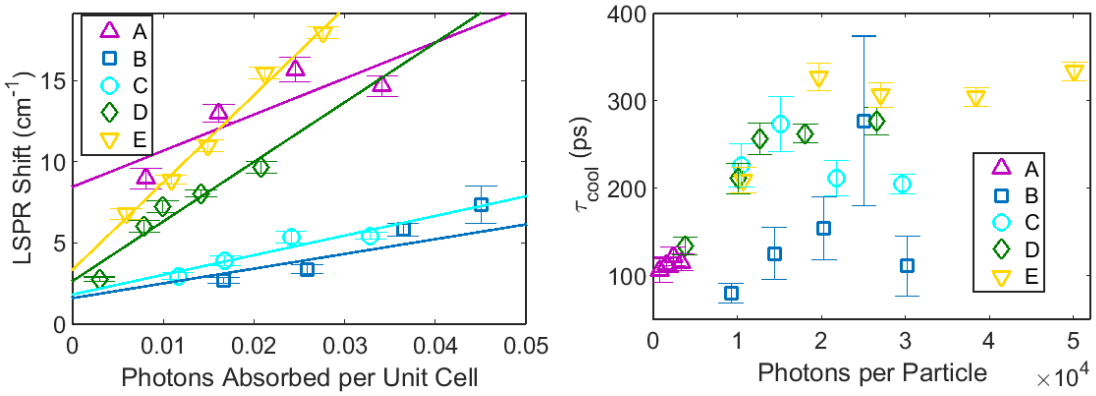

Figure D.1. (a) LSPR shift from lattice heating. (b) Fitted lattice cooling lifetimes.

D.3. Additional Damping Rate Information

The observed phonon coherence dephasing comprises several components. Damping arises from sample inhomogeneity (τ_2) as particles of different sizes in the sample will exhibit different phonon frequencies that cause oscillations to eventually become out of phase leading to an apparent damping effect. This process is well approximated by a Gaussian decay profile provided that the particle size distribution is Gaussian.[187] This lifetime can be approximated as $\tau_2 \approx T^2/\sqrt{2\pi}\sigma_T$ where σ_T is the standard deviation of the periods in the bipyramid sample with a mean period T.[187] The approximation $T/\sigma_T \approx L/\sigma_L$, where L and σ_L are the mean and standard deviation in particle length, is often applied to directly utilize distributions from TEM measurements.[75,76] By using this methodology, the accuracy of fitting τ_1 was improved, the remaining so-called homogenous decay processes which are due to energy loss. To compare decay constants between materials with drastically different oscillation periods, quality factor, $Q=\pi\tau_1/T$, was used which is the decay lifetime normalized by oscillation period. The model developed by Pelton *et al.*[70,76] was used to separate τ_1 into fluid damping (caused by solvent-phonon coupling) and intrinsic damping τ_i (caused by mechanisms within the nanoparticle). Briefly, based on particle size and geometry, the rate of damping caused by solvent interactions, Q_{fluid}, can be calculated. Once that coupling rate is determined, the intrinsic quality factor, Q_{int}, can be determined by the equation:

$$1/Q_1 = 1/Q_{fluid} + 1/Q_{int} \qquad \text{(D.3)}$$

We consider this intrinsic quality factor as it removes effects caused by differences in solvent-phonon coupling and offers comprehension of processes that occur within the various nanoparticles.

In Figures D.2 and D.3 (which display the same data but different scale bars) the dependence of Q_{int} and Q_1 on pump intensity is shown. Since the data comprises two decay terms (inhomogeneous and homogenous) it is possible for one of those decay terms to dominate the dynamics. Because the inhomogeneous damping term is determined by TEM images, it is constant throughout the fitting process. However, for several powers in samples A and C, the homogeneous lifetime was significantly higher than the inhomogeneous lifetime preventing effective parameter fitting. For these instances, only a lower error bars is plotted since this indicates the lower bound of that quality factor. However, the upper bound of this parameter or even its precise value cannot be accurately estimated. Therefore, while sample A might appear to exhibit relatively low quality factors, that is more a result of the sample inhomogeneity rather than actual low quality factors. To make this clearer, inhomogeneous lifetime normalized by oscillation period ($Q_{inh}=\pi\tau_2/T$) are included. Additionally, Q_{fluid} is included in these Figures to offer a sense of its relative effect.

Prior reports pointed to a linear relationship between excitation power and Q_1. [70,76] However, it is experimentally observed that quality factors plateau at higher excitation fluxes. It is unlikely that particle melting causes this trend as careful efforts was taken to minimize degradation as discussed in Figure D.5. The origin of this relationship is unclear, but may potentially be caused by heating changing the solvent viscosity. [70] It is worth noting that the quality factors observed here are higher than have been previously observed for bipyramids in water.[70,75,76] This trend could

be explained by the fact that the prior effort calculated a quality factor via linear extrapolating to zero power. Since quality factors increase with excitation power, it follows that the values reported here are larger.

Additionally, there seems to be a weak correlation between sample size and Q_{int} with larger particles exhibiting smaller quality factors. The exception is sample A, which is explained above. Examining the TEMs it seems that larger bipyramids exhibit rougher surfaces than smaller bipyramids, which could indicate lower crystalline quality leading to faster damping. This trend is demonstrated in the TEM images in Figure D.4. The smaller bipyramids have boundaries that are clearly defined by straight lines and correspondingly have very high quality factors. However, the outline of the larger particles are distorted and as a result they have lower quality factors. If larger particles present lower crystallinity, rather than having larger size directly cause the lower quality factors this would explain why the trend is so weak. This dependence on crystallinity is consistent with what has been proposed regarding quality factors of nanorods; higher crystallinity corresponds to larger quality factors.[215] These results suggest that it may be possible to increase phonon coherence lifetime by manipulating bipyramid crystallinity. It is worth noting, that additional analysis on less complete data sets yielded very similar results.

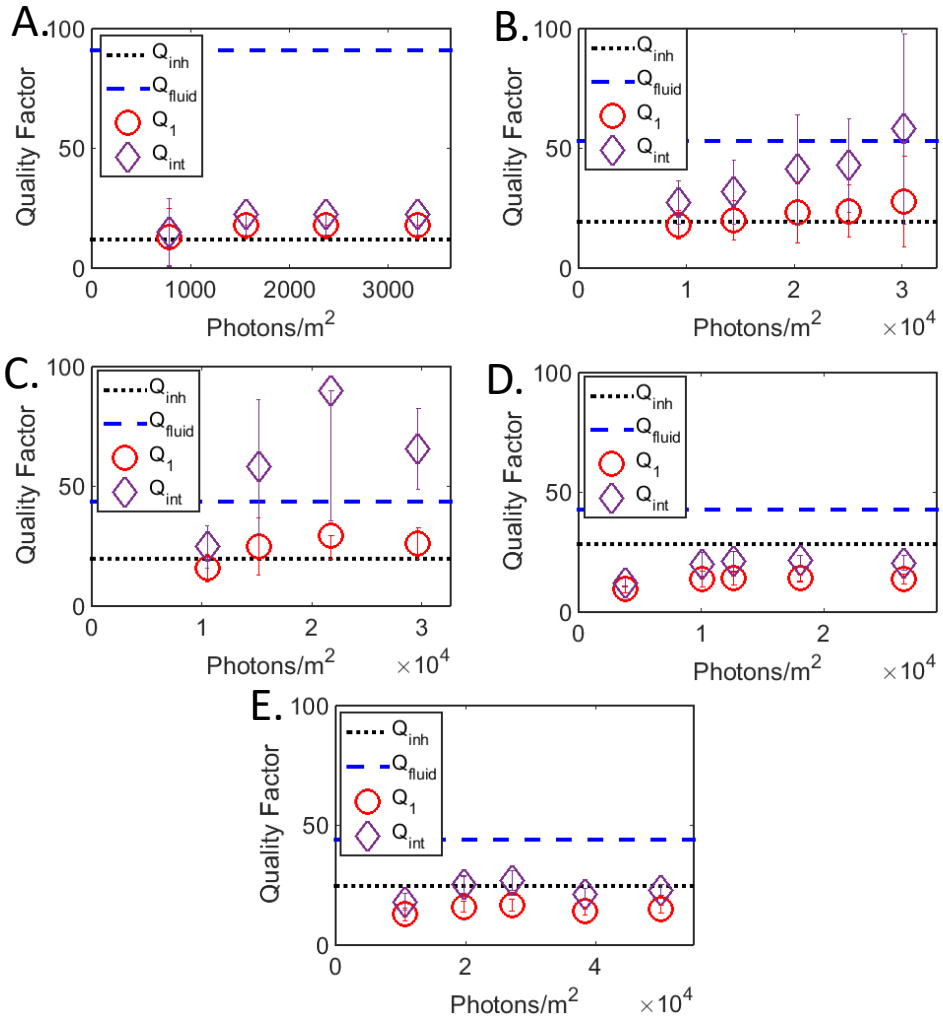

Figure D.2. Various quality factors of samples A-E.

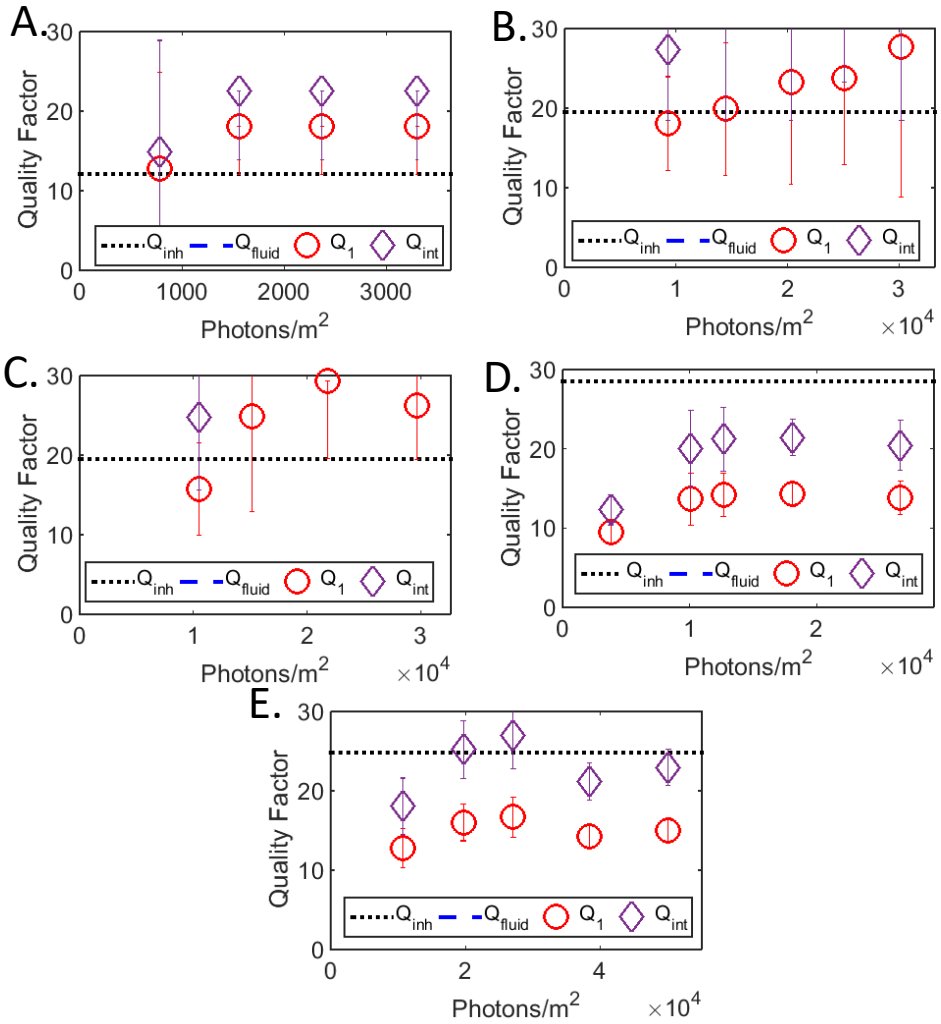

Figure D.3 . Zoomed-in sections of the data in Figure D.2.

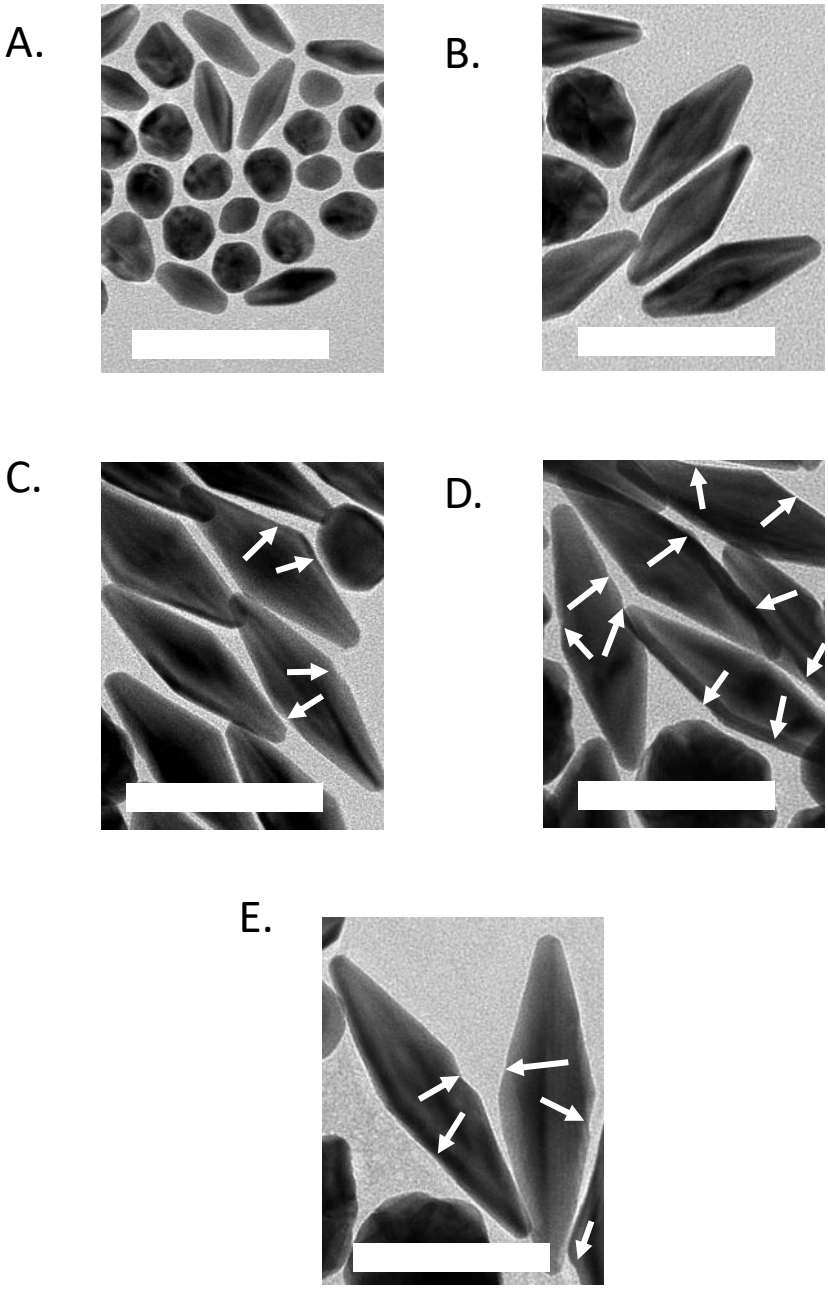

Figure D.4. Larger view of TEM images of the bipyramid samples discussed in Chapter 5. White scale bars represent 100 nm. Arrows point to notable surface irregularities.

D.4. Sample Damage

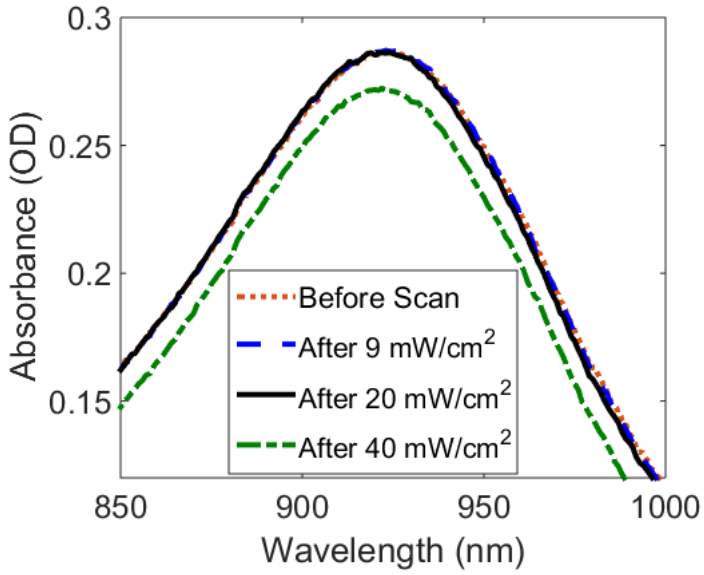

Figure D.5. Extinction spectra of sample E before and after several transient absorption scans where 1 kHz pump fluence is indicated. Probe fluence was negligible.

Solutions were rapidly stirred during transient optical experiments. To ensure properties of the bipyramids were measured rather than effects related to irreversible sample damage, extinction spectra before and after each scan were examined and only reproducible scans are examined. Figure D.5 shows the spectra of sample E before and after several scans.

D.5. Details of Sample Dimensions, Total Expansion, and Calculated Cross-Sections

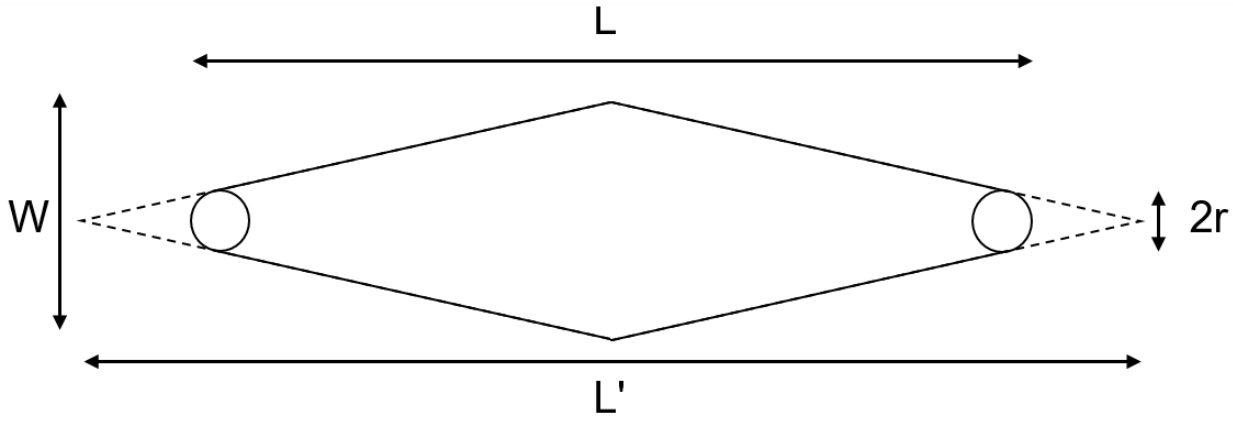

Figure D.6. Bipyramid with relevant dimensions labeled.

In addition to the particle length (L), width (W), and radius (r), an important parameter is projected length which is calculated geometrically for each particle using the formula:

$$(L' - (L - 2r))/(2r) = L'/W \qquad (D.4)$$

$$L'\left(1 - \frac{2r}{W}\right) = L - 2r \qquad (D.5)$$

$$L' = \frac{L-2r}{\left(1-\frac{2r}{W}\right)} \qquad (D.6)$$

The volume of the bipyramid is then calculated from the ensemble average using the formula:

$$V = \frac{\pi L'}{3}\left(\frac{W}{2}\right)^2 + \frac{4\pi r^3}{3} - 2\left(\frac{\pi r^2}{3}\left(\frac{L'}{2} - \frac{L}{2} + r\right)\right) \qquad (D.7)$$

From there, by using the density of gold, and the assumption of four atoms per unit cell, the number of unit cells is estimated.

Sample	Length (nm)	Width (nm)	Radius of Curvature (nm)	Aspect Ratio	Estimated Number of Unit Cells
A	45.6±2.7	18.7±0.9	5.2±0.3	2.45±0.14	9.67×10^{4}
B	94.0±3.4	33.1±1.5	6.8±0.4	2.85±0.16	5.57×10^{5}
C	122.9±4.5	38.3±2.9	6.1±0.4	3.23±0.28	9.03×10^{5}
D	146.4±3.6	41.9±2.2	6.3±0.5	3.51±0.21	1.28×10^{6}
E	168.6±4.8	46.6±3.5	6.8±0.6	3.64±0.29	1.81×10^{6}
F	139.9±5.9	29.3±1.0	7.5±0.6	4.77±0.27	7.70×10^{5}
G	198.1±4.7	33.0±1.3	8.71±1.5	6.01±0.30	1.46×10^{6}

Table D.1. Bipyramid and nanojavelin sizes measured via TEM images.

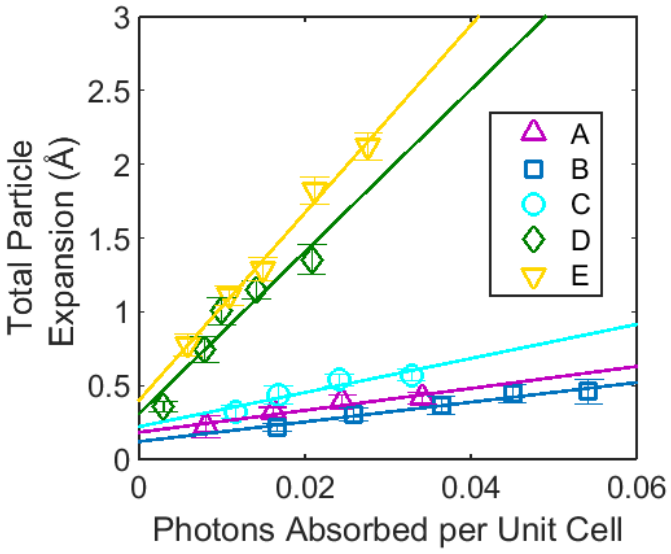

Figure D-7. Total expansions of the particles from the lowest-order coherent acoustic phonon.

Sample	Absorption Cross Section (m^2)	Scattering Cross Section (m^2)
A	3.86×10^{-15}	5.62×10^{-16}
B	1.78×10^{-14}	2.01×10^{-14}
C	2.37×10^{-14}	4.36×10^{-14}
D	2.63×10^{-14}	6.00×10^{-14}
E	2.73×10^{-14}	8.87×10^{-14}

Table D.2. Bipyramid Absorption and Scattering Cross Sections at λ_{max} from FDTD calculations

APPENDIX E:SUPPORTING INFORMATION FOR PHONON-DRIVEN OSCILLATORY PLASMONIC EXCITONIC NANOMATERIALS

E.1. Finite Difference Time Domain Calculations

The calculated extinction spectra of the TCC-AuBPs are shown in Figure E.1. Particle expansions took place in increments of 0.02% from -0.1% up to 0.1%.

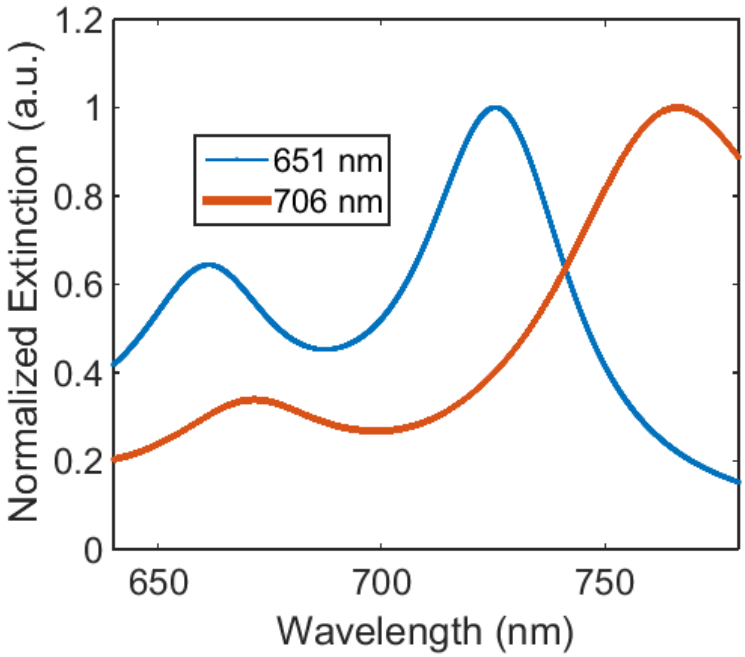

Figure E.1. Extinction spectra of TCC-AuBPs from FDTD calculations.

E.2. Time Resolved Photoluminescence

The AuBP-TCC complexes have short lived, fluorescent states. Figure E.2 shows how the photoluminescence intensity evolves with time as observed with a streak camera. Notably, the

photoluminescence decay is almost instrument limited and has decayed away within a few ps, consistent with the short electronic lifetimes of TCC and AuBPs.

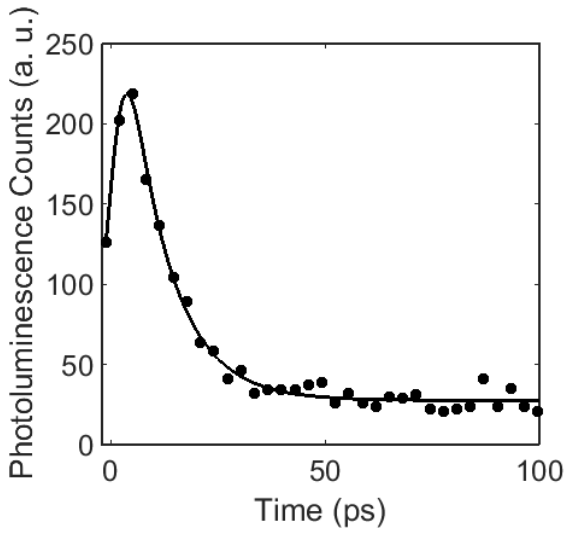

Figure E.2. Time Resolved Photoluminescence of a representative TCC-AuBP spectra along with an instrument response function convoluted single exponential fit.

APPENDIX F:SUPPORTING INFORMATION FOR OSCILLATION ASSOCIATED SPECTRA ELUCIDATE PHONON-INDUCED CHANGES IN PLASMON-EXCITON COUPLING

F.1. Additional Bipyramid Oscillation Associated Spectra Compared to Static Extinction

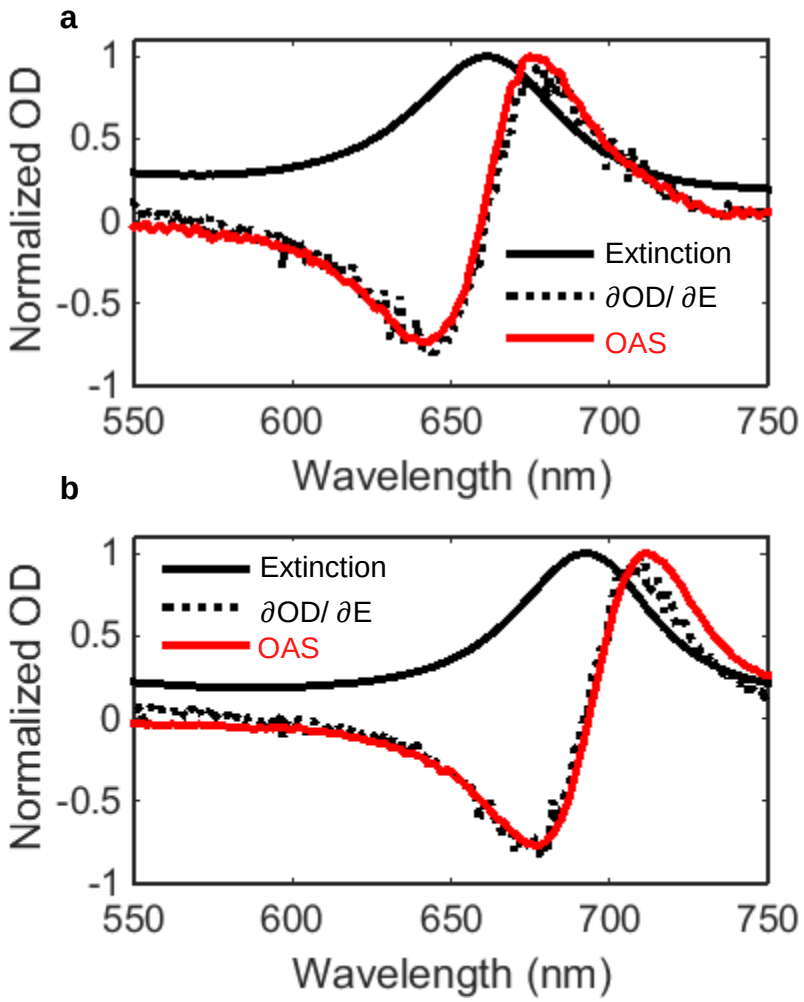

Figure F.1. Static extinction spectra (solid black), its derivative (dashed black), and oscillation associated spectra at the maximum Fourier transform magnitude (red) for two additional bipyramid ensembles.

F.2. Phase Behavior of an Oscillatory Plasmonic Excitonic Nanomaterial

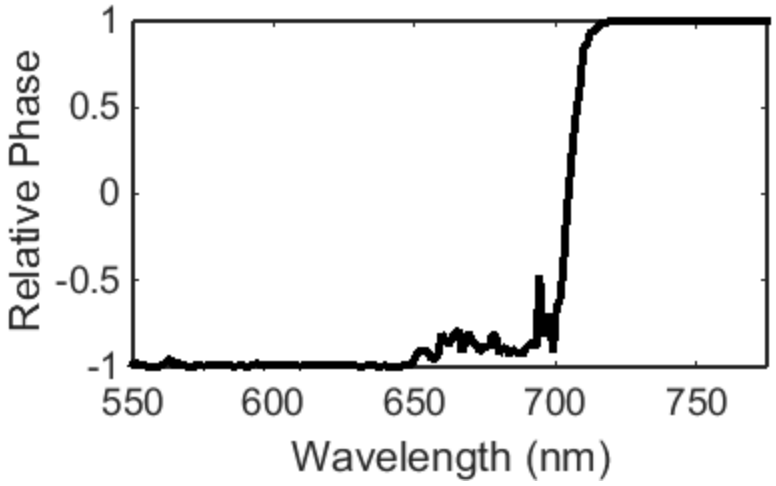

Figure F.2. Relative phase behavior of gold bipyramids functionalized with TCC as described in Chapter 8. Notably, there is some noise from 650-700 nm owing to the low oscillation magnitude at those wavelengths. Here λ_{max} =726 and λ_{end} =738 nm.

F.3. Other Parameters Derived While Calculating Oscillation Associated Spectra

Starting with the spectra in Figure 8.1b, it is trivial to calculate the magnitude and phase of the Fourier transform. Specifically discrete Fourier transformations were performed at every frequency of interest, although it is equivalent to performing a Fast Fourier transformation after zero padding the data. Figure F.3 shows the Fourier transform magnitude, averaged across all wavelengths. Figure F.4 shows the Fourier transform magnitude averaged across all frequencies. The region of high Fourier transform magnitude on the redder edge of the spectra was used to calculate the reference phase and is highlighted with a gray box. The cos of the reference phase (θ_0) versus oscillation period is displayed in Figure F5 and the resulting phase map ($\cos(\theta')$) is shown in Figure F.6.

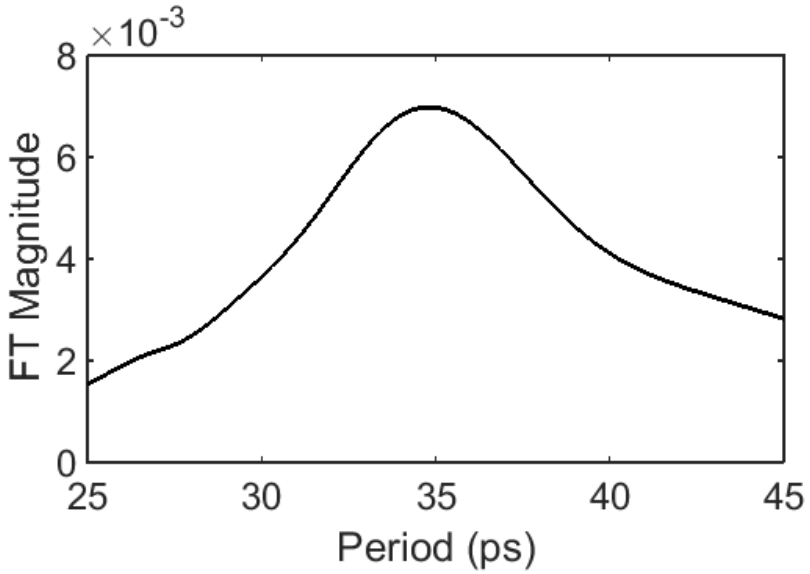

Figure F.3. The Fourier Transform magnitude averaged across all wavelengths versus oscillation period.

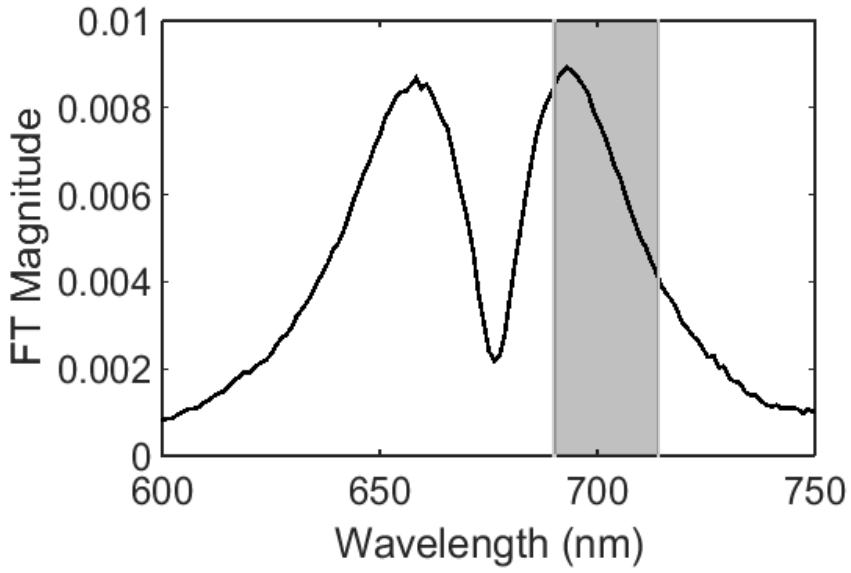

Figure F.4. The Fourier Transform magnitude averaged across all calculated frequencies versus wavelength. The region in gray was defined as λ_{max} to λ_{end} for the OAS.

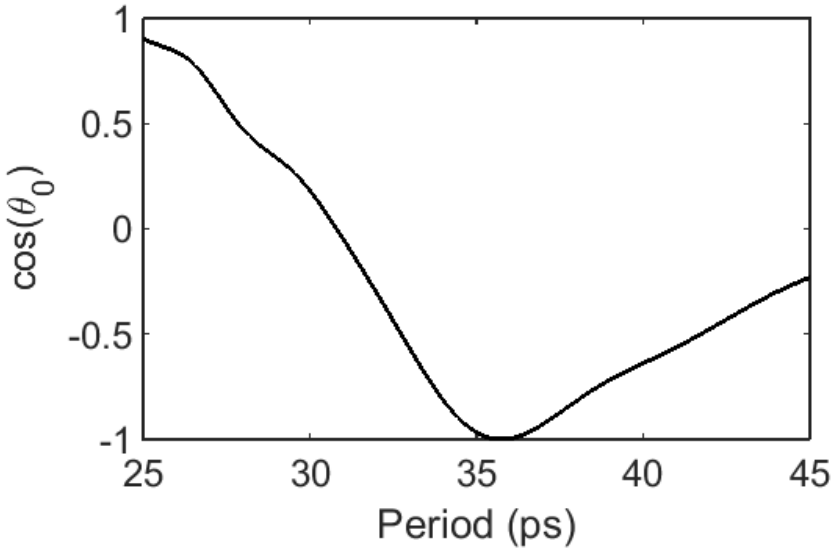

Figure F.5. The cosine of reference phase (θ_0) versus oscillation period.

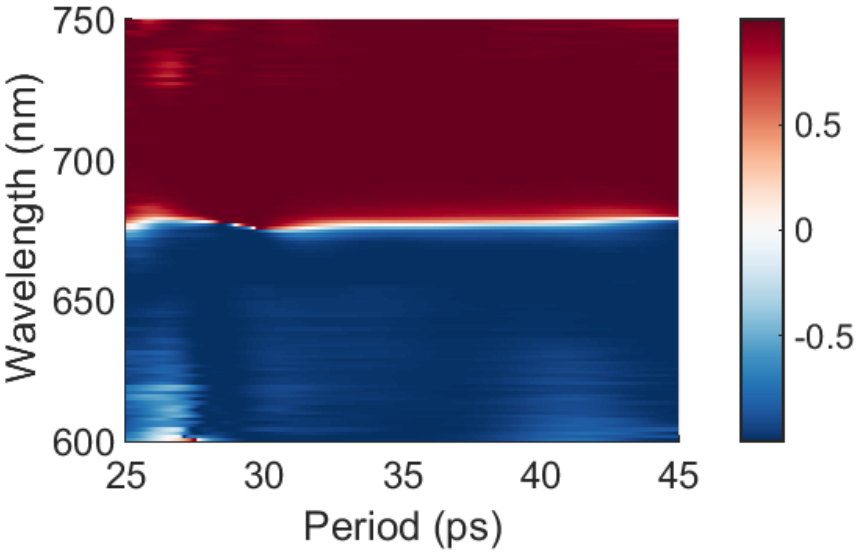

Figure F.6. The relative phase of the data, or $\cos(\theta'(\lambda, f))$.

CURRICULUM VITA

PERSONAL INFORMATION

Matthew S. Kirschner, Chicago, IL | (614) 390-6897 | kirschner.21@gmail.com

EDUCATION

PhD: Northwestern University, April 2019
Field of study: Chemistry

A.B. *Magna Cum Laude*, Princeton University June 2014
Field of study: Chemistry. Certificate in Material Science and Engineering

RESEARCH AND PROFESSIONAL EXPERIENCE

Graduate Student Researcher 2014-2019
Mentors: Richard Schaller and Lin Chen, Northwestern University
Project Title: Electronic Implications of Thermal Processes in Nanomaterials

My thesis addresses thermal processes in nanomaterials. I have used an array of ultrafast spectroscopic techniques including transient absorption, pump-pump probe, transient photoluminescence, and transient x-ray diffraction to study how nanomaterials dissipate energy after photoexcitation. My research has focused on low-order acoustic phonons in gold bipyramids, as well as the general phenomenon of photoinduced, reversible phase transitions in semiconductor nanocrystals. Through the course of these studies, I have written significant data processing software in MATLAB to visualize and fit the gathered data.

Undergraduate Student Researcher 2013-2014
Mentor: Herschel Rabitz, Princeton University
Project Title: Evaluating Incoherent Control of Population Dynamics as a Tool for Next Generation Photochemistry

I designed a system to demonstrate that relative energy level populations could be controlled by an incoherent light source that was shaped with a genetic algorithm. The specific systems I investigated were up-converting lanthanide ions embedded in crystalline matrices that were obtained through a collaboration I facilitated with a local company.

Leach Summer Scholars Program Summer 2012
Mentor: Herschel Rabitz, Princeton University
Project Title: Exploring Control Landscapes Using Nuclear Magnetic Resonance Spectroscopy

I worked on a project whose goal was to experimentally confirm several principles about quantum control landscapes using Nuclear Magnetic Resonance Spectroscopy. To this end, I performed numerous computational simulations to help design the eventual experiments.

Intern at The OSU Center for Materials Research Summer 2011
Mentor: Arthur Epstein, Ohio State University
Project Title: Thickness Dependence of Organic Spin Valves/Excited State Vibrations of PDI Derivatives

I assisted with two projects. In the first project—which involved investigating thickness dependence of organic spin valves—I assisted in the fabrication of said spin-valves. The second project involved determining the optical properties of organic photovoltaics. I assisted in the acquisition of femtosecond stimulated Raman spectroscopy spectra and independently acquired numerous UV-Vis and fluorescence spectra.

PUBLICATIONS

Kirschner, M.S.; Diroll, B.T.; Guo, P.; Harvey, S.M.; Helweh, W.; Flanders, N.C.; *et al.* Photoinduced, Reversible Phase Transitions in All-Inorganic Perovskite Nanocrystals. *Nature Comm*. 2019, 10, 504.

Kirschner, M.S.; Diroll, B.T.; Brumberg, A.; Leonard, A.A.; Hannah, D.C.; Chen, L.X.; Schaller, R.D. Optical Signatures of Transiently Disordered Semiconductor Nanocrystals. *ACS Nano* **2018**, *12,* 10008-10015.

Laforge, F.O.; **Kirschner, M.S.**; Rabitz, H.A. Shaped Incoherent Light for Control of Kinetics: Optimization of Up-Conversion Hues in Phosphors. *J. Chem. Phys.* **2018**, *149*, 054201.

Harvey, S.M.; Phelan, B.T.; Hannah, D.C.; Brown, K.E.; Young, R.M.; **Kirschner, M.S.**; Wasielewski, M.R.; Schaller, R.D. Auger Heating and Thermal Dissipation in Zero-Dimensional CdSe Nanocrystals Examined Using Femtosecond Stimulated Raman Spectroscopy. *J. Phys. Chem. Lett.* **2018**, *9*, 4481-4487.

Evans, A.M.; Parent, L.R.; Flanders, N.C.; Bisbey, R.P.; Vitaku, E.; **Kirschner, M.S.**; Schaller, R.D.; Chen, L.X.; Gianneschi, N.C.; Ditchel, W.R. Seeded Growth of Single-Crystal Two-Dimensional Covalent Organic Frameworks. *Science* **2018**, *361*, 52-57.

Kirschner, M.S.; Ding, W.; Li, Y.; Chapman, C.T.; Lei, A.; Chen, L.X.; Schatz, G.C.; Schaller, R.D. Phonon-Driven Oscillatory Plasmonic Excitonic Nanomaterials. *Nano Lett.* **2018**, *18*, 442-448.

Kirschner, M.S.; Hannah, D.C.; Diroll, B.T.; Zhang, X.; Wagner, M.J.; Hayes, D.; Chang, A.Y.; Rowland, C.E.; Lethiec, C.M.; Schatz, G.C.; Chen, L.X.; Schaller, R.D. Transient Melting and Recrystallization of Semiconductor Nanocrystals Under Multiple Electron–Hole Pair Excitation. *Nano Lett.* **2017**, 17, 5314-5320.

(**Editors' Choice)**

Kirschner, M.S.; Lethiec, C.M.; Lin, X.M.; Schatz, G.C.; Chen, L.X.; Schaller, R.D. Size-Dependent Coherent-Phonon Plasmon Modulation and Deformation Characterization in Gold Bipyramids and Nanojavelins. *ACS Photon.* **2016**, *3*, 758-763.

Diroll, B.T.; **Kirschner, M.S.**; Guo, P.; Schaller, R.D. Optical and Physical Probing of Thermal Processes in Semiconductor and Plasmonic Nanocrystals. *Ann. Rev. Phys. Chem. In Review.*

Fauvell, T.J.; Cai, Z.; **Kirschner, M.S.**; Helweh, W.; Kim, P.; Zheng, T.; Schaller, R.D.; Yu, L.; Chen, L.X. Transfer Character and Ultrafast Dynamics in Organic Semiconducting Polymer PTB7 Revealed by Oligomer Models. *J. Phys. Chem. C In Review*.

Kirschner, M. S.; Jeong, Y.; Spencer, A. P.; Watkins, N. E.; Lin, X.-M.; Schatz, G. C.; Chen, L. X.; Schaller, R. D Oscillation Associated Spectra Elucidate Phonon-Induced Changes in Plasmon-Exciton Coupling. *In Prep.*

Flanders, N. C.; **Kirschner, M. S.**; Kim, P.; Evans, A. M.; Fauvell, T. J.; Helweh, W.; Spencer, A. P.; Schaller, R. D.; Dichtel, W. R.; Chen, L. X. Ultrafast Dynamics in Two Dimensional Covalent Organic Frame-works Reveals Large Diffusion Coefficients. *In Prep.*

PRESENTATIONS & POSTERS

Talk at Material Research Society 2019
Title: Photoinduced, Reversible Phase Transitions in Semiconductor Nanocrystals
2019 Material Research Society Fall Meeting

Poster at Material Research Society 2019
Title: Oscillatory Plasmonic-Excitonic Nanomaterials
2019 Material Research Society Spring Meeting

Spectroscopy and Theory Seminar 2018
Title: Utilizing Nanomaterial Acoustic Phonons: The Future is OPEN
Northwestern University

APS User Science Symposium 2018
Title: Transient Melting and Recrystallization of Semiconductor Nanocrystals
Argonne National Laboratory

Talk at Material Research Society 2017
Title: Transient Melting and Recrystallization of Semiconductor Nanocrystals
2017 Material Research Society Fall Meeting

Poster at Material Research Society 2017

Title: Coherent-Phonon Plasmon Modulation and Deformation Characterization and Applications of Gold Bipyramids and Nanojavelins
2017 Material Research Society Fall Meeting
(**Session Best)**

AWARDS, FELLOWSHIPS, & GRANTS

Travel Grant 2017, 2019
The Graduate School at Northwestern University

Honorable Mention Poster 2019
Evanston Love Data Week Poster Contest

Session Best Poster 2017
2017 Material Research Society Fall Meeting

Travel Grant 2017
Northwestern Phi Lambda Upsilon Chapter

Editor's Choice Article 2017
Nano Letters

Hypercube Award 2014
Princeton University Chemistry Department

PPST Summer Internship 2013
Program in Plasma Physics at Princeton University

Leach Summer Scholar 2012
Princeton University Chemistry Department

National Merit Scholar Finalist 2010
National Merit Scholarship Corporation

Eagle Scout 2009
Boy Scouts of America

LEADERSHIP AND TEACHING

President of Academics for Careers in Data Science 2018-present

I founded a group at Northwestern for students to develop data science skills. In this capacity, I presented on data science techniques and strategies for solving coding challenges. I also lead data science projects on analyzing policing data and predicting topics of academic papers from their text.

Teaching Assistant 2014-2018
I taught lab sections for 8-16 undergraduate students in general chemistry in 2014 and 2015 as well as assisting in classes on thermodynamics/statistical mechanics and chemical kinetics for ~10~20 students and nanotechnology for ~40 students from 2015- 2018 (one class each year). My responsibilities included assisting in the writing and grading of homework problem sets and exams, holding weekly office hours, and lecturing at review sections and when the professor was absent.

Phi Lambda Upsilon Social Chair 2016-2017
I was the social chair of the Northwestern Chapter of Phi Lambda Upsilon, a chemistry graduate student organization. In addition to attending board meetings and awarding travel grants, I organized monthly social events with an annual budget around $10,000

Mentor in Junior Science Club 2015-2017
I guided primary school students through science and engineering modules that emphasized critical thinking skills in Junior Science Club at Northwestern University's Science in Society Office.

PROFESSIONAL SOCIETY MEMBERSHIPS

Material Research Society	2017-present
American Chemical Society	2016-present
Phi Lambda Upsilon	2016-present
Sigma Xi: The Research Society	2014